

**Ultracold Bose gases under rotation, in lattice
potentials, and both**

by

Volker Schweikhard

Diplom Physik, University of Stuttgart, 2001

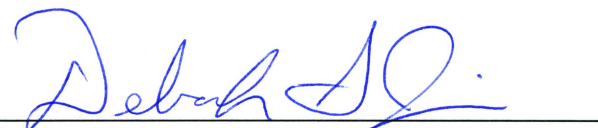
A thesis submitted to the
Faculty of the Graduate School of the
University of Colorado in partial fulfillment
of the requirements for the degree of
Doctor of Philosophy
Department of Physics

2008

This thesis entitled:
Ultracold Bose gases under rotation, in lattice potentials, and both
written by V. Schweikhard
has been approved for the Department of Physics



Eric A. Cornell



Deborah S. Jin

Date 12/4/08

The final copy of this thesis has been examined by the signatories, and we find that both the content and the form meet acceptable presentation standards of scholarly work in the above mentioned discipline.

Schweikhard, Volker (Ph.D., Physics)

Ultracold Bose gases under rotation, in lattice potentials, and both

Thesis directed by Prof. Eric A. Cornell

In the field of ultracold atoms, two major recent research directions have been rapidly rotating Bose-Einstein condensates, and condensates loaded into optical lattice potentials. While past optical lattice work has concentrated largely on the regime of few correlated particles per lattice site, in this thesis the opposite limit of tunnel-coupled arrays of macroscopic condensates – Josephson junction arrays – is studied. Combining such Josephson junction arrays with rapidly rotating BECs yields highly complex quantum fluid systems with many analogies to condensed-matter systems. In particular, optical lattice potentials allow the creation of low-dimensional, or *effectively low-dimensional* systems.

- In this thesis, the first *rotating* two-dimensional optical lattice potential for ultracold atoms was created, which served as a periodic pinning potential for vortices, and induced a structural crossover in the vortex lattice.
- The Berezinskii-Kosterlitz-Thouless superfluid transition was studied in a non-rotating, finite-temperature, two-dimensional array of Josephson junctions.
- Rapidly rotating BECs were loaded into a one-dimensional optical lattice aligned with the rotation axis. A crossover from a coherent array of Josephson-coupled rotating BECs, to an array of isolated, two-dimensional rotating BECs was observed, and the ensuing vortex lattice fluctuations were studied.
- Studies of vortex lattices in rotating BECs were extended to *two-component* BECs, where a self-organization of vortices in the two components into two interlaced square vortex lattices was observed.

Dedication

Für Isabell , für meine Eltern und für meine Brüder.

Acknowledgements

It has been an extraordinary time for me since this thesis begun, and there are many people I wish to acknowledge: First and foremost I would like to thank my advisor, Eric Cornell. I have enjoyed a very pleasant working relation with him, and benefitted enormously from his incredible intuition and enthusiasm for physics. I also thank him for his thoughtful advice on all other matters.

I had the pleasure of working with several extremely talented and and enthusiastic colleagues during the years – they really deserve most thanks: Peter Engels, Ian Coddington and Shihkuang Tung. Peter and Ian introduced me to the tricks and trades of B224, and taught me an immense amount of physics during my first years on the experiment. I also thank Peter for a thorough reading of this thesis and many helpful comments. Shihkuang worked tirelessly with me on almost all experiments described in this thesis – I wish him success with all his future plans. Giacomo Lamporesi very recently restored the European presence in the lab; I thank him for his very helpful comments on this thesis. I thank Debbie Jin and Carl Wieman for supervising our experiment and the whole group in that crazy winter 2004/2005, and for countless suggestions on anything from the experiment to presentation skills. I benefitted enormously from discussions and equipment loans from all members of the Tri-Group – they all helped make this thesis a very pleasant experience. A big thanks goes to Pam Leland for keeping everyone organized, safe, happy, and environmentally sound. Thanks also to Marco Cozzini, Veronique Mogendorff and Melissa Friedman who made contributions

as short-term visitors in the lab.

This work could not have been possible without the hard work of all earlier students and postdocs in B224, who did a terrific job in delivering an (almost) flawlessly working BEC machine on which all the successes of this thesis were built. Just as important were the contributions from the excellent staff of the JILA Electronics Workshop, the Instrument Shop, the Supply Office, and all the other people who make JILA work.

We were extremely lucky to capture the interest of a large number of theorists at various points. All of them contributed in one or the other way to an improved understanding of our experiments: Very welcome local support on condensed-matter related topics came from Leo Radzihovsky, Victor Gurarie and Dan Sheehy. Murray Holland, Rajiv Bhat and Meret Krämer taught us a lot about rotating BECs, optical lattices, and other things. We had a very insightful collaboration on shock waves with Mark Ablowitz and Mark Hoefer. An extraordinary amount of external input came from Jason Ho, Gordon Baym, Chris Pethick, Gentaro Watanabe, Alexander Fetter, Sandro Stringari, Iacopo Carusotto, Rob Ballagh, Eugene Demler, Erich Mueller, James Anglin, Nigel Cooper, Jasper Reijnders, Masahito Ueda, Kenichi Kasamatsu, Kazushige Machida, Henk Stoof, Nick Bigelow, and their coworkers.

Lastly, I thank Tom Parker, Steve Jefferts and Tom Heavner at NIST for introducing me to atomic fountain clocks, which made for a very good “first year experience” in Boulder.

Contents

Chapter	
1 Introduction	1
1.1 Background	1
1.2 Bose-Einstein condensation	5
1.2.1 Quantum statistics: Ideal gas Bose-Einstein condensation	5
1.2.2 Quantum fluids: Importance of interparticle-interactions	8
1.2.3 Thomas-Fermi regime	9
1.2.4 Condensates at finite temperature	10
1.3 Rotating Bose-Einstein condensates	11
1.3.1 Quantized vortices in a superfluid	11
1.3.2 Vortices – from one to many	13
1.3.3 Manipulating vortices	16
1.4 The two-dimensional (2D) Bose gas	19
1.4.1 The Berezinskii-Kosterlitz-Thouless transition	20
1.5 Josephson Junction arrays of BECs in optical lattice potentials	23
1.5.1 Optical dipole potentials - versatile tools for BEC manipulation	23
1.5.2 Two Josephson-coupled BECs	25
1.5.3 Arrays of Josephson-coupled BECs	29
1.5.4 Thomas-Fermi description of BECs in optical lattices	33
1.6 BEC imaging	35

1.7	History and organization of this thesis	37
2	Vortex pinning in rotating Bose-Einstein condensates	39
2.1	Motivation	39
2.2	Setup, alignment and diagnostics	41
2.3	Observation of vortex pinning in Bose-Einstein condensates	52
2.3.1	Angular locking of the vortex lattice to a hexagonal optical lattice	52
2.3.2	Pinning-induced structural vortex lattice crossover	56
2.3.3	Defects in pinned vortex lattices	60
2.3.4	Pinning with two vortices per pinning site	62
2.3.5	Pinning with one vortex per two pinning sites	63
3	A 2D Josephson junction array in the Berezinskii-Kosterlitz-Thouless regime	64
3.1	Motivation	64
3.2	The BKT transition in a Josephson junction array	65
3.3	Setup, calibrations and parameter determination	67
3.3.1	Optical lattice intensity calibration	69
3.3.2	Getting J/T right	70
3.3.3	The importance of the third (z) dimension	74
3.4	Experiments and results	74
3.4.1	Thermally activated vortex proliferation	75
3.4.2	Studying vortex pair sizes and vortex pair unbinding	81
4	Rapidly rotating 2D Bose gases in a 1D optical lattice	87
4.1	Motivation	87
4.1.1	The physics of a finite-temperature array of rotating 2D Bose gases	89
4.1.2	Setup and alignment	95
4.2	Initial optical lattice characterization with a static BEC	97

4.2.1	Optical lattice depth determination from matter wave diffraction	97
4.2.2	Bloch oscillations as a probe of phase coherence in the lattice . . .	99
4.3	Results: Rapidly rotating Bose-Einstein condensates in a 1D optical lattice	102
4.3.1	Spin-down of the rotating BEC in the optical lattice	103
4.3.2	Loss of vortex lattice visibility in the optical lattice	106
4.3.3	Technical considerations when loading a rotating BEC into a 1D optical lattice	111
4.4	Conclusions and outlook	115
5	Vortex lattice dynamics in rotating spinor Bose-Einstein condensates	118
5.1	Background and motivation	118
5.2	The magnetically trapped spinor BEC system in ^{87}Rb	120
5.3	Experiments and results	121
	Bibliography	130
	Appendix	
A	Accurate optical dipole potential calculation	141
B	Numerical determination of finite-T BEC parameters in a double well potential	143
C	Calculation of the vortex pinning potential	149
D	Rapidly rotating Bose gases: Vortex lattice physics and beyond	150
D.1	Lowest Landau level: Vortex core overlap and transition to normal state?	153
D.2	Vortex lattice melting in a quasi-2D BEC	155
D.2.1	Quantum melting	156
D.2.2	Thermal melting	157

- D.3 Fractional quantum Hall physics in a rotating Bose gas? 159

- E** Image magnification calibration 162
 - E.1 Top view calibration from in-trap vortex lattice images 162
 - E.2 Side view calibration by releasing a BEC from a 1D optical lattice . . . 164

- F** The End 166

Tables

Table

1.1	Condition for BEC in 2D and 3D, homogeneous / trapped, interacting / noninteracting systems.	7
2.1	Error budget for optical aberrations in a rotating 2D optical lattice. . .	45
3.1	Error budget on the Josephson coupling J	73

Figures

Figure

1.1	Vortices – from one to many	13
1.2	Schematic phase diagram of a rotating 2D Bose gas.	15
1.3	Principle of vortex pinning	18
1.4	Effect of vortices and vortex-antivortex pairs on phase coherence	21
1.5	Berezinskii-Kosterlitz-Thouless transition in a continuous 2D system . .	22
1.6	Sketch of retro-reflected optical lattice (OL), acute-angle OL, and 2D OL	24
1.7	Parameters of a double well BEC	25
1.8	Dependence on optical lattice depth of parameters relevant to the Berezinskii-Kosterlitz-Thouless transition	28
1.9	Vortices in a Josephson junction array.	29
1.10	Schematic phase diagram of a Josephson junction array.	32
1.11	Chemical potential in the effective Thomas-Fermi description for a BEC in a 2D optical lattice: Theory and experiment	35
1.12	Example of nondestructive BEC image and finite-T BEC fit results. . .	36
2.1	Pinning a vortex lattice	40
2.2	Schematic setup for a rotating 2D optical lattice	42
2.3	Optical path length fluctuations lead to lattice displacements.	43
2.4	Analysis of aberrations in a rotating 2D optical lattice setup	44

2.5	Light source and detailed setup for the rotating 2D optical lattice	47
2.6	Stability measurements of the rotating 2D optical lattice	48
2.7	Long exposure images of rotating 2D optical lattices	49
2.8	Experimental result: Spinning up a BEC using a rotating two-dimensional optical lattice.	51
2.9	Experimental result: Vortex lattice pinning in triangular optical lattice .	54
2.10	Experimental result: Pinning-induced structural vortex lattice crossover from hexagonal to square vortex lattice	56
2.11	Theoretical predictions [128, 130] for pinning-induced structural crossover	57
2.12	Definition of k-vectors for analyzing pinning-induced structural crossover	58
2.13	Experimental result: Structure factors show the pinning-induced struc- tural crossover	58
2.14	Experimental result: Phase diagram for pinning in a square optical lattice	59
2.15	Pinning-induced defects in a vortex lattice	60
2.16	Defects in pinned vortex lattices with varying rotation rate mismatch .	61
2.17	Vortex pinning with 2 vortices per pinning site	62
2.18	Theoretical predictions [128] for vortex pinning with 2 vortices per site .	63
3.1	Setup for static 2D optical lattice used to observe the BKT transition. .	67
3.2	Measured and calculated static 2D optical lattice intensity profile	70
3.3	Setup, system parameters and images showing vortex proliferation . . .	76
3.4	Converting phase winding defects in a Josephson junction array to vor- tices in a bulk BEC.	77
3.5	Experimental result: Quantitative study of thermally activated vortices in the BKT crossover	79
3.6	Image showing vortex-antivortex annihilation	81

3.7	Result: Varying the optical lattice ramp-down duration to distinguish free vortices from tightly bound vortex-antivortex pairs	82
3.8	Time-to-length scale mapping for vortex pair annihilation	83
3.9	Experimental result: Shift of vortex activation curve with ramp-down duration	85
4.1	Motivation for loading a rotating BEC into a 1D optical lattice	88
4.2	Idea: Study of single vortex dynamics in a 1D optical lattice	89
4.3	Parameters of the 1D optical lattice	90
4.4	Model for vortex lattice melting and 3D-2D crossover in a 1D optical lattice	93
4.5	Light Source and setup for 1D optical lattice	96
4.6	Characterization of 1D optical lattice depth	98
4.7	Bloch oscillations of a static phase coherent BEC in an optical lattice .	99
4.8	Bloch oscillations of a static BEC show the loss of phase coherence with increasing lattice depth	101
4.9	Upon reduction of optical lattice depth, Bloch oscillations of a static BEC show a revival of phase coherence.	102
4.10	Rotating BEC loaded into a 1D optical lattice: Vortex number decay vs. optical lattice hold time	104
4.11	Result: Vortex number decay vs. optical lattice depth	105
4.12	Result: BEC rotation rate decay in optical lattice vs. initial T/T_c	106
4.13	Result: Vortex lattice visibility vs. optical lattice depth	107
4.14	Result: Vortex lattice visibility decay time vs. Josephson coupling J . .	109
4.15	Result: Revival of vortex lattice visibility in optical lattice	110
4.16	$m = -2$ quadrupole mode excitation when loading into azimuthally distorted optical lattice potential	112

4.17	Tkachenko mode excitation due to radial anharmonicity when loading into optical lattice potential	113
4.18	Scissors mode excitation due orientation mismatch between symmetry axes of magnetic trap and optical lattice	114
5.1	Magnetically trapped states for two-component BEC in ^{87}Rb	120
5.2	Experimental sequence for creating two-component BEC.	121
5.3	Hexagonal and square vortex lattice in real- and Fourier space.	122
5.4	Experimental result: Evolution from hexagonal vortex lattice to inter-laced square lattices in a rotating two-component BEC.	123
5.5	Result: Tkachenko mode excitation in the square vortex lattice	125
5.6	Experimental sequence for two-component vortex lattice interference.	126
5.7	Resultt: Vortex lattice interference in two-component BEC	127
B.1	Numerical grid for simulation of the Gross-Pitaevskii equation (GPE) for a BEC in a double-well potential	144
B.2	Numerical GPE code schematic	145
B.3	Double-well GPE simulations at zero temperature	146
B.4	Finite temperature corrections to GPE simulation results	147
D.1	Side view images of BECs with increasing rotation rate	151
D.2	Physics of the lowest Landau level.	152
D.3	Experimental result: Fractional condensate area occupied by vortex cores	155
D.4	Experimental result: Tkachenko modes of the vortex lattice	156
E.1	Calibration of top view image magnification	163
E.2	Calibration of side view image magnification	165
F.1	Smiley BEC.	166

Chapter 1

Introduction

The experiments described in this thesis revolve around two topics: rotating Bose-Einstein condensates (BECs), and tunnel-coupled arrays of condensates in optical lattice potentials. It is shown that various combinations of both these themes yield highly complex quantum fluid systems with many analogies to condensed-matter systems, and thus lead to new avenues in ultracold atom research. In the following, the relevant aspects of superfluids, their rotation, their quantum and thermal fluctuations, and their manipulation with tailored optical potentials will be introduced.

1.1 Background

During the course of this thesis, the field of ultracold atoms has undergone significant developments. In the beginning, fundamental studies were in full bloom, which have in the meanwhile been described in two books [119, 122]. Nowadays, ultracold atoms in many cases merely serve as a starting point for further adventures, see e.g. the recent reviews [29, 101]. What makes these dilute-gas ultracold atom samples so special is that they represent a simple, to a large extent now well understood, macroscopic quantum mechanical system, combined with the experimental capability to turn a variety of “knobs” that take the system into fundamentally new and poorly understood regimes, often relevant to unsolved problems from other fields of physics. In a sense this opens up a “bottom-up” approach to studying many-body quantum mechanics, as

opposed to the “top-down” approach necessarily pursued e.g. in many other condensed matter systems. Such “knobs” include but are not limited to

- Optical lattices, i.e. spatially periodic potentials made from interfering laser fields. The regime of few particles per lattice site is the realm of Hubbard model physics [67, 85], relevant to high temperature superconductivity [80] and quantum magnetism [134]. In the opposite limit of many atoms per site, “classical” Josephson junction arrays [161] may be studied.
- Fast rotation of a quantum gas may allow the realization of a new system for studying fractional quantum Hall physics [47, 165], and the creation of anyonic excitations [118].
- Tunable interparticle interactions allow to access the full range from ideal (non-interacting) to strongly interacting quantum gases [29].
- Internal (spin) degrees of freedom add new complexity, see e.g. [137].
- Composite quantum systems, such as Rydberg-excited atoms in a BEC [75], trapped ions and BEC, as well as ultracold dipolar atoms [97] or molecules [113] will allow exploring the effects of new interactions on quantum systems.

In addition, new probing capabilities are being developed, such as coupling many-body quantum systems to high-finesse cavities [31], or the study of noise correlations [8], complementing the traditional absorption and phase contrast imaging.

Relevant to this thesis, rotating Bose-Einstein condensates provide a conceptual link between the physics of trapped quantum gases and the physics of condensed matter systems such as superfluids [53], type-II superconductors [161] and quantum Hall effect (QHE) systems [98]. In all these systems, striking counterintuitive effects emerge when an external flux penetrates the sample. For charged particles this flux can be provided

by a magnetic field, leading to the formation of Abrikosov flux line lattices in type-II superconductors, or in QHE systems to the formation of correlated electron-liquids and composite quasiparticles made of electrons with attached flux quanta. For neutral superfluids, the analog to a magnetic field is a rotation of the system, which similarly spawns vortices. Recently, the creation and study of large ordered Abrikosov lattices of vortices in rotating atomic BECs [102, 5, 73, 78] has become possible. Experiments have explored regimes of rotation far beyond the ones attainable in superfluid Helium [143, 44, 32]. In the limit of the highest possible rotation rates, analogies to integer quantum Hall systems become apparent [143], and even a phase transition into a regime of strongly correlated states and composite quasiparticle excitations, analogous to the fractional quantum Hall effect, has been envisioned by theorists. These developments have recently been excellently reviewed by Fetter [58].

In this thesis, several experiments were conducted that have expanded the range of studies of vortex lattices in rotating BECs: Periodic pinning potentials for vortices were created, which allowed to induce a structural crossover from a hexagonal vortex lattice to a pinned square lattice (Chapter 2). In Chapter 4, an array of two-dimensional rapidly rotating BECs was created, which allowed the study of thermal vortex lattice fluctuations, and realized a possible first step toward fractional quantum Hall states in rotating quantum gases with only few atoms per vortex. Finally, the first rapidly rotating two-component BECs were created (Chapter 5), and self-organization of vortices in the two components into two interlaced square vortex lattices was observed.

Optical lattices, the second ingredient to this thesis, are periodic potential configurations created by interfering laser beams. The structures are reminiscent of crystalline lattices in solid state physics, but are free of defects and phonons. Such lattices can form a very controlled environment for ultracold atoms: individual atoms can be confined to single lattice sites, prevented from colliding with neighboring atoms, and cooled to their motional ground state such that thermal motion is completely frozen out. In ad-

dition, optical lattices can turn a three-dimensional system into an array of two-, one-, or even zero-dimensional systems. This high level of control may be exploited for precision measurements, e.g. of the electron's electric dipole moment [40], the fine structure constant [43], and of absolute optical frequencies, e.g. in optical atomic clocks [30]. Optical lattices in the context of quantum degenerate gases have become a hot topic since the prediction [85] and realization [67] of a transition from the BEC superfluid to a Mott-insulator state. Experiments typically operated in a regime of few particles per site, where interactions and correlations between individual particles are important.

In this thesis we explored the opposite regime of large occupancy per site, where Josephson junction arrays are realized, with many connections to condensed matter systems. The first *rotating* two-dimensional optical lattice potential for ultracold atoms was created, which served as a periodic pinning potential for vortices (Chapter 2). In addition we made extensive use of optical lattice configurations to create arrays of low-dimensional systems (Chapter 4), or *effectively low-dimensional* systems (Chapter 3).

A third important ingredient to this thesis is thus the influence of reduced dimensionality on an ordered state such as a BEC. In low-dimensional systems the establishment of order is often hampered by the increased importance of low-energy fluctuations [29]. Atomic systems are ideally suited to probe this regime, for one part due to the ability to tailor very clean anisotropic optical potentials, based either on laser interference [146, 71] or beam shaping. Further, rather direct probes of order and correlations exist, such as the interference of two or many atomic samples [71], or noise correlations [8]. Reduced-dimensionality systems remain a very open field, both theoretically and experimentally, as both interparticle interactions and the trapping potential can lead to nontrivial effects.

In this thesis, the following low-dimensional systems were created: The Berezinskii-Kosterlitz-Thouless superfluid-to-normal transition was studied in a finite-temperature, *effectively* two-dimensional array of Josephson junctions (Chapter 3). A one-dimensional

optical lattice was employed to create a stack of two-dimensional rapidly rotating BECs, and to observe the vortex lattice fluctuations resulting from this low-dimensional geometry (Chapter 4).

1.2 Bose-Einstein condensation

In the following I will briefly review the topics of quantum degeneracy and condensation, with an emphasis on the roles of dimensionality, finite temperature, and interparticle-interactions as required for this thesis.

1.2.1 Quantum statistics: Ideal gas Bose-Einstein condensation

Bose-Einstein condensation (BEC) [54, 11] is defined as the occupation of a single quantum mechanical state – typically the lowest-energy single-particle state – by a macroscopic number of particles. Its most powerful consequence is the development of a macroscopic matter wave, in most instances with a high degree of phase coherence across the whole condensed sample. This is in stark contrast with ordinary matter, where each quantum mechanical state is negligibly occupied and ensembles of particles behave incoherently.

Quantum Degeneracy. To understand when BEC will occur, two ingredients - quantum mechanical uncertainty and the consequences of exchange symmetry of identical particles - are essential. The Heisenberg uncertainty relation states that position and momentum of a particle may not simultaneously be measured sharply, but with uncertainties Δx and Δp_x that obey $\Delta x \times \Delta p_x \approx \hbar$, where \hbar is Planck's constant divided by 2π . For an ideal gas, the typical momentum spread associated with random thermal motion at temperature T determines the width of the de Broglie wavepacket $\Delta x \equiv \lambda_{th}$

$$\lambda_{th} = \sqrt{\frac{2\pi\hbar^2}{mk_B T}} \quad (1.1)$$

where m is the mass of the particles and k_B is Boltzmann's constant. As de Broglie wavepackets grow with decreasing T , neighboring wavepackets begin to overlap in a D -dimensional system when the *phase space density* reaches unity (n_D is the D -dimensional total particle density)

$$n_D \times \lambda_{th}^D = \mathcal{O}(1) \quad (1.2)$$

This is called the *degeneracy condition*¹, under which identical particles are forced to reveal their quantum statistics: bosons will symmetrize their total wavefunction and hence allow unrestricted occupation of single-particle states, whereas fermions insist on antisymmetrization, restricting single-particle level occupancy to below unity. The quantum degeneracy condition (1.2) is thus an upper limit of when Bose-Einstein condensation might take place. But will it? The answer in many cases is yes, but in certain “marginal” situations (e.g. set by the dimensionality of the system, see below) it depends on additional factors, such as the presence and shape of a trapping potential, and importantly the interactions between particles.

Condensation. To give a more definitive answer if condensation will occur, one must examine how the quantum mechanical states of a system are occupied. The occupation of a state with energy E_i in thermal equilibrium at temperature T is given by Bose/Fermi statistics (+ for fermions, - for bosons)

$$f_i(E_i, \mu, T) = \frac{1}{\exp((E_i - \mu)/k_B T) \pm 1} \quad (1.3)$$

and we may set $E_0 \equiv 0$. μ is the chemical potential, fixed by the total number of particles, $N = \sum_i f_i$. For an ideal gas of bosons (but not for fermions), $\mu \leq 0$ is enforced in order to have physically meaningful positive occupation numbers $f_i > 0$. It is now tempting to approximate the sum $\sum_i f_i$ by an integral, $N \rightarrow N_0 + \int_{\varepsilon > E_0}^{\infty} f(\varepsilon, \mu, T) g(\varepsilon) d\varepsilon$. Here $g(\varepsilon)$ is the density of states (DOS), i.e. $g(\varepsilon)d\varepsilon$ is the number of states in an interval $d\varepsilon$ around an energy ε . The occupation N_0 of the lowest state, in which BEC is expected

¹ The air around you is non-degenerate, $n_{3D} \lambda_{th}^3 \sim 10^{-8}$, despite a 6 orders of magnitude higher density than typical BEC densities. This is because at room- T , λ_{th} is tiny, of order of atomic sizes.

to occur, is treated separately, as in some situations it is suppressed from the integral by a vanishing DOS. At this point we distinguish between a homogeneous system and a (harmonic) trapping potential. For a homogeneous D -dimensional system of size L

$$g(\varepsilon) \sim \frac{\varepsilon^{D/2-1}}{(\hbar^2/mL^2)^{D/2}} \quad (1.4)$$

while in a D -dimensional harmonic trap potential with frequencies ω_i [119]

$$g(\varepsilon) \sim \frac{\varepsilon^{D-1}}{(D-1)! \prod_{i=1}^D (\hbar\omega_i)} \quad (1.5)$$

The integral $N_{ex} \equiv \int_{\varepsilon > E_0}^{\infty} f(\varepsilon, \mu, T)g(\varepsilon)d\varepsilon$ gives the number of atoms in excited states. For bosons this number reaches a maximum when $\mu = 0$, and this enforces an upper limit on the number of bosons that can be accommodated in excited states. If the total number of particles exceeds this maximum,

$$N > N_{ex,max} \equiv \int_{\varepsilon > E_0}^{\infty} f(\varepsilon, \mu = 0, T)g(\varepsilon)d\varepsilon \quad (1.6)$$

then Bose-Einstein condensation of the excess atoms into the zero-energy state occurs. Results of this analysis for two/three dimensions and homogeneous/trapped systems are given in Table 1.1, as well as the effects of interparticle interactions.

Table 1.1: Critical temperature T_c and phase-space density (PSD) for occurrence of BEC in 2D/3D weakly interacting/noninteracting systems, both spatially homogeneous and in a harmonic trap [122, 119]. $n_{tot,D}$: total density in D -dimensions, $\bar{\omega}$: geometric average of trap frequencies. T_{BKT} , C , \tilde{g} : See Eq. (1.31). For interacting 2D systems (Section 1.4) and Josephson junction arrays (JJA, see Section 1.5), T_{BKT} refers to the normal-to-superfluid transition, not to the occurrence of BEC. J : Josephson energy.

	homogeneous system		trapped system
	transition temperature	PSD	transition temperature
3D nonint.	$k_B T_c = 3.3 \frac{\hbar^2}{m} n_{tot,3D}^{2/3}$	2.61	$k_B T_c = 0.94 \hbar \bar{\omega} N^{1/3}$
3D int.	$k_B T_c \approx 3.3 \frac{\hbar^2}{m} n_{tot,3D}^{2/3}$	≈ 2.61	$k_B T_c \approx 0.94 \hbar \bar{\omega} N^{1/3}$
2D nonint.	$k_B T_c = 0$	∞	$k_B T_{c,2D} = 0.78 \hbar \bar{\omega} N^{1/2}$
2D int.	$T_{BKT} = \frac{\hbar^2 n_{tot,2D}}{m k_B} \times \frac{2\pi}{\ln(C/\tilde{g})}$	4	$T_{BKT}/T_{c,2D} = \left(1 + \frac{3\tilde{g}}{\pi^3} \ln(C/\tilde{g})^2\right)^{-1/2}$ [81]
2D JJA	$k_B T_{BKT} \approx J$		no theory

Remarkably, in 3D the ideal Bose gas condenses at the maximum temperature allowed by quantum statistics! This result turns out to be fairly robust also in the

presence of weak interparticle interactions and a trap potential. In the 2D systems on the other hand, effects of interactions, finite-particle number and of a trap are clearly important [14]. The situation in 2D will be described in more detail below.

Macroscopic coherent matter wave. The many body wavefunction Ψ describing the condensed state is a product of *identical* single particle wavefunctions ψ

$$\Psi_{(r_1, \dots, r_N)} = \prod_i^N \psi_{(r_i)} \rightarrow \Psi_{(\vec{r})} \equiv |\Psi_{(\vec{r})}| e^{i\phi_{(\vec{r})}} \quad (1.7)$$

This is the so-called mean field approximation: The BEC is described by a complex-valued *macroscopic* wavefunction $\Psi_{(\vec{r})}$ whose squared modulus $|\Psi_{(\vec{r})}|^2 \equiv n_{(\vec{r})}$ describes the density of *the ensemble* of condensed particles, and whose phase gradient $\nabla\phi_{(\vec{r})}$ defines the superfluid velocity

$$\vec{v}_s = \frac{\hbar}{m} \nabla\phi_{(\vec{r})} \quad (1.8)$$

In the 3D weakly interacting Bose gas, neither quantum nor thermal fluctuations are strong enough to appreciably decohere the condensate phase. As a consequence, Bose-Einstein condensation, phase coherence, and superfluidity occur simultaneously. In lower dimensions the situation is more complicated, as discussed below.

1.2.2 Quantum fluids: Importance of interparticle-interactions

Neutral atoms interact through van der Waals interactions, and such interactions modify many properties of the condensate, while leaving others almost unchanged. At the low energies of ultracold atom experiments, an effective description of this interaction is valid, with the interaction strength parameterized by the s-wave scattering length a_{sc} . The sign and magnitude of a_{sc} are determined by the precise shape of the two-body molecular potential, and are even tunable by external fields. In practice, unless special steps are taken, interparticle interactions are “weak” in the sense that $n_{tot} a_{sc}^3 \ll 1$. This is the reason why interactions in general have little influence on the BEC transition as well as the condensate fraction, see Table 1.1.

Despite being characterized as “weak”, interparticle interactions have several profound effects. Interactions change the low-energy part of the BEC’s excitation spectrum from quadratic to linear in momentum, and this linear excitation spectrum is fundamentally responsible for superfluidity. The macroscopic wavefunction Ψ of such a weakly interacting Bose condensate is described by the Gross-Pitaevskii equation:

$$\left(-\frac{\hbar^2 \vec{\nabla}^2}{2m} + g |\Psi(\vec{r})|^2 + V(\vec{r}) \right) \Psi(\vec{r}) = \mu \Psi(\vec{r}) \quad (1.9)$$

In this nonlinear Schrödinger equation, the nonlinear term $g |\Psi(\vec{r})|^2 \Psi(\vec{r})$ describes the effective contact interaction of strength $g = \frac{4\pi\hbar^2 a_{sc}}{m}$. The external trapping potential $V(\vec{r})$ is typically harmonic, and in all experiments in this thesis cylindrically symmetric, $V(\vec{r}) = \frac{1}{2}m(\omega_r^2 r^2 + \omega_z^2 z^2)$. The chemical potential μ gives the energy needed to add a particle to the superfluid. It should be noted that, owing to the nonlinearity, (1.9) does not have discrete eigenvalues μ , but has a solution for *any* $\mu > 0$.

There are three length scales, found by balancing energy terms: the healing length ξ is the only trap-independent length scale, determined by the balance of kinetic energy and nonlinear interaction, with $n \equiv |\Psi|^2$

$$\xi = \left(\frac{\hbar^2}{2mgn} \right)^{1/2} \quad (1.10)$$

it determines the distance over which a density disturbance of the superfluid heals back to the bulk value, and hence sets the size of intrinsic condensate defects, such as solitons and vortices. Kinetic and potential energy determine the harmonic oscillator length, $a_{r,z} = \sqrt{\frac{\hbar}{m\omega_{r,z}}}$. Balancing the potential energy with the nonlinear interaction term gives the so-called Thomas-Fermi condensate radii, described in the next section.

1.2.3 Thomas-Fermi regime

The typical regime of condensate physics is the so-called Thomas-Fermi (TF) regime where the interaction energy is much larger than the kinetic energy, and interactions push the BEC outward, typically increasing its size R to many times the

noninteracting harmonic oscillator size, or in terms of length scales, $R \gg a_{r,z} \gg \xi$. In this regime, the chemical potential is given by

$$\mu = \frac{\hbar\bar{\omega}}{2} (15Na_{sc}/\bar{a})^{2/5} \quad (1.11)$$

where $\bar{a} = \sqrt{\hbar/m\bar{\omega}}$ and $\bar{\omega} = (\omega_x\omega_y\omega_z)^{1/3}$ is the geometric average of trap frequencies. The condensate density profile in the region $\sum(r_i/R_i)^2 \leq 1$ is an inverted parabola

$$n_{BEC}(\vec{r}) = \frac{\mu}{g} \left(1 - \sum(r_i/R_i)^2\right) \quad (i = x, y, z) \quad (1.12)$$

while it is zero where $\sum(r_i/R_i)^2 > 1$. Interactions thus cause a fairly sharp drop in the condensate density at its edge, making it visually easily distinguishable from the noncondensed background atoms. Very importantly the chemical potential, and hence using Eq. (1.11) the total BEC number, can be determined simply by measuring the BEC radii and trap frequencies:

$$R_i = \sqrt{\frac{2\mu}{m\omega_i^2}} \quad (1.13)$$

1.2.4 Condensates at finite temperature

At finite temperature T , only a fraction of atoms is condensed, with the remaining atoms occupying a lower-density “thermal cloud”. For the study of the finite-T Berezinskii-Kosterlitz-Thouless transition in Chapter 3, the accurate determination of BEC and thermal cloud parameters is essential. We thus give a detailed description of the density profile of a finite-T BEC and its thermal cloud.

The Bose distribution describing *noninteracting* bosons in equilibrium at temperature T in an external potential $V(\vec{r})$ is given by [119]

$$f(\vec{r}, \vec{p}) = \frac{1}{\exp((\vec{p}^2/2m + V(\vec{r}) - \mu)/k_B T) - 1} \quad (1.14)$$

where \vec{p} is the particle’s momentum and μ is the chemical potential. The spatial density $n_{th}(\vec{r})$ is obtained by integrating over the momentum coordinates, resulting in

$$n_{th}(\vec{r}) = \frac{g_{3/2}(z(\vec{r}))}{\lambda_{th}^3} \quad (1.15)$$

where $g_{3/2}(z) \equiv \sum_{n=1}^{\infty} \frac{z^n}{n^{3/2}}$ is called the Bose function, λ_{th} is given by Eq. (1.1) and

$$z(\vec{r}) = \exp(-(V(\vec{r}) - \mu)/k_B T) \quad (1.16)$$

In order to realistically describe our experiments we need an approximate description of *interacting* bosons at finite T . We follow the description of Naraschewski and Stamper-Kurn [112]. Repulsive interactions cause the high condensate density $n_{BEC}(\vec{r})$ in the center of the trap to repel the thermal cloud. They also cause a self-repulsion of the thermal cloud (which is a weaker effect due to the lower thermal cloud density). The resulting modification of the thermal cloud density profile is taken into account by treating the BEC and thermal cloud densities as an effective repulsive potential $2gn_{BEC}(\vec{r}) + 2gn_{th}(\vec{r})$, and including this effective potential in Eq. (1.16):

$$z(\vec{r}) = \exp(-(V(\vec{r}) + 2gn_{BEC}(\vec{r}) + 2gn_{th}(\vec{r}) - \mu)/k_B T) \quad (1.17)$$

Now, Eq. (1.15) with (1.17) forms an implicit equation for n_{th} that can be solved iteratively. The resulting “mean field modified thermal cloud profile” is used for fitting the thermal cloud of finite- T BECs, an example of which is shown below in Figure 1.12 in Section 1.6 on BEC imaging. On the other hand, the thermal cloud density $n_{th}(\vec{r})$ exerts a repulsive mean field pressure onto the BEC. This effect is small however, so that the BEC density $n_{BEC}(\vec{r})$ is only slightly altered by the thermal cloud and still follows the Thomas-Fermi profile, Eq. (1.12).

1.3 Rotating Bose-Einstein condensates

1.3.1 Quantized vortices in a superfluid

In this thesis there is no experiment that does not involve vortices in one form or another. Here we explain their main features. At first sight, superfluids, being described by a macroscopic wavefunction (1.7), are “irrotational”: Around any closed path inside the superfluid, the single-valuedness of the wavefunction enforces a vanishing circulation

$\Gamma \equiv \oint \vec{v}_s \cdot d\vec{l} = \frac{\hbar}{m}(\phi_{(end)} - \phi_{(start)}) = 0$, with \vec{v}_s given by (1.8) and $\phi_{(\dots)}$ the condensate phase at start and end point of the closed loop.

A vortex is nature's way to allow a superfluid to rotate nonetheless. Picture a vortex as a “quantum tornado”, with fluid circulating rapidly around a singular line (in a 2D system a point), where due to centrifugal pressure the superfluid density is forced to zero. This zero density region marks a phase singularity, around which the phase $\phi(\vec{r})$ is allowed to undergo (multiples of) 2π winding. This leads to a nonvanishing, quantized circulation Γ

$$\Gamma \equiv \oint \vec{v}_s \cdot d\vec{l} = q\kappa \quad (1.18)$$

where $\kappa = \frac{\hbar}{m}$ is the fundamental quantum of circulation, and q is the number of quanta enclosed by the loop (it is energetically favorable to distribute these q quanta onto q singly quantized vortices). Vortices thus come with two possible signs of circulation (q in (1.18) can be positive or negative). The azimuthal superfluid flow around a singly quantized vortex is given by (1.18) to be $v_s = \frac{\kappa}{2\pi r}$. The condensate wave function is suppressed as $\psi \propto r$ for $r \rightarrow 0$. In the limit of isolated vortices this suppression is governed by a balance of interaction energy and kinetic energy, and is hence expected to occur over a length scale comparable to the healing length ξ . From a numerical simulation of the Gross-Pitaevskii equation we estimate the root-mean-square vortex core radius

$$r_v = 1.94 \times \xi \quad (1.19)$$

The energy of a (straight) vortex line of length L in a condensate of radius R is dominated by the kinetic energy of the superflow, $E_v = \int_{\xi}^R dr 2\pi r n_{SF(r)} L \frac{1}{2} m v_s^2(r)$, with $v_s = \frac{\kappa}{2\pi r}$, the superfluid density n_{SF} , and a short-distance cutoff of order ξ , resulting in

$$E_v \approx \frac{\pi \hbar^2}{m} n_{SF} L \log(R/\xi) \quad (1.20)$$

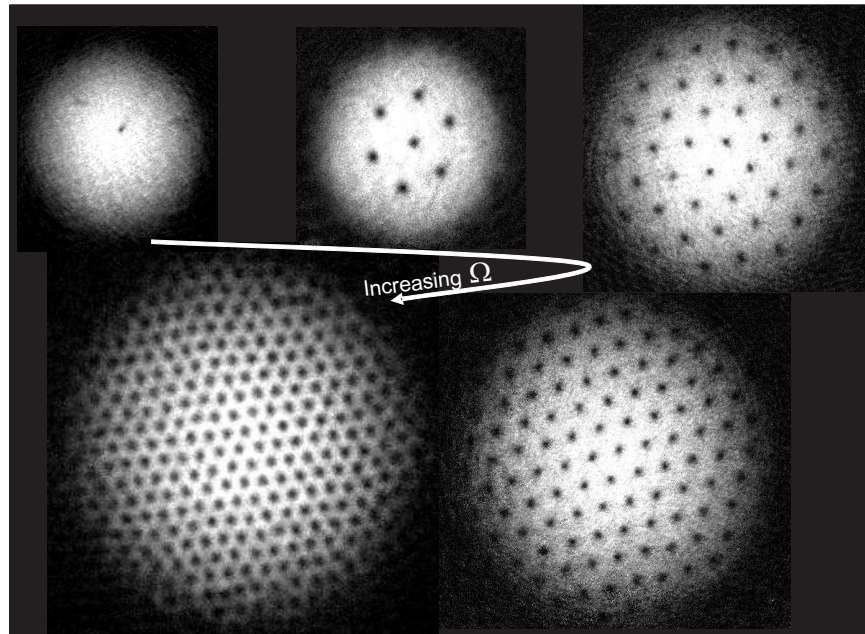


Figure 1.1: Images of vortex lattices in BECs rotating at different rates Ω . With increasing rotation, the vortex lattice's unit cell shrinks, whereas the vortex core area increases. At the same time, due to centrifugal forces the BEC expands outward.

1.3.2 Vortices – from one to many

If many vortices are present, a hexagonal vortex lattice (Abrikosov lattice [6]) forms due to repulsive vortex-vortex interactions, with all vortex lines straight and aligned along rotation axis. For large enough numbers of vortices in a superfluid, the correspondence principle suggests that the rotation field, coarse grained over the superfluid, should go over to the classical limit of rigid-body rotation

$$\vec{v}_{fluid} = \vec{\Omega} \times \vec{r} \quad (1.21)$$

In the frame rotating at $\vec{\Omega}$, the vortex lattice is stationary. Taking the contour of integration in Eqn. (1.18) around a loop containing many vortices, and identifying the integer $q \equiv N_v$ with the number of vortices inside the loop, the areal density of vortices n_v is found to increase with rotation rate

$$n_v \equiv \frac{N_v}{A} = \frac{m\Omega}{\pi\hbar} \quad (1.22)$$

The vortex density is often expressed in terms of two convenient length scales, either the “magnetic length” ℓ , i.e. the radius of the vortex lattice’s Wigner-Seitz unit cell

$$n_v \equiv \frac{1}{\pi\ell^2} \quad \ell = \left(\frac{\hbar}{m\Omega} \right)^{1/2} \quad (1.23)$$

or the directly observable vortex spacing b

$$n_v \equiv \frac{1}{b^2\sqrt{3}/2} \quad b = \ell \cdot \sqrt{2\pi/\sqrt{3}} \sim 1.9 \cdot \ell \quad (1.24)$$

In Fig. 1.1, images of vortex lattices in BEC at different rotation rates Ω are shown. The increase in vortex density with rotation rate is clearly visible.

The shape of rotating BECs is influenced by centrifugal forces, which pull the BEC radially outward. Chemical potential and BEC radii still follow the Thomas-Fermi description, Eqs. (1.11) and (1.13), respectively, with the replacement $\omega_\rho \rightarrow \sqrt{\omega_\rho^2 - \Omega^2}$ (Appendix D). The rotation rate Ω is thus accurately determined from the aspect ratio $AR_{(\Omega)} \equiv \frac{R_z(\Omega)}{R_\rho(\Omega)}$ of the rotating BEC, compared to the aspect ratio of the static BEC $AR_{(0)} \equiv \frac{\omega_\rho}{\omega_z}$, by the relation $\Omega/\omega_\rho = \sqrt{1 - (AR_{(\Omega)}/AR_{(0)})^2}$.

In a bigger picture, vortices have two, seemingly contradictory, roles in superfluidity:

Vortices are hallmarks of superfluidity. Although superfluidity is a multi-faceted phenomenon, many of its most spectacular manifestations are associated with vortices and its response to rotation. If a superfluid is placed into a slowly rotating container, the quantization of circulation (1.18) leads to a minimum rotation rate required for the first vortex to enter the system - this is the famous Hess-Fairbank effect, one of the hallmarks of superfluidity. An analogous effect exists for Type-II superconductors, where vortices are excluded from a sample below a critical applied magnetic field H_{c1} . A second phenomenon is the *(meta-)stability of superflow*. Once a vortex is nucleated in an annular-shaped superfluid, the rotation of its environment may be stopped, but the fluid will continue to rotate for astronomical timescales [99].

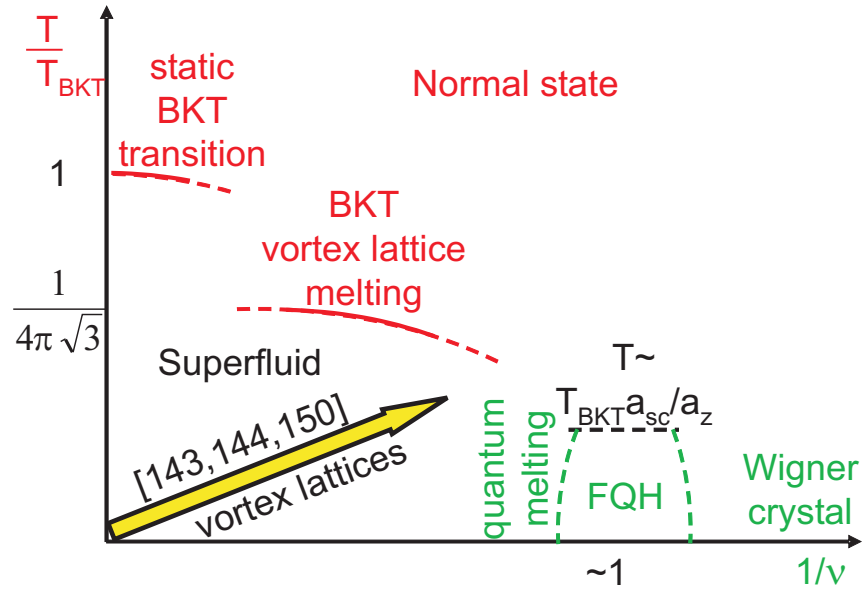


Figure 1.2: Schematic phase diagram of a rotating 2D Bose gas. $1/\nu$ parametrizes increasing rotation, see Eq. (1.25). The vertical axis is temperature in units of T_{BKT} – the temperature at which a *static* superfluid undergoes a Berezinskii-Kosterlitz-Thouless (BKT) transition, given in Eq. (1.36). A BKT-type melting of the *vortex lattice* [64] in rotating BECs occurs at a different, lower temperature, see Eq. (D.15) in Appendix D [82]. *Quantum* fluctuations are expected to melt the vortex lattice at a filling factor $\nu \sim 10$, see Eq. (D.11) [21]. At even faster rotation rates, strongly correlated quantum Hall (FQH) states induced by rotation [165] are expected. For the thermal destruction of FQH states around $T \sim T_{BKT} \frac{a_{sc}}{a_z}$ see Eq. (D.17). At extremely large rotation rates, a Wigner crystal [117] may form. [143, 144, 150]: Experiments in this thesis.

Too many vortices destroy superfluidity. Vortices may be induced either by rotation, either of the superfluid’s environment or of the normal cloud or, in the absence of rotation, by thermal agitation. Both situations lead to very different physics, which nonetheless share one common feature - too many vortices destroy superfluidity. Thermally activated vortices in a static BEC induce the Berezinskii-Kosterlitz-Thouless transition, described in Section 1.4. In the rapid rotation limit on the other hand, quantum fluctuations of the vortex lattice destroy the macroscopic wavefunction responsible for superfluidity, and induce a transition to strongly correlated fractional quantum Hall states. Such fluctuations are governed by the filling factor ν , i.e. the ratio of particles

N_p to vortices N_v , or the ratio of areal densities $n_{SF,2D}$ and n_v

$$\nu \equiv N_p/N_v \equiv n_{SF,2D}/n_v; \quad 1/\nu \propto \Omega \quad (1.25)$$

When $\nu \lesssim 10$, quantum fluctuations are predicted to melt the vortex lattice and correlated fractional quantum Hall states are expected to appear, see Appendix D. The prospect of enhancing quantum fluctuations of the vortex lattice has thus been a major motivation for the general direction of experiments conducted during this thesis.

Vortex lattices thus continue to be a fascinating research topic. In this thesis, we have extended vortex lattice studies to spinor Bose-Einstein-condensates (Chapter 5), created periodic pinning potentials for vortices (Chapter 2), and loaded rapidly rotating condensates into a one-dimensional optical lattice (Chapter 4) aligned with the rotation axis. Several further topics that have yet eluded experimental study are depicted in Fig. 1.2, and are detailed in Appendix D.

1.3.3 Manipulating vortices

Having established the self-organized response of superfluids to rotation, we are now in the position to think of ways to manipulate vortices, either on an individual basis or acting on the vortex lattice collectively. In Chapter 2 of this thesis, we show that vortex lattices can be collectively pinned to a rotating two-dimensional optical lattice. Beyond pure playfulness, such control may be desirable to establish defined initial conditions, e.g. in experiments studying vortex lattice fluctuations, or in experiments studying persistent superfluid flow [136].

A vortex in a dissipation-free superfluid behaves much like a massless particle, such that vortex motion is described by balancing all acting forces to zero. Two kinds of forces are at our disposal that act on a vortex. Spatial variations in the superfluid density lead to a pinning force, illustrated in Fig. 1.3. The vortex energy, given by Equation (1.20), depends on the superfluid density surrounding the vortex core. Application of a

repulsive potential $V(x)$ to the superfluid leads to an energy gain when the vortex moves to the lower-density location. In this way a repulsive potential for atoms is attractive for vortices. As is shown in Appendix C, the pinning energy for a single vortex is

$$E_{pin}(x) \approx -L/a_{sc} V(x) \quad (1.26)$$

where L is the vortex line length, a_{sc} is the scattering length and $V(x)$ is the applied external potential². Eq. (1.26) is valid for $V(x) < \mu$ and for potentials $V(x)$ smoothly varying on the scale of the healing length ξ . The resulting pinning force is

$$\vec{F}_{pin}(x) = -\vec{\nabla} E_{pin}(x) \approx L/a_{sc} \vec{\nabla} V(x) \quad (1.27)$$

The second force acting on a vortex is the Magnus force caused by relative motions between the vortex (v_{vortex}) and the superfluid (v_{fluid}),

$$\vec{F}_{mag}(x) = m n_{SF}(x) L (\vec{v}_{vortex} - \vec{v}_{fluid}) \times \vec{\kappa} \quad (1.28)$$

n_{SF} is the superfluid density and $\vec{\kappa} = h/m \hat{z}$. In the absence of pinning, a vortex will thus float in the velocity profile generated by all other vortices, while for a strongly pinned vortex, \vec{v}_{vortex} is determined by the motion of the pinning potential. There are thus two sides to the Magnus force. In case the relative motion between pinned vortices and the surrounding superfluid is too large, the Magnus force may overwhelm the pinning force and lead to depinning. On the other hand, establishing controlled superfluid flows may enable one to control vortex motion without acting directly on the vortex.

A rough dimensional argument gives insight in the conditions required for vortex pinning: The pinning force exerted by an applied potential V varying on a spatial scale

w is $F_{pin} \approx \frac{V}{w} \frac{L}{a_{sc}}$ while the Magnus force on a pinned vortex is $F_{mag} \approx (\mu - V) \frac{L}{a_{sc}} \frac{m \Delta v}{2\hbar}$

² One way to rationalize the prefactor L/a_{sc} in (1.26) is to note that $L/a_{sc} = 2n_{SF} L \pi r_v^2$, where n_{SF} is the superfluid density and r_v is given by (1.19). The pinning energy is thus approximately the collective potential energy of all the particles “missing” in the vortex core, $E_{pin}(x) \approx -n_{SF} L \pi r_v^2 \times V(x)$.

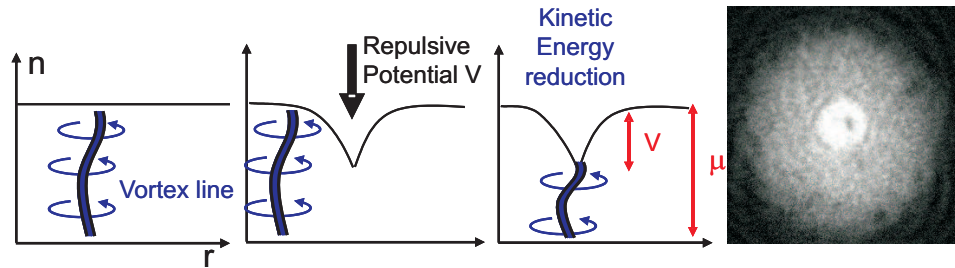


Figure 1.3: Principle of vortex pinning. Application of a repulsive potential (of depth V) to a superfluid (with chemical potential μ) allows a vortex to lower its kinetic energy when moving to the lower-density region. The ratio V/μ gives the relative suppression of superfluid density. Experimental demonstration using a single focused laser beam (532 nm , $V/\mu \approx 1$). A vortex was pinned from an initially rapidly rotating BEC, and trapped for up to 30 seconds. The bright spot surrounding the dark vortex core is a transient hydrodynamic effect of BEC fluid filling in the void after removal of the pinning potential just prior to imaging.

for a relative velocity Δv between superfluid and pinning potential. Using the speed of sound $c_s = \frac{\hbar}{\sqrt{2m\xi}}$ and healing length ξ , the ratio of pinning force to Magnus force is

$$F_{pin}/F_{mag} \approx \frac{V}{(\mu - V)} \frac{c_s \xi}{\Delta v w} \quad (1.29)$$

with limits of validity $\frac{\xi}{w} \ll 1$ and $\frac{V}{\mu} < 1$. Pinning occurs when $F_{pin}/F_{mag} > 1$: Either the pinning potential V must be of order of the chemical potential μ , or the relative velocity Δv between superfluid and pinning potential has to be kept much smaller than the speed of sound c_s and the spatial scale w should not be too large compared to the healing length ξ . In Chapter 2 we thus apply an optical lattice that roughly co-rotates with the vortex lattice ($\Delta v \rightarrow 0$) to facilitate pinning at small V/μ .

The concept of vortex pinning can be pushed to the quantum limit, where excitations are composite particles composed of atoms and flux quanta, so-called anyons with fractional (i.e. neither bosonic nor fermionic) statistics [98]. In this setting, an interferometric experiment[118] based on dragging pinned anyons around each other may one day be used to prove the existence of anyons and their fractional statistics.

1.4 The two-dimensional (2D) Bose gas

Effectively 2D systems form an important part of this thesis. In Chapter 4 we study an array of rotating 2D Bose gases in a one-dimensional optical lattice. In Chapter 3 the Berezinskii-Kosterlitz-Thouless (BKT) transition is studied in an effectively 2D system created in a 2D array of Josephson junctions. Here we summarize some distinctive features of 2D Bose gases.

As Table 1.1 shows, condensation and superfluidity in 2D are much more subtle issues than in 3D. The homogeneous *ideal* 2D Bose gas will not form a true condensate at any finite temperature, despite the overlapping of de Broglie waves. In general, in low-dimensional systems, the formation of phase-coherence is hampered by thermally induced fluctuations of the condensate phase. A simple argument shows why: Equation (1.8) implies that spatial phase fluctuations cost an associated kinetic energy $E = \int d^D x n_{SF} \frac{\hbar^2}{2m} (\nabla\phi)^2$ in D -dimensions (here, n_{SF} is the D -dimensional superfluid density). If we expand the phase in Fourier components $\phi(\vec{r}) = \sum_k S_k \exp(i\vec{k} \cdot \vec{r})$, then we can obtain the Fourier amplitudes $|S_k|$ using the result from equipartition that every Fourier mode of the phase contains an energy $\frac{k_B T}{2} = \frac{\hbar^2}{2m} n_{SF} k^2 |S_k|^2$. The phase variance in D -dimensions is then

$$\Delta\phi^2 = \sum_k |S_k|^2 \propto \int_{k_{min}}^{k_{max}} dk \frac{k^{D-1}}{k^2} \times \frac{m k_B T}{\hbar^2 n_{SF}} \quad (1.30)$$

The lower momentum cutoff $k_{min} \propto 1/R$ is given by the system size R , while $k_{max} \propto 1/\lambda_{th}$ gives the minimum physically reasonable length scale for a phase fluctuation. Eq. (1.30) shows that in $D \leq 2$ long wavelength fluctuations diverge with system size R . The result is that in 2D, a degenerate Bose gas can only form a “quasicondensate”, i.e. a condensate with spatially fluctuating phase. Local patches of quasicondensate “look like” BEC, but there is no phase correlation between such local patches. This statement holds irrespective of interparticle interactions.

The inclusion of interparticle interactions in 2D completely changes the nature of

the *normal-to-superfluid* transition: A homogeneous *interacting* Bose gas undergoes a BKT transition, at a transition temperature T_{BKT} determined by the *total* 2D density n_{2D} [127]

$$k_B T_{BKT} = \frac{\hbar^2 n_{2D}}{m} \times \frac{2\pi}{\ln(C/\tilde{g})} \quad (1.31)$$

with $C = 380 \pm 3$ [127] and $\tilde{g} = \frac{a_{sc}}{a_z} \sqrt{8\pi}$ (a_z is the axial oscillator length of the trap). The BKT transition is clearly driven by interactions, as may be seen from the limit $T_{BKT} \rightarrow 0$ when $\tilde{g} \rightarrow 0$. Although this expression is therefore non-universal, it means that already weakly repulsive interactions allow the 2D Bose gas to become superfluid close to the maximum temperature allowed by quantum statistics! This fact is rather robust due to its weak logarithmic dependence on \tilde{g} , with values of $\ln(C/\tilde{g}) \sim 6..10$ in practice. The region below T_{BKT} is characterized by the above-mentioned quasicondensate. The existence of such local quasicondensates is sufficient for global superfluidity.

1.4.1 The Berezinskii-Kosterlitz-Thouless transition

It had been well known long before BKT theory was developed, that in 2D a true BEC with long-range phase coherence exists only at $T = 0$, while at any finite $T > 0$ in 2D true long range phase coherence is destroyed by thermally populated long wavelength phase fluctuations, as described by Eq. (1.30). The new realization of Berezinskii [23, 24], and Kosterlitz and Thouless [94], was that in addition to long-wavelength excitations, another not-so-obvious type of low-energy excitation has to be taken into account in order to understand superfluidity in 2D: thermally activated vortex-antivortex pairs, i.e. pairs of vortices of opposite circulation.

To understand the influence of thermally activated vortices on superfluidity and phase coherence, it is essential to appreciate the difference between free vortices and bound vortex-antivortex pairs. In Fig. 1.4, the phase of an isolated vortex is shown - it extends over the whole superfluid. A random collection of vortices therefore destroys phase coherence over length scales larger than the mean vortex separation. A vortex-

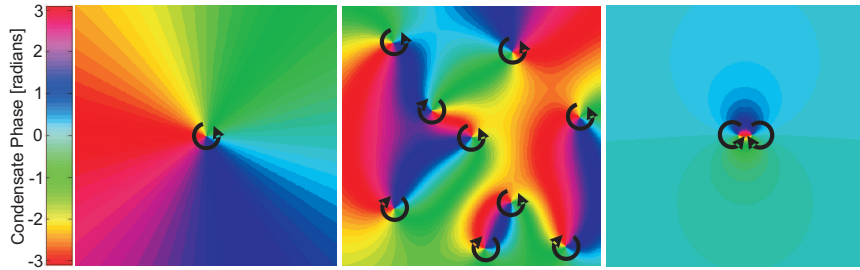


Figure 1.4: Effect of vortices and vortex-antivortex pairs on phase coherence. Condensate phase is encoded in color. Left: a single free vortex, with superfluid flow indicated by arrow. Center: phase decoherence caused by a random collection of vortices. Right: a vortex-antivortex pair on the other hand creates only a localized phase disturbance.

antivortex pair, in contrast, has its phase disturbance localized to the region in between the vortices. This difference between free vortices and vortex-antivortex pairs has two consequences: First, the energy required to place an isolated “free” vortex into a 2D superfluid of density $n_{SF,2D}$ is large, and increases with system size R as given by Eq. (1.20), with the replacement $n_S L \rightarrow n_{SF,2D}$ for a 2D system

$$E_v \approx \frac{\pi \hbar^2}{m} n_{SF,2D} \log(R/\xi) \quad (1.32)$$

(ξ is the healing length which sets the vortex core size), whereas the energy cost for creating a bound vortex-antivortex pair can be very small, of the order of

$$E_{pair} \approx \frac{\pi \hbar^2}{m} n_{SF,2D} \log(r_{12}/\xi) \quad (1.33)$$

for a pair separated by r_{12} (Eq. (1.33) is meaningful only for $r_{12} > \xi$). Owing to this small energy cost, such tightly bound vortex-antivortex pairs occur *at any finite* T . On the other hand, the very localized phase disturbance of small (tightly bound) vortex-antivortex pairs means that such pairs have very little influence on phase coherence, and the system remains superfluid. With increasing temperature however, the density of vortex-antivortex pairs increases, and the interaction between members of large pairs becomes screened by smaller interpenetrating pairs. This causes the pairs to become more and more loosely bound, and ultimately a plasma of free vortices forms. At this

point, superfluidity and phase coherence are fully destroyed, and a *finite* T transition to a normal state occurs. This “thermally activated proliferation of vortices” is sketched in Fig. 1.5.

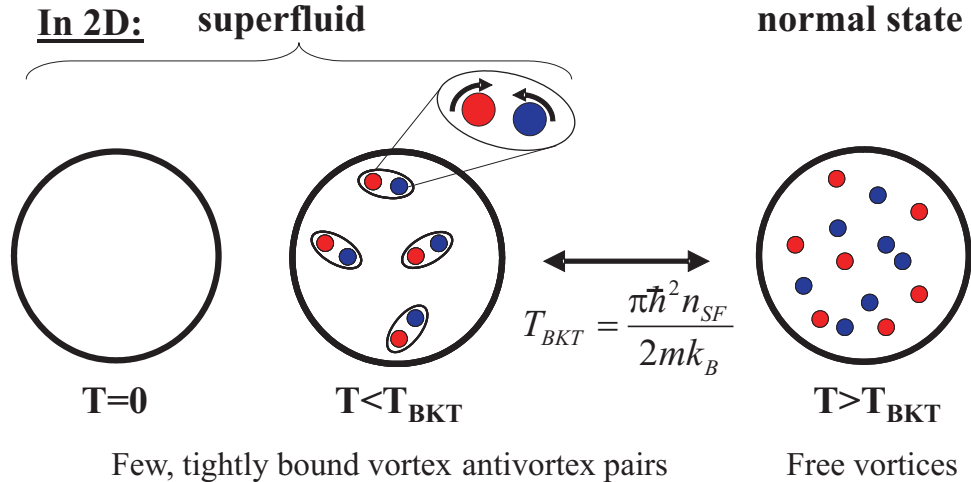


Figure 1.5: Vortex-antivortex pair unbinding triggers the BKT transition from a 2D superfluid to a normal state at the temperature T_{BKT} . Adapted from [29].

A simple and fairly accurate estimate of the BKT transition temperature can thus be made by asking the question “under what conditions is it thermodynamically favorable to have an isolated (*free*) vortex?” Placing a free vortex into a superfluid is thermodynamically favored (and hence will occur spontaneously) if its free energy

$$F = E_v - TS_v \leq 0 \quad (1.34)$$

The energy required to place a free vortex into a superfluid of density $n_{SF,2D}$ increases with system size R as given by Eq. (1.32), but may be offset by an entropy gain

$$S \approx 2k_B \log(R/\xi) \quad (1.35)$$

due to the $\approx R^2/\xi^2$ distinguishable locations for a vortex. Balancing energy and entropy term results in the famous *universal* relation between T_{BKT} and the 2D *superfluid* density n_{SF} at the transition temperature:

$$T_{BKT} = \frac{\pi \hbar^2 n_{SF,2D}}{2mk_B} \quad (1.36)$$

The difficulty, in contrast to Eq. (1.31), is that the superfluid density $n_{SF,2D}$ needs to be determined independently, and in 2D is not necessarily equal to the BEC density.

1.5 Josephson Junction arrays of BECs in optical lattice potentials

In Chapter 3, we study the BKT transition in a 2D array of Josephson-coupled BECs. In Chapter 4 we study vortex-lattice fluctuations in a one-dimensional Josephson-coupled array of rapidly rotating 2D BECs. Here we give a basic description of such arrays of Josephson-coupled condensates, and how we create them.

1.5.1 Optical dipole potentials - versatile tools for BEC manipulation

The optical dipole potential exerted on atoms by off-resonant light is the prime tool for BEC manipulation exploited in this thesis. Multi-beam interference patterns are used to create the periodic potentials from which Josephson junction arrays are constructed. Here I only give approximate formulae useful to gain intuition and for order-of-magnitude estimates, while the exact formulae used throughout this thesis to calculate dipole potential strengths are given in Appendix A.

Classically, an electric field \vec{E} induces a dipole moment $\vec{d} = \alpha\vec{E}$ in a particle with polarizability α , which then experiences an energy $-\vec{d} \cdot \vec{E} \propto \alpha I(\vec{r})$ proportional to the local intensity $I(\vec{r})$. A useful approximation for the resulting dipole potential is

$$U_{dip}(\vec{r}) = \frac{1}{8} \hbar \Gamma \frac{I(\vec{r})}{I_{sat}} \left(\frac{\Gamma}{\delta} \right) \quad (1.37)$$

where $I_{sat} = \hbar \Gamma \omega_{at}^3 / (4\pi c^2) = 1.64 \text{ mW/cm}^2$ for the dominant $5S \rightarrow 5P$ transition in ^{87}Rb . c is the speed of light, $\delta = \omega - \omega_{at}$ is the detuning of the light field at frequency ω from the atomic resonance at ω_{at} , and Γ is the natural linewidth of the atomic transition. A negative (“red”) detuning creates an attractive potential localizing the atoms to intensity maxima, while at positive (“blue”) detuning the potential is repulsive. At the same time, decoherence and heating are caused by the spontaneous scattering of

photons by the atoms, which occurs at a rate of approximately

$$\Gamma_{scat}(\vec{r}) = \frac{1}{8} \Gamma \frac{I(\vec{r})}{I_{sat}} \left(\frac{\Gamma}{\delta} \right)^2 \quad (1.38)$$

From equations (1.37) and (1.38) it can be seen that by increasing the detuning δ and the intensity I a fixed potential depth may be maintained while keeping a low enough scattering rate for the desired experiment: $\frac{U_{dip}}{\hbar\Gamma_{scat}} = \frac{\delta}{\Gamma}$.

Optical lattices have become a versatile tool owing to their variable geometry and length scale, as well as time-dependent control over their strength. The lattice geometries relevant to this thesis are depicted in Figure 1.6. Depending on the number

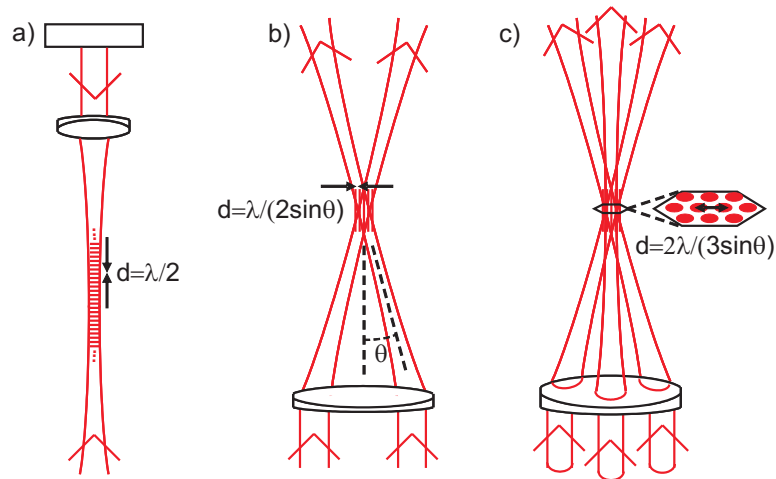


Figure 1.6: Different optical lattice geometries employed in this thesis. a) Retro-reflected optical lattice (OL) used in Chapter 4, b) acute-angle OL, and c) two-dimensional acute-angle OL used in Chapters 2 and 3.

of atoms per lattice site, two very different regimes of optical lattices are possible. For large numbers of atoms per lattice site, such that each site contains an individual BEC with well-defined phase, a “classical” Josephson junction array is realized. Here the individual superfluids communicate (i.e. exchange particles) by tunneling. In the other extreme limit of single- (or few-) particle occupation of lattice sites, a strongly correlated system results, which undergoes a superfluid- to Mott-insulator transition with increasing lattice depth, and holds promise for studying physics relevant to high-

temperature superconductivity [80] and quantum magnetism [134].

1.5.2 Two Josephson-coupled BECs

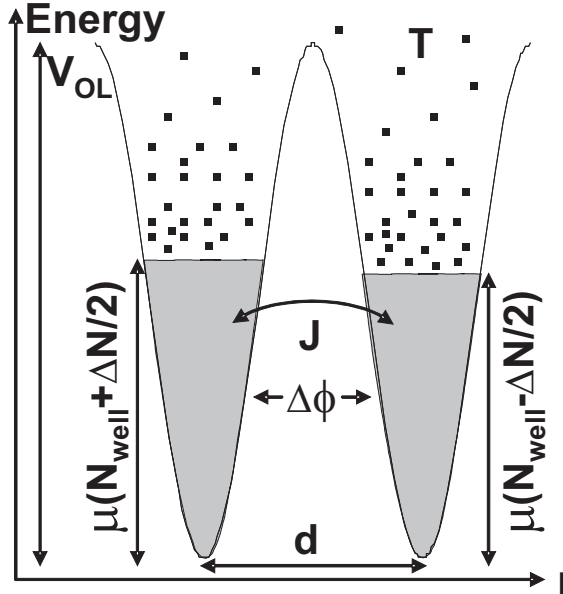


Figure 1.7: A double well BEC. The barrier height V_{OL} and the chemical potential μ (fixed by the number of condensed atoms per well N_{well}), control the Josephson coupling J , which acts to lock the relative phase $\Delta\phi$. A cloud of uncondensed atoms at temperature T induces thermal fluctuations when $J < T$. The charging energy E_c disfavors population imbalance ΔN between the wells, but is negligible in our system.

In order to build up the intuition for an array of Josephson junctions, we begin with a brief look at a condensate loaded into a double-well potential, see Fig. 1.7. If we restrict the dynamics of the system to two degrees of freedom, the relative number ΔN of particles in the two wells and the relative phase $\Delta\phi$ between the two condensates, then the effective Hamiltonian reads [99]

$$H = \frac{1}{8} E_c \Delta N^2 - J \sqrt{1 - \left(\frac{\Delta N}{N_{well}} \right)^2} \cos(\Delta\phi) \quad (1.39)$$

where N_{well} is the average population per site. E_c , in analogy to superconducting systems, is called the charging energy. In our neutral system, it is caused by the typically repulsive contact interactions between condensate atoms. J is the Josephson (collective

tunneling) energy. We note here that the inclusion of additional degrees of freedom beyond the relative number and phase, such as spatial phase variations *inside* the wells, complicates the picture. (1.39) is therefore valid for small Josephson junctions, where the dynamics of condensates *inside* respective wells is frozen out, as it would occur at higher energies than the particle / phase dynamics.

Quantum fluctuations. It may be immediately inferred from (1.39) that the two energy terms lead to incompatible ground states: The charging energy alone disfavors population imbalances, and if dominant leads to fixed equal numbers of condensed atoms on both sites. As a consequence, the quantum mechanical uncertainty between relative number and relative phase, $\Delta N \cdot \Delta\phi > 1/2$ renders the relative phase between the two sites completely uncertain. The Josephson coupling term on its own, on the other hand, favors phase coherence $\Delta\phi = 0$ between the two states. This in turn is incompatible with well-defined particle numbers on each site. The competition between the two terms implies a crossover as a function of E_c/J . Quantitatively, one finds the following quantum fluctuations of the relative number and phase:

$$\Delta\phi_q^2 = \frac{1}{2}\sqrt{(E_c + J/N_{well}^2)/J} \quad \Delta N^2 = \frac{1}{2}\sqrt{J/(E_c + J/N_{well}^2)} \quad (1.40)$$

The transition between a phase coherent and a dephased system occurs roughly when $\Delta\phi_q^2 \rightarrow 1/2$, i.e. in the case of $N_{well} \gg 1$ when $E_c \approx J$.

Following Leggett [99], not only two but three different regimes of zero-temperature Josephson junction arrays have to be distinguished, based on the two energy scales, E_c and J , and the number of condensed particles per well N_{well} :

Rabi regime. Here $E_c/J \ll N_{well}^{-2}$, i.e. the charging energy is unimportant, both for the dynamics and the phase fluctuations ($\Delta\phi_q^2 = 1/N_{well}$).

Josephson regime. Here $N_{well}^{-2} \ll E_c/J \ll 1$, i.e. the charging energy speeds up the dynamics of particle exchange (see ‘‘Dynamics’’ below), and begins to dominate the quantum phase fluctuations ($\Delta\phi_q^2 = \sqrt{E_c/J}$), which however remain small in absolute

magnitude.

Fock regime. Here $1 \ll E_c/J$, i.e. finally E_c is strong enough to localize most atoms ($\Delta N \rightarrow 0$) and quantum fluctuations dephase the system ($\Delta\phi_q > 1$).

Thermal fluctuations. The experiments described in this thesis are performed in the Josephson regime, but with the additional ingredient of a finite temperature T . The topic of study is a competition between J and T , with E_c unimportant. The effects of finite temperature lead to thermal phase fluctuations, which scale as

$$\Delta\phi_{th} \simeq \sqrt{T/J} \quad (1.41)$$

as long as $T < J$. The thermal fluctuations (1.41) of the double well system are shown in Fig. 1.8. J and E_c have been calculated numerically, see Appendix B, under the conditions relevant to our studies of the BKT transition in Chapter 3. It turns out that the condition under which thermal fluctuations become important in a double well BEC, i.e. $J \approx T$, remains the same in an *array* of wells, allowing a rough estimate of the experimental conditions under which the BKT transition is expected in a 2D Josephson junction array. Experiments on finite- T double well systems were pioneered in Oberthaler's group [60].

Dynamics. The dynamics of the double well system, for small displacements from equilibrium $\Delta N = 0$ and $\Delta\phi = 0$, is that of a harmonic oscillator, exchanging energy between the phase and number degree of freedom, at the so-called Josephson plasma frequency (with J and E_c measured in *rad/s*)

$$\omega_p = \sqrt{J(E_c + J/N_{well}^2)} \approx \sqrt{JE_c} \quad (1.42)$$

with the approximation valid in the Josephson regime. The Josephson (particle) current is given by $J \times \sin(\Delta\phi)$. Experiments have recently confirmed this oscillation [61]. For larger displacements, the nonlinearities in the Hamiltonian (1.39) create more complex behavior, such as population self-trapping in one well.

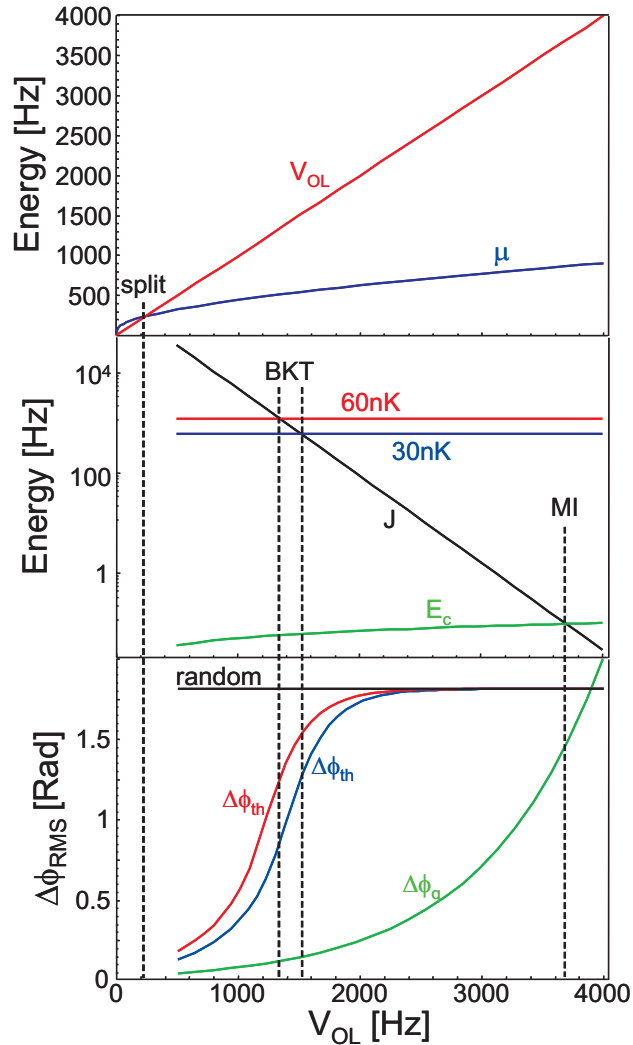


Figure 1.8: Dependence of relevant parameters of the double well BEC on barrier height V_{OL} , under conditions typical for the experiments in Chapter 3. Upper panel: the chemical potential μ increases rather weakly with V_{OL} , caused by increasing compression of the BEC into the bottom of the well. As a result, already a weak ~ 300 Hz barrier physically splits the BEC into two. As soon as the BEC is split, the Josephson coupling J is well defined and decreases approximately exponentially with Barrier height (central panel). Thermal fluctuations $\Delta\phi_{th}$ grow when $J \approx T$, for realistic temperatures around $V_{OL} \approx 1300$ Hz – this is where the BKT transition is expected for a 2D Josephson junction array. Quantum fluctuations $\Delta\phi_q$ become important only when $J \approx E_c$, i.e. when thermal fluctuations have long dephased the system. Hence the Mott-insulator (MI) transition is not observed. J and E_c have been calculated numerically, see Appendix B.

1.5.3 Arrays of Josephson-coupled BECs

In analogy to the double-well system, the Hamiltonian for a D -dimensional Josephson junction array (JJA) is given by

$$H = \frac{1}{8}E_c \sum_j \Delta N_j^2 - J \sum_j \sqrt{1 - \left(\frac{\Delta N_j}{N_{well}}\right)^2} \cos(\Delta\phi_j) \quad (1.43)$$

where j represents a D -dimensional sum over all Josephson *junctions*. Several new features arise in an array compared to a single junction:

(i) Vortices on a JJA. For a two-dimensional array, topological defects such as vortices, can occur. A vortex in a JJA is defined by the phase differences it induces along a closed loop of array sites, see Fig. 1.9. Vortex cores “live” in between lattice sites – individual condensates are too small to sustain vortices *inside* them.

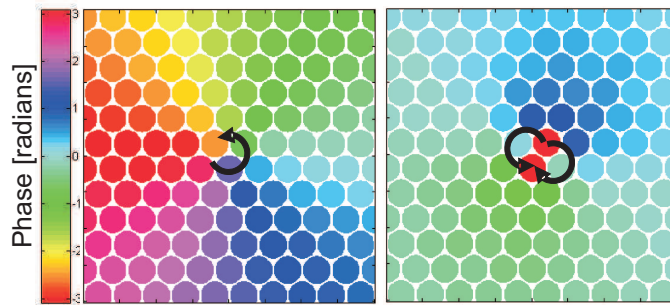


Figure 1.9: Vortices in a Josephson junction array. Condensate phases on array sites (circles) are color-coded. Left: single vortex, right: vortex-antivortex pair. The direction of Josephson current flow is indicated by arrows.

(ii) Size scaling. In an extended 2D JJA one can expect sharper variations of quantities such as phase fluctuations e.g. with J/T , compared to the behavior shown in Fig. 1.8 for a single Josephson junction.

(iii) Phonon modes of the JJA. The Josephson plasma frequency Eq. (1.42), i.e. the single frequency at which particle exchange occurs in a double-well system, is replaced by a whole spectrum of phonon modes. The phonon modes of a one-dimensional JJA were described in Refs. [87, 35]. The spectrum resembles that of acoustic phonons

(lattice vibrations) in a 1D crystal lattice of period d :

$$\omega_q = \sqrt{2J \sin^2(qd/2) \left(E_c + \frac{2J}{N_{well}^2} \sin^2(qd/2) \right)}. \quad (1.44)$$

Here, $q = 2\pi/\lambda_{phonon}$ is the wavevector of the excitation, in a finite system of size $2R$, $q \approx i\frac{\pi}{2R}$. The maximum frequency ω_{max} at the edge of the Brillouin zone ($q = \pi/d$) is related to the Josephson plasma frequency, but with the replacement $J \rightarrow 2J$, i.e. $\omega_{max} = \sqrt{2J(E_c + 2J/N_{well}^2)}$. In the Josephson regime, the long-wavelength spectrum is linear, $\omega_q \rightarrow \sqrt{2JE_c} \frac{qd}{2}$. The lowest frequency mode in a finite system is $\omega_{min} = \sqrt{2JE_c} \frac{\pi d}{2R}$, i.e. it can be estimated from the double-well plasma frequency (1.42) and the number of lattice sites across the array R/d : $\omega_{min} \approx \omega_p \times d/R$. The timescale required for adiabaticity with respect to these modes, e.g. when ramping up the optical lattice, can be very long, an aspect to be kept in mind in experiments.

(iv) 2D XY model. In the regime relevant to our experiments, the Hamiltonian (1.43) approximates the so-called XY Hamiltonian,

$$H_{xy} = -J \sum_j \cos(\Delta\phi_j) \quad (1.45)$$

which describes a system of spins constrained to rotate in the plane of the lattice ($\Delta\phi_j$ is the difference in spin orientation across junction j). This system was shown to undergo a BKT transition in the seminal paper by Kosterlitz and Thouless [94]. In such a ‘‘Josephson network’’, it is not de Broglie wave overlap, but the strength of the Josephson coupling between sites, which decides on the development of (at least local) phase coherence. In Chapter 3 I will describe our experiments on the BKT transition in a 2D Josephson junction array, which occurs under condition

$$T_c \approx J \quad (1.46)$$

(v) Frustrated 2D JJA. A highly fascinating topic is the application of an external field, or a rotation of the array. This induces a vector-potential term A_j in the

relative phase, which renders the problem highly nontrivial [124, 25].

$$H_{xy} = -J \sum_j \cos(\Delta\phi_j - A_j) \quad (1.47)$$

A_j measures the integrated vector potential across a junction: $A_j = \int_{\text{junction } j} \vec{A}(x) \cdot \vec{dx}/(2\pi)$. We introduce the frustration index f , which measures the number of flux quanta associated with the vector potential, per plaquette of the optical lattice ³

$$f = \oint \vec{A}(x) \cdot \vec{dx}/(2\pi\hbar) \quad (1.48)$$

the loop integral is around one plaquette of the array. In the case of rotation-induced flux, $\vec{A} = m\vec{\Omega} \times \vec{r}$ (see Appendix D), and f is identical to the number of vortices per plaquette, e.g. for a square JJA with the density of lattice sites $n_{OL} = 1/d^2$

$$f \equiv n_v/n_{OL} = 2m\Omega d^2/h \quad (1.49)$$

while for a triangular JJA with $n_{OL} = 1/(d^2\sqrt{3}/4)$ ⁴

$$f = m\Omega d^2\sqrt{3}/(2h) \quad (1.50)$$

with the areal density of vortices n_v given by Eq. (1.22). Around rational values of f , commensurate-incommensurate transitions occur between regular and irregular arrangements of vortices on the array [88], see Fig. 1.10. At finite temperature, these vortex configurations undergo BKT transitions to a normal state, with an especially interesting situation given for $f = 1/2$ [124] where the interplay between a BKT transition and an Ising-type transition is neither theoretically nor experimentally fully understood. With further increased rotation rate and at low temperature, fractional quantum Hall states are expected to form, in analogy to the bulk rotating BEC. Experiments on a deep rotating 2D optical lattice were only touched upon in this thesis, but may well form the topic of another thesis to follow.

³ The frustration index is identical to the ‘‘filling factor’’ used in the literature relevant to vortex pinning. We do not use this terminology here to avoid confusion with the filling factor used in the context of vortex lattice melting.

⁴ In a triangular array, the triangular ‘‘plaquette’’ on which f is calculated according to (1.48) is *half* the conventional unit cell!

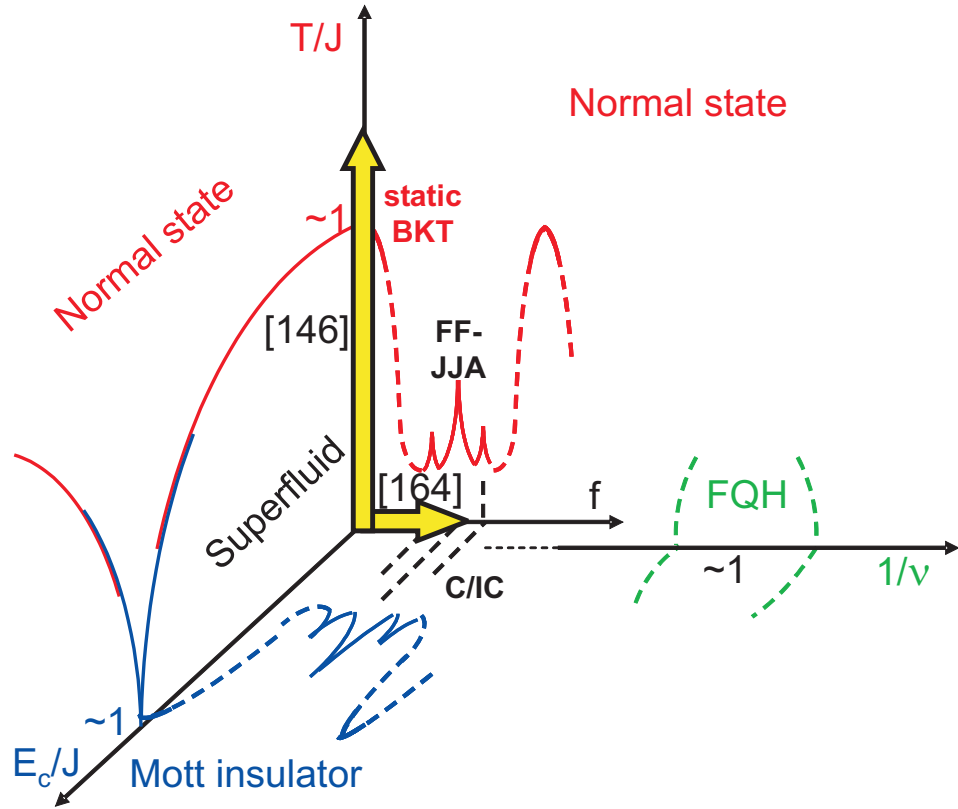


Figure 1.10: Schematic phase diagram of a Josephson junction array. The vertical axis is temperature, measured in units of the Josephson coupling J . Rotation rate increases along the axis to the right: $f = n_v/n_{OL}$ is the frustration index, Eq. (1.49), and $\nu = n_{at}/n_v$ is the filling factor (1.25), i.e. the number of atoms per vortex. f and $1/\nu$ are related by $f = N_{well}/\nu$ where $N_{well} = n_{at}/n_{OL}$ is the lattice site occupation. The E_c/J axis describes increasing quantum phase fluctuations and decreasing number fluctuations, which drive the Mott insulator phase transition. C/IC: commensurate-incommensurate phase transitions of the vortex lattice inside the JJA; FF-JJA: fully frustrated JJA at $f = 1/2$, Ref. [124]; FQH: strongly correlated quantum Hall states induced by rotation [25]; BKT: finite-T normal phase via Berezinskii-Kosterlitz-Thouless transition of the frustrated JJA, Ref. [160]. Mott-insulator – superfluid boundary for rotating lattices: Ref. [114]. [164, 146]: Experiments in this thesis.

Josephson junction parameters. The important energy scale underlying most parameters of optical lattice experiments, is the recoil energy

$$E_r = \frac{\hbar^2 \pi^2}{2md^2} \quad (1.51)$$

where d is the lattice period. Both J and E_c are governed by it, and in addition it is customary to quote optical lattice depths in units of this energy scale.

In the limit where interparticle interactions are negligible compared to the energy separation of Bloch bands at zero momentum, which is always larger than $4E_r$, the Josephson energy is given by $J = N_{well} \times t$, with the single-particle tunneling energy t given e.g. by Zwerger [170]

$$t = \frac{4}{\sqrt{\pi}} E_r (V_{OL}/E_r)^{3/4} \exp(-2\sqrt{V_{OL}/E_r}) \quad (1.52)$$

As soon as interparticle interactions are not negligible compared to the recoil energy, J must be found from a numerical solution of the GPE, Eq. (1.9). Our procedure is detailed in Appendix B. The physical reason for the modification of J by interactions is the interaction-induced increase of the BEC's chemical potential, which in turn reduces the tunneling barrier to neighboring lattice sites. An order-of-magnitude estimate for J is possible by replacing $V_{OL} \rightarrow (V_{OL} - \mu_{lat})$ in the exponent of Eq. (1.52), with μ_{lat} the chemical potential of a BEC loaded into an optical lattice, given by Eq. (1.54) below.

The interaction energy of N_{well} particles on one lattice site is conventionally written as $\frac{U}{2} \times N_{well}(N_{well} - 1)$, with U related to the charging energy E_c by $E_c = 2U$. The charging energy depends on the strength of interparticle interactions, because a repulsively interacting BEC grows in size. E_c can be estimated as [122]

$$E_c = 2 \frac{\partial \mu_{lat}}{\partial N_{well}} \approx \frac{4}{5} \frac{\mu_{lat}}{N_{well}} \quad (1.53)$$

with the chemical potential μ_{lat} given by Eq. (1.54) below.

1.5.4 Thomas-Fermi description of BECs in optical lattices

Stringari and coworkers [126] devised a useful concept for experimental determination of the parameters of a BEC loaded into an optical lattice. The central observation, from an experimental point of view, is that in-situ images of BEC in most cases do not resolve individual lattice sites – instead a coarse-grained envelope density profile is observed. Stringari and coworkers show that this coarse-grained profile in many cases

follows a renormalized Thomas-Fermi (TF) description. The renormalized chemical potential μ_{lat} depends only on the *total* number of condensed particles N in the array, and other known or measurable quantities⁵ :

$$\mu_{lat} = \frac{\hbar\bar{\omega}}{2} \left(\frac{15Na_{sc}}{\bar{a}} \left(\frac{d}{\sqrt{2\pi}\sigma} \right)^D \right)^{2/5} \quad (1.54)$$

here, D is the dimensionality of the lattice and d is its period⁶, σ is the width of an *individual* condensate on a lattice site, and $\bar{a} = \sqrt{\hbar/m\bar{\omega}}$ and $\bar{\omega} = (\omega_x\omega_y\omega_z)^{1/3}$ are the oscillator lengths and frequencies of the *envelope potential* formed by optical lattice beam envelope and magnetic trap. As long as interparticle interactions are insignificant, $\sigma = \sigma_0 \equiv \frac{d}{\pi(V_{OL}/E_r)^{1/4}}$ is governed by the optical lattice depth and period alone, while repulsive interactions further increase the width $\sigma \approx \sigma_0 \times \sqrt{\frac{2\mu_{lat}}{\hbar\omega_{lat}}}$. Here ω_{lat} is the lattice-site oscillator frequency. When including interparticle interactions in σ , Eq. (1.54) becomes an implicit equation that can be solved for μ_{lat} .

Eq. (1.54) most importantly allows the determination of the overall BEC number N by simply measuring the coarse-grained BEC radii $R_i = \sqrt{\frac{2\mu_{lat}}{m\omega_i^2}}$, as shown in Fig. 1.11. The important number of particles in the central lattice site, N_{well} , then follows from $N = \sum_i N_{(site\ i)}$ where the number of particles $N_{(site\ i)}$ on each site follows from an integral of the coarse-grained TF density over the site volume V_{site} : $N_{(site\ i)}/N_{well} = \frac{1}{V_{site}} \int_{site\ i} d^3x (1 - (x/R_x)^2 - (y/R_y)^2 - (z/R_z)^2)$. This results, e.g. in a 1D lattice in the z-direction, in

$$N_{well} = \frac{15}{16} \frac{d}{R_z} \times N \quad (1.55)$$

or in a 2D hexagonal lattice in the xy plane,

$$N_{well} = 2 \frac{d^2 \sqrt{3}/2}{\pi R_\rho^2} \times N \quad (1.56)$$

where R_ρ is the envelope TF radius in the xy plane.

⁵ Note that μ_{lat} in Eq. (1.54) is measured with respect to the zero-point energy of the trap potential, as is Eq. (1.11) above. While usually this zero-point energy is negligible compared to the chemical potential, this is no longer true in strong optical lattices.

⁶ V_{OL} and d are assumed identical in all lattice dimensions but (1.54) can be generalized.

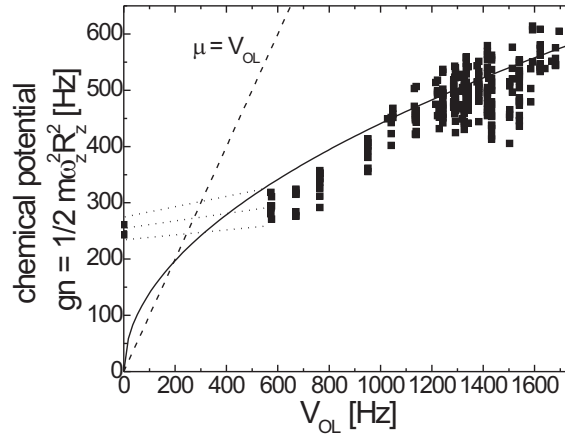


Figure 1.11: Chemical potential $\mu_{lat} \equiv gn$ (symbols) measured from axial Thomas-Fermi radii R_z of BECs loaded into a hexagonal 2D optical lattice (period $d = 4.7 \mu m$) in the xy plane, showing good agreement with effective Thomas-Fermi formula (solid line) Eq. (1.54). The condensate number extracted from the data was $N = 520000$, i.e. $N_{well} = 7000$ using Eq. (1.56). This agrees with an independent analysis of the same experimental data based on numerical simulations described in Appendix B. Dashed: optical lattice depth V_{OL} . For $V_{OL} = \mu$ (at $200 - 300 Hz$) the bulk BEC is split into a Josephson junction array.

We note here that for our experiments on the BKT crossover in Chapter 3, where precise knowledge of N_{well} is crucial to determine J , we do *not* rely on this approximate formalism, but employ numerical simulations of the Gross-Pitaevskii equation to provide a relation between measured cloud radii and N_{well} .

1.6 BEC imaging

For a detailed quantitative analysis of imaging, refer to the excellent chapters in Haljan’s [74] and Matthews’ [105] theses. In this thesis we exploit two types of images, both of which measure the density of atoms, *integrated along the probe laser propagation axis*. Nondestructive sideview images (or sequences thereof) of BECs *in trap* provide *all* quantitative condensate parameters. An example is shown in Fig. 1.12.

Top view absorption images *of the same condensate* after expansion usually contain the “science” information. A note of caution is in order at this point: In most other BEC experiments, expansion is used as a means to study the *momentum* distribution.

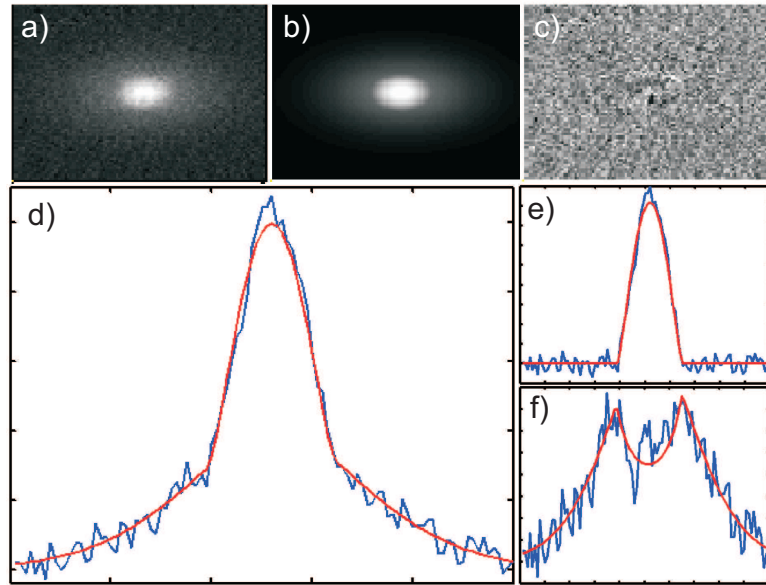


Figure 1.12: (a) Nondestructive image of a finite T BEC, (b) fit and (c) residuals. The images show the density of atoms, integrated along the line of sight. The image area is $230 \times 160 \mu m$. The BEC actually resides in an optical lattice and is split into a Josephson junction array. Individual lattice sites remain unresolved, and the image is analyzed according to the effective Thomas-Fermi description by Stringari and coworkers, see section 1.5.4. The thermal cloud fit follows the description in Section 1.2.4. Horizontal cut through (d) full density profile and fit, (e) extracted BEC profile, (f) extracted thermal cloud profile - the dip in the center is caused by mean-field repulsion from the BEC density.

In our system, on the other hand, expansion is employed as a means of magnifying *spatial* information beyond the imaging resolution. This works for two reasons: (a) we employ a “forced” (or “anti-trapped”) expansion on an inverted parabola potential that merely “stretches the fabric of the universe” [46], in contrast to the conventional “free” expansion, which converts potential and interaction energy to kinetic energy. Our expansion is in addition designed to be almost exclusively in the two spatial dimensions of the image plane. (b) we are often interested in topological defects such as vortices, and these largely preserve their structure upon two-dimensional expansion. This technique allows a great detail of spatial information to survive the expansion – almost all BEC images shown in this thesis are of this type. Possible systematic effects of dynamics during expansion nonetheless have to be kept in mind for quantitative analysis and

should be considered every time new quantities are sought to be retrieved from images.

1.7 History and organization of this thesis

Rotating BECs had been studied in our lab since 1999 [74]. Shortly after my arrival in the lab in 2002, we discovered how to reach the “rapidly rotating” regime [56, 44, 143] described in Ian Coddington’s thesis [46]. After finishing our fundamental studies on this new system [45, 150, 57], we immediately started introducing various optical lattice potentials [145, 164, 146] into the system, interrupted only at times by “side projects” [144, 79] when offline developments were needed to make progress. This thesis therefore could alternatively be entitled “bringing optical lattice potentials to the Cornell labs”.

It consists of four essentially independent experiments, which are organized as follows. Chapter 2 details results of experiments on vortex pinning in rotating BECs loaded into a shallow ($V_{OL}/\mu < 1$) co-rotating two-dimensional optical lattice potential. Chapter 3 presents our observation of the Berezinskii-Kosterlitz-Thouless crossover in a finite- T two-dimensional array of Josephson-coupled BECs. Chapter 4 summarizes experiments on loading a rapidly rotating BEC into a one-dimensional optical lattice with its axis aligned along the rotation axis. In this way a stack of two-dimensional rapidly rotating BECs with low filling factor is created, a possible first step toward fractional quantum Hall states in rotating BECs. The extended Appendix D provides additional background information relevant to Chapter 4. Chapter 5 reports on the first study of vortex lattices in a rotating two-component BEC, where self-organization of two interlaced square vortex lattices in the two components is observed.

The underlying “BEC factory” has remained essentially unchanged since it has been described in previous theses [74, 46]. Exceptions include the introduction of a more reliable repump laser system as well as slight changes to the setup for microwave excitation. The major experimental additions to the machine all have to do with (a)

setting up laser sources for various optical lattice experiments and (b) the design and implementation of various extremely stable optical lattice beam paths, each tailored for the envisioned experiment. These setups are detailed in the respective chapters.

Chapter 2

Vortex pinning in rotating Bose-Einstein condensates

In this chapter we report the first observation of vortex pinning in rotating gaseous Bose-Einstein condensates (BEC) [1]. A co-rotating two-dimensional optical lattice is superimposed on the rotating BEC. The density of the superfluid is suppressed at the antinodes of the two-dimensional standing wave pattern of the optical lattice. These antinodes therefore form an array of columnar pinning sites, regions of low potential energy, for the superfluid vortices, as has been shown in Figure 1.3. We study the effects of two optical lattice structures, triangular and square. In both geometries we see an orientation locking between the vortex and the optical lattices. At sufficient intensity the square optical lattice induces a structural cross-over in the vortex lattice.

2.1 Motivation

Some of the most appealing results from recent work in superfluid gases have had to do with lattices, either optical lattices [67, 93, 159] or vortex lattices [102, 143, 5]. As distinct as these two periodic structures may be, there are reasons for trying to marry them in the same experiment. For one thing, the extreme limits of rapid rotation (in the case of vortex lattices) [47] and deep potentials (in the case of optical lattices) [85] both lead to the same thing: correlated many-body states. For another, there is considerable precedent, from various subdisciplines of physics, for interesting effects arising from the interplay between competing lattices [158, 15, 66]. Moreover, the

pinning of superconducting flux vortices to an array of pinning sites in solids is an area of very active research [13, 69, 167, 129]. In superconductors, unpinned vortices are a source of dissipation, so pinning as a way of freezing vortex degrees of freedom is of both fundamental and technical interest. Here we are able to study this effect in a clean system with well-controlled pinning potential and vortex-vortex interaction, and with time-dependent control over pinning potential strength and rotation rate.

With these considerations in mind, we undertook a preliminary experimental study of the effects of a rotating optical lattice on a vortex lattice in a Bose-condensed sample of ^{87}Rb .

Pinning of vortex lattices. When a periodic pinning potential is superimposed on a rotating BEC, an ordered pinned structure, such as shown in Fig. 2.1, may be expected for certain commensurate ratios $r \equiv p/q$ of vortices p to pinning sites q ¹. For $r = 1$, the vortex lattice can be pinned one-to-one to the pinning lattice. For rational $r < 1$, vortices will form superlattice structures locked to the pinning lattice, whereas for $r > 1$, some pinning sites contain more than one vortex. In the limit of strong pinning, these may merge to form multiply quantized vortices.

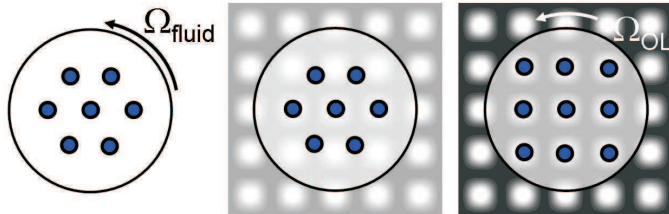


Figure 2.1: A vortex lattice (left) rotating at a rate Ω_{fluid} is exposed to a square optical lattice rotating at Ω_{OL} . Once the pinning potential strength overcomes vortex-vortex interactions (right), vortices are pinned to the antinodes (bright) of the optical lattice.

For any pinned vortex structure other than a hexagonal lattice of vortices, the pinning potential has to overcome the difference in vortex-vortex interaction between

¹ I do not use the frustration index f here, which is defined as number of vortices *per plaquette* of the optical lattice (Eq. (1.49)): For a triangular lattice there are *two* triangular plaquettes per lattice unit cell, but only one pinning site per unit cell – so $r = 2f$. For a square lattice, $r = f$.

the pinned structure and the unpinned hexagonal vortex lattice. Consider the pinning-induced transition to a square vortex lattice: In the absence of a pinning potential, the interaction energy of a square vortex lattice is calculated to exceed that of a triangular lattice by less than 1 % [36], thus it is predicted [130, 131, 128] that the influence of even a relatively weak square optical lattice will be sufficient to induce a structural transition in the vortex lattice. Prior to our experiments, numerical and analytical work existed for some specific situations, regarding the phase transitions between pinned and unpinned vortex phases [130, 131, 128]. Also [168, 25] discuss similar systems in the strongly interacting regime. Following the publication of our results, numerical simulations by Kasamatsu and Tsubota [89] have qualitatively confirmed our results on the structural crossover from hexagonal to square vortex lattice, and have added more information on the dynamical behavior of vortices under the influence of a weak pinning potential. Angular locking of the hexagonal vortex lattice to a hexagonal optical lattice was studied numerically by Sato, Ishiyama and Nikuni [140]. The topic of rotating lattices has become a very active field of ultracold atom theory. Several articles discussing related issues have been published, e.g. [34], [114], [166].

Away from commensurate lattices: defects and vortex glass. Another question concerns the properties of vortices and vacancies at incommensurate frustration index, i.e. when the number of vortices is not a rational fraction of the number of pinning sites. Under certain conditions one expects that vortices could become frozen into a disordered but stationary phase known as a “vortex glass”. The statistical properties and the finite-temperature behavior of this phase could be a very exciting subject of study.

2.2 Setup, alignment and diagnostics

There are various possible ways of creating a rotating optical lattice potential. Possibilities include a scheme based on crossed electro-optical modulators [37], holo-

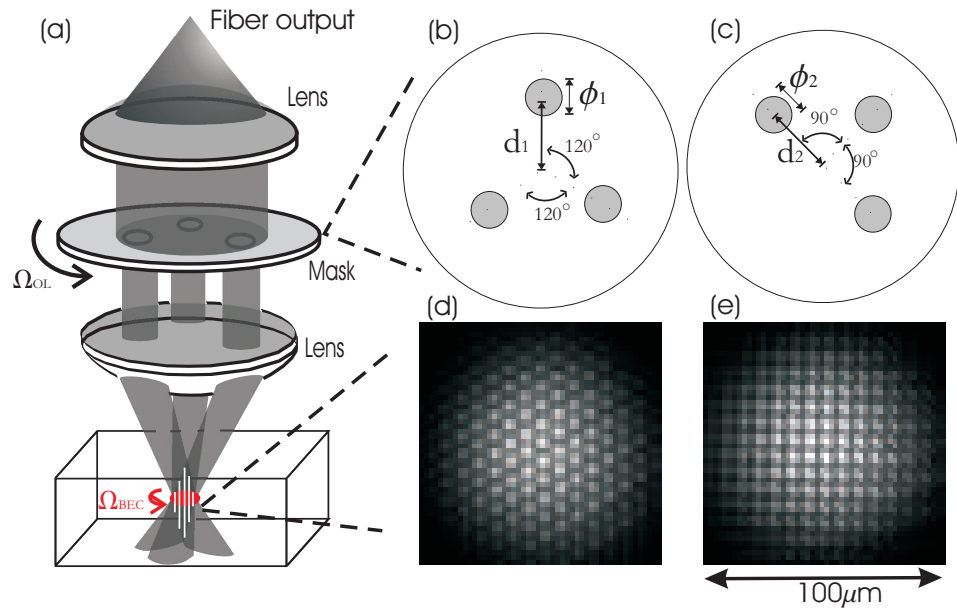


Figure 2.2: (a) Schematic diagram of our setup for the rotating 2D optical lattice. Layouts of the masks for a triangular (b) and square (c) optical lattices. (d) and (e) are pictures of triangular and square optical lattices, respectively.

graphic masks, or simply interference patterns created by a rotating shadow mask placed placed in a large, cylindrically symmetric laser beam. We employed this last technique.

Making this experiment work was actually a quite laborious endeavor. For the pinning sites to appear static in the frame of a rotating BEC, the rotation of optical lattice and vortex lattice must be concentric, and such a *quietly* rotating optical lattice pattern with few micron period is not exactly what you get when you try the first time. Mechanical instabilities and optical aberrations (which lead to epicyclic motion of the pinning sites) had to be canceled meticulously, as suggested in Fig. 2.3. Even after optimization, residual undesired motion was such that the strength of the optical lattice had to be kept at less than 30 – 50% of the condensate’s chemical potential or unacceptable heating resulted over the experiment duration of tens of seconds. The experiments in the following sections were thus performed in the weak pinning regime.

A conceptual view of the setup for creating a rotating optical lattice is shown in Fig. 2.2(a). A mask with a set of holes is mounted onto a motor-driven rotary stage with

a 2" clear aperture ² , and a laser beam (532 nm) emerging from a single-mode fiber is expanded, collimated, and passed through the mask. After the mask the resulting three beams are focused onto the BEC. The interference pattern at the focus constructs a 2D optical lattice. The geometry and spatial extent of the triangular or the square optical lattice are determined by the size and layout of the holes and the focal length of the second lens. We create a hexagonal optical lattice using three holes at 120°, or a square OL using three holes at 90°. The intuitively expected fourth hole is left out, for the reason that three interfering laser beams create a stable interference structure, while for four beams the topology of the lattice depends on the relative phases of the laser beams [121]. The only consequence of omitting the fourth beam is that each site is of elliptical shape, with the major axis at 45° with respect to the lattice axes.

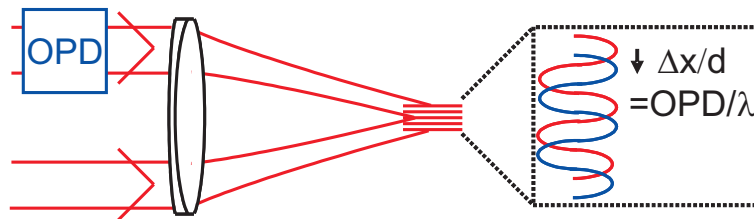


Figure 2.3: Fluctuations in the optical path length difference (OPD) between lattice beams lead to lattice displacements Δx , which ultimately lead to heating. d : optical lattice period; λ : laser wavelength. Such fluctuations are *easily* introduced for a rotating lattice by lens aberrations, optical imperfections, or mechanical vibrations.

Feasibility estimate. A first feasibility estimate for creating a smoothly rotating optical lattice is obtained by a ray tracing analysis of the experimental setup of Fig. 2.2(a), taking into account expected imperfections in alignment.

Optical path length difference (OPD) curves provide a well suited measure of the effect of aberrations on a rotating optical lattice: in a lattice of period d , a time-varying optical path length difference between the beams leads to a time-varying displacement Δx of the lattice, given by $OPD/\lambda = \Delta x/d$, as shown in Fig. 2.3. Only azimuthally

² Aerotech ADRT 150 direct rotary stage.

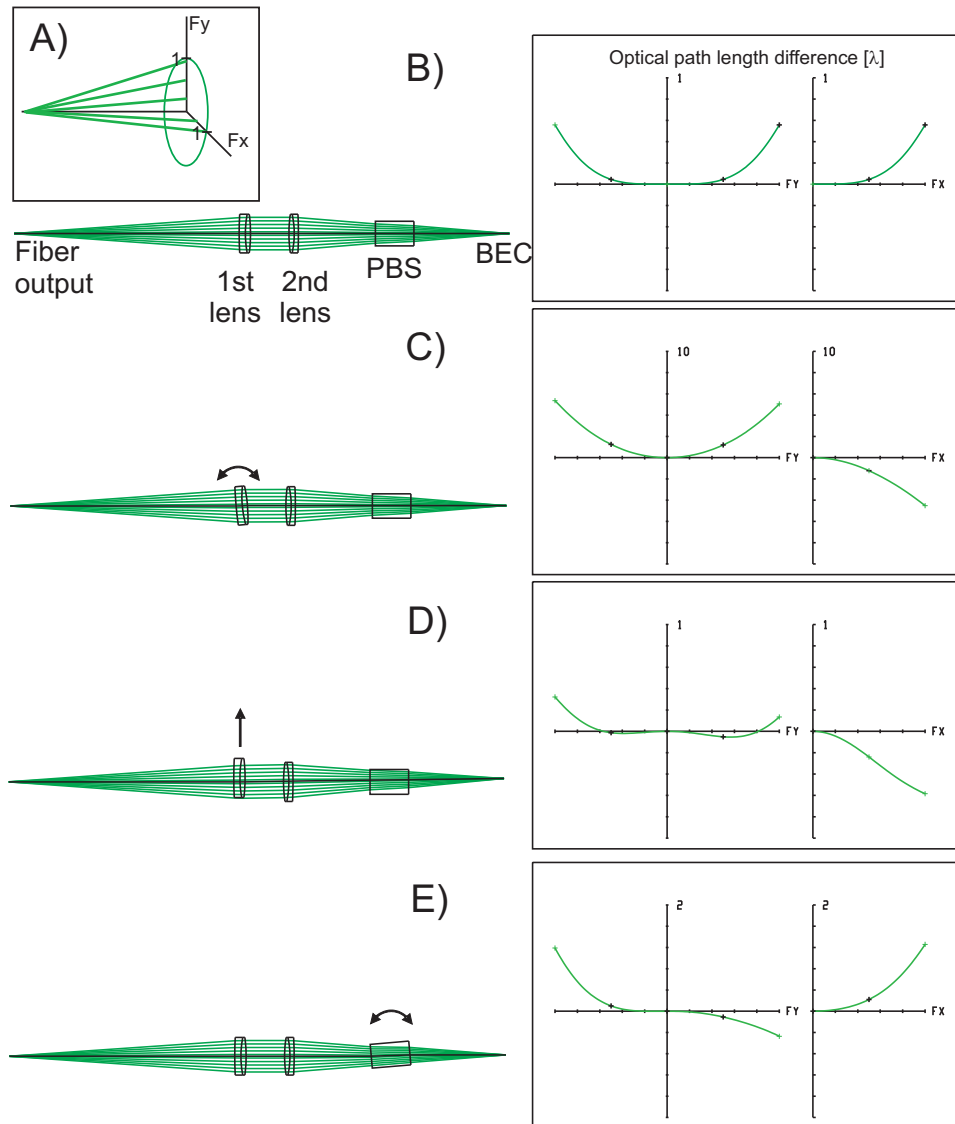


Figure 2.4: Analysis of aberrations for the rotating 2D optical lattice used for the pinning experiments. A) Fans of rays in sagittal and paraxial plane. Coordinates F_x (in sagittal plane), F_y (in tangential plane) range from 0 to +1 from center to edge of this fan of rays. Optical path length differences are calculated in the image plane where the optical lattice is formed. In the sagittal plane, by symmetry, only the range 0 to +1 is plotted. B) Perfectly aligned system (the glass block (material: SF6) symbolizes a 2" polarizing beamsplitter cube), showing only residual spherical aberrations, seen as identical wavefront distortions in sagittal and paraxial plane. C) tilting the first lens by 5° induces astigmatism, seen as opposite curvatures in sagittal and paraxial plane. Here the image plane is chosen between sagittal and paraxial waist - wavefronts still converge in F_y , but already diverge in F_x . D) decentering the first lens by 5 mm . E) tilting the polarizing beamsplitter cube by 5° .

dependent aberrations such as astigmatism constitute a problem. Spherical aberration is not a problem, as ideally the 3 beams trace spherically symmetric orbits. However, off center lenses convert spherical aberrations into azimuthally dependent aberrations. In Fig. 2.4 examples of alignment imperfections relevant to the experimental setup and the resulting aberrations (OPD curves) are shown ³.

Table 2.1: Estimated error budget from ray-tracing analysis of aberrations in a rotating 2D optical lattice. In a lattice of period d , an optical path length difference (OPD) leads to a displacement Δx given by $OPD/\lambda = \Delta x/d$. Such OPD may be introduced by the indicated misalignments of optical elements, either in the optical lattice beam path between light source and BEC, or in the imaging beam path between BEC and CCD camera where lattice stability is diagnosed. Note that the actual performance in the experiment was found to be significantly better than 0.32λ .

Element	Error	Amount	OPD [λ]
Optical Lattice Setup			
first lens	tilt	0.2°	0.1
first lens	decenter	1 mm	0.07
shadow mask	decenter	2 mm	0.05
second lens	tilt	0.25°	0.15
second lens	decenter	1 mm	0.03
cube	tilt	1.5°	0.1
OPD _{RMS} at BEC due to optical lattice setup			0.225
Imaging Setup			
first imaging lens	tilt	3°	0.2
first imaging lens	decenter	2.5 mm	0.1
second imaging lens	tilt		negligible
second imaging lens	decenter		negligible
OPD _{RMS} due to imaging setup			0.225
OPD _{RMS} at camera, due to OL and imaging			0.32

Table 2.2 shows the expected error budget on vibrations of a $7\ \mu\text{m}$ period rotating 2D optical lattice. The cumulative displacement Δx due to aberrations is less than one lattice period, showing the feasibility of such a setup. Of additional concern were possible optical imperfections of the glass cell windows, as well as the possibility of aberrations from imperfections of the fiber output facet, but experimentally we later

³ Simulations performed using the software Oslo LT.

found no indications of such effects.

Detailed description of the actual setup. Fig. 2.5 (a) shows the light source we set up for creating both blue-detuned (532 nm) and red-detuned ($810 - 850\text{ nm}$) optical lattices. Output from a 10W Coherent Verdi is either directly coupled into a single-mode fiber, or is used to pump a Tekhnoscan TIS-SF-077 Ti:Sapphire laser⁴. A temperature-stabilized reference cavity serves as a frequency reference for the Ti:Sapphire laser, while the Verdi is free-running⁵. In both cases, acousto-optical modulators that control the optical lattice intensity are positioned before the fiber. This setup delivers a fiber output of 600 mW at 532 nm , limited by thermal effects in the fiber, or 550 mW at 810 nm , limited by the Ti:Sapphire laser output.

The rotating optical lattice setup is shown in Fig. 2.5 (b). The light exits from a fiber of $NA = 0.12$ and is collimated using a 2" achromatic doublet ($f = 300\text{ mm}$). A shadow mask selects three beams on a cone of $NA \approx 0.04$ ⁶. We use 2" coated achromatic doublet lenses and protected silver mirrors everywhere in the beam path. A $f = 250\text{ mm}$ lens focuses the beams onto the BEC. A broadband 2" polarizing beamsplitter cube (Karl Lambrecht) is used to combine the 532 nm lattice light with 780 nm MOT and imaging light. Following the glass cell, the light is collected on a CCD camera through our $\sim 6\times$ magnification vertical imaging setup (the dichroic mirror before the CCD reflects $> 99\%$ of the optical lattice light; the remaining light level is safe for the CCD and provides good signal/noise).

The optical lattice intensity is stabilized to the desired intensity waveform using feedback from a photodiode monitoring a peripheral portion of light exiting the fiber. A second photodiode monitors the actual optical lattice intensity.

Alignment procedure and diagnostics. To achieve an alignment of beams

⁴ The Ti:Sapph in addition allows for $720 - 810\text{ nm}$ operation using a second set of cavity mirrors.

⁵ The Verdi linewidth, measured on a timescale of 0.1 ms , is 0.02 MHz . It drifts by 0.5 MHz within 1 ms and on order of 10 MHz over tens of seconds [142].

⁶ Triangular optical lattice, period $d = 7.8\text{ }\mu\text{m}$: $\phi_1 = 2.5\text{ mm}$, $d_1 = 11.5\text{ mm}$ (Fig. 2.2(b)). Square lattice, period $d = 7.0\text{ }\mu\text{m}$: $\phi_2 = 2.5\text{ mm}$ and $d_2 = 13.5\text{ mm}$ (Fig. 2.2(c)).

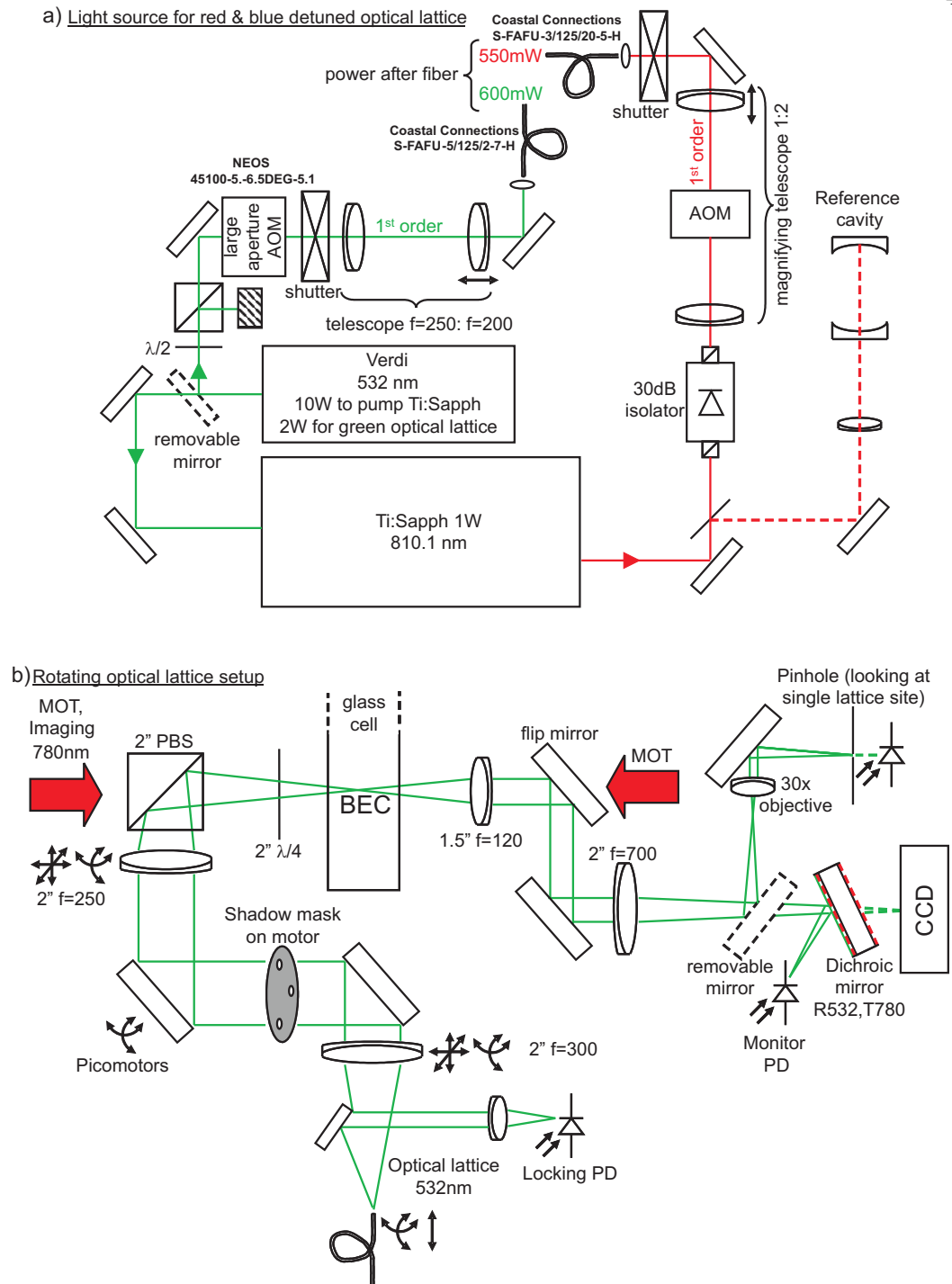


Figure 2.5: a) Laser source for generating red- and blue-detuned optical lattices. Light at 532 nm is either directly fiber-coupled to form a blue-detuned optical lattice, or is used to pump a Ti:Sapphire laser for a red-detuned optical lattice. b) Setup for rotating 2D optical lattice used for pinning experiments and 2D frustrated Josephson junction arrays. A single-mode fiber supplies optical lattice light at 532 nm , which passes through a shadow mask mounted onto a motor-driven rotary stage, to define three rotating lattice beams. These are combined with the MOT/imaging beam path and overlapped on the BEC to form the rotating 2D lattice. The beams are imaged onto the CCD camera used to optimize beam overlap, rotating lattice stability, and alignment with respect to the BEC. Important alignment degrees of freedom are indicated. PD: photodiode.

and lenses of the accuracy given in Table 2.2, we begin by perfect centering of the lattice beams onto the lenses, and orthogonal alignment of beams onto lenses and other optical elements (waveplates, polarizing beam splitter cube). For this purpose both lenses in the optical lattice beam path are mounted on 5-axis aligners. We use a narrow, central beam created by inserting an aperture into the beam center (the beam center is found by maximizing the transmitted light using a photodiode). We first align the reflections from the first lens' back and front surfaces back into this aperture. The central beam is then aligned with the center of the shadow mask, and the orientation of the mask is made perpendicular to the beam using the reflection from an auxiliary mirror. The second lens is aligned as the first one, using a second aperture.

The optical lattice light is then imaged onto a CCD camera using our ‘vertical’ imaging system consisting of $f = 120\text{ mm}$ and $f = 700\text{ mm}$ achromatic doublet lenses. Here we do not have as good control over the lens alignment, as these lenses do not have tilt degrees of freedom. This is reflected in larger wavefront errors in Table 2.2.

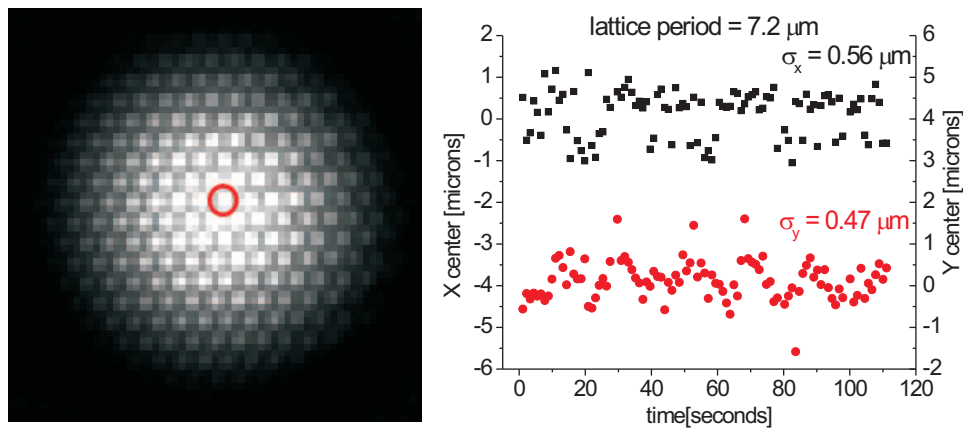


Figure 2.6: Rotating 2D optical lattice, $7.2\text{ }\mu\text{m}$ period. The central lattice site is marked red. Position fluctuations of the central lattice site when rotating slowly (90 s rotation period). Fluctuations are identical for a static lattice, possibly limited by fitting accuracy, camera pixelation, and vibrations of the camera mounting platform.

Using the CCD camera image of the optical lattice pattern we have two modes of diagnosis. A slowly rotating lattice allows real-time following of the optical lattice

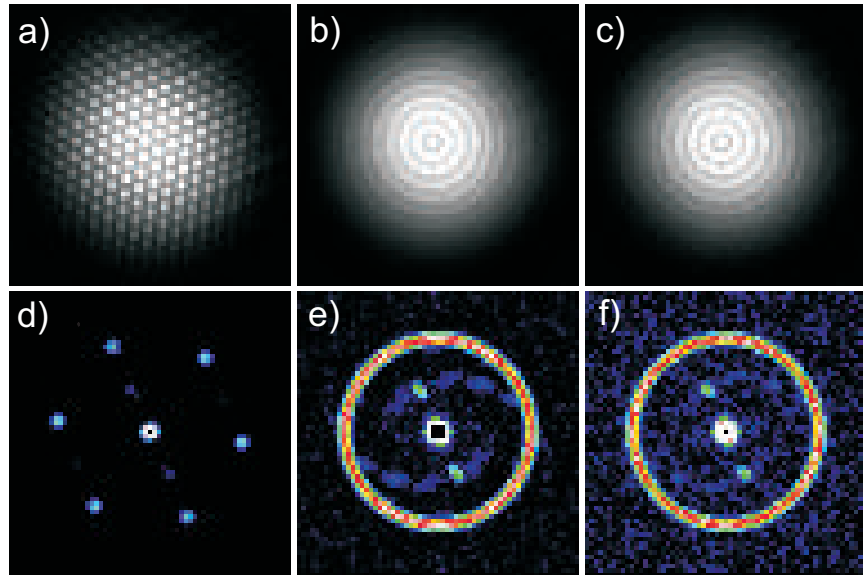


Figure 2.7: (a)-(c) Long exposure images of rotating 2D optical lattice, $7.2 \mu\text{m}$ period. (a) static, (b) rotation rate 1.3 Hz , (c) 8 Hz . In (b),(c) images are exposed for one lattice revolution. The contrast of the central spot is 53%, for static and rotating lattices, for exposure times of 1 as well as 10 revolutions, indicating that neither aberrations nor vibrations significantly deteriorate stability. (d)-(f) FFTs of (a)-(c).

motion while performing adjustments to lenses. An example of such analysis is shown in Fig. 2.6, where the two-dimensional position of the central interference maximum is shown vs. time. This is the typical day-to-day mode for alignment. Alternatively, long-time-exposure images of a fast-rotating lattice show the time-averaged contrast of lattice sites and thus allow assessment of the mean displacements during rotation, as shown in Fig. 2.7. We consistently find the imperfections of optical lattice rotation to be comparable at slow and fast rotation. We note that optical lattice imperfections may be introduced either in the optical lattice beam path between the light source and the BEC, or in the imaging beam path between BEC and CCD camera where lattice stability is diagnosed, see Fig. 2.5. Thus a reliance solely on CCD camera diagnostics may be dangerous, and we ultimately use the BEC itself as a diagnostic, as described below.

It is worth noting that the initial step of perfect lens alignment never produces the

best smoothly rotating optical lattice pattern. We consistently have to tilt one lens by a significant amount to achieve best performance. Such lens tilt introduces astigmatism, i.e. an optical path length difference varying as $\propto \cos^2(\phi)$, where ϕ is the azimuthal angle on the lens, see Fig. 2.4.C). Transverse lens translation, i.e. “decentering” of the beams, introduces path length differences $\propto \cos(\phi)$, see Fig. 2.4.D). With these two adjustments, and using the CCD camera as a precise monitor for optical lattice motions, we are able to achieve a performance superior to the estimates in Table 2.2.

Alternatively, vibrations of the optical pattern may be quantified by imaging the single central OL site onto a pinhole and monitoring the transmitted intensity on a photodiode. This allows very quantitative measurements of position jitter, not limited by CCD camera exposure time and repetition rate, but is not feasible for in-situ monitoring of adjustments made to the beam path, as the position of central spot will change and would have to be repositioned onto the pinhole after every adjustment.

As a last probe of lattice alignment we employ the atoms themselves. The consistently required significant tilt of one lens had lead us to doubt whether this was an artifact, e.g. introduced on the beam path from BEC to CCD and thus *not* present at the BEC position. This question was finally settled by performing both heating measurements on the atoms loaded into the optical lattice, and measurements of the minimum optical lattice strength required to lock the vortex lattice to the optical lattice. The results of both these measurements confirm that stability of the optical lattice pattern on the CCD camera is the correct criterion, i.e. no significant lattice imperfections are introduced in the beam path between the BEC and the CCD camera.

Having created a perfectly rotating optical lattice potential, as a last step it remains to align the pattern perfectly centered onto the rotating BEC. A rough daily alignment is performed using picomotors, taking CCD images of both the optical lattice pattern and the BEC. A fine position alignment is then achieved using magnetic shim coils to shift the position of the BEC. As a diagnostic, initially static BECs are spun up

using the rotating optical lattice pattern rotating at a constant frequency. We find that, when perfect alignment is achieved, the BEC can be spun up and come to rotational equilibrium with the optical lattice at rotation rates as high as $\Omega/\omega_\rho = 0.95$. This is comparable to what can be achieved by evaporative spin-up [73] starting from a rotating thermal cloud. The final condensate number is $\approx 2/3$ of that of the initial static BEC.

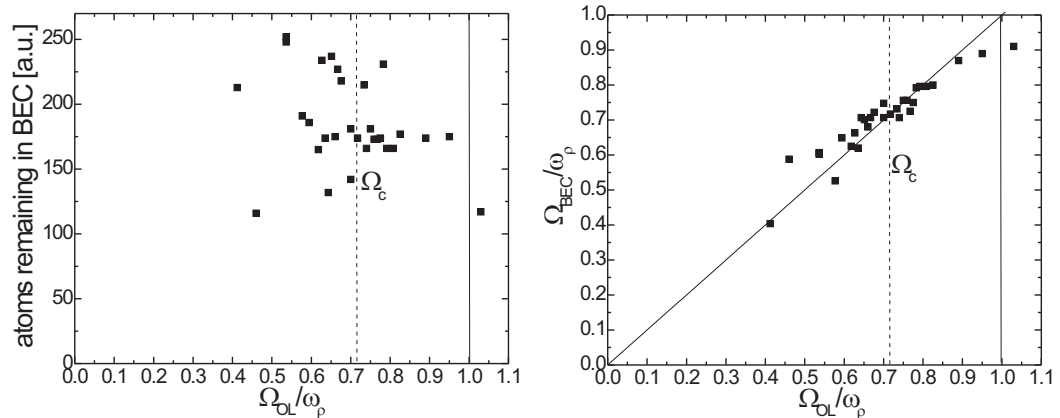


Figure 2.8: Spinning up a BEC using a rotating two-dimensional optical lattice. Ω_c : commensurate rotation rate, given by Eq. (2.1) for this $d = 8.4 \mu\text{m}$ period hexagonal optical lattice. The BEC is spun up to rotation rates around $\Omega = 0.9\omega_\rho$ and reaches equilibrium with the optical lattice, without increase in number loss. Note that in other runs we achieved $\Omega = 0.95\omega_\rho$, and that *evaporatively pre-spun-up* BECs can equilibrate with the rotating optical lattice up to $\Omega \approx 0.97\omega_\rho$.

We tested the achievable precision of BEC – optical lattice center alignment by sequences of phase contrast images of the BEC loaded into the optical lattice pattern. Alignment was optimized by monitoring the amount of angular momentum imparted by the rotating optical lattice onto an initially static BEC. From the images, the location of the central optical lattice site as well as the BEC center were extracted, and found to coincide within approximately $2 \mu\text{m}$, i.e. $\approx 1/4$ of the optical lattice period, and $\approx 1/30$ of the condensate radius.

After the first-time alignment outlined above, the setup requires only a slight daily tweak and is usually stable throughout the day.

2.3 Observation of vortex pinning in Bose-Einstein condensates

Here we describe the results of three experiments. We first study the angular locking of the vortex lattice to a hexagonal optical lattice with one vortex per pinning site. Secondly, the structural crossover of a vortex lattice pinned to a square optical lattice is examined. Finally we report preliminary efforts of pinning to hexagonal optical lattices with two vortices per pinning site, and with one vortex per two pinning sites. For all results presented here, the vortex lattice has had sufficient time to come to rotational equilibrium with the optical lattice.

2.3.1 Angular locking of the vortex lattice to a hexagonal optical lattice

The experiments begin with condensates containing $\sim 3 \times 10^6$ ^{87}Rb atoms, held in the Zeeman state $|F = 1, m_f = -1\rangle$ by an axial symmetric magnetic trap with trapping frequencies $\{\omega_r, \omega_z\} = 2\pi\{8.5, 5.5\} \text{ Hz}$. Before the optical lattice, rotating at angular frequency Ω_{OL} , is ramped on, the BEC is spun up [143] close to Ω_{OL} . This leads, before application of an optical lattice, to the formation of a near perfect triangular vortex lattice with a random initial angular orientation in inertial space. Through dissipation a vortex lattice can come to equilibrium with an optical lattice, with their rotation rates and angular orientations locked. In the absence of pinning sites, a vortex lattice with areal density of vortices n_v will rotate at (approximately [45, 147]) $\Omega = (\frac{\hbar\pi}{m})n_v$, as described in the introduction, see Eq. (1.22). This suggests that for an optical lattice with an areal density of pinning sites n_{OL} ⁷, locking between the two lattices will be facilitated if the optical lattice rotates at the *commensurate rotation rate*

$$\Omega_c \equiv \left(\frac{\hbar\pi}{m}\right)n_{OL} \quad (2.1)$$

We measure the angular difference $\theta_{OL} - \theta_{VL}$ between the orientation of the optical and vortex lattice in reciprocal space (see Figs. 2.9(a),(b)). Fig. 2.9(c) shows

⁷ For a triangular optical lattice, $n_{OL} = \frac{2}{a^2\sqrt{3}}$, while for a square lattice, $n_{OL} = \frac{1}{a^2}$.

$\theta_{OL} - \theta_{VL}$ as a function of the pinning strength with an optical lattice rotation rate $\Omega_{OL} = 1.133\Omega_c = 0.913\omega_r$. The strength of pinning is characterized by the ratio U_{pin}/μ (μ is the chemical potential of the condensate⁸), which gives the relative suppression of the superfluid density at pinning sites. We can see the initially random angular difference between the two lattices becomes smaller as the pinning strength U_{pin}/μ increases. For $U_{pin}/\mu \gtrsim 0.08$, the angular differences become very close to the locked value. Figure 2.9(d) shows the phase diagram. The data points and error bars mark the minimum pinning strength $(U_{pin}/\mu)_{min}$ above which the lattices lock. We observe two distinct regimes. First, for small rotation-rate mismatch $\Omega_{OL} - \Omega_c$, $(U_{pin}/\mu)_{min}$ is rather independent of $\Omega_{OL} - \Omega_c$. Second, for rotation-rate mismatch beyond the range indicated by the dashed line in Fig. 2.9(d), angular orientation locking becomes very difficult for any U_{pin}/μ in our experiment. Instead, an ordered vortex lattice with random overall angular orientation observed at low U_{pin}/μ transforms into a disordered vortex arrangement at high U_{pin}/μ .

This box-like shape of the locked region in $U_{pin} - \Omega_{OL}$ space is worth considering. Vortex motion in our system is governed by a balance of pinning force and Magnus force (Section 1.3.3). The pinning force arising from our sinusoidal optical lattice potential is

$$\vec{F}_{pin}(x) \propto \nabla E_{pin}(x) \propto U_{pin}/d \quad (2.2)$$

where U_{pin} and d are the pinning potential's strength and period. The Magnus force, acting on a vortex moving with velocity \vec{v}_{vortex} in a superfluid with velocity \vec{v}_{fluid} is

$$\vec{F}_{mag}(x) \propto n(x) (\vec{v}_{vortex} - \vec{v}_{fluid}) \times \vec{\kappa} \quad (2.3)$$

where $\vec{\kappa} = (\frac{\hbar}{m})\hat{z}$, and $n(x)$ is the superfluid density. With the pinning potential applied, the superfluid density is modulated as $n(x) \propto \mu - U_{pin}(x)$. A pinned vortex lattice is constrained to move at the angular velocity set by the pinning potential, giving

⁸ The chemical potential is determined from the axial Thomas-Fermi radius of the condensate obtained from in-trap images, and is proportional to the peak density of the condensate.

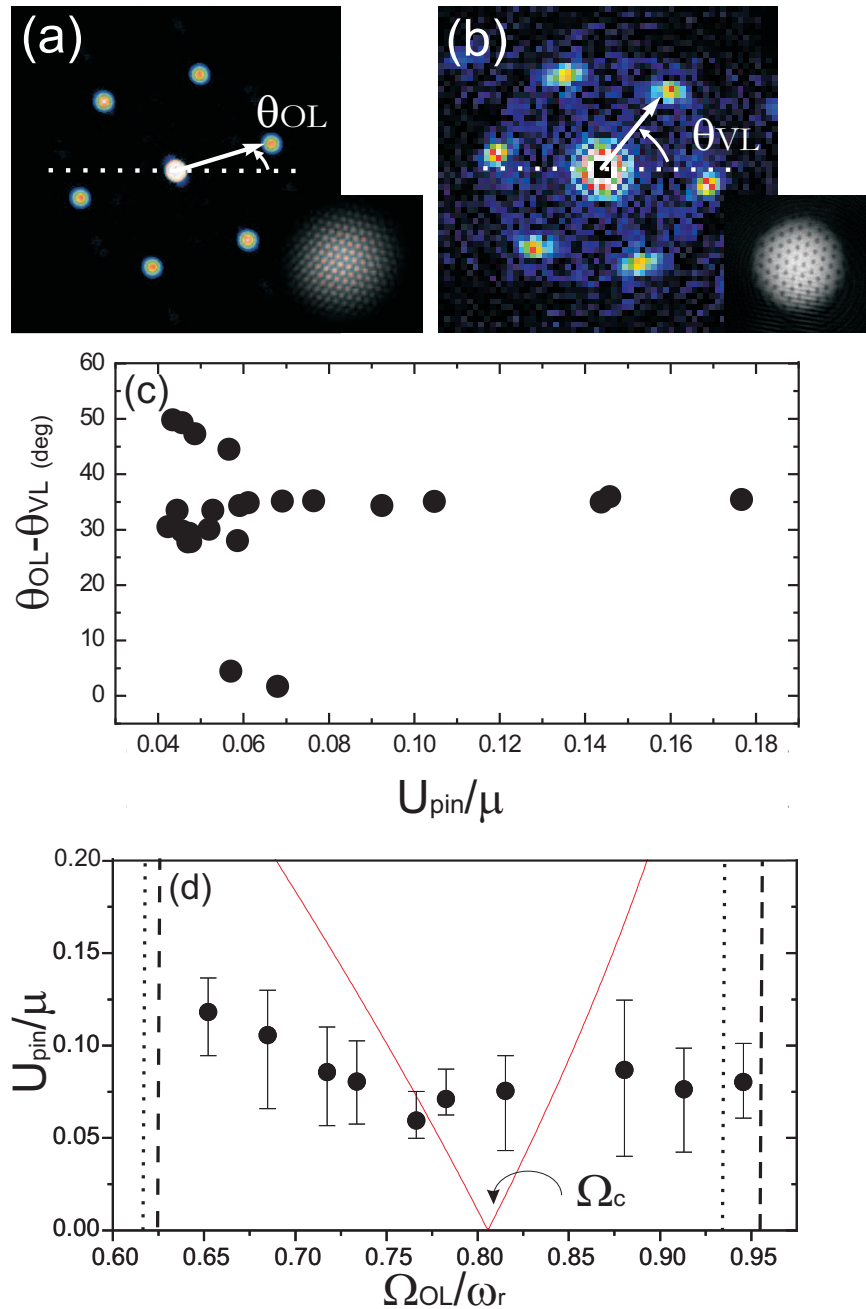


Figure 2.9: (a) Triangular optical lattice (period $7.8 \mu m$) and (b) vortex lattice in reciprocal space. Inset are the corresponding original real-space CCD-camera images. (c) The difference in orientation $\theta_{OL} - \theta_{VL}$ versus the strength of pinning U_{pin}/μ (the peak of the optical potential normalized by the condensate's chemical potential) for the rotation rates $\Omega_{OL} = 1.133 \Omega_c = 0.913 \omega_r$. With increasing pinning strength, $\theta_{OL} - \theta_{VL}$ tends towards its locked value (the constant offset to the values of $\theta_{OL} - \theta_{VL}$ in (c) is not physical, but is an artifact of our measurement procedure in this dataset – in independent experiments we have used in-trap images of vortex lattices to confirm that the absolute value of $\theta_{OL} - \theta_{VL}$ is zero for locked lattices). (d) Minimum pinning strength needed for orientation locking between the two lattices as a function of the optical lattice rotation rate. Dashed: minimum and maximum rotation rates for which pinning was observed. Solid red and dotted lines: see text.

$\vec{v}_{vortex}(r) = \vec{v}_{OL}(r) = \vec{\Omega}_{OL} \times \vec{r}$. On the other hand the superfluid in solid-body approximation rotates at a velocity $\vec{v}_{fluid}(r) = \vec{\Omega}_{fluid} \times \vec{r}$, where $\Omega_{fluid} = \frac{\pi\hbar}{m}n_v\hat{\theta}$ is set by the vortex density n_v . When the optical lattice rotates at the commensurate rotation rate the Magnus force vanishes, and pinning should result even for extremely weak pinning strengths.

Comparing the magnitudes of both forces at $r = R(\Omega_{fluid})/2$, where $R(\Omega_{fluid})$ is the centrifugal-force modified Thomas-Fermi radius, we obtain a minimum strength for pinning

$$(U_{pin}/\mu)_{min} \approx \left(\frac{1}{2\sqrt{3}} R(\Omega_{fluid})/d \right) \times (\Omega_{OL} - \Omega_{fluid})/\Omega_c \quad (2.4)$$

What will be the fluid rotation rate Ω_{fluid} in the presence of the pinning potential? On the one hand, if vortices are tightly locked to the optical lattice sites, we have $\Omega_{fluid} = \Omega_c$. The minimum strength $(U_{pin}/\mu)_{min}$ resulting from this assumption is plotted as solid red line in Fig. 2.9(d). The lack of decrease of measured $(U_{pin}/\mu)_{min}$ to zero around Ω_c may be due to long equilibration times in a very shallow pinning potential, as well as slight mismatches in alignment and initial rotation rate of the BEC and the pinning potential. The ease of orientation locking with increasing rotation rate mismatch $\Omega_{OL} - \Omega_c$ is less easy to explain in this model. On the other hand, in the weak-pinning regime, the vortex lattice can accommodate a rotation rate mismatch by stretching/compressing away from the pinning sites. This allows the fluid to co-rotate with the optical lattice ($\Omega_{fluid} \approx \Omega_{OL}$) and reduce the Magnus force. This leads to a very low minimum pinning strength over a wide range of rotation rates, as suggested by our data. However, the vortex lattice's gain in pinning energy decreases rapidly in the locked orientation when the mismatch between vortex spacing and optical lattice constant increases to the point where the outermost vortices fall radially in between two pinning sites. Then the preference for the locked angular orientation vanishes. This predicted limit is indicated by the vertical dotted lines in Fig. 2.9(d).

Our data thus reveal a major difference between our finite system and extended systems: In extended systems, the pinned vortex density n_v has to equal the density of pinning sites, else defects will be induced - the physics, even for small rotation rate mismatch, lies in the competition between ordered states and defect generation. In our finite system on the other hand, the pinned vortex lattice can stretch or compress slightly away from the pinning sites to find a balance between Magnus and pinning force. This induces a vortex density different from the density of pinning sites, but allows the fluid to continue to remain pinned and to rotate with the lattice, even in the presence of a modest rotation rate mismatch.

2.3.2 Pinning-induced structural vortex lattice crossover

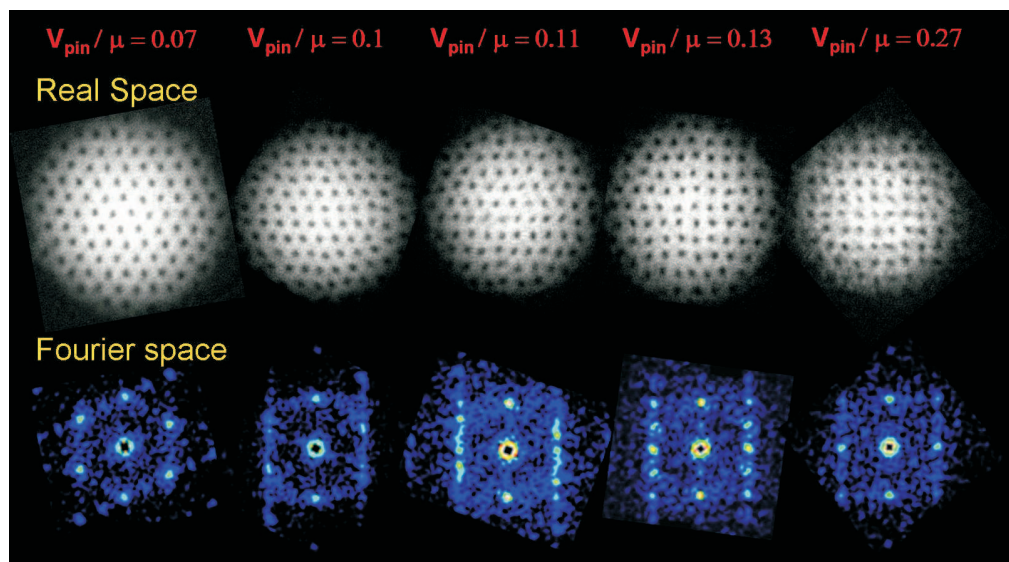


Figure 2.10: Images of rotating condensates pinned to a square optical lattice (period $7.0 \mu m$) at $\Omega_{OL} = \Omega_c = 0.866\omega_r$ with increasing pinning strength, showing the structural cross-over of the vortex lattice. Upper row: real-space absorption images of vortex lattices after expansion. Bottom row: Fourier transforms of images in upper row.

In a second set of experiments we applied a square optical potential to the vortex lattice. In the absence of a pinning potential, the interaction energy of a square vortex lattice is calculated to exceed that of a triangular lattice by less than 1% [36], thus it

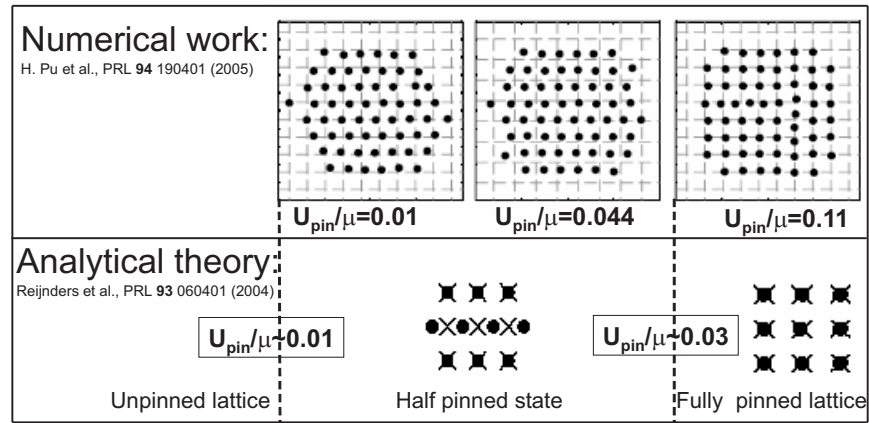


Figure 2.11: Theoretical predictions for pinning-induced structural crossover (Refs. [128], [130]). Numerically simulated vortex patterns coincide with our results in Fig. 2.10; pinning strengths for the structural crossover agree qualitatively.

is predicted [130, 131, 128] that the influence of even a relatively weak square optical lattice will be sufficient to induce a structural transition in the vortex lattice. This structural vortex lattice crossover is observed in our experiment. Figure 2.10 shows how the vortex lattice evolves from triangular to square as the pinning strength increases. Over a wide range of pinning strengths, we observe that there is always at least one lattice peak in reciprocal space that remains very strong. We define this peak to be k_o . Lattice peaks at 60° and 120° from k_o are referred to as k_{tr} , and, together with k_o , their strength is a measure of the continued presence of a triangular lattice. A peak at 90° , referred to as k_{sq} , is instead a signal for the squareness of the vortex lattice. With increasing pinning strength in Fig. 2.10 we see the triangle to square crossover evolve. At intermediate strengths the vortex pattern shows ordering in one of the two lattice directions, while vortex planes in the other direction remain unlocked, as seen in Fig. 2.10 at $U_{pin}/\mu = 0.11$; in reciprocal space we see the presence of structure at k_{tr} and k_{sq} .

We quantify the crossover by means of an image-processing routine that locates each vortex core, replaces it with a point with unit strength, Fourier transforms the resultant pattern, and calculates structure factors $|S|$ [128] based on the strength of

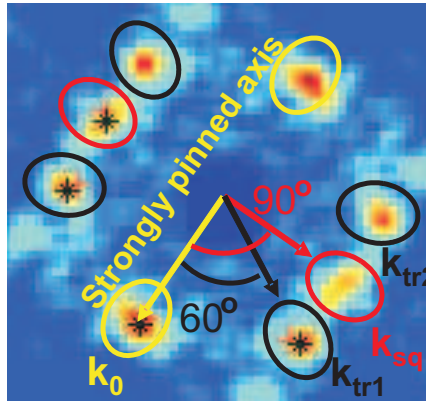


Figure 2.12: Definition of k -vectors for pinning-induced structural crossover: k_o is taken to be the strongest peak; k_{tr1} , k_{sq} , k_{tr2} are at 60° , 90° , 120° , respectively, from k_o .

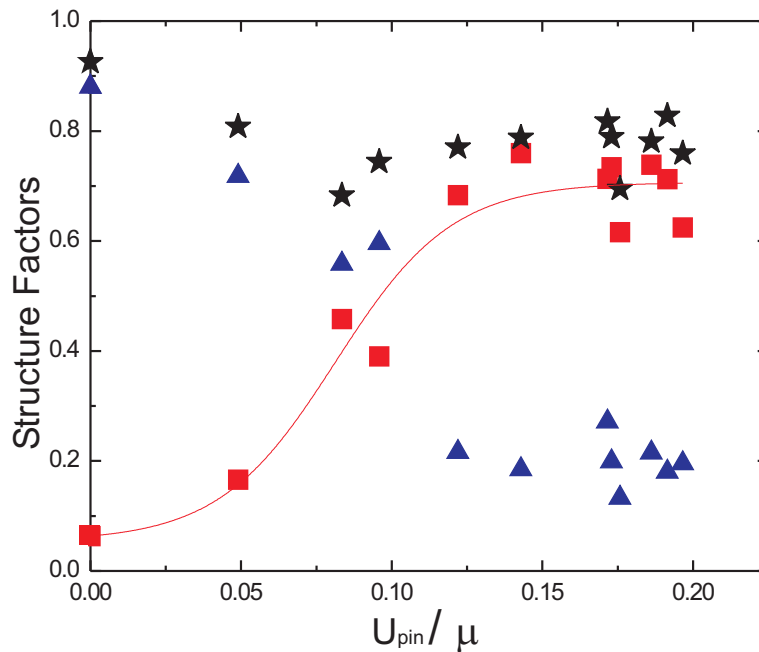


Figure 2.13: Structure factors (a) $|S(k_{sq})|$ (■), (b) $|S(k_{tr})|$ (▲) (average of $|S(k_{tr1})|$ and $|S(k_{tr2})|$), and (c) $|S(k_o)|$ (★) versus the strength of the pinning lattice at the commensurate rotation rate Ω_c . $|S(k_{sq})|$ is fitted to a smooth functional form: $|S(k_{sq})| = A_2 + \frac{A_1 - A_2}{1 + \text{Exp}[\frac{U - U_0}{\delta U}]}$ where A_1 , A_2 , U_0 , and δU are fit parameters. The fitting leads to a maximum value 0.707 of $|S(k_{sq})|$. An ideal square vortex lattice would have $|S(k_{sq})| = 1$.

the images at lattice vectors k_{sq} , k_{tr} , and k_o . In Fig. 2.13, we see with increasing optical potential the turn-on of $|S(k_{sq})|$ balanced by the turn-off of $|S(k_{tr})|$. We use a fitting function to smooth the noisy data of $|S(k_{sq})|$. The structural crossover takes

place around $U_{pin}/\mu \approx 8\%$, in rough agreement (see Fig. 2.11) with predictions of $U_{pin}/\mu \approx 5\%$ from numerical simulations [128] and $U_{pin}/\mu \approx 1\%$ from analytic theory for infinite lattices [130, 131]. The fact that one lattice peak remains strong for all pinning strengths (the stars (★) in Fig. 2.13) suggests that as the pinning strength is increased, one family of vortex rows represented by k_o in Fourier space locks to the square pinning lattice and remains locked as the shape cross-over distorts the other two families of vortex rows into a square geometry.

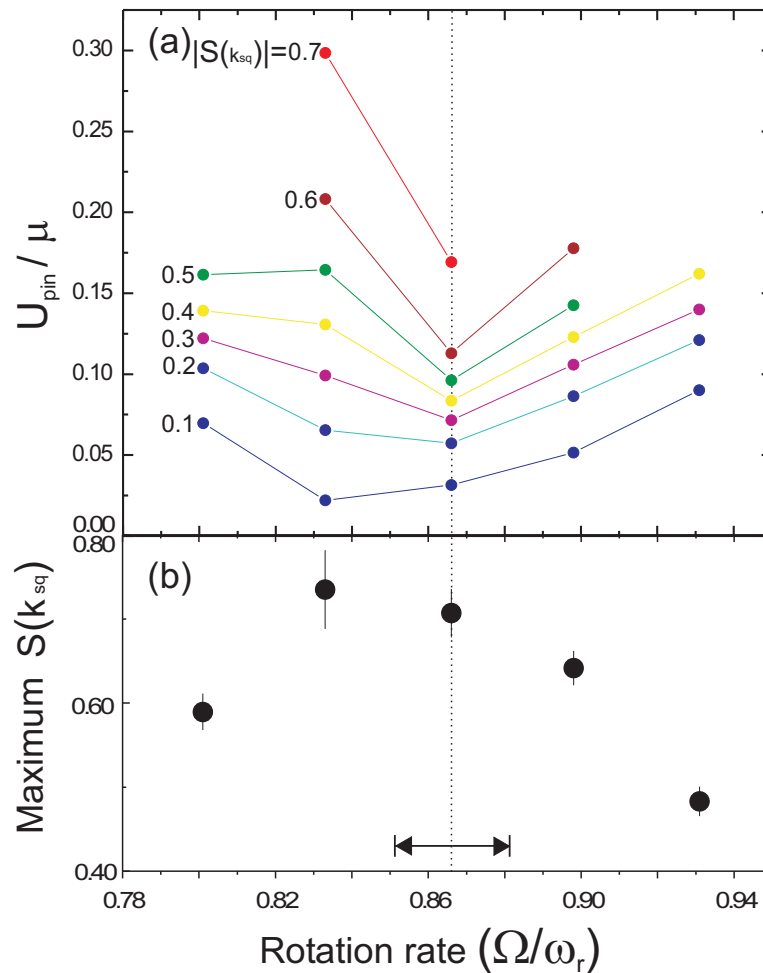


Figure 2.14: Effect of a square pinning lattice. (a) Contours of $|S(k_{sq})|$, showing the effect of the rotation rate and pinning strength on the squareness of the vortex lattice. (b) Maximum observed squareness. In (a) and (b), for each rotation rate, the data points are extracted from fits such as that shown in Fig. 2.13 for $\Omega_{OL} = \Omega_c$. Vertical dotted line plus arrow: possible range of Ω_c consistent with the uncertainty in n_{OL} .

The effects of various rotation rates and optical potential strengths on the squareness of the vortex lattice is summarized in Fig. 2.14. We surmise that there are a number of effects at play. When Ω_{OL} differs from Ω_c , pinning strength is required not only to deform the shape of the vortex lattice from triangular to square, but also to compress or expand it to match the density of the optical lattice sites. At higher optical intensities, we know from separate observations that imperfections in the rotation of the optical lattice lead to heating of the condensate, which may limit the obtainable strength of the square lattice.

2.3.3 Defects in pinned vortex lattices

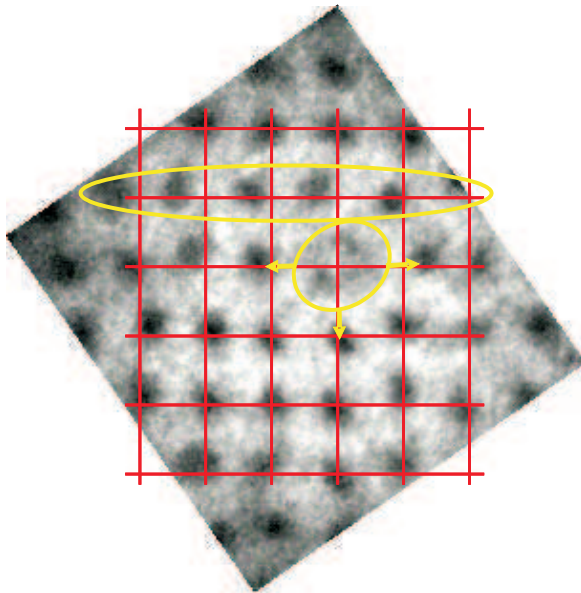


Figure 2.15: Image of a dumbbell-shape defect consisting of two vortices locked to one pinning site during the formation of the square vortex lattice. It is clearly visible how adjacent vortices are pushed outward by the repulsion due to the additional vortex. Above, a “sliding row” defect is visible too.

A dumbbell-shape lattice defect (Fig. 2.15), consisting of two vortices pinned to the same site, is sometimes observed in the early stages of the square vortex lattice formation when $\Omega_{OL} > \Omega_c$. In the weak-pinning regime, the defect will relax towards the equilibrium configuration by pushing extra vortices at the edge of the condensate

outside the system. Defects of this nature, involving extra (or missing) vortices, are the exception and not the rule in our observations, even for $\Omega_{OL} \neq \Omega_c$. In an infinite system, the physics of the lattice-lattice interaction would likely be dominated by these point defects. In our finite system, would-be incommensurate lattices can accommodate by stretching or compressing.

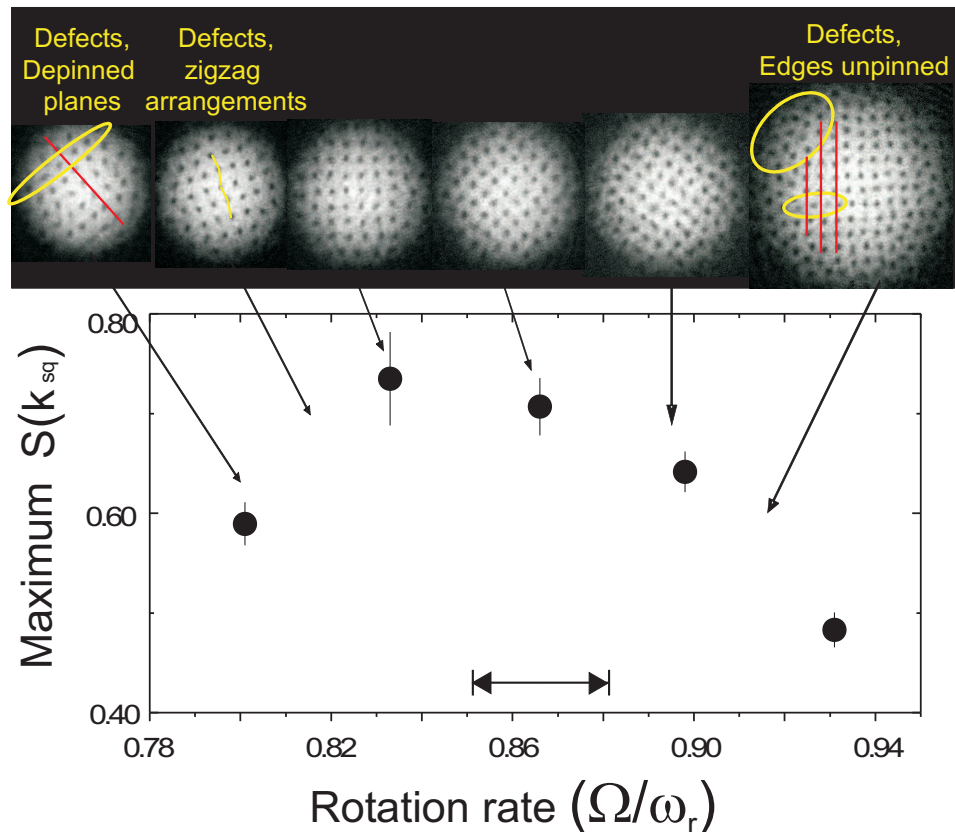


Figure 2.16: Defects in pinned vortex lattices with varying rotation rate mismatch. Defects reduce the maximum attainable square structure factor of the pinned lattices.

Figure 2.16 shows typical images of vortex lattices pinned at increasingly non-commensurate rotation rates. Increasing numbers of defects can be seen towards the edge of the pinning range, indicating that the amount of compression/stretching that allows vortex lattices to remain pinned over this large range of rotation rates, is limited by the increasingly frequent appearance of defects.

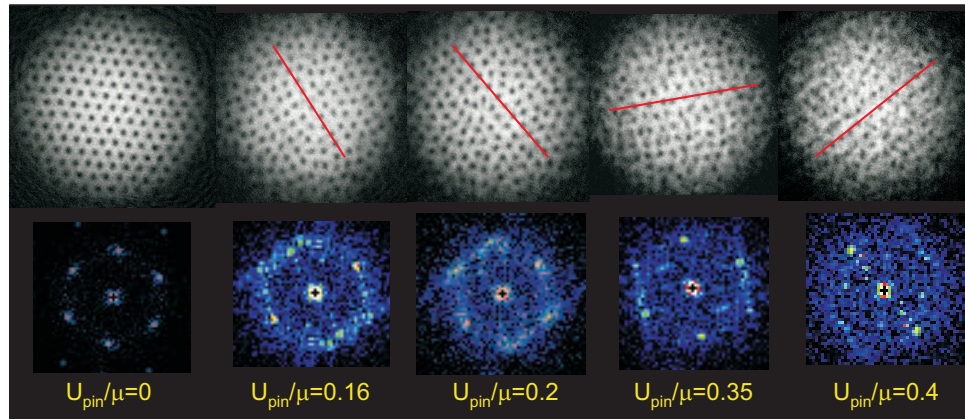


Figure 2.17: Vortex pinning in a triangular optical lattice with 2 vortices per pinning site. One-dimensional ordering is seen in real-space and Fourier images. This ordering was not predicted theoretically.

2.3.4 Pinning with two vortices per pinning site

Here we describe experiments with, on average, two vortices per pinning site. The expected evolution with increasing pinning potential, according to numerical simulations by Pu and coworkers [128] on a square pinning lattice, is shown in Fig. 2.18 – a transition from two singly quantized vortices to doubly quantized vortices is seen. A similar evolution is also expected in a triangular pinning potential.

In our experiments we used a triangular $9.54 \mu m$ period lattice, where two vortices per pinning site are obtained at a rotation rate $\Omega = 0.957\omega_r$. To our surprise we found signs of one-dimensional ordering, as shown in Fig. 2.17: Parallel rows of vortices are seen, with roughly equidistant spacing to adjacent rows, but no obvious correlations between vortex positions in neighboring rows, and also lacking perfect periodicity within each row. We did however not observe fully ordered systems, and we never observed the merging of multiple vortices pinned to one pinning site to one multiply quantized vortex. A simple calculation shows that the vortex-vortex repulsion overcomes the pinning force arising from our sinusoidal potential unless the pinning strength $V_{OL}/\mu \approx 1$. As discussed, this regime is difficult to work in due to strong heating effects. One would

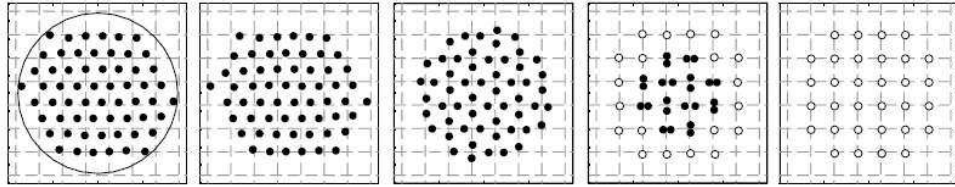


Figure 2.18: Numerical simulations of vortex pinning with 2 vortices per pinning site, from Ref. [128]. Full (hollow) circles represent singly (doubly) quantized vortices. A transition to a pinned lattice of doubly quantized vortices is expected.

need steeper pinning sites to force vortices closer together. We have attempted to synthesize such potentials using the present setup, simply by adding more holes to the shadow mask. We found that such multi-beam potentials do not preserve their structure while rotating, as we do not actively control the relative phases between different beams against unwanted perturbations. I am optimistic that a future generation of graduate students will be able to benefit from the development of fast enough spatial light modulators that will do this kind of job sooner or later.

2.3.5 Pinning with one vortex per two pinning sites

We have also conducted experiments with one vortex per two pinning sites. Here, a superstructure of vortices is expected. We used a triangular $6.3\ \mu\text{m}$ period lattice. Due to various constraints in optical access, this period is close to the minimum period achievable for a rotating lattice using the setup shown in Fig. 2.5. In this lattice and in our “cigar” magnetic trap, one vortex per two pinning sites is obtained at $\Omega = 0.548\omega_r$.

Experimentally, no ordered vortex structures were observed. The problem was likely linked to the fact that due to the constraint on the lattice period we had to work at slow rotation rates, i.e. with a small BEC and a small number of vortices. In this situation, strong radial density gradients and boundary effects are expected to be important for vortex dynamics. In addition the BEC was not even close to quasi-2D, i.e. vortices could bend axially, making this experiment a more complicated 3D problem.

Chapter 3

A 2D Josephson junction array in the Berezinskii-Kosterlitz-Thouless regime

3.1 Motivation

In this chapter [2] I describe experiments on a finite-temperature two-dimensional array of Josephson-coupled Bose-Einstein condensates undergoing a Berezinskii-Kosterlitz-Thouless (BKT) transition from a superfluid to a normal state. Detailed data on the thermal activation of vortices are presented, providing a direct “microscopic” look at the physical processes underlying the transition.

This study thus adds to a large body of work dealing with fluctuations in superfluids, which affect long-range phase coherence [99]. Fluctuations may be quantum in nature, as in the Mott-insulator transition [67, 85], or thermal fluctuations, as studied e.g. in one-dimensional Bose gases [135, 76] and in a double-well system [60]. In two dimensions (2D), Berezinskii [23, 24], Kosterlitz and Thouless [94] (BKT) in the 1970’s developed an elegant description of thermal phase fluctuations based on the thermal excitation and unbinding of vortex-antivortex pairs (i.e. pairs of vortices of opposite circulation). The BKT picture applies to a wide variety of 2D systems, among them Josephson junction arrays (JJA), i.e. arrays of superfluids in which phase coherence is mediated via a tunnel coupling J between adjacent sites.

Transport measurements, both in continuous superfluids [7, 138] and superconducting JJA [133] have confirmed the predictions of BKT, without however directly

observing its microscopic mechanism, vortex-antivortex unbinding. Ultracold atomic gases, on the other hand, appear ideally suited to complement the traditional studies, because of the favorable length scales of vortex defects and direct “wavefunction imaging” capabilities. A recent beautiful experiment in Dalibard’s group at ENS in Paris [71, 96], performed in a continuous 2D Bose gas, opened up the field, and measured the phase-phase decay function through the BKT cross-over, and saw evidence for thermal vortex formation. For related theoretical studies see e.g. [149, 65, 125]. In our work we present detailed data on thermally activated vortex-formation, collected in a 2D array of BECs with experimentally controllable Josephson couplings. The system was studied theoretically by Trombettoni et al. [163].

Since the completion of our studies, we have become aware of additional, yet unpublished, work in Phillips’ group at NIST Gaithersburg [42], and Kasevich’s group in Stanford [91]. The group of Rob Ballagh in Otago, New Zealand, have begun numerical studies of our lattice system [17].

3.2 The BKT transition in a Josephson junction array

The BKT transition in a Josephson junction array proceeds very similarly to the continuous system described in the introduction. Vortex formation is governed by two competing energy scales: the Josephson (tunnel) coupling J between nearest-neighbor condensates acts to keep the relative phases of the condensates locked. A cloud of uncondensed atoms, on the other hand, interacts with the condensates and induces thermal phase fluctuations, which we observe as vortices. As long as the Josephson energy J exceeds the thermal energy T , the array is vortex-free. With decreasing J/T , vortices appear in the system in ever greater numbers.

As for the BKT transition in a continuous superfluid, an estimate of the conditions for the BKT transition is obtained by computing the free energy F of an isolated (*free*) vortex in a JJA, and demanding $F = E - TS \leq 0$. In an array of period d the vortex

energy [161] diverges with array size R as ¹

$$E \approx J \log(R/d) \quad (3.1)$$

but may be offset by an entropy gain ²

$$S \approx \log(R/d) \quad (3.2)$$

due to the available $\approx R^2/d^2$ sites. This leads to a critical condition

$$(J/T)_{crit} \approx 1 \quad (3.3)$$

independent of system size, below which free vortices will proliferate. In contrast, *tightly bound* vortex-antivortex *pairs* are less energetically costly and show up even above $(J/T)_{crit}$. The overall vortex density is thus expected to grow smoothly with decreasing J/T in the BKT crossover regime. Condition (3.3) for the BKT transition on a lattice is really very similar to the one for the bulk 2D superfluid, Eq. (1.36). To see how similar the two conditions are, consider the well-established relation $J \sim \frac{\hbar^2}{2m^*} \frac{N_{well}}{d^2}$. Here, m^* is effective mass of the bosons tunneling through the lattice, and $\frac{N_{well}}{d^2}$ is equivalent to the 2D superfluid density $n_{SF,2D}$. Thus $J \sim \frac{\hbar^2 n_{SF,2D}}{2m^*}$ and it becomes obvious that Eqs. (3.3) and (1.36) really represent the same condition.

There are however two important differences to a continuous 2D system: First, analogously to superconductive Josephson junction arrays [161], there are *two* separated transitions: Upon lowering the temperature of the system, first a BEC forms at each individual lattice site, with no coherent phase relation to neighboring condensates. Only at lower temperature, the array undergoes a BKT transition, upon which (at least local) phase coherence is established between lattice sites. This separation of the transitions has significant advantages in the experimental determination of system parameters: Due to the separated transition to BEC on the individual lattice sites, the coherent coupling

¹ Here I ignore factors of order unity related to the precise lattice geometry, as well as finite-system-size corrections amounting to a finite ‘‘vortex core energy’’

² Throughout this chapter I use energy units to express temperature, hence entropy is unitless.

J can be rather accurately defined experimentally as well as calculated numerically, while the determination of the superfluid density $n_{SF,2D}$ is an experimental challenge [96]. The second large experimental advantage of an array over the continuous system is the ability to tune the Josephson coupling J over orders of magnitude by changing the lattice depth. This is in contrast to the parameters of the continuous BKT transition, i.e. the temperature T and the 2D superfluid density $n_{SF,2D}$, which are much harder to adjust accurately, especially while leaving other parameters equal.

3.3 Setup, calibrations and parameter determination

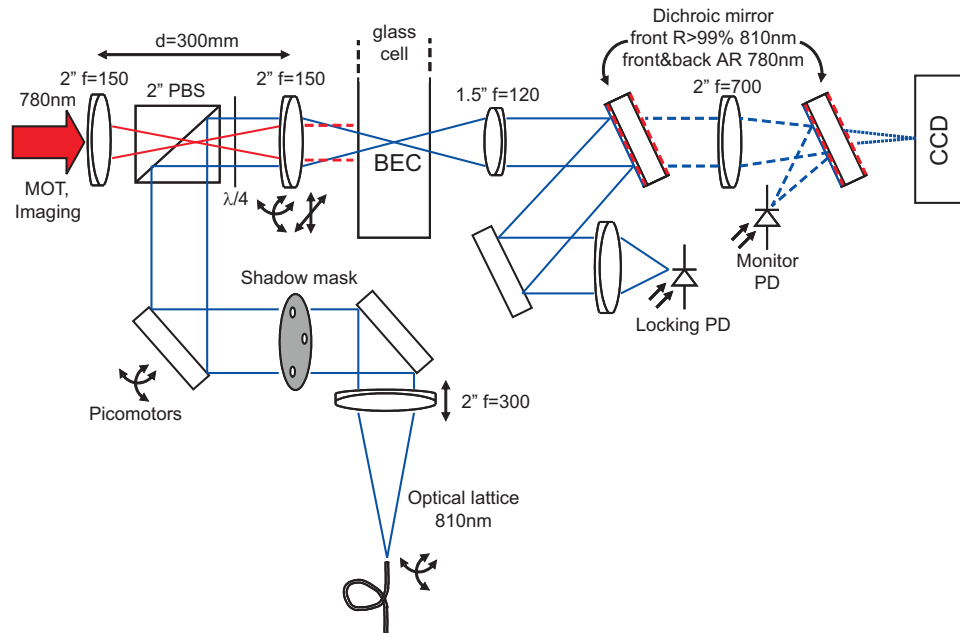


Figure 3.1: Optical lattice setup for creating a 2D Josephson junction array. 810 nm light from a single-mode fiber passes through a shadow mask which defines three lattice beams. These are combined with the MOT/imaging beam path using a polarizing beam splitter cube (PBS), and overlapped on the BEC, where interference forms the 2D lattice. Diagnostic photodiodes and a CCD camera are used to optimize beam overlap and alignment with respect to the BEC. Important degrees of freedom for alignment are indicated by arrows.

The setup, shown in Fig. 3.1, is similar in schematic to the one employed in the vortex pinning experiments, however the whole beam path was redesigned to provide

maximum stability to eliminate technical heating of the sample. The heating rate of the BEC loaded into an optical lattice of $V_{OL} = 1.33 \text{ kHz}$ depth was measured to be 1 nK/s , close to the value estimated from photon scattering. With a BEC transition temperature around $50 - 100 \text{ nK}$ this leaves plenty of time for experiments.

A lattice period of $d = 4.7 \mu\text{m}$ was chosen, as a compromise between precise control over J (facilitated by a small d), and minimization of phase fluctuations along the lattice axis (see below) requiring large d . To reach $4.7 \mu\text{m}$ lattice periods using 810 nm light (as opposed to $d = 7.2 \mu\text{m}$ using 532 nm light as in Chapter 2), a shorter focal length lens ($f = 150 \text{ mm}$) was used to focus the lattice beams onto the BEC. This lens needed to be placed into the MOT/imaging beam path, with the associated insertion of compensating lenses to the MOT and imaging beam paths. An important improvement was to change the position of the photodiode used for locking the lattice intensity to behind the glass cell. The point is the following: thermal effects, e.g. associated with varying light level during lattice intensity ramps, in the single-mode fiber delivering the lattice light can cause significant polarization changes of the fiber output on few-second timescales. The polarizing beam splitter cube converts such polarization fluctuations into intensity fluctuations. The present setup compensates for the resulting intensity fluctuations, in contrast to the setup for vortex pinning experiments (Fig. 2.5), where the locking photodiode was placed before the polarizing beamsplitter cube.

One important issue with acute-angle optical lattices is a precise longitudinal focusing of the lattice onto the BEC, to achieve maximal beam overlap. This focusing was achieved experimentally by monitoring the axial BEC radius, which grows when loaded into a deep 2D lattice, and is thus maximized when the lattice beams are optimally spatially overlapped on the BEC. The accuracy of this method was shown to be close to the BEC size, within $\pm 50 \mu\text{m}$. This is very accurate compared to the longitudinal beam overlap region of $w/\sin(\theta) = 580 \mu\text{m}$, given by the beam waist $w = 67 \mu\text{m}$ and the inclination angle of the beams $\theta = 6.6^\circ$.

3.3.1 Optical lattice intensity calibration

The standard method of measuring an optical lattice depth, i.e. pulsing the lattice and analyzing the resulting matter-wave diffraction pattern [116, 51] does not work for our long-period lattice, as the resulting momentum components do not cleanly separate from each other. Therefore an accurate intensity measurement based on the optical power, lattice beam waist and modulation contrast was required. Using the measured wavelength $\lambda = 810.1 \text{ nm}$, the optical lattice depth can then be calculated using Eq. (A.2) in Appendix A. The power P in the three beams was measured using a power meter that was calibrated against several other power meters. Losses between the measurement location and the BEC position were taken into account. The single-beam intensity profile is given by an Airy pattern due to diffraction from the holes in the shadow mask. The single-beam peak intensity is $I_{pk} = 0.555 \times \frac{P}{w^2}$ for a $1/e^2$ waist w (for a Gaussian it would be $I_{pk} = \frac{2P}{\pi w^2}$).

The optical lattice contrast, i.e. intensity $(max - min)/max$, was measured on the CCD camera, taking into account the finite camera pixel size ³. The expected contrast was calculated for comparison. The hexagonal geometry does not lead to fully constructive and destructive interference *along the axis connecting neighboring sites*, but instead gives $(max - min)/max = 88.8\%$. Known imperfections, such as slight (3%) intensity imbalances, slightly imperfect beam overlap (3% of beam waist) and slightly elliptical beam shapes (see Fig. 3.2) reduce the expected contrast to 86%. As the measured (79%) and calculated (86%) contrast did not fully agree, we used the average of measured and calculated contrast, 82.6(3.6)%. This is the largest contribution to the uncertainty in lattice depth. To calculate the intensity, the beam waist is measured on

³ In this measurement, “image resolution” is not limited in the conventional sense by the finite f -number of the imaging system, nor deteriorated as usual by aberrations, as the image is formed from three k -vectors only. We thus know that *all* k -vectors are collected by the imaging system, and in addition traverse the imaging system at identical radial displacements. This is in contrast to usual images composed of a whole spectrum of k -vectors, of which only a finite cone is collected, and each of which may be affected differently by aberrations.

the CCD camera. The imaging magnification is known within 3%, see Appendix E.

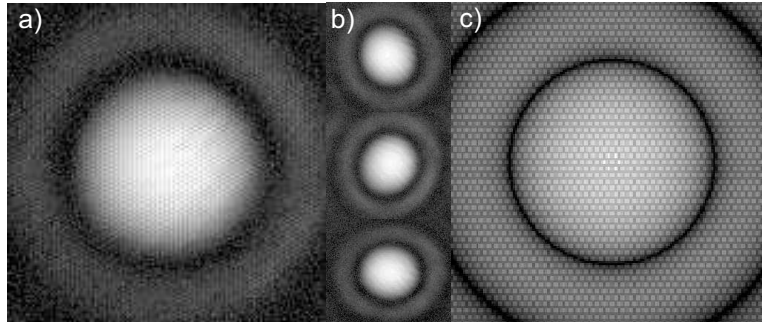


Figure 3.2: All images are shown using logarithmic intensity scale. (a) measured optical lattice intensity profile shows Airy pattern envelope. (b) individual beam profiles show slight ellipticity with major axes orientation differing by 120° - a direct consequence of the acute-angle lattice geometry. (c) calculated intensity profile.

3.3.2 Getting J/T right

Vortex proliferation in a JJA is expected to depend on the ratio of Josephson coupling to temperature, J/T – here I describe the accurate determination and error analysis of J and T .

Determination of J and T . As I will explain, the only experimental parameters required to obtain J are the axial condensate radius R_z , the lattice depth V_{OL} and the sample temperature T ⁴. These are measured independently for every shot. R_z and T are determined from non-destructive side-view images of the finite- T BEC loaded into the optical lattice. The images are analyzed using finite- T fits of the thermal cloud and BEC density profile, as described in Section 1.2.4. The condensate density is analyzed according to the coarse-grained Thomas-Fermi description of BECs in optical lattices (Section 1.5.4). V_{OL} is determined according to the above Section 3.3.1.

As I describe in Appendix B, numerical simulations result in a prediction for the

⁴ Note that the combined optical lattice and magnetic trap potential may be anharmonic in the radial direction (the optical lattice envelope Airy pattern is not infinitely large compared to the BEC size). This anharmonicity would complicate image analysis beyond the description of Sections 1.2.4 and 1.5.4. The axial (z) potential however is purely harmonic even in the presence of the optical lattice. We thus use only parameters extracted from the axial direction for our quantitative analysis.

Josephson coupling energy J as a function of the number of particles per well N_{well} , the applied optical lattice depth V_{OL} , and temperature T , which is valid in the range of N_{well} and V_{OL} employed in our experiments

$$J(V_{OL}, N_{well}, T) \approx 0.315 \text{ nK} \times N_{well} \exp\left(\frac{N_{well}}{3950} - \frac{V_{OL}}{244 \text{ Hz}}\right) \times \left(1 + \frac{0.59T}{100 \text{ nK}}\right) \quad (3.4)$$

as well as a prediction for the axial condensate radius R_z

$$R_z(V_{OL}, N_{well}, T) = R_z(V_{OL}, N_{well}, T = 0) - 0.55(10)\mu\text{m} \times T/60\text{nK} \quad (3.5)$$

with

$$R_z(V_{OL}, N_{well}, T = 0) = 22.69 \mu\text{m} \times (N_{well}/7000)^{(1/3.8)} \times (V_{OL}/1300 \text{ Hz})^{(1/4.5)} \quad (3.6)$$

The experimentally measured R_z , V_{OL} and T can be converted into the required N_{well} using equation (3.6), which then allows determining J for every shot using (3.4)⁵. The exponential dependence of J on N_{well} and V_{OL} therefore demands utmost care in the experimental determination of R_z and V_{OL} .

Systematic effects and error budget. In the following we describe the most critical aspects in the determination of each parameter. There are in general two separate concerns, (i) systematic differences between “hot” and “cold” clouds which need to be controlled in order to prove that vortex activation is thermally driven, and (ii) overall systematics in the absolute value of J/T , which might prevent accurate estimates of the BKT crossover position. The resulting error budget is summarized in Table 3.3.2.

Temperature T. We determine T from a fit to the BEC and thermal cloud, using a fit function including the BEC Thomas-Fermi profile and a mean-field modified thermal cloud, as described in Section 1.2.4. We first fit the wings of the thermal cloud outside a chosen ellipsoidal cut, then fix the thermal cloud parameters and fit the whole distribution to the BEC Thomas-Fermi profile and the mean-field modified

⁵ For the most accurate parameter determination we do NOT employ the approximations (3.4) and (3.6), but interpolate for every shot between nearest numerical data points, see Appendix B.

thermal cloud. The cut position for fitting the thermal cloud is critical: If chosen too close to BEC, one underestimates T by $O(10\%)$. This is a well known effect, see [157]. The largest overall systematic in the temperature determination is the side image magnification, which is uncertain within 3%. This leads to a temperature uncertainty of 6%, very small in comparison to uncertainty in J , see below.

Josephson coupling J . As described, three primary parameters enter the extraction of J : R_z , V_{OL} and T . The most crucial parameter for accurate comparison between “hot” and “cold” samples is R_z . In the determination of R_z from the above-mentioned fitting procedure, a subtle systematic effect occurs: the fitted value of R_z very slightly depends on the above mentioned fitting cut as well, and it does so differently for cold and hot samples. However an interval of cut positions exists where fits to both hot and cold clouds are reliable. Nonetheless, we assign a $\pm 0.75\%$ relative systematic uncertainty in R_z between hot and cold clouds. Although this appears tiny, it leads to a sizeable systematic uncertainty in J between hot and cold samples of $\Delta J / J = 8\%$. A second systematic effect from R_z between hot and cold samples arises from the modelling of the thermal cloud in the numerical simulations. We have to include a smoothing function that prevents a kink of length scale less than λ_{th} at the boundary between BEC and thermal cloud, and the precise choice of this smoothing function residually influences (a) $J(N_{well}, V_{OL})$ for a fixed T and (b) the compression of the BEC by the thermal cloud and hence $R_z(N_{well}, V_{OL})$ at fixed T – see Appendix B. The overall result is a further $\approx 10\%$ uncertainty in J between hot and cold samples. The *total* uncertainty in J between hot and cold samples is thus $\Delta J / J = 13\%$.

From here on we are dealing with overall uncertainties in J , as opposed to differences between “hot” and “cold” samples. The *absolute* uncertainty in R_z is dominated by the side view magnification. It enters the correct determination of N_{well} and leads to $\Delta J / J \approx 30\%$.

The uncertainty in V_{OL} is dominated by the optical lattice contrast of 82.6(3.6)%,

as described in Section 3.3.1. In addition the calibration of our optical power meter, as well as the accuracy and reproducibility of our daily optical power calibration are taken into account in Table 3.3.2.

The *absolute* value of J depends exponentially on the lattice constant d , which is determined from top-view CCD camera images, and therefore depends on the uncertainty in the absolute top view imaging magnification calibration. However there are two correlated effects: First, if we overestimate d , we underestimate V_{OL} by overestimating the beam waist. Second, an error in the lattice period d due to error in top view magnification calibration influences the relation between R_z and N_{well} in numerical simulations. In Table 3.3.2 we give the combined result on J of these three correlated effects.

Table 3.1: Error budget on the Josephson coupling J . The different contributions are explained in the text. s.e.: standard error; stdev: standard deviation.

Technical Source	Amount	Couples to	Amount	$\Delta J, +$	$\Delta J, -$
top view magnification	$\pm 3\%$	d	$\pm 3\%$		
top view magnification	$\pm 3\%$	V_{OL}	$\pm 6\%$		
top view magnification	$\pm 3\%$	calc. $R_z(N_{well})$			
combined effect				+14 %	-12 %
abs. Power meter calib.	3 % s.e.				
daily OL cal. procedure	2.2 % stdev				
combined effect				+33 %	-24 %
side magnification	$\pm 3\%$	N_{well}	11 %	+32 %	-27 %
OL mod. contrast	$(82.6 \pm 3.6)\%$	V_{OL}		+42 %	-29 %
syst. fit uncertainty		R_z	$\pm 0.75\%$	+8 %	-8 %
sim. finite-T corr. to J				+2 %	-2 %
sim. BEC compr. by THC		calc. $R_z(N_{well})$		+7 %	-7 %
Total $\Delta J / J$				+65 %	-50 %

As a last note, the *statistical* shot-to-shot fit uncertainty in R_z leads to an uncertainty in J , $\Delta J / J = 12\%$. This uncertainty leads to a shot-to-shot scatter in the data and is not taken into account here.

3.3.3 The importance of the third (z) dimension

Each lattice site in our setup is really an elongated tube. Axial phase fluctuations *inside* each condensate may thus affect the 2D nature of this experiment. The scale of axial phase fluctuations in each tube is set by equating the thermal energy $k_B T$ to the energy cost of a phase fluctuation Φ_{ax} . For long-wavelength fluctuations (length scale R_z) which dominate at low temperatures, this cost is $\int d^3\vec{r} \hbar^2/(2m) n(\vec{r}) \Phi_{ax}^2/R_z^2 \sim \hbar^2/(mR_z^2) N_{well} \Phi_{ax}^2$, where $n(\vec{r})$ is the condensate density. A more detailed, and experimentally verified ([135, 76, 83]), calculation by Walraven and coworkers [120] shows the RMS fluctuations between positions $-z, +z$ to be

$$\Phi_{ax,rms}(z) = \sqrt{\frac{32}{30} \frac{k_B T}{N_{well} \hbar^2/(mR_z^2)} \frac{2z}{R_z}} \quad (3.7)$$

We consider the region $z = R_z/3$ where according to our simulations 85% of the tunnel current between adjacent condensates is localized, and hence the relative phase between the condensates is measured. Using $N_{well} = 7000$, $T = 62.5 \text{ nK}$ and $R_z = 22 \mu\text{m}$, i.e. typical parameters for the worst-case scenario of a deep lattice and the “hot” dataset (see below), we get $\Phi_{ax,rms} \sim 0.7 \text{ rad}$. Alternatively, considering $z = 0.6R_z$ i.e. the region occupied by 90% of atoms in a Thomas-Fermi profile, we get $\Phi_{ax,rms} \sim 1 \text{ rad}$. These numbers show that while axial fluctuations cannot be completely ignored, they are not expected to destroy the quantitative picture of a two-dimensional system undergoing a BKT transition.

3.4 Experiments and results

The experiments reported below show vortex proliferation in a finite- T Josephson junction array, confirm thermal activation as the vortex formation mechanism, and provide information on the growth of bound vortex pairs, as J/T is lowered past the critical value for the BKT transition.

3.4.1 Thermally activated vortex proliferation

Our experiment starts with production of a partially Bose-condensed sample of ^{87}Rb atoms in a harmonic, axially symmetric magnetic trap with oscillation frequencies $\{\omega_{x,y}, \omega_z\} = 2\pi\{6.95, 15.0\}$ Hz. The number of *condensed* atoms is kept fixed around 6×10^5 as the temperature is varied. We then transform this system into a Josephson junction array, as illustrated in Fig. 3.3. In a 10 s linear ramp, we raise the intensity of a 2D hexagonal optical lattice ⁶ of period $d = 4.7\mu\text{m}$ in the x-y plane. The resulting potential barriers of height V_{OL} between adjacent sites [Fig.3.3(b)] rise above the condensate's chemical potential around $V_{OL} \approx 250 - 300$ Hz, splitting it into an array of condensates which now communicate only through tunneling. This procedure is adiabatic even with respect to the longest-wavelength phonon modes of the array [87, 35] over the full range of V_{OL} in our experiments. Each of the ≈ 190 occupied sites (15 sites across the BEC diameter $2 \times R_{TF} \approx 68\mu\text{m}$ ⁷) now contains a macroscopic BEC, with $N_{well} \approx 7000$ condensed atoms in each of the central wells at a temperature T that can be adjusted between $30 - 70$ nK. By varying V_{OL} in a range between 500 Hz and 2 kHz we tune J between $1.5\mu\text{K}$ and 5 nK, whereas the ‘‘charging’’ energy E_c , defined in [99], is on the order of a few pK, much smaller than both J and T . In this regime, thermal fluctuations of the relative phases $\Delta\phi_{Th} \approx \sqrt{T/J}$ are expected, while quantum fluctuations $\Delta\phi_Q \approx (E_c/4J)^{1/4}$ are negligible [99].

The suppression of the Josephson coupling greatly suppresses the energy cost of phase fluctuations in the x-y plane, *between* condensates, $J[1 - \cos(\Delta\phi)]$, compared to the cost of axial (z) phase fluctuations *inside* the condensates [120]. As a result, axial phase fluctuations remain relatively small, and each condensate can be approximated

⁶ Three circularly polarized laser beams ($\lambda = 810.1\text{nm}$) intersect in a tripodlike configuration, with $\theta = 6.6^\circ$ angles to the z-axis. Calculation of the optical dipole potential [70] includes counterrotating terms and interaction with both the D1 and D2 lines, as well as the ‘fictitious magnetic field’ due to the circular polarization. The tilted bias field of the TOP trap makes \mathcal{P} in Ref. [70] ≈ 0.5 .

⁷ To avoid radial flows during V_{OL} ramp-up, R_{TF} is kept constant by balancing the lattice-enhanced mean field pressure with radial confinement due to the optical lattice envelope, by the choice of a $67\mu\text{m}$ $1/e^2$ intensity waist. Axial (z) confinement is due to the magnetic trap alone.

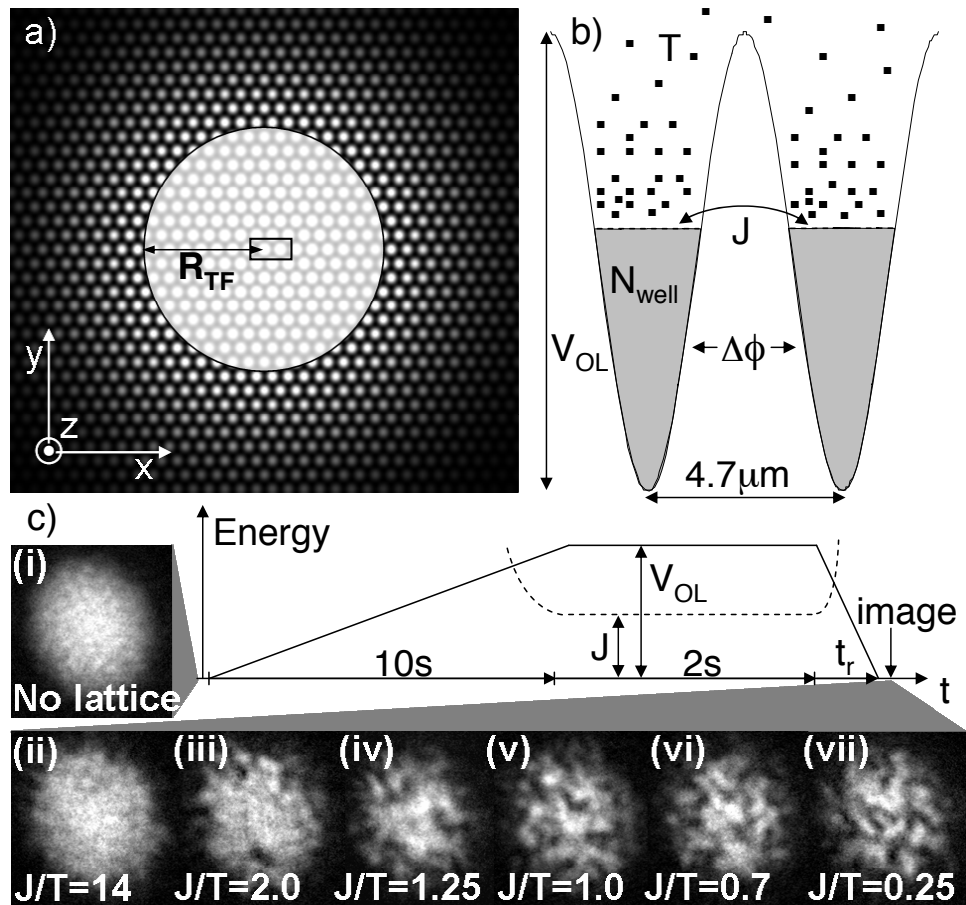


Figure 3.3: Experimental system. (a) 2D optical lattice intensity profile. A lattice of Josephson-coupled BECs is created in the white-shaded area. The central box marks the basic building block of our system, the double-well potential shown in (b). The barrier height V_{OL} and the number of condensed atoms per well, N_{well} , control the Josephson coupling J , which acts to lock the relative phase $\Delta\phi$. A cloud of uncondensed atoms at temperature T induces thermal fluctuations and phase defects in the array when $J < T$. (c) Experimental sequence: A BEC (i) is loaded into the optical lattice over 10 s, suppressing J to values around T . We allow 2 s for thermalization. To probe the system, we ramp off the lattice on a faster timescale t_r and take images of the recombined condensate. When J is reduced below T (ii)-(vii), vortices (dark spots) appear as remnants of the thermal fluctuations in the array.

as a single-phase object ⁸.

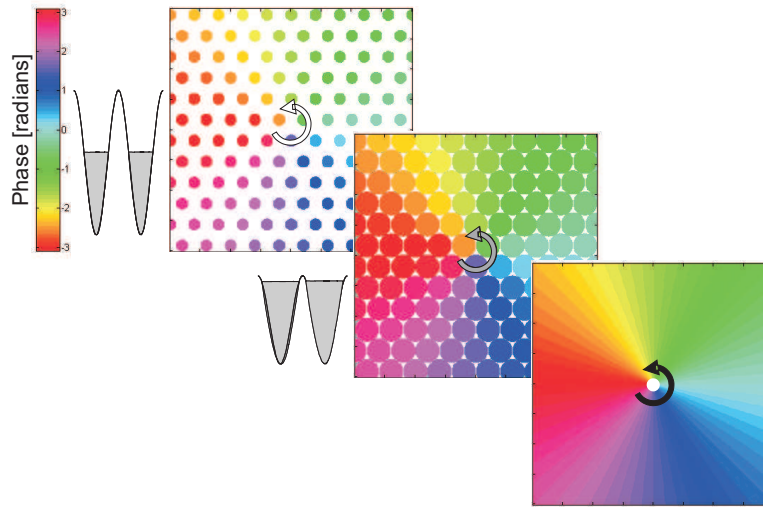


Figure 3.4: Ramping down the optical lattice depth converts phase winding defects in the JJA (left) to vortices in a bulk BEC (right). The increasing circulating current is indicated by arrow grayscale.

After allowing 2 s for thermalization, we initiate our probe sequence. We first take a nondestructive thermometry image in the x-z plane, from which the temperature T and, from the axial condensate size R_z , the number of condensed particles per well, N_{well} , is obtained (see below). To observe the phase fluctuations we then turn down the optical lattice (Fig. 3.4) on a time-scale t_r ⁹, which is fast enough to trap phase winding defects, but slow enough to allow neighboring condensates to merge, provided their phase difference is small. Phase fluctuations are thus converted to vortices in the reconnected condensate, as has been observed in the experiments of Scherer *et al.* [141] and analyzed theoretically by Ghosh and Sols [62]. We then expand the condensate by a factor of 6 and take a destructive image in the x-y plane.

Figure 3.3(c) illustrates our observations: (ii)-(vii) is a sequence of images at

⁸ In the axial condensate region between $z = -R_z/3, +R_z/3$, where according to our 3D GPE simulations 85% of the tunnel current is localized and hence the relative phase is measured, axial phase fluctuations [120] vary between $\approx 600 mrad$ (“cold” data in Fig. 3.5) and $800 mrad$ (“hot”) in the regime $J/T \approx 1$.

⁹ Within a dataset, the ramp-down rate is kept fixed, $t_r = \tau \times V_{OL}/1.3 kHz$, $\tau = 18 ms$ if not otherwise indicated.

successively smaller J/T (measured in the center of the array). Vortices, with their cores visible as dark “spots” in (iii)-(vii), occur in the BEC center around $J/T = 1$. Vortices at the BEC edge appear earlier, as here the magnetic trap potential adds to the tunnel barrier, suppressing the *local* J/T below the quoted value. That the observed “spots” are indeed circulation-carrying vortices and antivortices is inferred from their slow $\approx 100\text{ms}$ decay after the optical lattice ramp-down, presumably dominated by vortex-antivortex annihilation. From extensive experiments on vortices in our system we know that circulation-free “holes” fill so quickly due to positive mean field pressure, that they do not survive the pre-imaging expansion. Vortices with identical circulation would decay by dissipative motion to the BEC edge, in our trap over $\gtrsim 10\text{s}$.

To investigate the thermal nature of phase fluctuations, we study vortex activation while varying J at different temperatures. For a quantitative study, accurate parameter estimates are required. The Josephson-coupling energy J is obtained from 3D numerical simulations of the Gross-Pitaevskii equation (GPE) for the central double-well system [9, 60] [Fig.3.3(b)], self-consistently including mean-field interactions of both condensed and uncondensed atoms [112]. A useful approximation for J in our experiments is ¹⁰ : $J(V_{OL}, N_{well}, T) \approx N_{well} \times 0.315\text{ nK} \exp[N_{well}/3950 - V_{OL}/244\text{Hz}](1 + 0.59 T/100\text{nK})$. The finite- T correction to J arises from both the lifting-up of the BEC’s chemical potential and the axial compression by the thermal cloud’s repulsive mean field, but does *not* take into account the effects of phase fluctuations on J (in condensed-matter language, we calculate the *bare* J). N_{well} is determined by comparison of the experimentally measured R_z , to $R_z(V_{OL}, N_{well}, T)$ obtained from GPE simulations. Both experimental and simulated R_z are obtained from a fit to the distribution of condensed and uncondensed atoms, to a Thomas-Fermi profile plus mean-field-modified Bose function [112]. In determination of all J values, there is an overall systematic multiplicative uncertainty

¹⁰ J is averaged over junctions within the central 11% of the array area, from which all quantitative experimental results are extracted.

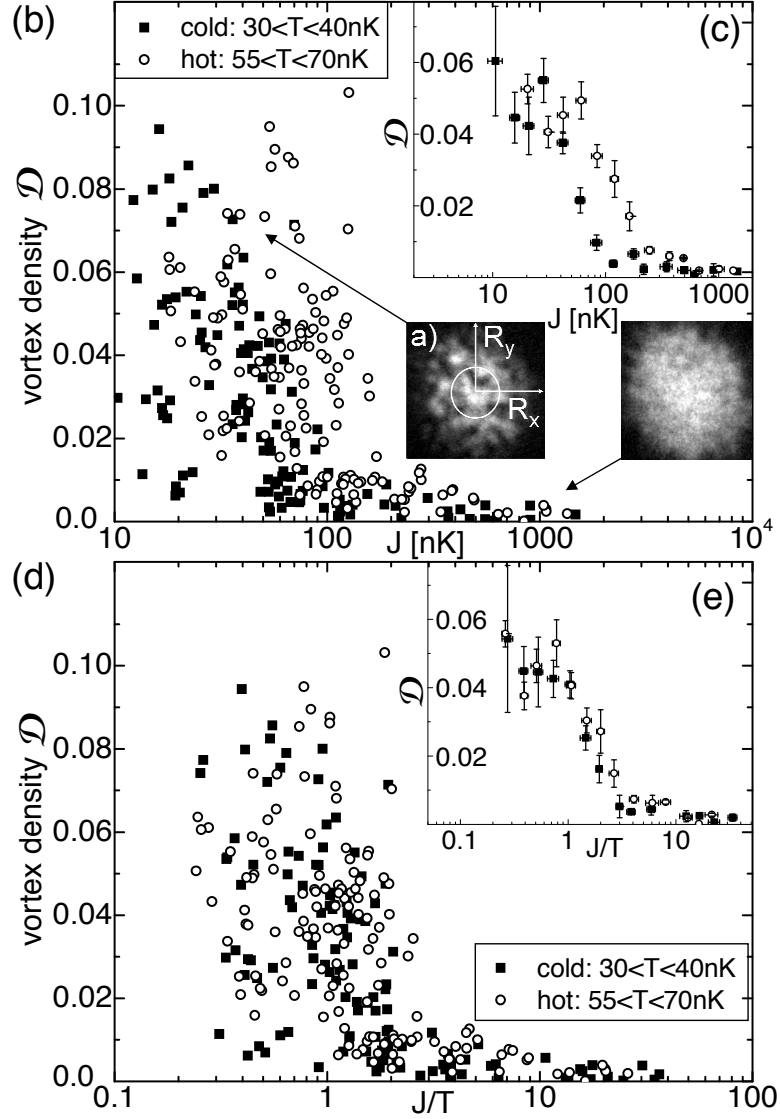


Figure 3.5: Quantitative study of vortices. The areal density of vortices is quantified by the plotted \mathcal{D} defined in the text. \mathcal{D} is extracted only from the central 11% of the condensate region [circle in inset (a)] to minimize effects of spatial inhomogeneity. (b) \mathcal{D} vs J for two datasets with distinct “cold” and “hot” temperatures. Each point represents one experimental cycle. The increase in \mathcal{D} with decreasing $J \lesssim 100$ nK signals the spontaneous appearance of vortices, while the “background” $\mathcal{D} \lesssim 0.01$ for $J \gtrsim 200$ nK is not associated with vortices. Vortices clearly proliferate at larger J for the “hot” data, indicating thermal activation as the underlying mechanism. The large scatter in \mathcal{D} at low J is due to shot noise on the small average number of vortices in the central condensate region. (c) same data as in (b), but averaged within bins of size $\Delta[\log(J)] = 0.15$. Error bars of \mathcal{D} are standard errors. (d) same data as (b), but plotted vs J/T . “Cold” and “hot” datasets almost overlap on what appears to be a universal vortex activation curve, as confirmed by averaging [inset (e)], clearly revealing the underlying competition of J and T .

$\Delta J/J = \frac{\times}{\div} 1.6$, dominated by uncertainties in the optical lattice modulation contrast, the absolute intensity calibration, and magnification in the image used to determine N_{well} . In comparing J for “hot” and “cold” clouds (see Fig. 3.5) there is a relative systematic error of 15% associated with image fitting and theory uncertainties in the thermal-cloud mean-field correction to J .

The qualitative results of our work are consistent whether we use an automated vortex-counting routine or count vortices by hand, but the former shows signs of saturation error at high vortex density, and the latter is vulnerable to subjective bias. As a robust vortex-density surrogate we therefore use the “roughness” \mathcal{D} of the condensate image caused by the vortex cores. Precisely, we define \mathcal{D} as the normalized variance of the measured column density profile from a fit to a smooth finite- T Bose profile [112], with a small constant offset subtracted to account e.g. for imaging noise. To limit spatial inhomogeneity in J , caused by spatially varying condensate density and optical lattice intensity, to $< 10\%$, \mathcal{D} is extracted only from the central 11% of the condensate area which contains 20 lattice sites [Fig. 3.5(a)]. Comparison to automated vortex-counts shows that \mathcal{D} is roughly linear in the observed number of vortices, irrespective of the sign of their circulation, with a sensitivity of $\approx 0.01/\text{vortex}$.

Figure 3.5 shows results of our quantitative study. In Fig. 3.5(b), we plot \mathcal{D} vs J for two datasets with distinct temperatures. At large $J \gtrsim 200 nK$ a background $\mathcal{D} \lesssim 0.01$ is observed, that is not associated with vortices, but due to residual density ripples remaining after the optical lattice ramp-down. Vortex proliferation, signaled by a rise of \mathcal{D} above ≈ 0.01 , occurs around $J \approx 100 nK$ for “hot” BECs and at a distinctly lower $J \approx 50 nK$ for “cold” BECs [confirmed by the averaged data shown in Fig. 3.5(c)], indicating thermal activation as the vortex formation mechanism. Plotting the same data vs J/T in Fig. 3.5(d) shows collapse onto a universal vortex activation curve, providing strong evidence for thermal activation. A slight residual difference becomes visible in the averaged “cold” vs “hot” data [Fig.3.5(e)], perhaps because of systematic

differences in our determination of J at different temperatures.

3.4.2 Studying vortex pair sizes and vortex pair unbinding

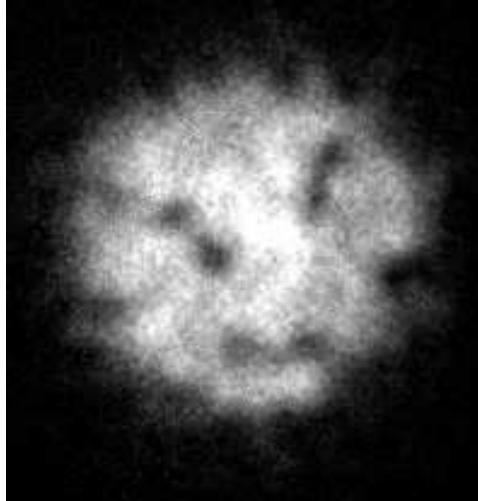


Figure 3.6: Vortex-antivortex pairs, imaged just prior to their annihilation. Following the optical lattice ramp-down, tightly bound pairs annihilate faster than loosely bound pairs, providing a time-to-length mapping that allows to extract information on vortex pair sizes.

The vortex density \mathcal{D} studied so far, by itself provides no distinction between *bound* vortex-antivortex *pairs* and *free* vortices. In the following we exploit the flexibility of optical potentials to distinguish free or loosely bound vortices from tightly bound vortex-antivortex pairs. Our technique for inferring vortex antivortex pair sizes makes use of the fact that, once the optical lattice potential has been turned off, vortices and antivortices annihilate in the bulk condensate over a $\approx 100\text{ ms}$ timescale. Figure 3.6 shows an example image of pairs of vortices just prior to their annihilation. It is intuitively obvious that tightly bound vortex pairs will annihilate on a much faster timescale than loosely bound pairs. A “slow” optical lattice ramp-down therefore allows time for tightly bound pairs to annihilate before they can be imaged. By slowing down the ramp-down duration τ [inset of Fig. 3.7], we can thus selectively probe vortex pairs of increasing size. This represents an attempt to approach the “true” BKT vortex

unbinding crossover that is complementary to transport measurements employed so
su

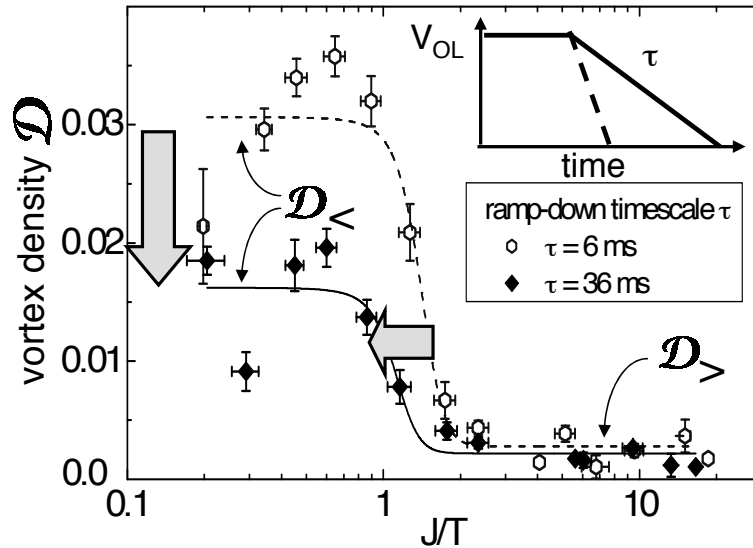


Figure 3.7: Vortex density \mathcal{D} probed at different optical lattice ramp-down timescales τ . A slow ramp provides time for tightly bound vortex-antivortex pairs to annihilate, allowing selective counting of loosely bound or free vortices only, whereas a fast ramp probes both free and tightly bound vortices. A fit to the vortex activation curve determines its midpoint $(J/T)_{50\%}$, its 27% – 73% width $\Delta(J/T)_{27-73}$, and the limiting values $\mathcal{D}_<$ ($\mathcal{D}_>$) well below (above) $(J/T)_{50\%}$.

Figure 3.7 shows vortex activation curves, probed with two different ramp-down times. Two points are worth noticing: First, a slow ramp compared to a fast one shows a reduction of the vortex density $\mathcal{D}_<$ in arrays with fully randomized phases at low J/T . The difference directly shows the fraction of tightly bound pairs that annihilate on the long ramp. Second, a slower ramp shows vortex activation at lower $(J/T)_{50\%}$, confirming that free or very loosely bound vortices occur only at higher T (lower J). Specifically, the data clearly show a range around $J/T \approx 1.4$ where only tightly bound pairs exist.

To map the experimental ramp-down time-scale to theoretically more accessible vortex-antivortex pair sizes, we compare the observed number of vortices in fully randomized arrays at low J/T to simulations of vortex distributions in a hexagonal array

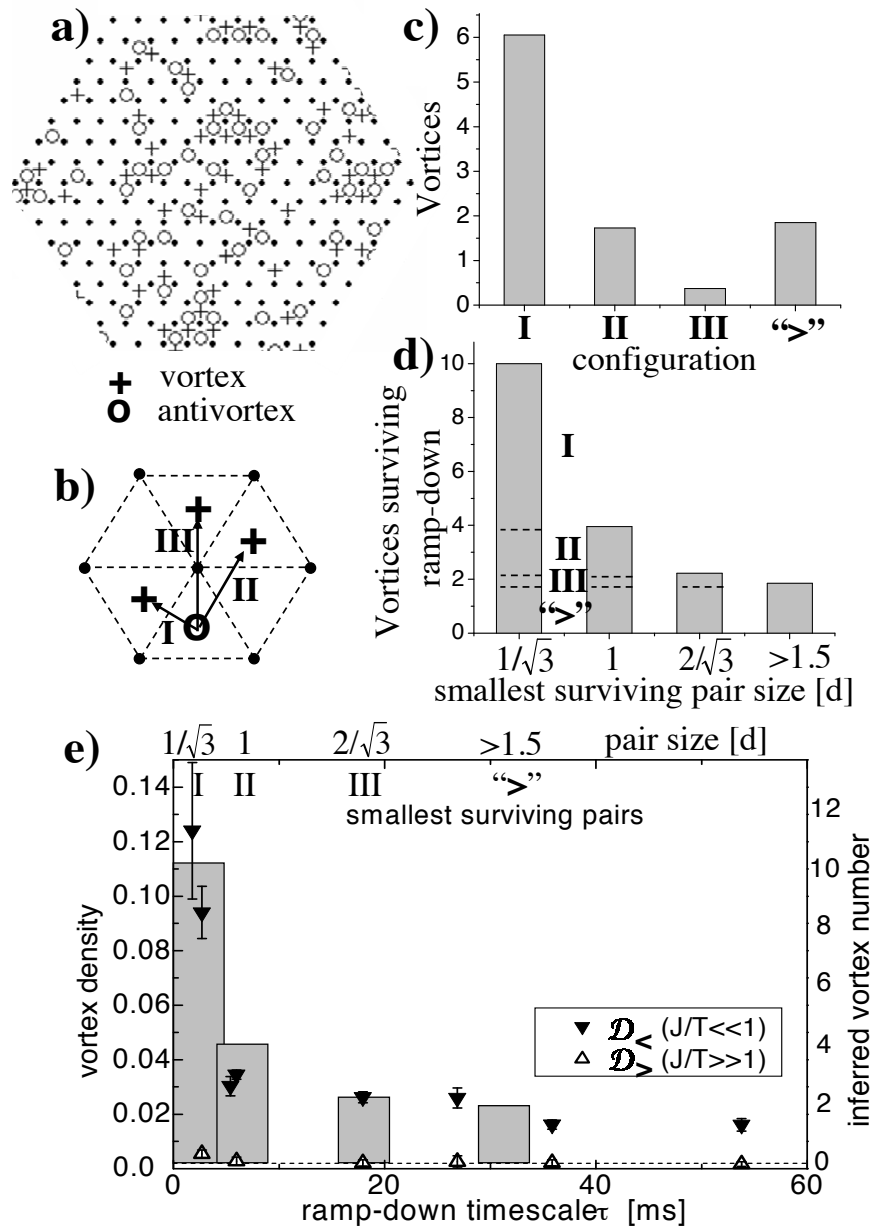


Figure 3.8: Time-to-length mapping based on vortex-antivortex annihilation. (a) simulation of vortices and antivortices in an array with random phases, (b) smallest possible pair sizes in a hexagonal array of period d : configuration I - pair size $d/\sqrt{3}$, II: size d , III: size $2d/\sqrt{3}$. (c) simulated vortex pair size distribution (“>”: free vortices or pairs larger config. III), (d) cumulative distribution. (e) Mapping between ramp-down timescale τ and estimated size of the smallest pairs surviving the ramp (upper axis). The difference $\mathcal{D}_< - \mathcal{D}_>$ measures the number of observed vortices surviving the ramp (right axis). Comparison to the simulated vortex distribution yields a size estimate of the smallest surviving pairs (upper axis).

with random phases. In these simulations, following Ref. [141], we count a vortex if all three phase differences in an elemental triangle of junctions are $\in (0, \pi)$, or if all are $\in (-\pi, 0)$. A snapshot of a simulated vortex distribution is shown in Fig. 3.8(a). Within the central 20 lattice sites, comparable to the experimental region of interest we find, on average, a total of 10 vortices. 6 vortices occur in nearest-neighbor vortex-antivortex pairs [configuration I in Fig. 3.8(b)], 1.7 (0.4) occur in configuration II (III) respectively, and 1.9 occur in larger pairs or as free vortices. To relate these time-independent simulations to the experiment, we show in Fig. 3.8(d) the relevant cumulative vortex distributions, i.e. all vortices occurring in pairs larger than a given lower cutoff size. For a given experimental ramp-down duration, we expect only those vortex configurations to survive which are above a lower cutoff pair size imposed by the ramp-down rate.

In Fig. 3.8(e) we compare the simulated cumulative vortex distributions to experimentally measured vortex numbers as a function of ramp down timescale, to obtain the desired time-to-length mapping. Downward triangles show the decrease of the experimentally measured saturated (low- J/T) vortex density $\mathcal{D}_<$ with increasing ramp timescale τ . The right axis shows the inferred number of vortices that survived the ramp. Approximately 11 vortices are observed for the fastest ramps, in good agreement with the *total* number of vortices expected from the simulations (indicated as grey bars). For just somewhat slower ramps of $\tau \approx 5 \text{ ms}$, only 3 vortices survive, consistent with only vortices in configuration II & III or larger remaining (indicated in Fig. 3.8(e), top axis).¹¹ For $\tau \gtrsim 30 \text{ ms}$ ramps less than 2 vortices remain, according to our simulations spaced by more than $2d/\sqrt{3}$. Thus we infer that ramps of $\tau \approx 30 \text{ ms}$ or longer allow time for bound pairs of spacing $\lesssim 2d/\sqrt{3}$ to decay before we observe them.

With this time-to-length mapping we now return to the observations in Fig.3.7. For the slower ramp we observe vortex activation at lower $(J/T)_{50\%}$, confirming that

¹¹ The very short annihilation time of configuration I pairs [$\tau < 5 \text{ ms}$ in Fig. 3.8] is not unexpected: their spacing $d/\sqrt{3} = 2.8 \mu\text{m}$ is comparable to the diameter of a vortex core in the bulk condensate (after V_{OL} rampdown).

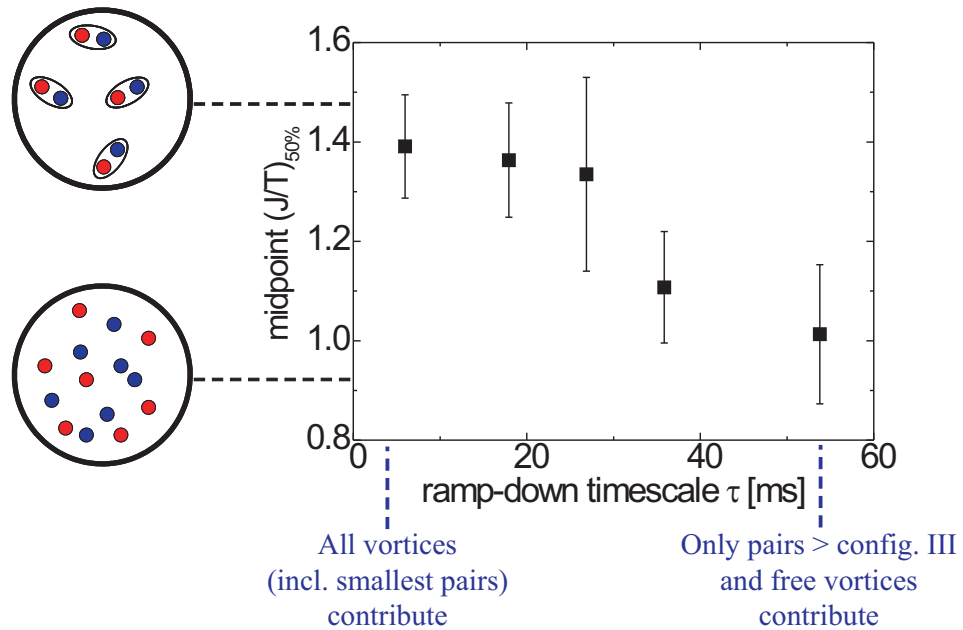


Figure 3.9: A glimpse at BKT vortex pair unbinding: A downshift in the midpoint $(J/T)_{50\%}$ of vortex activation curves, such as shown in Fig. 3.7, is seen for slow ramp-down times. This is consistent with the occurrence of tightly bound pairs around $J/T \sim 1.4$, whereas loosely bound or free vortices occur at low $J/T \sim 1$ only.

free or very loosely bound vortices occur only at higher T (lower J). In Fig. 3.9 we plot the midpoint $(J/T)_{50\%}$ of vortex activation curves versus the applied ramp-down time. The data quantitatively show a shift of $(J/T)_{50\%}$ from 1.4 for fast ramp times when all vortices are expected to contribute to the signal, to 1.0 for slow ramp times when only loosely bound vortices survive. The data therefore reveal that loosely bound pairs of size larger than $2d/\sqrt{3}$, or indeed free vortices, do not appear in quantity until $J/T \leq 1.0$, whereas more tightly bound vortex pairs appear in large number already for $J/T \leq 1.4$. This result clearly illustrates the mechanism of vortex-antivortex unbinding with increasing temperature or decreasing superfluid coupling, which underlies BKT theory.

A further interesting observation concerns the width of the vortex activation curve. The relative width, determined from fits to data such as the ones shown in Fig. 3.7, is $\Delta(J/T)_{27-73}/(J/T)_{50\%} \approx 0.3$, independent of ramp-down duration. This

width is neither as broad as in a double-well system [123, 60], where the coherence factor rises over a range $\Delta(J/T)_{27-73}/(J/T)_{50\%} \approx 1.4$, nor as broad as expected from our simulations¹² of an array of uncoupled phases, each fluctuating independently with $\Delta\phi_{RMS} = \sqrt{T/J}$, for which we find $\Delta(J/T)_{27-73}/(J/T)_{50\%} \approx 0.85$. Presumably collective effects in the highly multiply connected lattice narrow the curve. On the other hand, the width is 3 times larger than the limit due to spatial inhomogeneity in J , suggesting contributions to the width due to finite-size effects or perhaps revealing the intrinsically smooth behavior of vortex activation in the BKT regime.

In conclusion, we have probed vortex proliferation in the BKT regime on a 2D lattice of Josephson-coupled BECs. Allowing variable time for vortex-antivortex pair annihilation before probing the system provides a time-to-length mapping, which reveals information on the size of pairs with varying J/T .

¹² Following [141], in simulations we count a vortex if all three phase differences in an elemental triangle of junctions are $\in (0, \pi)$, or if all are $\in (-\pi, 0)$.

Chapter 4

Rapidly rotating 2D Bose gases in a 1D optical lattice

4.1 Motivation

In this chapter I describe a set of experiments where rapidly rotating Bose-Einstein condensates are loaded into a one-dimensional optical lattice aligned with the rotation axis. In this way a stack of two-dimensional rotating Bose gases is created (Fig. 4.1). There are several conceptual motivations for these experiments.

The first one is the possibility of achieving low filling factors, i.e. low numbers of condensate atoms per vortex, as is required to reach fractional quantum Hall (FQH) states in a rotating BEC (see Appendix D). This field has attracted a vast amount of theoretical interest, e.g. [47, 118, 152, 165, 29], and spurred several previous experimental efforts [143, 32]. The idea is sketched in Fig. 4.1: A rotating BEC with 3×10^6 atoms and 150 vortices, i.e. a filling factor $\nu = 2 \times 10^4$, is split by the optical potential into a stack of ≈ 200 rotating two-dimensional “pancake” condensates. For each pancake the filling factor is now $\nu \approx 100$, tantalizingly close to values around $\nu \approx 10$, where vortex lattice melting due to quantum fluctuations, and the transition to FQH states, is expected (see Appendix D). With a relatively modest further reduction of the number of condensate atoms and careful attention to keeping temperatures low, this first step toward fractional quantum Hall physics appeared to be within reach. Vortex lattice melting in an optical lattice was analyzed theoretically e.g. in [154, 153].

The second motivation is that a layered stack of rotating superfluids bears many

analogies with the layered structures of high-temperature superconductors in a magnetic field. By this analogy, a large range of finite-temperature physics of low-dimensional systems might be accessible, the study of vortex lattice fluctuations being one example. In addition, the ability to vary the interlayer tunnel coupling may allow studies of the rich physics associated with the 2D-3D dimensional crossover [169].

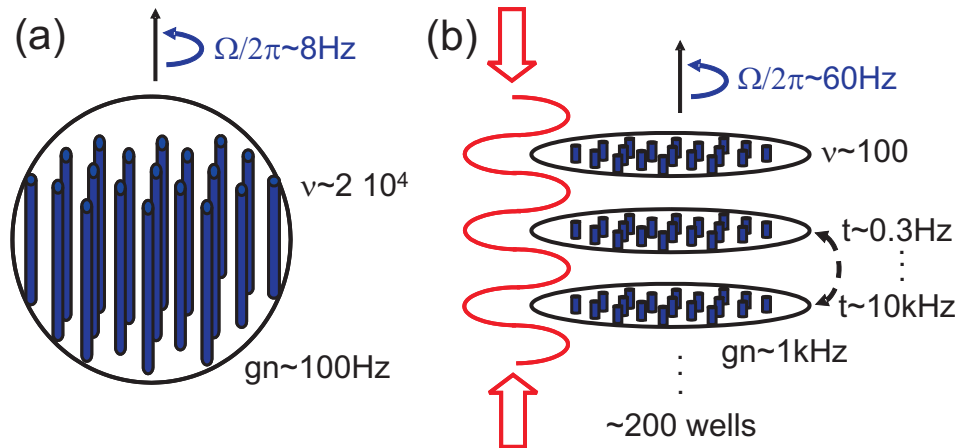


Figure 4.1: (a) “Bulk” rotating BEC with $\nu \approx 2 \cdot 10^4$ atoms per vortex. (b) Rotating BEC loaded into a 1D optical lattice. The most dramatic changes are the reduction of dimensionality of the individual “pancake” BECs, and the reduction of the filling factor to $\nu \approx 100$ for each pancake. Also indicated are typical values for interaction energy gn and single-particle tunneling frequency t .

As a third possible topic of study, even the physics of a single vortex in an optical lattice is rich and surprising, see the work of Stoof and coworkers [103], as well as [84]. Kelvin modes, the helical oscillations of the vortex line, in a continuous BEC of radius R follow the dispersion relation [59] (k : Kelvin mode wavevector):

$$\omega_K(k) = \hbar k^2 / 2m \log\left(\frac{R}{\xi \sqrt{1 + (kR)^2}}\right) (1 - 2/(kR)^2) \quad (4.1)$$

The negative frequencies of long-wavelength modes indicate an energetic (but not dynamical) instability of the vortex. These modes contribute to the vortex spiraling out of the BEC. In particular, the zero-energy mode is expected to be heavily thermally excited. In an axial optical lattice of period d and single-particle tunneling frequency t ,

the Kelvin mode dispersion relation is transformed to

$$\omega_{K,OL}(k)/(2\pi) \approx 7.2t \times \sin^2(kd/2) - \hbar/(mR^2) \log(R/\xi) \quad (4.2)$$

This expression shows that tuning the tunneling strength t allows control over the vortex dispersion relation; in particular it alters the wavevector at which the zero-energy mode occurs, which should be observable in side-view images of the vortex. A possible experiment studying such vortex-fluctuations is shown in Fig. 4.2.

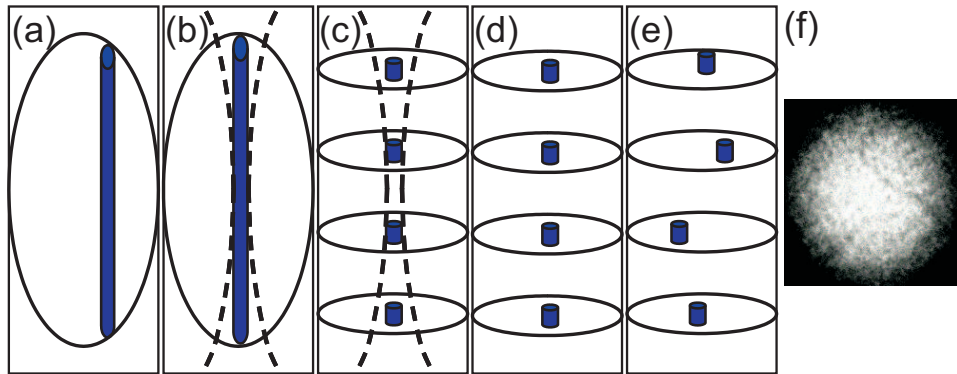


Figure 4.2: Study of single vortex dynamics in a 1D optical lattice. (a) A single vortex in a bulk BEC is pinned (b) on a tightly focused single laser beam (dashed) to create a controlled initial condition. (c) The optical lattice is applied and (d) the vortex is released from the pinning potential, allowing the study of its subsequent fluctuating dynamics (e). (f) Expansion image of a single vortex line as in (a), demonstrating the feasibility of imaging a single vortex in side-view.

4.1.1 The physics of a finite-temperature array of rotating 2D Bose gases

Rotating BECs in a one-dimensional lattice represent a complicated system, as can be guessed from Fig. 4.1(b). Coherence along the lattice is established by the Josephson coupling $J = N_{well} \times t$ between lattice sites. However as the Josephson coupling is weakened in a deep lattice, a dimensional crossover occurs from a bulk 3D BEC to a stack of 2D BECs on individual lattice sites. Even before the two-dimensional rotating BECs in individual lattice sites become completely independent, increasing thermal fluctuations of the 2D vortex lattices additionally weaken the axial

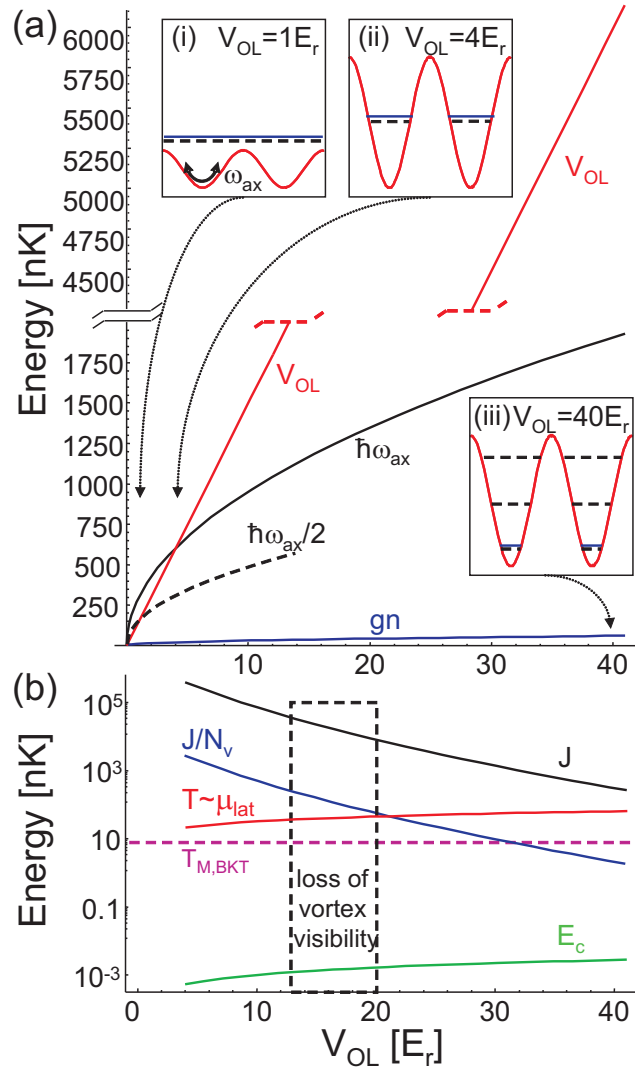


Figure 4.3: (a) Optical lattice depth (red), lattice-site harmonic oscillator frequency $\hbar\omega_{ax}$ (black, solid) and zero point energy $\hbar\omega_{ax}/2$ (dashed), and interaction energy $gn = \mu_{lat}$ (Eq. (1.54), blue) vs. lattice depth measured in units of $E_r = 152 \text{ nK}$. A total of 2×10^6 atoms rotating at $\Omega/\omega_\rho = 0.925$ was assumed. Insets: (i) Optical potential (red), approximate bound state energy (black), chemical potential (blue) at $V_{OL} = 1 E_r$ – the lattice potential does not yet support a bound state, the BEC remains connected across the lattice. (ii) At $V_{OL} = 4 E_r$ a bound state exists at $\approx \hbar\omega_{ax}/2$, and the BEC is split into an array of condensates. Interactions and temperature are small compared to $\hbar\omega_{ax}$, i.e. axial motion is frozen out and the condensates enter the 2D regime. (iii) Deep lattice at $V_{OL} = 40 E_r$. (b) Josephson coupling J (black), and coupling per vortex lattice unit cell J/N_v (blue). Temperature $T \approx \mu_{lat}$ (red) is always larger than the expected 2D vortex lattice melting temperature (magenta, Eq. (D.15), Appendix D). Once J/N_v is sufficiently reduced (see text), 2D vortex lattice fluctuations develop on each lattice site. Experimentally, for $V_{OL} \gtrsim (13.5 - 20) E_r$ vortex visibility is lost (Section 4.3.2) in images that are integrated through the whole optical lattice array.

phase coherence. In the following we will approach this problem piece by piece. The important parameters of this system are shown in Fig. 4.3.

1.) Josephson coupling between lattice sites. At low lattice depth we expect this to be the dominant energy scale. In all experiments in this chapter, interparticle interactions are negligible compared to the energy separation of Bloch bands, thus the single-particle tunnel coupling t (and hence the Josephson coupling $J = N_{well} \times t$) and the charging energy E_c are quite accurately described by equations (1.52) and (1.53), respectively. Similarly to the experiments on the BKT transition, the lattice system here is in the Josephson regime described in Section 1.5.2, where $J \equiv N_{well} \times t \gg E_c$, but $E_c \gg \frac{J}{N_{well}^2}$ (see Fig. 4.3). Upon reducing J by raising the lattice depth we thus expect to see a competition between the coherence-preserving Josephson coupling and thermal phase fluctuations along the lattice direction, which will lead to decoherence between lattice sites. Quantum fluctuations are not expected to play a significant role. Based on the results from Chapter 3, the naive expectation for the condition when phase coherence is lost between the the pancake lattice sites due to thermal fluctuations would be $J \approx T$ (reached at $V_{OL} \approx 45 E_r$), similar to the BKT transition of a static BEC in a 2D optical lattice.

But in the case of a rotating BEC in a 1D lattice we need to think harder: Clearly, a vortex lattice on each lattice site violates the assumption of a spatially uniform condensate phase on each site, which was the basis of the simple description of a Josephson junction array only in terms of J , E_c and T . On intuitive grounds, if the 2D vortex lattice undergoes significant fluctuations, each vortex lattice unit cell of size $\sim \ell^2$ may act as an independent “piece” of the condensate, with a coupling strength to an adjacent optical lattice site of order $J \times \ell^2 / R^2 \equiv J / N_v$ where R is the 2D condensate radius and $N_v = R^2 / \ell^2$ is the number of vortices. This single-vortex-lattice-cell coupling strength J / N_v is also shown shown in Fig. 4.3, and I will explicitly demonstrate its relevance shortly.

2.) Rotating, finite-T, 2D BEC on each lattice site. For deep optical lattices the Josephson coupling is essentially zero, leaving us with a stack of individual rotating pancake condensates. According to the discussion in Appendix D, under the present experimental conditions such 2D vortex lattices will undergo significant thermal fluctuations, while quantum fluctuations of the vortex lattice are almost certainly not significant (the filling factor in all experiments is $\nu \sim 100$, still a factor 10 above the critical filling factor for which quantum melting is predicted).

First, consider BKT-type vortex lattice melting due to the thermally activated occurrence and unbinding of vortex-antivortex pairs, which disturbs and ultimately melts the surrounding ordered vortex lattice. The predicted melting temperature, Eq. (D.15), is on the order of $T_{M,BKT} = (6 - 8) nK$ over the range of optical lattice depths $V_{OL} = (10 - 40) E_r$. The actual temperature of even the coldest samples (Fig. 4.3(b), solid red line) is $T \approx \mu_{lat} \approx 50 nK$ ¹, i.e. much higher than the melting temperature. From this we conclude that, as soon as the 2D BECs experience a sufficiently suppressed axial Josephson coupling, the 2D vortex lattice should melt.

Secondly, also long-wavelength, phonon-like vortex lattice thermal fluctuations are expected to be strong enough to induce vortex lattice melting. According to Eq. (D.14), the respective melting temperature is $T_{M,long} \approx (13 - 18) nK$ for $V_{OL} = (10 - 40) E_r$, smaller than estimated sample temperatures.

3.) 3D - 2D crossover with increasing lattice depth. As shown in Fig. 4.3(a), as soon as the lattice depth reaches $V_{OL} \gtrsim 4 E_r$ the BECs on individual lattice sites become two-dimensional, in the sense that only the lowest axial oscillator state on each site is occupied and axial motion on-site is frozen out. However at this point the stack of 2D BECs is still strongly Josephson-coupled along the lattice direction and still forms an *effectively* 3D system.

¹ Careful inspection of in-situ images reveals hardly any normal cloud, and if present its size hardly extends beyond the BEC. In cases where a fit to this normal component is possible, $T \approx (1 - 1.5)\mu_{lat}$ is found.

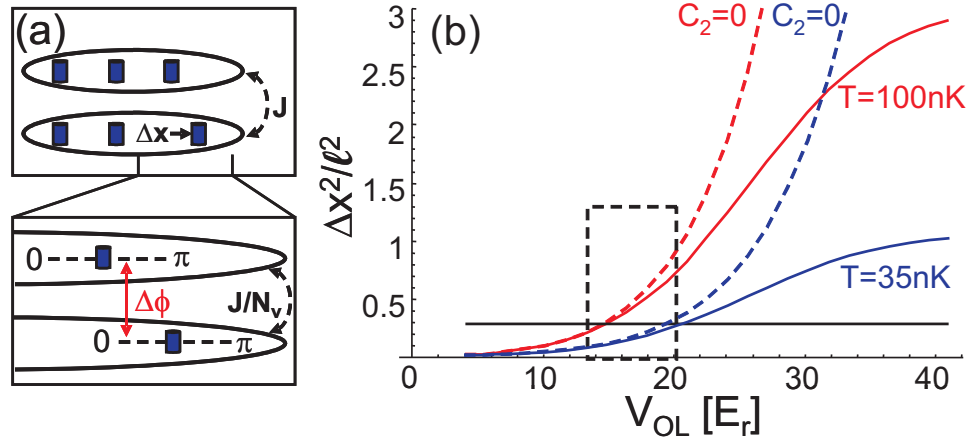


Figure 4.4: (a) Simple model (see text) for thermally activated vortex displacements Δx in a stack of rotating BECs in an optical lattice (normalized to the vortex lattice unit cell size ℓ , Eq. (1.23)). Displacement of a single pancake vortex costs an in-plane energy $\propto C_2 \Delta x^2$ due to vortex lattice deformation, and (zoom-in) a fraction $\propto \Delta x^2 / \ell^2$ of the Josephson coupling energy J/N_v due to the resulting phase difference $\Delta \phi_{(\vec{r})}$ between lattice sites. (b) Results: Blue (red) solid lines: sample $T = 35$ (100) nK, respectively. Dashed lines: same, but assuming vanishing in-plane energy cost $T_{M,BKT} \propto C_2 = 0$. Solid black line: $\Delta x / \ell \gtrsim 0.28$ is the Lindemann criterion for melting of the vortex lattice. Dashed black line: region of observed loss of vortex lattice visibility.

Here we develop a simple model for the crossover between this *effectively* 3D vortex lattice and a stack of truly independent 2D rotating BECs, that occurs upon *further* reduction of the Josephson coupling. We consider the thermally activated vortex displacements under the influence of both the Josephson coupling and the in-plane vortex lattice stiffness. We focus on a single vortex lattice unit cell and two adjacent optical lattice sites. The situation is sketched in Fig. 4.4. The displacement of a single pancake vortex by Δx costs an in-plane energy ² $E_{2D} \approx 2C_2 \Delta x^2$ due to the vortex lattice deformation (C_2 is the vortex lattice shear modulus). In addition, this displacement results in a nonzero phase difference between condensates on adjacent optical lattice sites, and thus costs a fraction of the Josephson coupling energy per unit cell J/N_v : $E_{ax} = (J/N_v) \times \langle 1 - \cos(\Delta \phi_{(\vec{r})}) \rangle_{cell}$ where $\Delta \phi_{(\vec{r})}$ is the local phase difference

² This expression comes from $E_{2D} = \int d^2x C_2 \left(\left(\frac{\partial \varepsilon_x}{\partial x} \right)^2 + \left(\frac{\partial \varepsilon_x}{\partial y} \right)^2 \right)$ [21] where ε_x is the vortex displacement, here chosen along x (Fig. 4.4). Both derivatives are of order $\frac{\partial \varepsilon_x}{\partial x} \approx \frac{\partial \varepsilon_x}{\partial y} \approx \frac{\Delta x}{\ell}$, and integration is over one unit cell of area $\sim \ell^2$.

between adjacent optical lattice sites, and $\langle \dots \rangle_{cell}$ is a spatial average over one vortex lattice unit cell. Numerically we find $E_{ax} \approx (J/N_v) \times 1.8\Delta x^2/\ell^2$, where ℓ is the size of the vortex lattice unit cell, Eq. (1.23). Equipartition tells us that there should be an amount $k_B T$ of thermal energy ($k_B T/2$ kinetic and potential energy) available for this one degree of freedom of the vortex lattice, i.e. $k_B T = E_{ax} + E_{2D}$, resulting in a prediction for the average vortex displacements:

$$\frac{\Delta x^2}{\ell^2} = \frac{k_B T}{2C_2 \ell^2 + 1.8J/N_v} \quad (4.3)$$

with $\ell^2 = \hbar/(m\Omega)$, $C_2 = n_{SF,2D}\hbar\Omega/8$ for our parameter regime [50]. Using the 2D vortex lattice melting temperature $T_{M,BKT}$, Eq. (D.15), we can rewrite this in the more meaningful form

$$\frac{\Delta x^2}{\ell^2} = \frac{k_B T}{2\sqrt{3}T_{M,BKT} + 1.8J/N_v} \quad (4.4)$$

This prediction is plotted in Fig. 4.4 for the expected range of condensate temperatures ($T = (35 - 100) nK$) in the optical lattice. An ordered lattice will melt as soon as the mean-square displacements exceed a fraction of the lattice constant $\Delta x \sim 0.28\ell$ (the Lindemann criterion, see e.g. [21]), which occurs in Fig. 4.4 between $V_{OL} = (15 - 20) E_r$ lattice depth³. The dashed lines in Fig. 4.4 are obtained by setting $T_{M,BKT} = 0$, or equivalently $C_2 = 0$, showing that, as long as $T > T_{M,BKT}$ as in our experiments, the precise value of the in-plane energy cost does not significantly influence the vortex lattice melting condition.

Once the 2D vortex lattices have melted in our system, we also expect position correlations between vortices in adjacent pancakes to get lost due to *axial* decoherence across the lattice: Even if some degree of position correlation between vortices in different sites remains in the vortex liquid, it is now very clearly the Josephson coupling *per vortex*, J/N_v , that competes with $k_B T$ for axial coherence, and as Fig. 4.3 shows, J/N_v

³ To check our model we also apply it to an isolated 2D pancake ($J = 0$). With $\frac{\Delta x^2}{\ell^2} = \frac{k_B T}{2\sqrt{3}T_{M,BKT}}$ and the Lindemann criterion we obtain a condition for vortex lattice melting, $T/T_{M,BKT} \approx 0.3$, close to the expected value of unity.

approaches T for $V_{OL} = (15 - 20) E_r$, i.e. as soon as the 2D vortex lattices have melted. Once axial coherence is lost, there is no incentive for vortices in different optical lattice sites to remain locked together.

We expect the prediction of this two-site model for the 3D-2D crossover to carry over to the full optical lattice system in a way similar to the double-well physics correctly predicting the approximate conditions for the BKT transition in a 2D Josephson junction array.

In summary, raising an optical lattice in the axial dimension induces confinement of rotating BECs to the two-dimensional lattice sites. Upon further reduction of the Josephson coupling between lattice sites, phase fluctuations develop in the vortex lattices on each site. On the other hand, the developing phase fluctuations in the 2D plane act to *enhance* the decoherence between lattice sites. Once the 2D pancakes are sufficiently isolated from each other, in our system with temperatures T larger than the vortex lattice melting temperature $T_{M,BKT}$, the vortex lattice is certainly expected to melt. Vortices on adjacent optical lattice sites act independently, and the 3D-2D crossover is complete. It is thus the competition between $k_B T$ and J/N_v that ultimately decides on both the 2D vortex lattice melting and the 3D-2D crossover. Similar physics (but without rotation of the condensate, instead with 2D fluctuations arising from the BKT transition of the *static* 2D superfluids) was investigated experimentally in Kasevich's group [91], and was studied theoretically by Giamarchi and coworkers [38].

4.1.2 Setup and alignment

The experimental setup is shown in Fig. 4.5. The light source for the optical lattice is a power amplifier seeded by an external cavity diode laser (ECDL) at 852 nm ⁴. This system delivers 130 mW of light through a single-mode fiber. The optical

⁴ The amplifier chip was designed for 830 nm , but an available master laser diode and easy locking to the ^{133}Cs line at 852 nm made us decide for 852 nm ; the amplifier gain at 852 nm is reduced by $1/2$, but is sufficient for our purposes

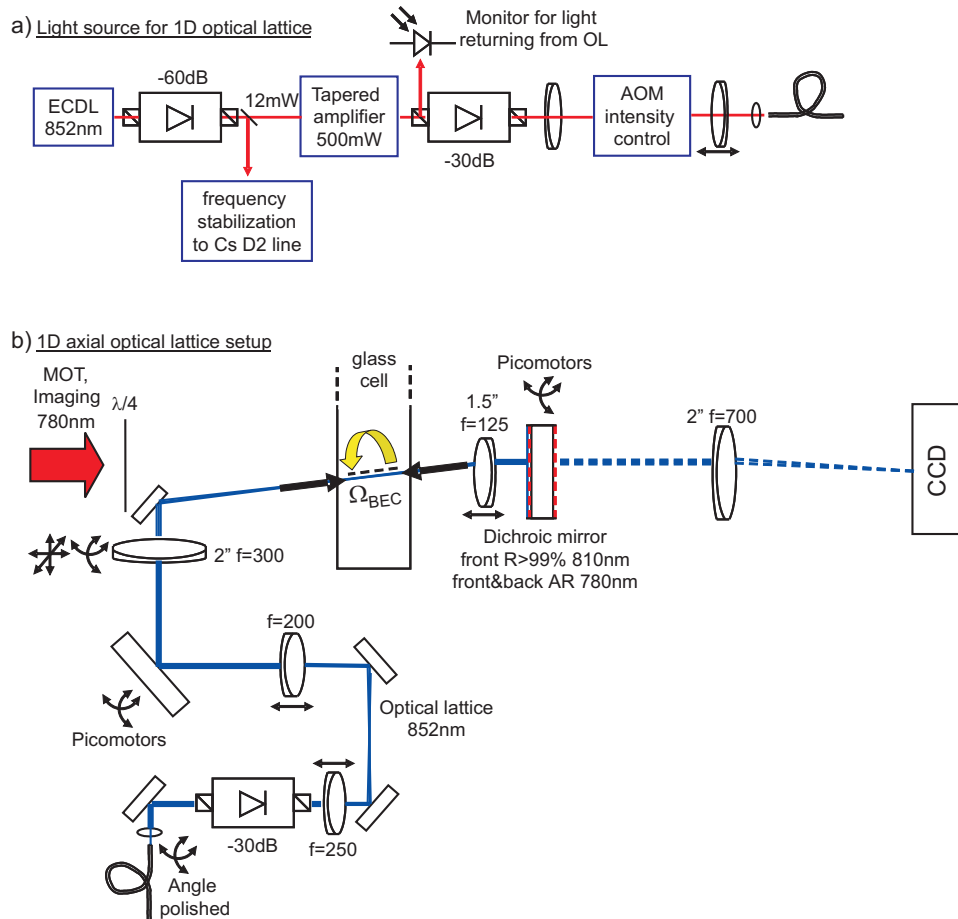


Figure 4.5: (a) Light Source for the 1D optical lattice at 852 nm . An external cavity diode laser (ECDL), frequency locked to the D2 transition of ^{133}Cs at 852 nm , seeds a tapered amplifier chip. The light is intensity controlled by an acousto-optical modulator (AOM) and sent to the experiment via single-mode fiber. Optical isolators prevent frequency noise caused by optical feedback to the ECDL. (b) Lattice setup. The optical lattice light is focused and noncollinearly combined with MOT and imaging beams. A dichroic mirror retroreflects the lattice light onto the BEC where the optical lattice is formed, parallel to the BEC rotation axis Ω_{BEC} .

lattice beam path, depicted in Fig. 4.5(b), is set up $\approx 1''$ above the optical table to achieve maximum immunity to vibrations. A -30 dB optical isolator is inserted to prevent a cavity effect between the fiber output and the retroreflecting mirror. We tried several options of combining optical lattice and MOT beam path using various polarizing beamsplitter cubes (PBS), but found significantly reduced perturbation of rotating BECs using a noncollinear geometry without PBS, as shown in Fig. 4.5(b).

This setup in addition removes the quarter wave plate for the MOT from the lattice beam path. The incoming lattice beam is focused to a $1/e^2$ beam waist of $128\ \mu\text{m}$ on the BEC, and retroreflected by a dichroic mirror.

The initial lattice alignment is performed in the following steps: We first focus the incoming lattice beam longitudinally (and of course transversely) onto the BEC, by maximizing the aspect ratio R_z/R_ρ of static BECs loaded into a single beam dipole trap along the z -axis. The retroreflected beam is then overlapped with the incoming beam by maximizing the power propagating back through the beam delivery fiber (we monitor the light rejected by the optical isolator close to the fiber on the laser source side in Fig. 4.5(a)). This step allows optimization of both longitudinal and transverse beam overlap. A last fine adjustment of longitudinal overlap is done monitoring the BEC aspect ratio when loaded into the lattice. Day-to-day alignment involves only transverse beam overlap.

4.2 Initial optical lattice characterization with a static BEC

Before attempting to load a rotating BEC into the optical lattice, we conducted a careful study of the optical lattice using *static* condensates. The goal of these studies was (a) to make sure that our understanding of the optical lattice depth based on Eq. (A.2) was in agreement with experimental results, (b) to verify a procedure for adiabatically loading BECs into the lattice, and (c) to ensure that the optical lattice quality was sufficient to avoid heating effects beyond the unavoidable photon scattering.

4.2.1 Optical lattice depth determination from matter wave diffraction

As in the studies of the BKT transition, the precise knowledge of the optical lattice depth is essential for accurate knowledge of the site-to-site tunnel coupling. The modulation contrast of the interference pattern creating the optical lattice is the largest uncertainty. It depends crucially on longitudinal and transverse overlap of the the

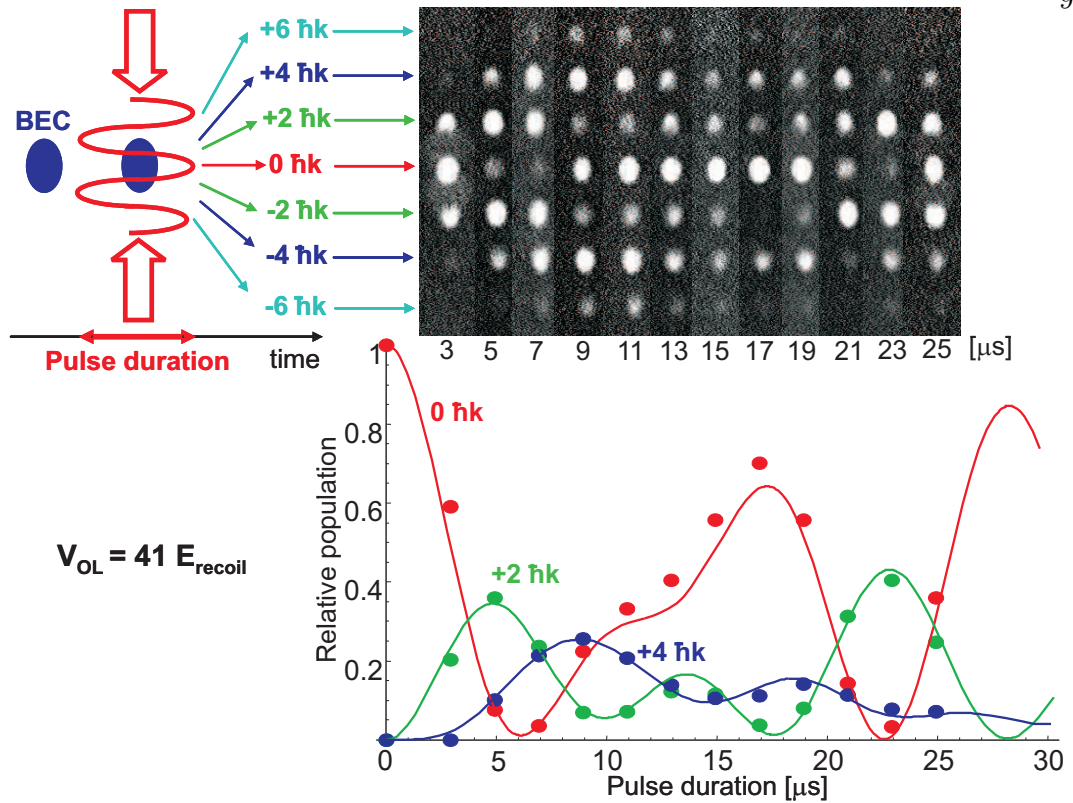


Figure 4.6: Characterization of 1D optical lattice depth by matter wave diffraction. Upper left: schematic of the experiment. A 1D optical lattice is pulsed on briefly, causing the BEC to diffract into discrete momentum components corresponding to transfer of a number N_p of photons (of momentum $\hbar k$) from one lattice beam to the other, imparting momentum $2N_p\hbar k$ to the BEC. Population of the momentum components depends on lattice depth. Upper right: resulting matter wave diffraction pattern vs. pulse duration. Bottom: extracted relative population of momentum components (symbols) vs. pulse duration, and calculation following Ref. [51] using the lattice depth $V_{OL} = 41E_r$ calculated from independent measurements of beam waist and laser power.

incoming and retroreflected beams. In addition, the retroreflected beam intensity is attenuated by $\approx 20\%$ due to losses in the beam path. Fortunately, the optical lattice depth can be measured precisely by pulsing on the lattice for very short amounts of time, and recording the resulting matter-wave diffraction pattern as a function of pulse duration for fixed intensity (or as a function of intensity at fixed pulse duration) [116, 51]. The result of such a measurement and a calculation following Ref. [51] is shown in Fig. 4.6. The theoretical curve is obtained without free parameters – we use the optical lattice

depth calculated from independently measured optical power and beam waist. The agreement between theory and experiment is very good, confirming the good alignment of lattice beams and our understanding of the optical dipole potential, Eq. (A.2).

4.2.2 Bloch oscillations as a probe of phase coherence in the lattice

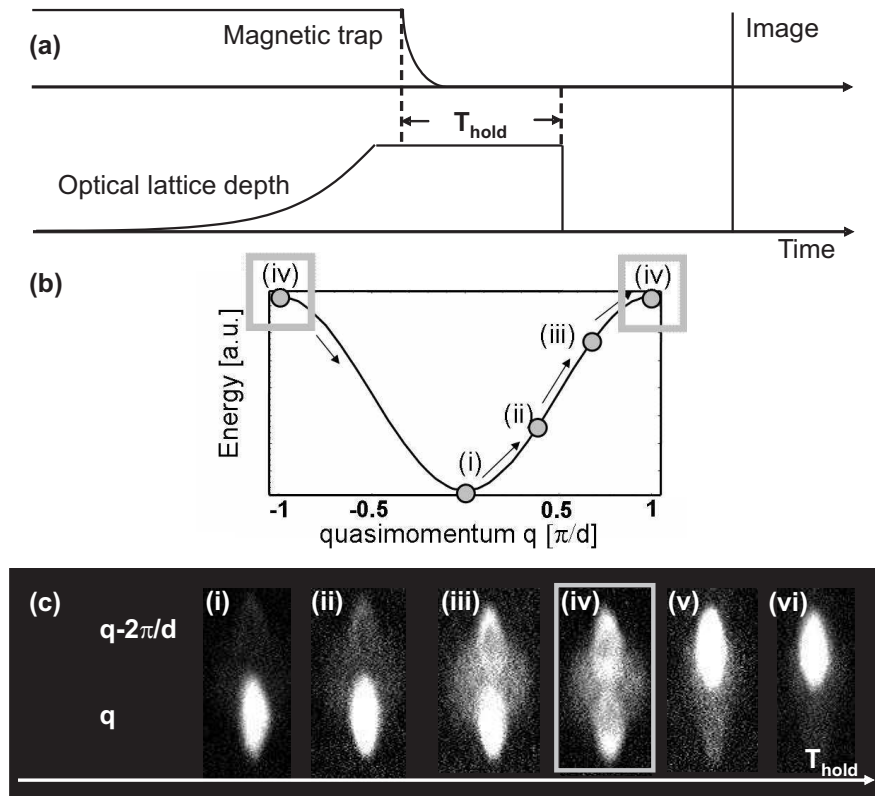


Figure 4.7: Bloch oscillations of a static, phase coherent BEC in an optical lattice. (a) time sequence: A BEC is loaded adiabatically (250 ms ramp time) into the optical lattice; the magnetic trap is turned off while the lattice remains on. The BEC accelerates under the influence of gravity, causing its narrow momentum wavepacket to traverse the optical lattice's Brillouin zone (BZ) (b), following $q(t) = \frac{mg}{h}t$. Upon reaching the BZ edge $q = \pi/d$, the wavepacket is briefly split into two by Bragg reflection ($q = \pm\pi/d$), before completely reflecting to $q = -\pi/d$, and repeating the oscillation. (c) Momentum images of BECs released from the optical lattice at various times T_{hold} during the Bloch oscillation (see associated labels in (b)). These momentum images are obtained by suddenly switching off the lattice and imaging the cloud after 14 ms expansion. (iv) is at the edge of the BZ – this timing is used in the following figures.

The previous matter wave diffraction experiment involves an extremely short

pulse of optical lattice light and hence tells us nothing about long-term heating and decoherence effects in the lattice. On the other hand, the final goal here is to load BECs into optical lattices adiabatically. In this adiabatic case, phase coherence may be destroyed either by technical fluctuations in the lattice potential, or by fundamental quantum or thermal fluctuations. In order to test for such effects, we adiabatically (250 *ms* intensity ramp time) load static BECs into the optical lattice and employ Bloch oscillations (see e.g. [108]) as a probe of phase coherence across the resulting array of mini-condensates. Figure 4.7 explains the basic physics of Bloch oscillations. In the following we concentrate on condensates released from the lattice after half a Bloch oscillation, i.e. split into two momentum components at the edge of the optical lattice's Brillouin zone, as shown in Fig. 4.7(c)(iv). Phase decoherence across the optical lattice is signalled by blurring, and eventually merging, of these two momentum components.

Figure 4.8 shows condensates released from the edge of the Brillouin zone, with increasing optical lattice depth. In our case of a fairly large BEC ($N_{BEC} \approx 1.1 \times 10^6$ for these experiments) it is difficult to disentangle several effects occurring simultaneously: (a) s-wave scattering between the two momentum components released from the lattice, e.g. visible in Fig. 4.8 at $V_{OL} = 5.5 E_r$ as a diffuse cloud centered between the two momentum components, (b) additional mean field effects in the lattice seen e.g. in Ref. [108], increasing the complexity of the Bloch oscillation pattern, and (c) dephasing of the array due to thermal [123] (or possibly quantum [115]) effects. Our results are in good qualitative agreement with earlier results obtained e.g. in Kasevich's group [115]. Significant technical decoherence effects can thus be ruled out. However due to the above-mentioned difficulties we did not attempt to push these experiments towards a quantitative understanding. It must however be clarified that the blurring of the density distributions in Bloch oscillation images in Fig. 4.8 is *NOT* due to strong heating: (a) the energy released in the horizontal direction for the cloud at $V_{OL} = 48.5 E_r$ can be converted to a temperature assuming the cloud is uncondensed. We obtain $T = 76 nK$.

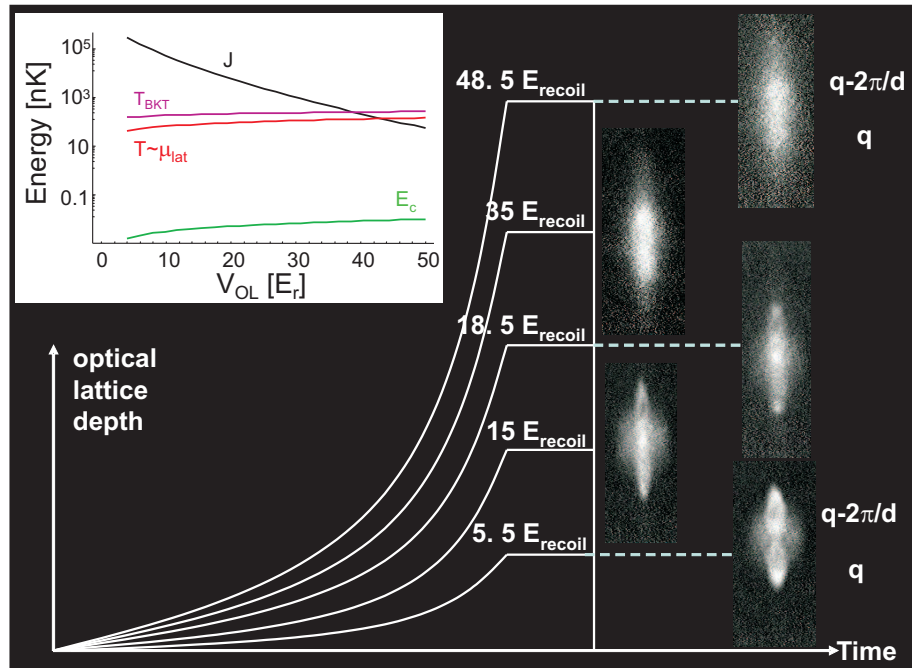


Figure 4.8: Bloch oscillations of a non-rotating BEC show loss of phase coherence. At $V_{OL} = 5.5 E_r$ two clearly separated momentum components are visible. With increasing lattice depth, the components blur out and merge, partly due to phase decoherence, partly due to axial spreading of the BECs due to lattice-enhanced mean field repulsion. Blurring of the density distributions is *NOT* due to strong heating, see text. Inset: For a static BEC, the temperature $T \approx \mu_{lat}$ (red) remains smaller than the static BKT temperature of 2D BECs on each lattice site T_{BKT} (magenta) – in contrast to rotating BECs, large in-plane fluctuations are not expected. Axial coherence is governed by competition between J (black) and T (red).

The ideal-gas BEC transition temperature for the 2D pancakes is much higher, $T_c = 218 nK$, confirming the sample must be largely condensed. Also a hypothetical BKT transition of the 2D BECs is not expected, as $T_{BKT} \approx 200 nK$ (Eq. (1.31)). (b) an in-situ image of the BEC in-lattice at $V_{OL} = 48.5 E_r$ shows no bimodal distribution. Fitting a zero-temperature Thomas-Fermi profile gives a condensate radius within 20% of the expectation from Section 1.5.4. Fitting a thermal cloud profile gives a temperature $T = 85 nK$, similar to the result from release energy, and much lower than T_c . (c) we have loaded static BECs into $V_{OL} = 41 E_r$ deep lattices and adiabatically released them back to the magnetic trap, with no significant heating.

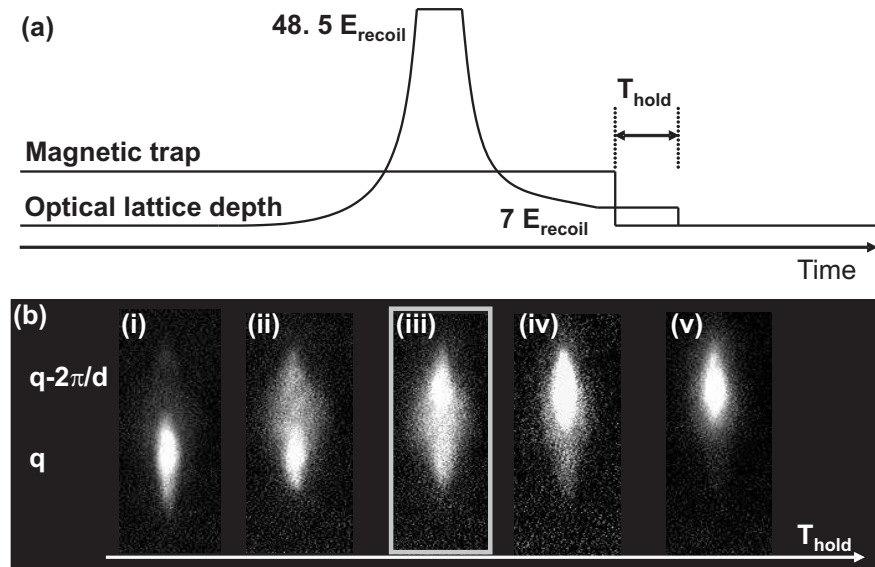


Figure 4.9: Revival of phase coherence of a non-rotating BEC after optical lattice ramp to $V_{OL} = 48.5E_r$, 10 ms hold, and return to $V_{OL} = 7E_r$, followed by half a Bloch oscillation. This experiment proves the absence of strong technical sources of decoherence.

A final test for the adiabaticity of the loading process and the amount of irreversible decoherence mechanisms is the ability to recover phase coherent Bloch oscillations after ramping the optical lattice intensity slowly up (over 250 ms), and then back to a low lattice depth. Results are shown in Fig. 4.9. The optical lattice is ramped up to $V_{OL} = 48.5E_r$ and then down to $V_{OL} = 7E_r$, where a significant coherent fraction of atoms undergoing Bloch oscillations is recovered, further confirming the absence of strong technical sources of decoherence.

4.3 Results: Rapidly rotating Bose-Einstein condensates in a 1D optical lattice

The following first results on rotating BECs loaded into an optical lattice fall into three categories:

- First, even under optimized conditions, we observe a spin-down of rotating condensates loaded adiabatically into an axial optical lattice. The reason for

this spin-down is suspected to be of technical nature.

- Second, we observe a loss of *visibility* of the vortices in expansion images, when integrated over the full 1D lattice. This loss of visibility is indicative of the breaking up of vortex lines of the bulk BEC into pancake vortices in individual layers. The driving force for the loss of register between pancakes may well be the thermal fluctuations in the two-dimensional vortex lattices, as described in Section 4.1.1, with the caveat that we cannot definitively exclude technical reasons as well.
- Third, before even being able to observe the above effects, we encountered and solved various technical difficulties unique to the process of loading rotating BECs into an axial optical lattice.

For most results, I quote the *single-particle tunneling element* t , as opposed to the full Josephson coupling $J = N_{well} \times t$, or the Josephson coupling per vortex lattice unit cell J/N_v . For almost all experiments however, $N_{well} = (1 - 2) \times 10^4$ and $N_v \approx 50 - 150$.

4.3.1 Spin-down of the rotating BEC in the optical lattice

Although the spin-down of rotating condensates in an axial optical lattice is likely of technical nature, we give details of our results here, as this is completely unexplored territory. The optical lattice intensity ramp used in the experiments in this section is a roughly exponential 250 *ms* long ramp-up, followed by a specified “hold-time”, and a mirror-symmetric ramp-down back to the magnetic trap.

When loading a rotating BEC into the optical lattice, a decay of vortices from the condensate is observed, roughly exponential with increasing optical lattice hold time (Fig. 4.10). From experiments at different optical lattice depths we find that the $1/e$ vortex decay time scale τ_{vortex} decreases approximately inversely proportional to the lattice depth, $\tau_{vortex} \approx 4 \text{ s}/(V_{OL}/E_r)$. From experiments with different initial vortex

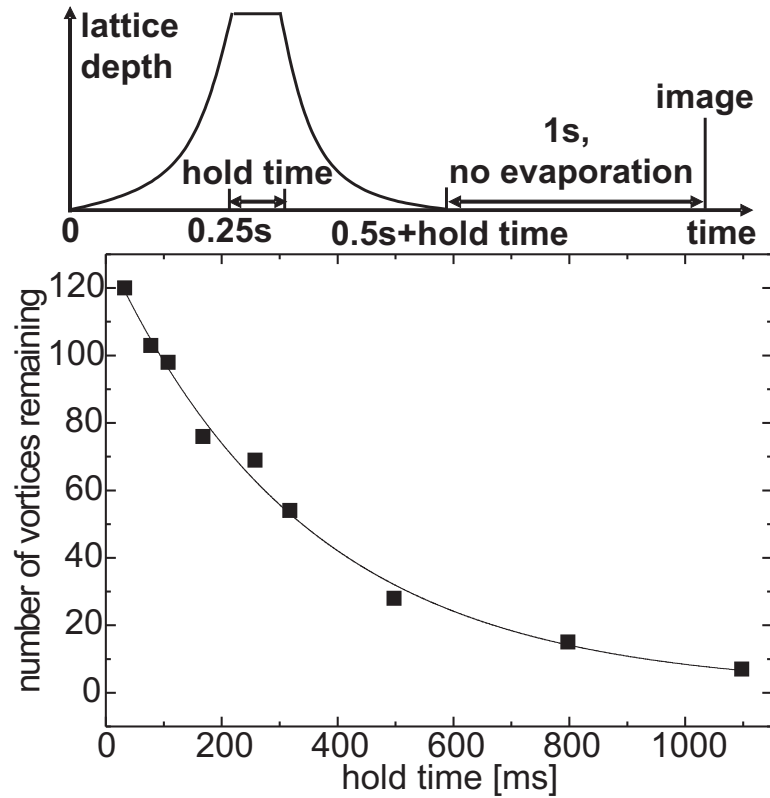


Figure 4.10: A rotating BEC is loaded into a $V_{OL} = 10 E_r$ deep optical lattice, held for a variable time, and released back to the magnetic trap. The remaining vortex number shows exponential decay with hold time. One radial trap period, which is the timescale of vortex lattice rotation, is 30 ms .

number at fixed lattice depth we find the decay timescale to be roughly independent of initial vortex number.

For our typical optical lattice loading procedure, this vortex decay means that we can load a rotating BEC, initially containing a vortex lattice with 150 vortices, into a $V_{OL} = 41 E_r$ deep lattice and back to the magnetic trap, with $\approx 40 - 50$ vortices remaining, as shown in Fig. 4.11. Under the conditions of $V_{OL} = 41 E_r$, $J/N_v \approx 2 nK$, i.e. at typical temperatures of $(50 - 100) nK$ the system is way beyond the expected vortex lattice melting and loss of axial phase coherence (Section 4.1.1). As a side note, we also find that after a lattice hold time of 1.5 s at $V_{OL} = 20 E_r$, repeatedly one single remaining vortex is observed, a good starting place for single-vortex experiments.

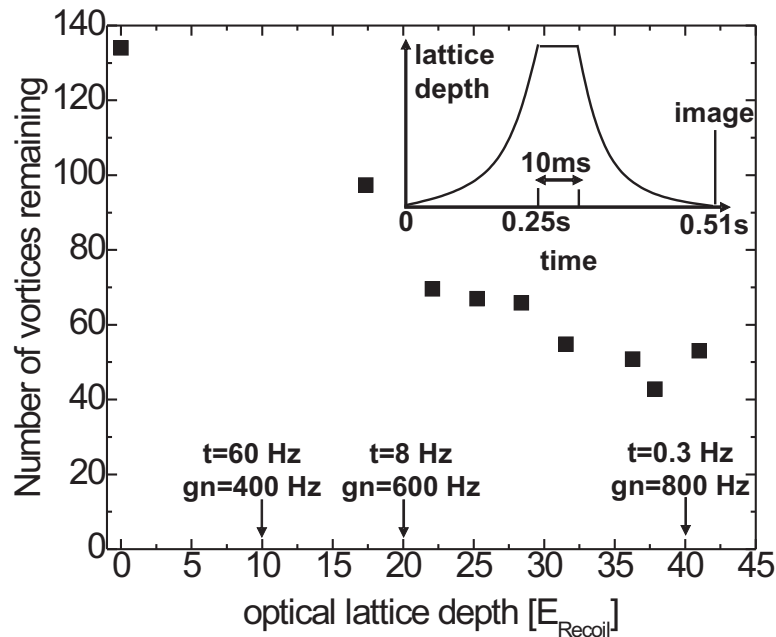


Figure 4.11: Number of vortices surviving adiabatic ramp to the given optical lattice depth and back to the magnetic trap. Inset: time sequence – the optical lattice is ramped up over 250 *ms*, held for 10 *ms*, ramped back down over 250 *ms*, and an in-situ image is taken. Vortex number is calculated from BEC number and rotation rate. Single-particle tunneling rates t and BEC chemical potential gn are indicated.

From experiments with varying initial condensate temperature T/T_c , shown in Fig. 4.12, we find that the vortex number decay (i.e. rotation loss of the BEC) speeds up with increasing T/T_c . For these experiments, the initial rotation rate is kept constant while varying T/T_c (initial rotation rate and T/T_c are measured from a first in-situ image in the magnetic trap). The finite- T rotating BEC is then loaded into an optical lattice of $V_{OL} = 9.5 E_r$ depth, and adiabatically released back to the magnetic trap, where its final rotation rate is measured from a second in-situ image. In Fig. 4.12(b), measured initial and final rotation rates are shown, revealing a clearly enhanced loss of rotation for $T/T_c \gtrsim 0.3$, while rotation loss is negligible for cold BECs at this lattice depth. These results indicate that interactions of the rotating condensate with its thermal cloud contribute to the condensate's spin-down, but do certainly not exclude additional effects unrelated to the thermal cloud. The results however point to the necessity of an

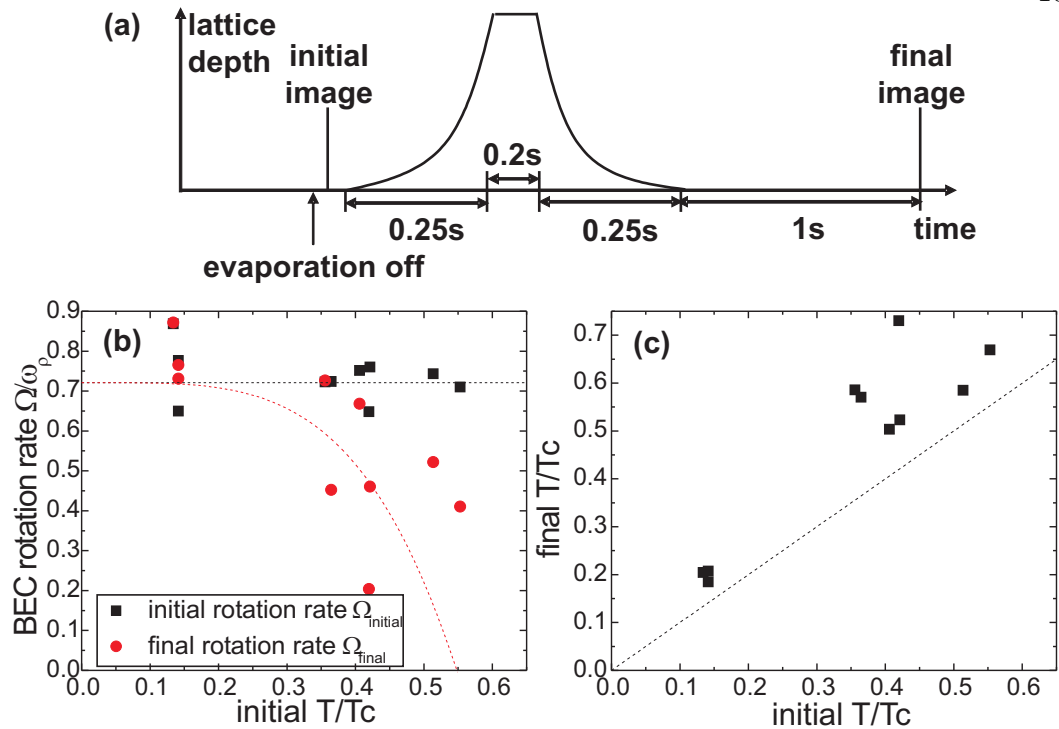


Figure 4.12: BEC rotation rate decay vs. initial T/T_c at fixed optical lattice depth $V_{OL} = 9.5E_r$. (a) time sequence. (b) initial and final BEC rotation rate vs. initial T/T_c showing increased loss of rotation with increasing T/T_c . Lines are guides to the eye. (c) final T/T_c vs. initial T/T_c . The dashed line corresponds to no heating.

efficient cooling scheme applicable to BECs inside the optical lattice.

4.3.2 Loss of vortex lattice visibility in the optical lattice

While the reason for condensate spin-down is likely technical, its timescale can be much longer than the timescale for the loss of *vortex visibility* discussed in this section, allowing the separate study of this likely more fundamental process.

The optical lattice intensity ramp for experiments in this section is a roughly exponential, 190 *ms* long ramp-up, followed by a specified “hold-time”. For most experiments, the optical lattice and magnetic trap are then turned off abruptly and simultaneously as shown in Fig. 4.13(a). This causes all 2D condensates from individual lattice sites to recombine, followed by rapid radial expansion of the combined bulk condensate.

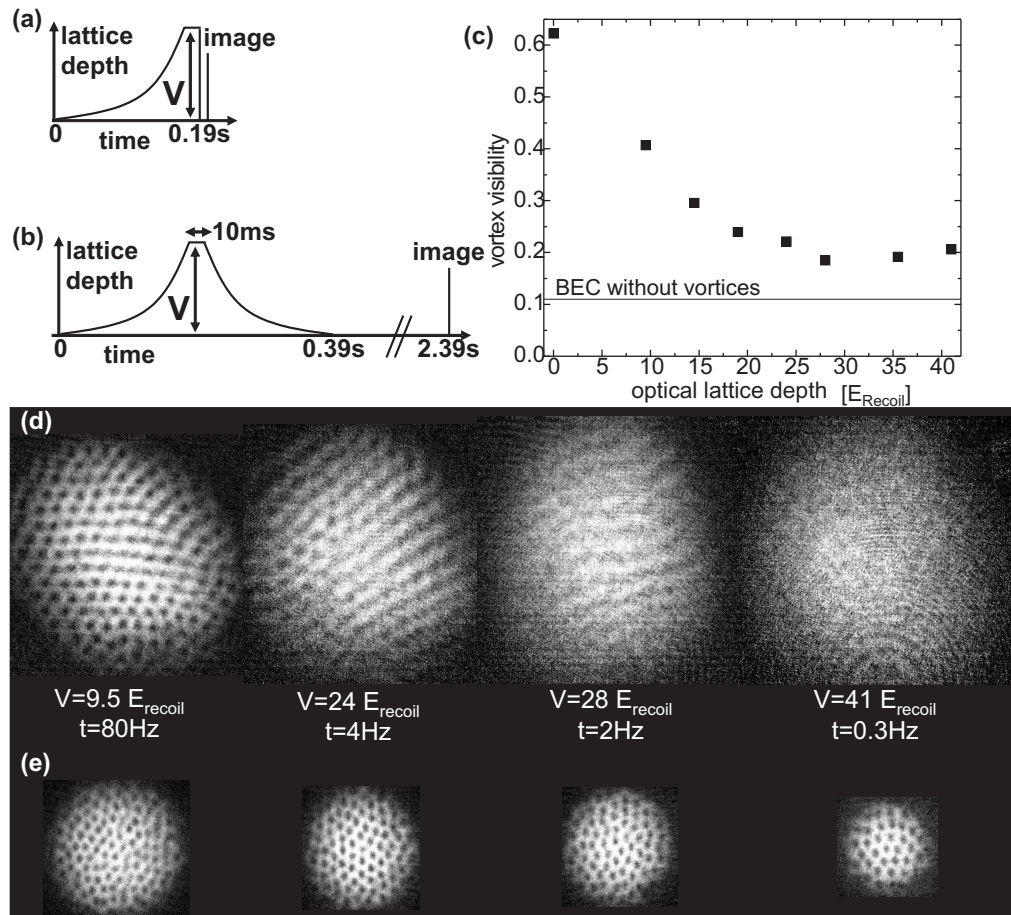


Figure 4.13: Vortex lattice visibility vs. optical lattice depth. (a) time sequence for results shown in (d). Rotating BECs are loaded adiabatically into the optical lattice. For imaging of vortex lattices inside the optical lattice, the optical lattice is turned off abruptly. The released 2D pancake BECs recombine and expand before the image is taken. (b) time sequence for results in (e). Here the optical lattice is ramped down adiabatically, to smoothly recombine vortices. A 2s wait time in the magnetic trap is inserted to allow vortices to straighten up after rampdown. (c) sample-averaged vortex visibility extracted from data in (d). Results in (d), (e) show a complete loss of vortex visibility in the optical lattice above $V_{OL} = 28E_r$, while BECs returned to the magnetic trap show that large numbers of vortices are still present.

A destructive image is then taken, showing the full recombined condensate in the plane perpendicular to the optical lattice axis. For control experiments, where indicated, a 190 ms exponential optical lattice ramp-down back to the magnetic trap is employed and images are taken after an additional specified wait time in the magnetic trap.

Figure 4.13(d) shows images of vortex lattices loaded into optical lattices of in-

creasing depth, and then abruptly released. At low lattice depths, e.g. $V_{OL} = 9.5 E_r$ in Fig. 4.13(d), a vortex lattice is clearly visible, albeit somewhat distorted, either by excitations resulting from the optical lattice loading procedure, or possibly by long-wavelength thermal fluctuations. With increasing optical lattice depth, vortex visibility gradually degrades until it is fully lost. A sceptic might suspect that e.g. for the image at $V_{OL} = 41 E_r$ the condensate was heated above the condensation temperature, and what we observe is a normal cloud. The control experiment in Fig. 4.13(e) however reveals that, when adiabatically released into the magnetic trap, a rotating condensate with a significant remaining vortex lattice is obtained.

For the 190 ms lattice intensity ramps employed in both Fig. 4.13 and Fig. 4.14, the vortex lattice initially retains some visibility up to $V_{OL} \approx 30 E_r$. For $V_{OL} \gtrsim 15 E_r$ however this visibility then decays with time, as shown for $V_{OL} = 20 E_r$ in Fig. 4.14(a), lower panel. Figure 4.14(b) shows the time constant for vortex *visibility* loss (black symbols), versus the single-particle tunneling rate t . The timescale for the vortex visibility loss scales with t , indicating that the underlying reason is not an in-plane process but associated with the weakening tunnel coupling. This appears consistent with our model for vortex lattice melting in the 3D-2D crossover which is governed by the competition between T and J/N_v , as described in Section 4.1.1. Also shown in Fig. 4.14(b) is the timescale for vortex *number* loss (red symbols). The dependencies of *vortex visibility loss* and *vortex number loss* are markedly different, so that it appears that these two effects have different origins. Specifically, below $t \lesssim 30 Hz$ (i.e. $V_{OL} \gtrsim 15 E_r$) vortex *visibility* is lost much faster than vortex *number*, allowing vortex visibility to be studied relatively undisturbed from condensate spin-down.

Loss of vortex visibility *under equilibrium conditions* occurs around $V_{OL} \approx 15 E_r$: For lower lattice depth, some degree of vortex visibility remains at all times, indicating that some degree of phase coherence across the whole optical lattice is preserved, while for deeper lattices vortex visibility is lost after some equilibration time. We compare

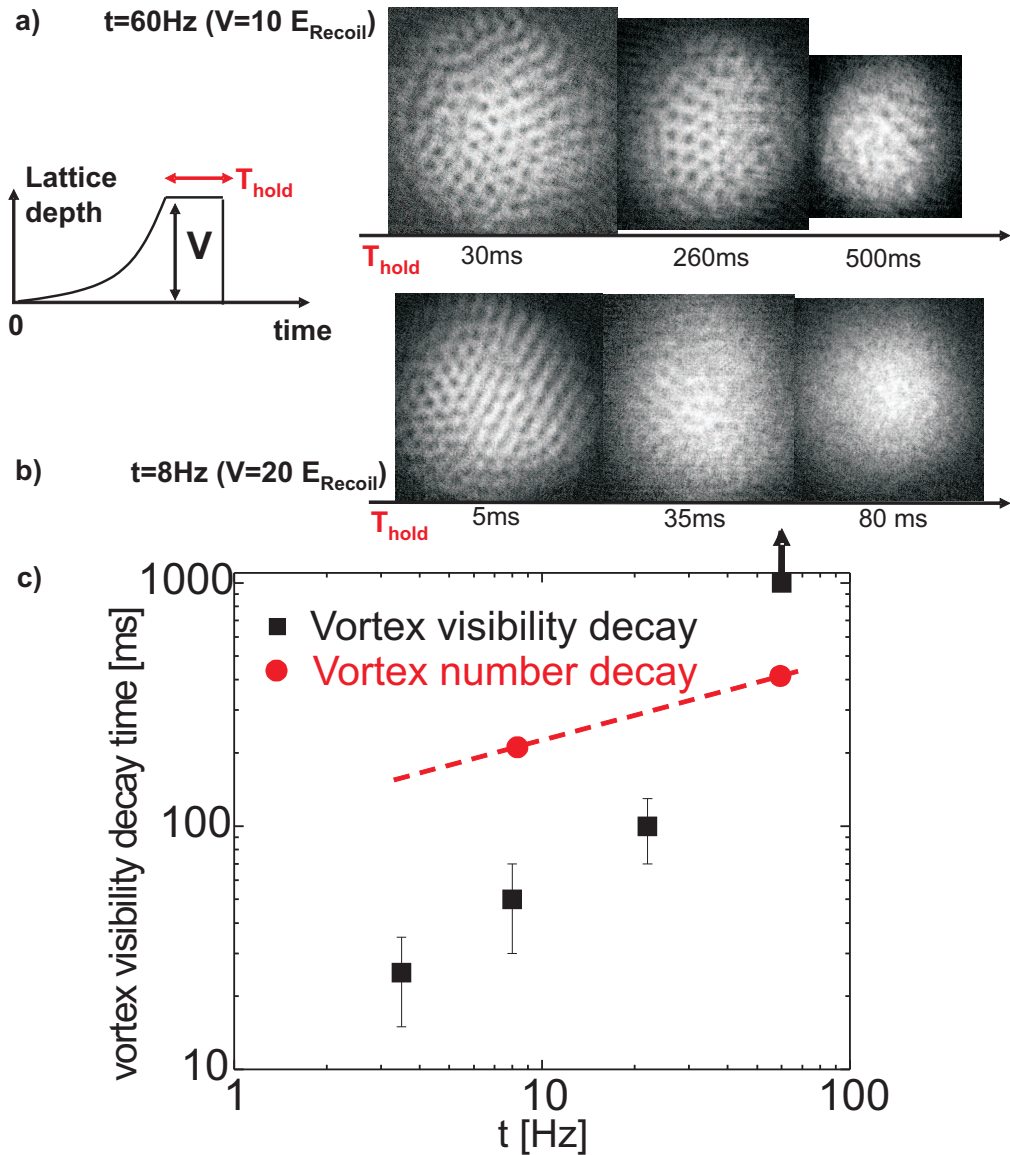


Figure 4.14: Vortex lattice visibility decay time vs. J . (a),(b) rotating BECs are loaded adiabatically into optical lattices, and the hold time is varied. Vortex lattice images after abrupt optical lattice turn-off show time-dependent loss of vortex visibility. Data are shown for weak (a) $V_{OL} = 10 E_r$, and moderately strong (b) $V_{OL} = 20 E_r$ lattice. (c) extracted timescale for loss of vortex *visibility* vs. tunneling strength t (black squares). For $t \gtrsim 60 \text{ Hz}$ vortices remain visible at all times (data point at $t = 60 \text{ Hz}$ is a lower limit on vortex visibility decay time). Red symbols: timescale for vortex *number* decay shows a markedly different behavior than timescale for *visibility* decay. Importantly, for low t (high V_{OL}) visibility is lost much faster than vortex number, allowing us to separately study the two processes.

the conditions around $V_{OL} \approx 15 E_r$ in these experiments, to the expected conditions for

vortex lattice melting and the 3D-2D crossover (see the discussion around Eq. (4.4)): We have $t \approx 30 \text{ Hz}$, $N_{well} \approx 16000$ and $N_v \approx 100$, resulting in $J/N_v \approx 230 \text{ nK}$. The chemical potential is $\mu_{lat} \approx 35 \text{ nK}$ resulting in an estimate for the temperature of $T \approx (35 - 50) \text{ nK}$. According to Eq. (4.4) this results in $\Delta x/\ell \approx 0.14 - 0.2$, very close to the Lindemann condition for vortex lattice melting $\Delta x/\ell|_{melt} \approx 0.28$ (melting according to Eq. (4.4) would be expected around $V_{OL} = (17 - 19) E_r$). We therefore speculate that the observed loss of vortex visibility is directly related to thermally activated in-plane vortex lattice melting and the resulting 3D-2D crossover, in which position correlations between vortices in different lattice sites are lost.

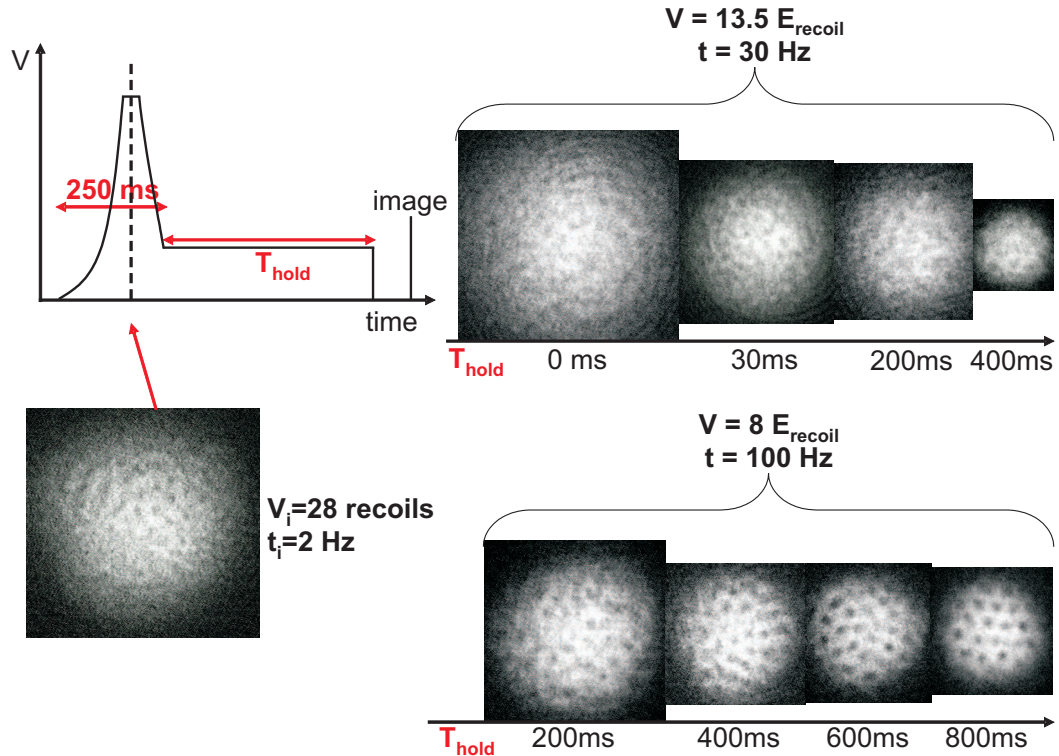


Figure 4.15: Vortex lattice visibility can be destroyed and restored in an optical lattice. Upper left: The lattice is initially ramped to ($V_{OL} = 28E_r$), where vortex visibility is lost (lower left). Visibility is restored upon ramping the lattice depth down to ($V_{OL} = 8E_r$) (lower right), whereas when ramping to ($V_{OL} = 13.5E_r$) it takes much longer to restore and reaches a lower final value.

As a last result, we show that vortex visibility, and even vortex lattice ordering can

be restored *while the BEC remains in the optical lattice*: In Fig. 4.15 the optical lattice is initially ramped to a depth where vortex visibility is fully destroyed. The lattice is then ramped back to a lower depth, and held for a time t_{hold} . When ramping back down to $V_{OL} = 8 E_r$, visibility of vortices is restored after a hold time $t_{hold} \approx 0.5 s$ *while in the optical lattice*. After a longer hold time $t_{hold} \approx 1 s$ even an ordered vortex lattice is observed. When instead ramping back down to $V_{OL} = 13.5 E_r$, just below the conditions for loss of vortex lattice visibility, restoration of vortex visibility is incomplete, indicating the vicinity of vortex lattice melting. This experiment shows that both the locking of pancake vortices in different layers of the optical lattice to a more or less straight vortex line across the full lattice array, as well as positional order in the vortex lattice is not lost irreversibly, but can be restored once the optical lattice is returned to conditions where three-dimensional coherence across the array is expected. This appears to be further proof that the loss of vortex visibility is not due to strong irreversible technical decoherence mechanisms, but is likely of a fundamental nature.

4.3.3 Technical considerations when loading a rotating BEC into a 1D optical lattice

Before being able to observe the results detailed above, we have seen, and largely removed, a host of excitations that are unique to the process of loading a rotating (as opposed to static) BEC into the optical lattice. A quadrupole ($m = -2$) surface mode [55] is excited by slight azimuthal ellipticity of the optical lattice potential, but can be canceled by precise relative position alignment of incident and retroreflected optical lattice beams. Tkachenko modes [44] can be excited by radial anharmonicity of the combined trapping potential of magnetic trap and optical lattice, but can be minimized by choice of a large enough optical lattice beam waist. A scissors mode [39] of the vortex lattice may be excited by symmetry axis misalignment between magnetic trap and optical lattice, but can be avoided by tilting the magnetic trap to align it with the

optical lattice axis.

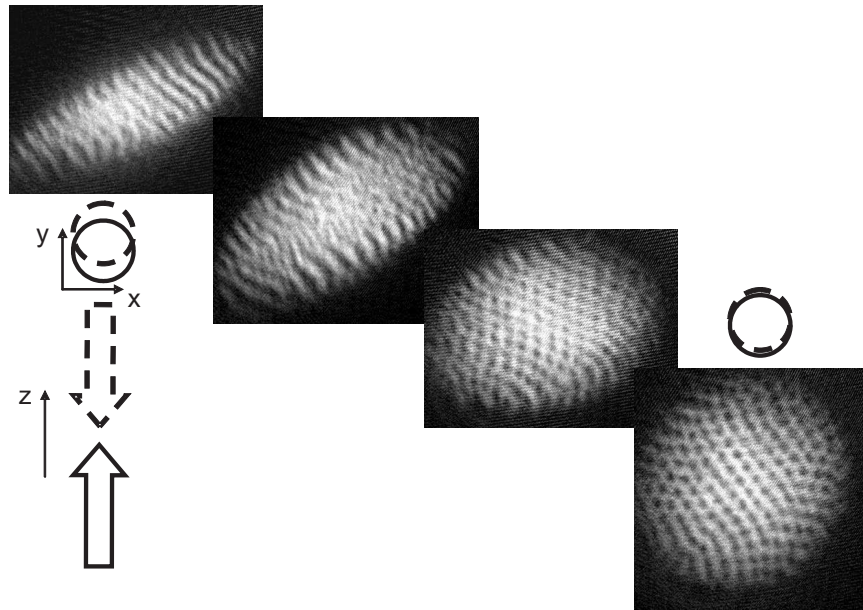


Figure 4.16: $m = -2$ quadrupole surface mode excitation [55] when loading into azimuthally elliptical optical lattice potential, e.g. created by imperfect overlap (left sketch) of incident (solid) and reflected (dashed) lattice beam. This excitation can be cancelled by slight adjustments to the lattice beams' overlap in the xy -plane. Upper left, imperfect overlap, strong excitation; lower right, good overlap, reduced excitation.

Surface waves. The first attempt to load a rapidly rotating lattice is almost guaranteed to end up with the excitation of large-amplitude $m = -2$ quadrupole mode excitation [55], as shown by the large amplitude elliptical deformation of the rotating BEC in Fig. 4.16. Such modes in a rapidly rotating BEC are known to be near-resonantly driven by a static azimuthal ellipticity of the trap potential, and possibly higher-order imperfections of the optical lattice intensity profile. To lowest order, this excitation can be removed by fine-tuning the transverse overlap between incoming and retroreflected lattice beam.

Tkachenko waves excited by anharmonicity. Stringari and coworkers [49] have shown that an anharmonic perturbation to the radial trap potential can excite Tkachenko oscillations. While loading from magnetic trap to optical lattice potential,

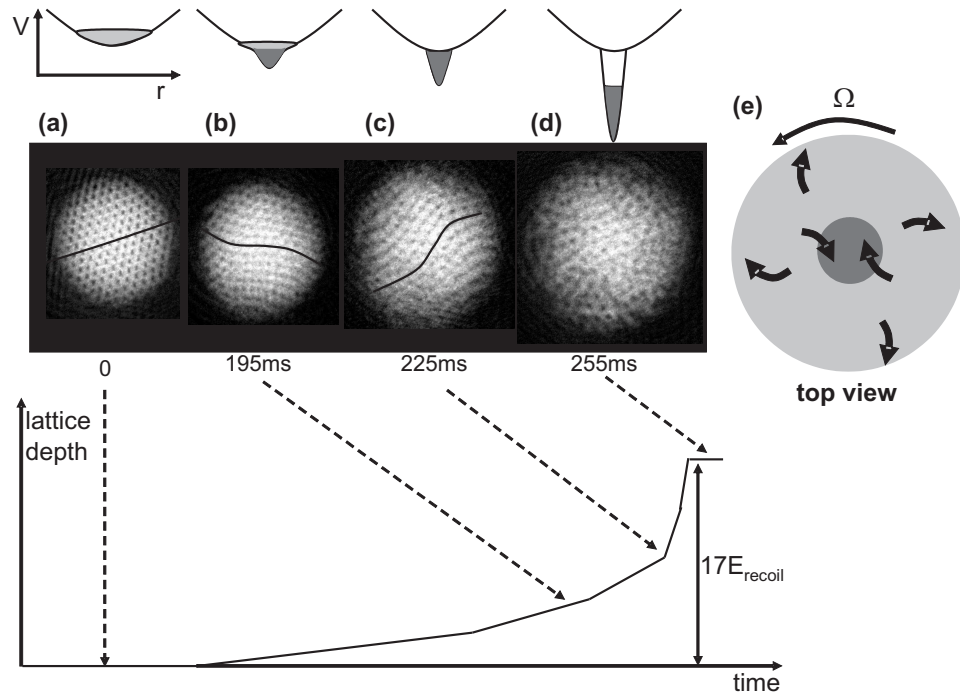


Figure 4.17: Tkachenko mode [44] excitation due to radial anharmonicity [49] when loading a rotating BEC into the optical lattice. (a)-(d) time sequence of images during optical lattice ramp-up showing the growing Tkachenko excitation, and sketches of the BEC (grey) in the combined radial potential formed by optical lattice (narrow dimple) and magnetic trap (sketches not to scale). The optical lattice intensity ramp is shown below. (e) flow pattern of atoms *in the rotating frame* causing Tkachenko oscillation.

the BEC experiences some degree of radial anharmonicity (sketched in Fig. 4.17(a)-(d), not to scale), and the resulting Tkachenko excitation could be observed. This effect was removed by increasing the optical lattice waist, such that the BEC is confined at all times in the harmonic region of the trapping potential, and is also reduced by a slower loading procedure.

Scissors mode due to optical lattice axis-tilt. The optical lattice axis initially was misaligned by a few degrees with respect to the magnetic trap symmetry axis. When the BEC was loaded too rapidly from magnetic trap to optical lattice, a small-amplitude scissors mode [39] was excited. The effect is the same as the result of tipping a spinning top, i.e. a precessing motion of the rotation axis. To mitigate this effect, the axis of the TOP trap was tilted to match up with the optical lattice axis. As

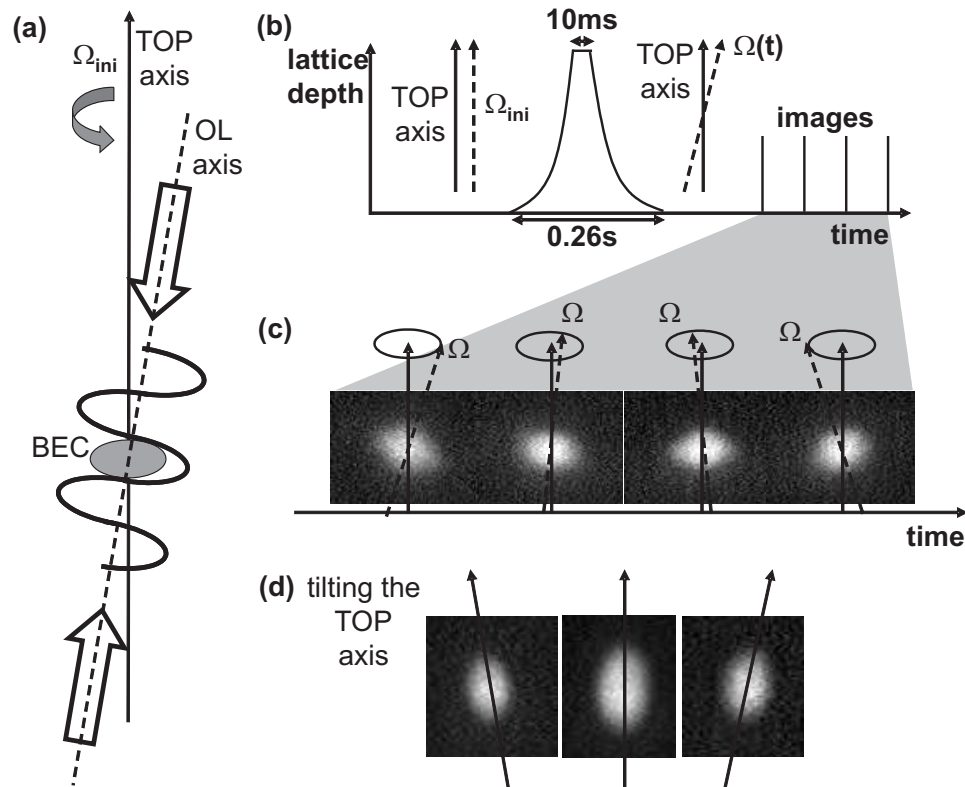


Figure 4.18: Scissors mode excitation due orientation mismatch (a) between magnetic trap and optical lattice. (b) experimental time sequence for observing the scissors mode, induced by transient application of the slightly tilted optical lattice. (c) time sequence of in-situ side-view images showing the precessing motion of the BEC. Excitation of this mode was minimized by tilting the TOP magnetic trap axis which defines the initial rotation axis. (d) images of BECs in tilted TOP traps – the TOP trap axis can be aligned with the optical lattice.

a diagnostic, a large-amplitude scissors mode was excited by loading the rotating BEC rather rapidly into the optical lattice (and releasing it back into the magnetic trap for easier diagnosis), as shown in Fig. 4.18. When the magnetic trap and optical lattice axes are aligned, no scissors mode is observed.

Multiple reflections. Multiple reflections of the optical lattice beam in our cell, which is not antireflection-coated, may interfere (likely non-collinearly) with the main optical lattice beams, causing uncontrolled changes to the interference pattern, including modulations of the potential *in the plane of the optical lattice sites*. These modulations are suspected to act as “speed bumps” to rotating BECs, while leaving

static BECs largely unaffected. This effect may be suspected to be responsible for unexplainable heating and fast spin-down that we observed for certain optical lattice alignments but not for others. This last technical difficulty was avoided by using a large angle of incidence ($\approx 5^\circ$) with respect to the glass cell surfaces. However multi-pass reflections are not fully controlled in this way.

An order of magnitude estimate of the amount of uncontrolled light that can cause trouble is as follows: A perturbation Δ that reaches a significant fraction of the BEC's chemical potential gn would certainly affect the vortex lattice. Interference of the full lattice potential with a perturbing potential V_{pert} leads to a perturbation Δ given by the peak-peak interference modulation of $\frac{\Delta}{V_{OL}} = 4\sqrt{\frac{V_{pert}}{V_{OL}}}$. Assuming V_{pert} to result from a n th order reflection from the glass cell windows (intensity I_n) compared to the single-lattice-beam intensity $I_0 \propto V_{OL}/4$ we have $\frac{\Delta_n}{gn} = 4\sqrt{\frac{I_n}{4I_0} \frac{V_{OL}}{gn}}$. At $V_{OL} = 30 E_r$ the barrier height is $V_{OL} = 4 \mu K$ (see Fig. 4.3), whereas the chemical potential is $gn = 50 nK$, so $\frac{V_{OL}}{gn} = 80$. This results in $\frac{\Delta_1}{gn} = 20$, $\frac{\Delta_2}{gn} = 3$, $\frac{\Delta_3}{gn} = 0.5$ and $\frac{\Delta_4}{gn} = 0.06$ for first, second, third and fourth order reflections, respectively⁵. Geometrically, with ($\approx 5^\circ$) angle of incidence on the glass cell, we are sure up to third order no reflection can hit the BEC, but higher order reflections are not controllable and still could present a significant problem.

4.4 Conclusions and outlook

In this section, we have shown that it is possible to load rapidly rotating BECs into a 1D optical lattice, and to create a stack of rotating 2D BECs. We have observed a loss of vortex visibility in images that are integrated along the rotation axis, through the whole array of 2D rotating condensates. This loss of vortex visibility occurs under conditions where we expect growing thermally activated in-plane vortex lattice fluctua-

⁵ I assume 4% reflection from glass cell windows and take into account beam spreading from the focus (Rayleigh range is 6 cm, roughly equal to the distance a reflected beam travels before returning to the BEC). The intensity I_n is thus $I_n/I_0 = (4 \cdot 10^{-2})^n \times \frac{w_0^2}{w_n^2}$ with the ratio of beam waists $\frac{w_0^2}{w_n^2} = 1/(1+n^2)$.

tions and a resulting 3D-2D crossover, in which position correlations between vortices in different lattice sites are lost. Vortex visibility can in part be reversibly restored when ramping back to lower optical lattice depths, where coherence across the array again creates an effectively 3D system.

In our experiments, the filling factor is $\nu \approx 100$, to our knowledge the lowest value reached to date. This is only a factor ≈ 10 away from the predicted melting of the vortex lattice due to quantum fluctuations and a possible transition to fractional quantum Hall states. To possibly reach this regime, however several technical difficulties will have to be overcome: First, the observed fast spin-down of the vortex lattice has to be slowed down significantly, as the timescales required to reach equilibrium in the fragile vortex lattices of rapidly rotating BECs can be very long. Second, the temperature of condensates has to be reduced significantly, in order to suppress the presently dominant thermal fluctuations, and to prevent thermal excitations of the very fragile fractional quantum Hall states, as discussed in Appendix D. Third, a further fill factor reduction to $\nu \approx 10$ appears feasible.

With our experiments we certainly did not reach a full quantitative understanding of a stack of rotating pancake BECs in an optical lattice. As we suspected from the beginning, the experiments described here had to overcome large technical difficulties, and so the results presented in this chapter are at least in part technical in nature. Nonetheless I think there is promise, especially for further studies of thermal effects on rotating 2D quantum gases.

For future experiments one would certainly like to develop more sophisticated ways of probing the properties of the rotating 2D BEC and vortex lattice *on each lattice site*. The vertical images in this thesis are integrated through the whole array of lattice sites, and can thus not distinguish between long-wavelength vortex excitations and short-range phase fluctuations between sites. Can Bloch oscillations provide complementary information?

In addition, the 3D-2D dimensional crossover deserves further study: How do vortices influence the site-to-site phase coherence of a BEC in an axial optical lattice? Are there connections to work on “large superconductive Josephson junctions” where spatial variations of the phase are important? What is the role of dissipation when “re-connecting” vortices by ramping down the optical lattice? This question also concerns the reconnection of vortices upon sudden optical lattice turn-off employed for imaging of vortex lattices in this chapter.

I am confident that this work was not the last attempt at answering these questions about this interesting system.

Chapter 5

Vortex lattice dynamics in rotating spinor Bose-Einstein condensates

5.1 Background and motivation

In this chapter, a rotating *two-component* superfluid is studied, that is described by a pseudo-spin-1/2 order parameter [3]. The work is an extension of our earlier work on rapidly rotating *scalar* BECs to the case of multicomponent, or *spinor* BECs. No optical lattice potentials are involved.

As described in the introduction, a lot can be learned about a superfluid system when it is set rotating. Depending on the complexity of the order parameter a superfluid can carry angular momentum in different ways. A single-component superfluid exhibits quantized vortices that, in a dilute-gas single-component BEC, organize into a regular hexagonal Abrikosov lattice [6][see Fig. 5.3(a)]. Such lattices are also formed in Type II superconductors in a magnetic field [6] and in rotating superfluid ^4He [53]. Multi-component superfluids, with their pseudo-spin order parameters, carry angular momentum in spin textures (Skyrmions) [92, 110], which may again form lattices [111, 90, 132], such as in the superfluid phases of liquid ^3He [139] and in certain regimes of two-dimensional electron systems [33].

The two-component, pseudo-spin-1/2, superfluid under study here consists of two magnetically trapped internal states of ^{87}Rb [48, 104]. State $|1\rangle$ represents spin-down and state $|2\rangle$ represents spin-up, and the azimuthal component of the spin is fixed by the relative phase Φ between the state $|1\rangle$ and $|2\rangle$ wavefunctions. Both the large-

scale density profiles and the vortex lattice structure depend on the nature of inter- and intracomponent interactions. The interaction energy, determined by three scalar coupling constants g_{11} , g_{22} and g_{12} and the population densities n_1 and n_2 , is given by

$$E_{int} = \int d^3x [g_{11}n_1^2 + g_{22}n_2^2 + g_{12}n_1n_2] \quad (5.1)$$

For attractive intercomponent interaction ($g_{12} < 0$) it is energetically favorable for the spatial profiles of both components to coincide, and a hexagonal vortex lattice is expected, as in the one-component case. For repulsive intercomponent interaction, realized in our ^{87}Rb system, it may be energetically favorable for the two components to reduce spatial overlap. In a static BEC this may be achieved by macroscopic phase separation, which occurs when $g_{12} > \sqrt{g_{11}g_{22}}$. In a *rotating* two-component BEC on the other hand, the presence of vortex lattices in both components allows for more subtle separation effects, such as interlacing the two lattices. Vortices in either component may be filled by fluid of the other component, making this phase separation favorable already for $g_{12} > 0$. The pseudo-spin-1/2 order parameter then forms a Skyrmion lattice.

Studies by Mueller and Ho [111] and Kasamatsu et al. [90] predict many different stable vortex configurations in the vicinity of $g_{11}g_{22} = g_{12}^2$, which is approximated by our ^{87}Rb system, and it appears conceivable that different structures might be accessed e.g. by population imbalances. Among the predicted structures, interlaced square lattices occur over a wide range of parameters. Presumably this is because in a square lattice, unlike in a triangular lattice, each vortex in component $|1\rangle$ can have all its nearest-neighbor vortices be in component $|2\rangle$, and vice versa [100].

Under suitable conditions we indeed observe a spatial separation of vortices in the two components, followed by the formation of ordered interlaced square lattice structures, as shown in Fig. 5.3(b). Its formation and decay dynamics, as well as its static and dynamic properties are examined in this work. In summary, we first prepare a hexagonal vortex lattice in a one-component BEC in an internal atomic state $|1\rangle$,

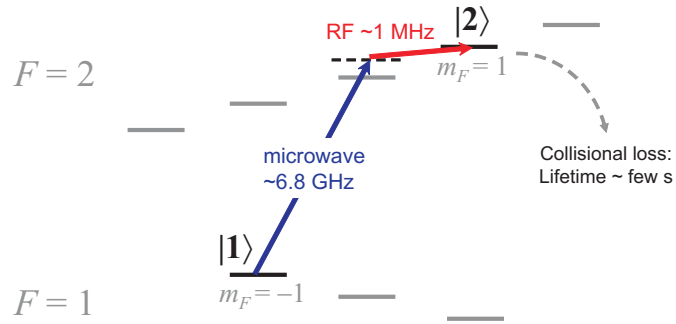


Figure 5.1: Magnetically trapped states $|1\rangle$, $|2\rangle$ used to create two-component BEC in ^{87}Rb . A coherent coupling between the states is achieved by a resonance-enhanced two-photon transition involving a microwave and an RF photon.

and then coherently transfer a fraction of the superfluid to a different state $|2\rangle$. The subsequent evolution of this pseudo-spin-1/2 superfluid towards a state of offset square lattices involves an intriguing interplay of phase-separation and -mixing dynamics, both macroscopically and on the length scale of the vortex cores, and a stage of vortex turbulence. The stability of the square structure is proved by its response to applied shear perturbations. An interference technique shows the spatial offset between the two vortex lattices. Vortex cores in either component are filled by fluid of the other component, such that the spin-1/2 order parameter forms a Skyrmion lattice.

5.2 The magnetically trapped spinor BEC system in ^{87}Rb

Our ^{87}Rb two-state system [48, 104], depicted in Fig. 5.1, consists of two magnetically trappable hyperfine-Zeeman levels of the ^{87}Rb atom - $|F = 1, m_F = -1\rangle$, henceforth called $|1\rangle$, and $|F = 2, m_F = 1\rangle$, henceforth called $|2\rangle$. Spatial overlap of the two states is realized in a harmonic, axially symmetric magnetic trap with oscillation frequencies $\{\omega_\rho, \omega_z\} = 2\pi\{7.7, 4.9\}$ Hz. An electromagnetic coupling between the two states can be achieved via a two-photon transition, involving a microwave photon at ~ 6.833 GHz and a radio frequency photon at ~ 1 MHz. A short-pulse application of this coupling drive yields a desired, spatially uniform amount of population transfer

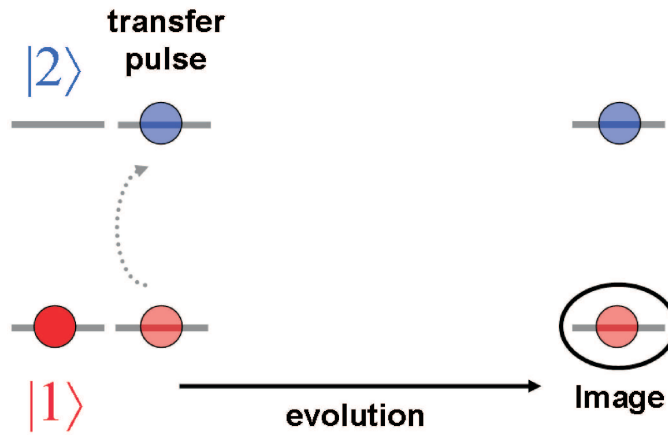


Figure 5.2: Experimental time sequence for creating a two-component BEC.

between the two states, instantaneous with respect to the external dynamics of the two states. In the pseudo-spin-1/2 picture the effect of the coupling drive is to cause spin-rotations [48, 104]. Inelastic atomic collisions limit the lifetime of the $|2\rangle$ population to a few seconds. The decay does not cause $|2\rangle$ atoms to convert back to the $|1\rangle$ state but rather to leave the trap altogether.

5.3 Experiments and results

To study the rotational properties of this two-superfluid system, we initially create regular hexagonal vortex lattices in BECs in state $|1\rangle$, as described in earlier work [56, 143, 45]. Here we start with near-pure condensates containing $(3.5 - 4) \times 10^6$ atoms, rotating at a rate $\Omega \approx 0.75 \times \omega_\rho$ about the z-axis. As shown in Fig. 5.2 a “transfer pulse” of the coupling drive then transfers a fraction of the population into state $|2\rangle$, in this work 80 – 85 % as discussed below. After a variable wait time we take two images of the system. A nondestructive phase-contrast image is taken either of one component alone or of both components simultaneously [48, 104], along an axis perpendicular to the rotation axis (“side view”) while the system is still trapped. In order to optically resolve the vortex structures we expand either the $|1\rangle$ or $|2\rangle$ component of the condensate by a factor of 9, to a diameter of $\sim 600 \mu\text{m}$, before a second, destructive image is taken along

the rotation axis (“top view”). The other component is removed at the beginning of the expansion. The details of expansion and imaging have been described in Ref. [45].

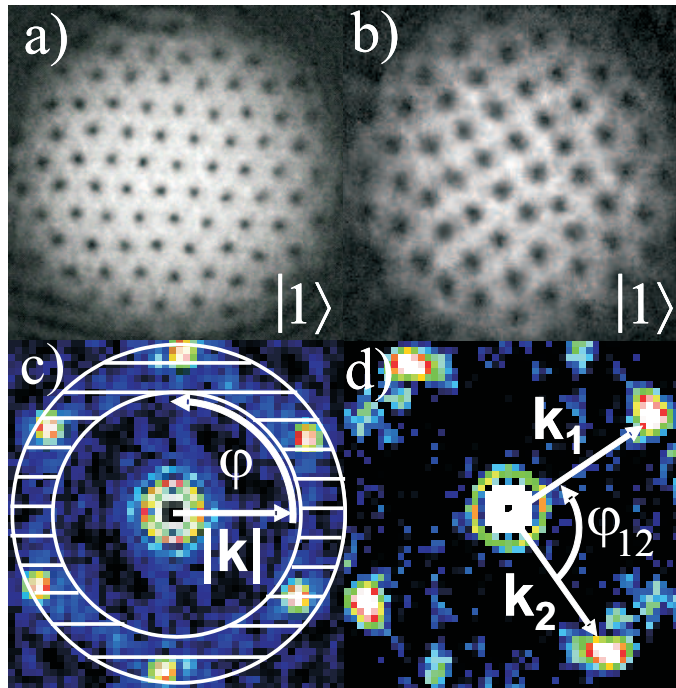


Figure 5.3: (a) Hexagonal vortex lattice in a one-component BEC. (b) Square lattice, viewed in the $|1\rangle$ component of a two-component BEC. (c) Reciprocal (k -) space of the hexagonal lattice, obtained by 2D Fourier transform of (a), showing 6 peaks spaced by 60° . (d) k - space of the square lattice. The reciprocal lattice vectors k_1 and k_2 enclose an angle $\varphi_{12} = 90^\circ$.

In Fig. 5.4 we analyze the formation and decay dynamics of the square lattice structure. Figs. 5.4(a) and (b) show time sequences of top-view images of the expanded $|1\rangle$ and $|2\rangle$ states, taken in different experimental runs. The time evolution after the transfer pulse involves several stages. For the first $\sim 0.1 - 0.25$ s surprisingly little dynamics is visible and certainly no structural transition in the vortex lattice is seen in either component. From $\sim 0.25 - 2$ s a turbulent stage evolves in both components in which vortex visibility degrades significantly, shown in Fig. 5.4[a(ii)] and Fig. 5.4[b(ii)]. As we will show, this turbulence is directly linked with the transition from overlapping hexagonal vortex lattices to interlaced square lattices. From $2 - 3$ s square

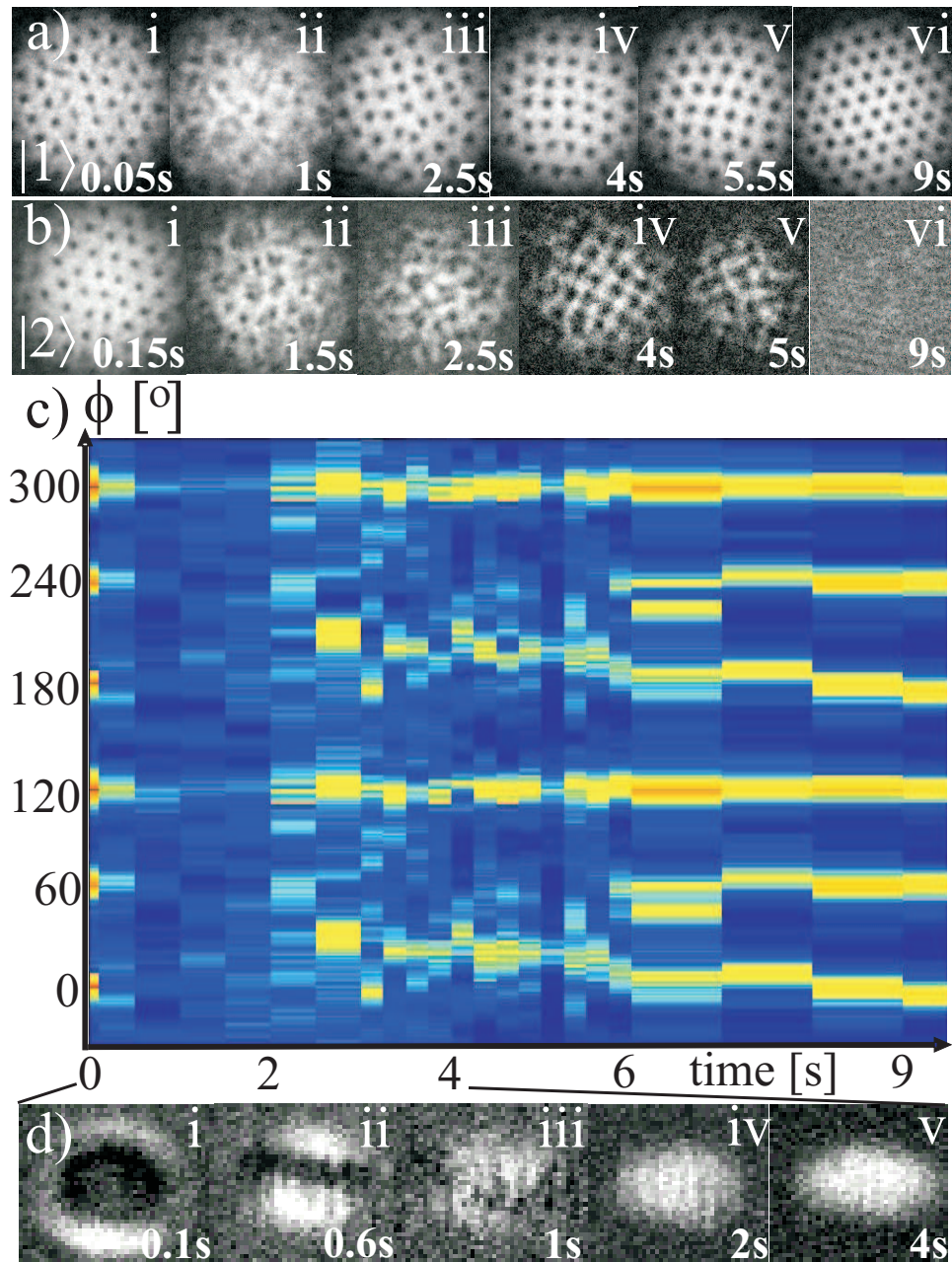


Figure 5.4: (a) Time sequence of images of state $|1\rangle$, after $\sim 80\%$ population transfer to $|2\rangle$, showing evolution from a hexagonal lattice over a turbulent stage to a square structure and back to a hexagonal lattice. (b) Also state $|2\rangle$ forms a square lattice (iv) before its decay. (c) Detailed time evolution in reciprocal space. Intensity in an annulus along the φ coordinate [defined in Fig. 5.3(c)] is shown on the ordinate. The initial 6-peak structure of the hexagonal lattice vanishes quickly because of turbulence. From 3 – 5.5s square lattices give rise to a 4-peak structure. Around 6 – 9s a transition back to hexagonal lattices occurs. (d) Two-color side view images of the initial turbulent evolution. State $|1\rangle$ ($|2\rangle$) appears bright (dark) on gray background. The fine vertical filament structures in (ii-v) are due to mutual filling of vortex cores.

domains emerge from the turbulent state, and defects propagate out of the lattice {Fig. 5.4[a(iii)]}. From 3 – 5.5 s stable square lattices are observed in both components {Fig. 5.4[a(iv)] and Fig. 5.4[b(iv)]}. At this stage, around 4 s, despite the large (80 – 85 %) initial population transfer to state $|2\rangle$, the number of $|2\rangle$ atoms has decreased to only 1.5×10^5 , while state $|1\rangle$ contains $(5 - 7) \times 10^5$ atoms. As the $|2\rangle$ state population continues to decay, the vortex lattice planes bend {Fig. 5.4[a(v)]} and a transition back to a hexagonal lattice in state $|1\rangle$ takes place {Fig. 5.4[a(vi)]}. During the transition from square lattices to a hexagonal lattice no turbulence occurs.

A more quantitative analysis of these dynamics is possible in reciprocal space. Figure 5.4(c) shows the time evolution of the intensity within an annulus in reciprocal space, defined in Fig. 5.3(a), which contains the reciprocal lattice peaks. Initially six peaks are visible, separated by 60° , forming the reciprocal lattice of a hexagonal vortex lattice. Because of turbulence these peaks vanish between ~ 200 ms and 2 s. After 2 – 3 s a four-peak structure appears, that is stable for a period of ~ 2.5 s. The observed ratio of reciprocal lattice vector lengths [defined in Fig. 5.3(d)] $k_1/k_2 = 0.98(2)$ and the angle $\varphi_{12} = 95(3)^\circ$ between k_1 and k_2 , clearly identify a square lattice. At ~ 5.5 s the appearance of two additional peaks signals the onset of a transition back to the hexagonal state, which is completed by ~ 9 s.

To examine the origin of the initial turbulence, we show in Fig. 5.4(d) a time sequence of in-trap side-view images, where the $|1\rangle$ ($|2\rangle$) state appears bright (dark). As visible in Fig. 5.4[d(i)], a macroscopic component separation from the initially homogeneous two-component superposition to a ball-shell structure takes place within 50 – 100 ms [48, 104]. During this period of dramatic axial separation, both the individual vortices and the overall vortex lattice remain remarkably quiet, as viewed along the rotation axis {see Fig. 5.4[a(i)] and Fig. 5.4[b(i)]}. Around 600 ms, fine filament structures appear at the intercomponent boundary {Fig. 5.4[d(ii)]}, coincident with the full development of vortex turbulence seen in top-view images {Fig. 5.4[a(ii)]}. The

filament structures distort and fill out the whole BEC as the vortex turbulence peaks at around 1 s {Fig. 5.4[d(iii)]}, and straighten up at around 2 s {Fig. 5.4[d(iv)]} coincident with the restoration of vortex visibility in top view images. Subsequently the filaments become less visible as state $|2\rangle$ decays {Fig. 5.4[d(v)]}. We interpret these structures as vortex cores in either component being filled by fluid of the other component, forming a Skyrmion lattice [110]. Filled vortex cores grow in size above the resolution limit of our side view images and become observable, while empty vortices in single-component BECs in equilibrium are well below this resolution limit and are not observed in-trap [10]. The initial *macroscopic*, predominantly axial phase separation has thus evolved into a *microscopic* separation of two interlaced vortex lattices. It is this *microscopic* separation which gives rise to the observed turbulence.

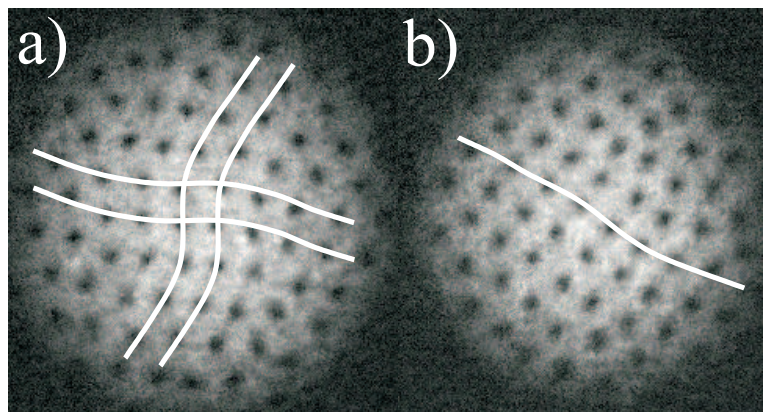


Figure 5.5: (a) Tkachenko mode excitation in the square lattice, observed 250 ms after beginning of excitation, and (b) after relaxation back to a square lattice structure (at 850 ms).

To study the stability of the square lattice, we excite shear perturbations (Tkachenko modes) [12, 20] in the square lattice by focusing a resonant laser beam onto the center of the condensate [44]. As shown in Fig. 5.5, the perturbation relaxes to the equilibrium square configuration within 500 – 800 ms after excitation. However, in contrast to single-component triangular lattices [44], no clear oscillation is observed. Two effects may contribute: The excitation may be overdamped because of ill-defined boundary

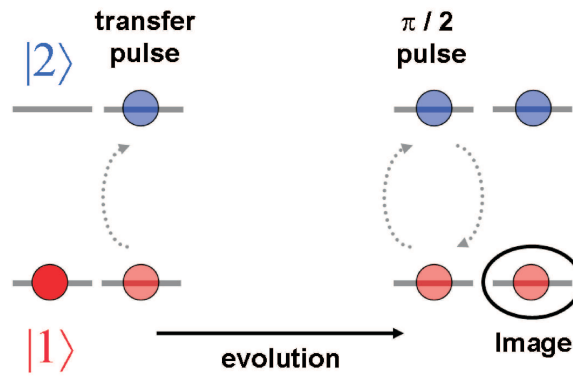


Figure 5.6: Experimental sequence for two-component vortex lattice interference.

conditions caused by imperfections in the outer region of the square lattice, where the $|2\rangle$ state population has already decayed. The oscillation may also be masked by random lattice excitations of comparable amplitude that cannot be completely removed in the short time between formation and decay of the square lattice. However, the return of the lattice to its square configuration is sufficient to demonstrate the stability of the square structure in the two-component system.

So far we have presented evidence that both components separately form regular and stable square lattices. Filament structures indirectly indicate a microscopic-scale spatial separation of vortices. In the following, we employ an interference technique between the two superfluids to more precisely address two questions: Are the vortex lattices really offset from each other? Do the vortices really only separate from each other during the turbulent stage, after a surprising delay of 200 ms? Figures 5.7[a(i)] and (iii) show results of a simple simulation of interference between two square vortex lattice wavefunctions, spatially offset by $1/2(\vec{a} + \vec{b})$, where \vec{a} , \vec{b} are the two basis vectors of the square lattice. Two values ($\Phi = 0$ and $\Phi = 45^\circ$) of the relative quantum phase Φ between the two wavefunctions ¹ are considered. A population ratio of $N_{|2\rangle} : N_{|1\rangle} = 20 : 80$

¹ The relative phase Φ is well-defined and measurable but is relevant only in the presence of coupling between the states. Directly after population transfer it is zero and uniform across the sample, but with each experimental run it quickly acquires an arbitrary value, e.g. because of slight irreproducibility in the trapping potentials.

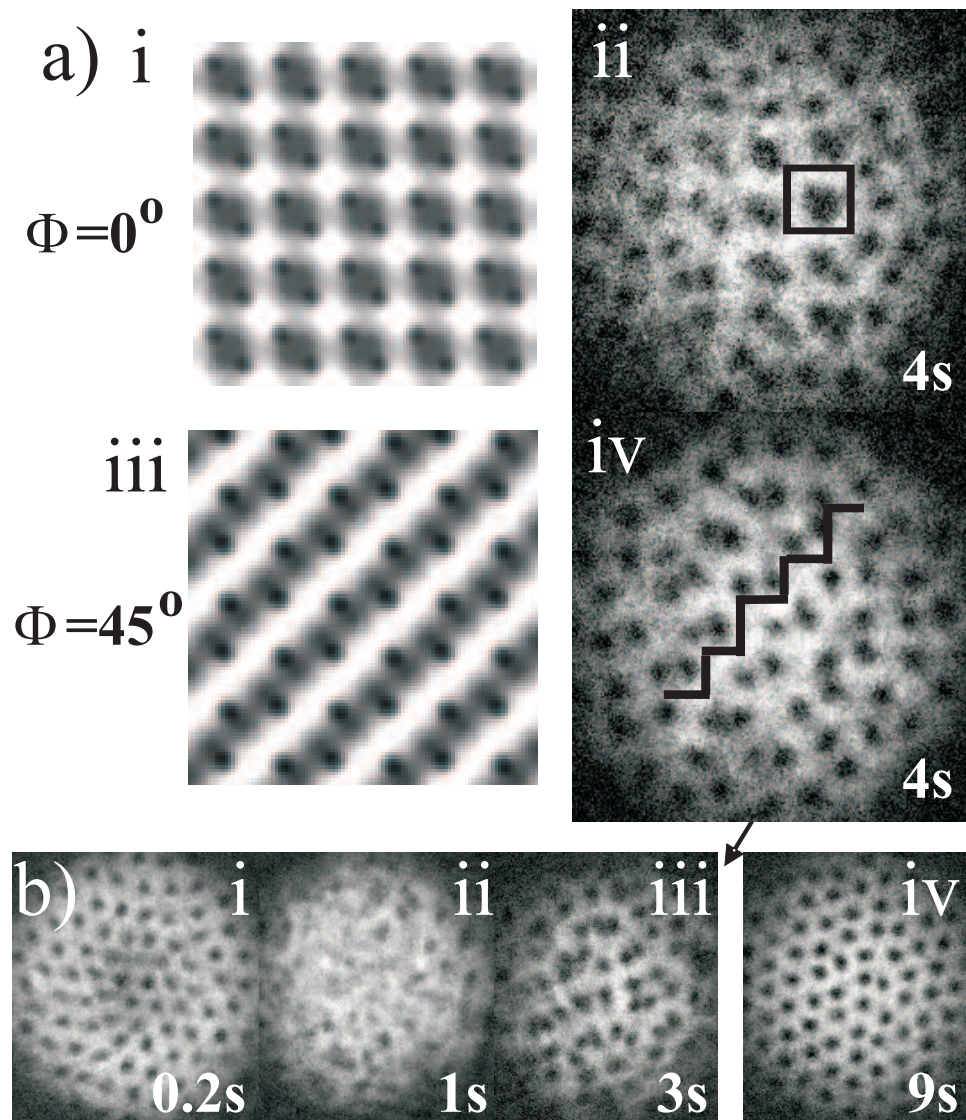


Figure 5.7: (a) Vortex lattice interference. (i) and (iii): Simulations for different values of the relative phase Φ between the $|1\rangle$ and $|2\rangle$ state wavefunctions. (ii) and (iv): Experimental results. (b) Time evolution of the interference patterns shows no vortex offset before the turbulence (i) but patterns characteristic of offset vortices afterwards [b(iii)], [a(ii)], [a(iv)].

was assumed, as in the experiment at 4s. Evidently two very dissimilar patterns are seen, consisting either ($\Phi \sim 0$) of dark patches in between two vortices, surrounded by a bright square structure, or ($\Phi \sim 45^\circ$) of staircase-like vortex arrangements separated by bright stripes. We checked that the qualitative appearance of such simulations changes drastically when altering the spatial offset from $1/2(\vec{a} + \vec{b})$.

To observe such structures experimentally, we apply a $\pi/2$ “interference” pulse to the two-component system just before expansion for the top view image, as shown in Fig. 5.6. This pulse results in a phase-coherent transfer of population between the two states, thus creating interference. If the $\pi/2$ pulse is applied under conditions when regular square lattices are expected in both components, the observed images, Fig. 5.7[a(ii)] and (iv), agree qualitatively with the simulations, clearly demonstrating a spatial offset close to $1/2(\vec{a} + \vec{b})$ between the vortex lattices.

The qualitative agreement between experimental results and simulation indicates that vortex lattice interference may be employed to examine the separation process of the vortex lattices. When varying the wait time between the transfer pulse and the $\pi/2$ interference pulse, we observe the following qualitative features [Fig. 5.7(b)]: Until turbulence occurs (after 200 – 300 ms) there are no indications for separation of the vortex lattices. Figure 5.7(b)(i) shows a hexagonal lattice with good vortex contrast, very similar to images of each single component at this time. This confirms that during the initial 200 – 300 ms of dramatic macroscopic component separation, vortices in the two components continue to form identical and overlapped lattice structures, when viewed along the rotation axis. Only after this surprisingly long delay, and after the turbulent stage do interference patterns show a grouping characteristic of offset vortices {Fig. 5.7[b(iii)]}. This observation is further proof of the direct link between the turbulent period and the microscopic separation of the vortex lattices.

In conclusion, we have observed a new vortex lattice structure in rotating two-component BEC. Each component carries a square vortex lattice, and the lattices are

interlaced. Vortices in both components are filled by fluid of the other component, forming a Skyrmion lattice. This structure is stable, as evidenced by relaxation of applied shear excitations back to the square structure. An intriguing turbulent stage accompanies the transition from overlapped hexagonal lattices to interlaced square lattices. Vortex lattice interference has been used to study the offset dynamics of the two lattices.

Bibliography

- [1] This chapter is an expanded version of [164].
- [2] This chapter is an expanded version of [146].
- [3] This chapter is a revised version of [144].
- [4] This appendix contains some previously published material from [143],[44], and [45].
- [5] J. R. Abo-Shaeer, C. Raman, J. M. Vogels, and W. Ketterle. Observation of vortex lattices in Bose-Einstein condensates. Science, 292:476, 2001.
- [6] A. A. Abrikosov. On the magnetic properties of superconductors of the second group. Sov. Phys. JETP, 5:1174, 1957.
- [7] G. Agnolet, D.F. McQueeney, and J. D. Reppy. Kosterlitz-Thouless transition in helium films. Phys. Rev. B, 39:8934, 1989.
- [8] Ehud Altman, Eugene Demler, and Mikhail D. Lukin. Probing many-body states of ultracold atoms via noise correlations. Phys. Rev. A, 70(1):013603, 2004.
- [9] D. Ananikian and T. Bergeman. Gross-Pitaevskii equation for Bose particles in a double-well potential: Two-mode models and beyond. Phys. Rev. A, 73:013604, 2006.
- [10] B. P. Anderson, P. C. Haljan, C. E. Wieman, and E. A. Cornell. Vortex precession in Bose-Einstein condensates: Observations with filled and empty cores. Phys. Rev. Lett., 85:2857, 2000.
- [11] M.H. Anderson, J.R. Ensher, M.R. Matthews, C. E. Wieman, and E. A. Cornell. Observation of Bose-Einstein condensation in a dilute atomic vapor. Science, 269:198, 1995.
- [12] J. R. Anglin and M. Caccioppo. Inhomogeneous vortex matter. cond-mat/0210063, 2002.
- [13] M. Baert, V.V. Metlushko, R. Jonckheere, V.V. Moshchalkov, and Y. Bruynseraede. Composite flux-line lattices stabilized in superconducting films by a regular array of artificial defects. Phys. Rev. Lett., 74:3269, 1995.

- [14] V. Bagnato and D. Kleppner. Bose-Einstein condensation in low-dimensional traps. Phys. Rev. A, 44:7439, 1991.
- [15] P. Bak. Commensurate phases, incommensurate phases and the devil's staircase. Rep. Prog. Phys., 45:587, 1982.
- [16] L. O. Baksmaty, S. J. Woo, S. Choi, and N. P. Bigelow. Tkachenko waves in rapidly rotating Bose-Einstein condensates. Phys. Rev. Lett., 92:160405, 2004.
- [17] R. Ballagh. personal communication. 2007.
- [18] M.A. Baranov, K. Osterloh, and M. Lewenstein. Fractional quantum Hall states in ultracold rapidly rotating dipolar Fermi gases. Phys. Rev. Lett., 94:070404, 2005.
- [19] G. Baym. private communication.
- [20] G. Baym. Tkachenko modes of vortex lattices in rapidly rotating Bose-Einstein condensates. Phys. Rev. Lett., 91:110402, 2003.
- [21] G. Baym. Vortex lattices in rapidly rotating Bose-Einstein condensates: Modes and correlation functions. Phys. Rev. A, 69:043618, 2004.
- [22] G. Baym and C. J. Pethick. Vortex core structure and global properties of rapidly rotating Bose-Einstein condensates. Phys. Rev. Lett., 69:043619, 2004.
- [23] V. Berezinskii. Destruction of long-range order in one-dimensional and 2-dimensional systems having a continuous symmetry group. 1 - classical systems. Sov. Phys.-JETP, 32:493, 1971.
- [24] V. Berezinskii. Destruction of long-range order in one-dimensional and 2-dimensional systems possessing a continuous symmetry group. 2 - quantum systems. Sov. Phys.-JETP, 34:610, 1972.
- [25] R. Bhat, M. J. Holland, and L. D. Carr. Bose-Einstein condensates in rotating lattices. Phys. Rev. Lett., 96:060405, 2006.
- [26] R. Bhat, M. Krämer M, J. Cooper, and M. J. Holland. Hall effects in Bose-Einstein condensates in a rotating optical lattice. Phys. Rev. A, 76:043601, 2007.
- [27] Aranya B. Bhattacharjee. Tkachenko modes and quantum melting of Josephson junction type of vortex array in rotating Bose-Einstein condensate. Journal of Physics B, 37:2699, 2004.
- [28] S. G. Bhongale, J. N. Milstein, and M. J. Holland. Resonant formation of strongly correlated paired states in rotating Bose gases. Phys. Rev. A, 69:053603, 2004.
- [29] I. Bloch, J. Dalibard, and W. Zwerger. Many-body physics with ultracold gases. arxiv:0704.3011, to appear in Rev. Mod. Phys., 2008.
- [30] M. Boyd, A. Ludlow, S. Blatt, S. Foreman, T. Ido, T. Zelevinsky, and J. Ye. ^{87}Sr lattice clock with inaccuracy below 10^{-15} . Phys. Rev. Lett., 98:083002, 2007.

- [31] F. Brennecke, T. Donner, S. Ritter, T. Bourdel, M. Köhl, and Tilman Esslinger. Cavity QED with a Bose-Einstein condensate. *Nature*, 450:268–271, 2007.
- [32] V. Bretin, S. Stock, Y. Seurin, and J. Dalibard. Fast rotation of a Bose-Einstein condensate. *Phys. Rev. Lett.*, 92:050403, 2004.
- [33] L. Brey, H. A. Fertig, R. Cote, and A. H. MacDonald. Skyrme crystal in a two-dimensional electron gas. *Phys. Rev. Lett.*, 75:2562, 1995.
- [34] A.A. Burkov and E. Demler. Vortex-Peierls states in optical lattices. *Phys. Rev. Lett.*, 96:180406, 2006.
- [35] K. Burnett, M. Edwards, C.W. Clark, and M. Shotter. The Bogoliubov approach to number squeezing of atoms in an optical lattice. *J. Phys. B*, 35:1671, 2002.
- [36] L. J. Campbell, M. M. Doria, and J. B. Kadtko. Energy of infinite vortex lattices. *Phys. Rev. A*, 39:5346, 1989.
- [37] I. Carusotto. Generation of a rotating optical lattice. private communication, 2003.
- [38] M. A. Cazalilla, A. Iucci, and T. Giamarchi. Competition between vortex unbinding and tunneling in an optical lattice. *Phys. Rev. A*, 75:051603(R), 2007.
- [39] F. Chevy and S. Stringari. Kelvin modes of a fast rotating Bose-Einstein condensate. *Phys. Rev. A*, 68:053601, 2003.
- [40] C. Chin, V. Leiber, V. Vuletić, A.J. Kerman, and S. Chu. Measurement of an electron’s dipole moment using Cs atoms trapped in optical lattices. *Phys. Rev. A*, 63:033401, 2001.
- [41] S. Choi, L. O. Baksmaty, S. J. Woo, and N. P. Bigelow. Excitation spectrum of vortex lattices in rotating Bose-Einstein condensates. *Phys. Rev. A*, 68:031605, 2003.
- [42] P. Cladé. Presentation at DAMOP 2007 conference, Calgary, Canada. 2007.
- [43] P. Cladé, E. de Mirandes, M. Cadoret, S. Guellati-Khélifa, C. Schwob, F. Nez, L. Julien, and F. Biraben. Determination of the fine structure constant based on Bloch oscillations of ultracold atoms in a vertical optical lattice. *Phys. Rev. Lett.*, 96:033001, 2006.
- [44] I. Coddington, P. Engels, V. Schweikhard, and E. A. Cornell. Observation of Tkachenko oscillations in rapidly rotating Bose-Einstein condensates. *Phys. Rev. Lett.*, 91:100402, 2003.
- [45] I. Coddington, P. C. Haljan, P. Engels, V. Schweikhard, S. Tung, and E. A. Cornell. Experimental studies of equilibrium vortex properties in a Bose-condensed gas. *Phys. Rev. A*, 70:063607, 2004.
- [46] Ian R. Coddington. *Vortices in a Highly Rotating Bose Condensed Gas*. PhD thesis, University of Colorado (Boulder), 2004.

- [47] N. R. Cooper, N. K. Wilkin, and J. M. F. Gunn. Quantum phases of vortices in rotating bose-einstein condensates. Phys. Rev. Lett., 87:120405, 2001.
- [48] E. A. Cornell, D. S. Hall, M. R. Matthews, and C. E. Wieman. Having it both ways: Distinguishable yet phase-coherent mixtures of Bose-Einstein condensates. J. Low Temp. Phys., 113:151, 1998.
- [49] M. Cozzini, L. P. Pitaevskii, and S. Stringari. Tkachenko oscillations and the compressibility of a rotating Bose-Einstein condensate. Phys. Rev. Lett., 92:220401, 2004.
- [50] M. Cozzini, S. Stringari, and C. Tozzo. Vortex lattices in Bose-Einstein condensates: from the Thomas-Fermi regime to the lowest-Landau-level regime. Phys. Rev. A, 73:023615, 2006.
- [51] J. Hecker Denschlag, J. E. Simsarian, H. Häffner, C. McKenzie, A. Browaeys, D. Cho, K. Helmerson, S. L. Rolston, and W. D. Phillips. A Bose Einstein condensate in an optical lattice. J. Phys. B: At. Mol. Opt. Phys., 35:3095, 2002.
- [52] I. H. Deutsch and P. S. Jessen. Quantum-state control in optical lattices. Phys. Rev. A, 57:1972, 1998.
- [53] R. J. Donnelly. Quantized Vortices in Helium II. Cambridge University Press.
- [54] A. Einstein. Quantentheorie des einatomigen idealen Gases. Zweite Abhandlung. Sitzungber. Preuss. Akad. Wiss., 1925:3, January 1925.
- [55] P. Engels, I. Coddington, P. C. Haljan, and E. A. Cornell. Nonequilibrium effects of anisotropic compression applied to vortex lattices in Bose-Einstein condensates. Phys. Rev. Lett., 89:100403, 2002.
- [56] P. Engels, I. Coddington, P. C. Haljan, V. Schweikhard, and E. A. Cornell. Observation of long-lived vortex aggregates in rapidly rotating Bose-Einstein condensates. Phys. Rev. Lett., 90:170405, 2003.
- [57] P. Engels, I. Coddington, V. Schweikhard, and E. A. Cornell. Vortex lattice dynamics in a dilute gas BEC. J. Low Temp. Phys., 134:683, 2004.
- [58] A. L. Fetter. Rotating trapped Bose-Einstein condensates. arxiv:0801.2952, to appear in Rev. Mod. Phys., 2008.
- [59] A.L. Fetter. Kelvin mode of a vortex in a nonuniform Bose-Einstein condensate. Phys. Rev. A, 69:043617, 2004.
- [60] R. Gati, B. Hemmerling, J. Fölling, M. Albiez, and M.K. Oberthaler. Noise thermometry with two weakly coupled Bose-Einstein condensates. Phys. Rev. Lett., 96:130404, 2006.
- [61] R. Gati and M. K. Oberthaler. A bosonic Josephson junction. J. Phys. B, 40:R61, 2007.
- [62] P. Ghosh and F. Sols. Vortex trapping in suddenly connected Josephson junctions of Bose-Einstein condensates. PRA, 77:033609, 2008.

- [63] S. A. Gifford and G. Baym. Vortex lattice stability and phase coherence in three-dimensional rapidly rotating Bose condensates. Phys. Rev. A, 70:033602, 2004.
- [64] S. A. Gifford and Gordon Baym. Dislocation-mediated melting in superfluid vortex lattices. arXiv:0807.2436, 2008.
- [65] L. Giorgetti, I. Carusotto, and Y. Castin. Semiclassical field method for the equilibrium Bose gas and application to thermal vortices in two dimensions. Phys. Rev. A, 76:013613, 2007.
- [66] T. Goto, T. Kimura, G. Lawes, A. P. Ramirez, and Y. Tokura. Ferroelectricity and giant magnetocapacitance in Perovskite rare-earth Manganites. Phys. Rev. Lett., 92:257201, 2004.
- [67] M. Greiner, O. Mandel, T. Esslinger, T.W. Hänsch, and I. Bloch. Quantum phase transition from a superfluid to a Mott insulator in a gas of ultracold atoms. Nature, 415:39, 2002.
- [68] A. Griessner, A. J. Daley, S. R. Clark, D. Jaksch, and P. Zoller. Dark-state cooling of atoms by superfluid immersion. Phys. Rev. Lett., 97:220403, 2006.
- [69] A.N. Grigorenko, S.J. Bending, M.J. Van Bael, M. Lange, V.V. Moshchalkov, H. Fangohr, and P.A.J. de Groot. Symmetry locking and commensurate vortex domain formation in periodic pinning arrays. Phys. Rev. Lett., 90:237001, 2003.
- [70] Rudolf Grimm, Matthias Weidemüller, and Yurii B. Ovchinnikov. Optical dipole traps for neutral atoms. Adv. At. Mol. Opt. Phys., 42:95, 2000.
- [71] Z. Hadzibabic, P. Krüger, M. Cheneau, B. Battelier, and J. Dalibard. Berezinskii-Kosterlitz-Thouless crossover in a trapped atomic gas. Nature, 441:1118, 2006.
- [72] M. Hafezi, A.S. Sørensen, E. Demler, and M.D. Lukin. Fractional quantum Hall effect in optical lattices. Phys. Rev. A, 76:023613, 2007.
- [73] P. C. Haljan, I. Coddington, P. Engels, and E. A. Cornell. Driving Bose-Einstein-condensate vorticity with a rotating normal cloud. Phys. Rev. Lett., 87:210403, 2001.
- [74] Paul C. Haljan. Vortices in a Bose-Einstein Condensate. PhD thesis, University of Colorado (Boulder), 2003.
- [75] R. Heidemann, U. Raitzsch, V. Bendkowsky, B. Butscher, R. Lw, and T. Pfau. Rydberg excitation of Bose-Einstein condensates. Phys. Rev. Lett., 100:033601, 2008.
- [76] D. Hellweg, L. Cacciapuoti, M. Kottke, T. Schulte, K. Sengstock, W. Ertmer, and J. J. Arlt. Measurement of the spatial correlation function of phase fluctuating Bose-Einstein condensates. Phys. Rev. Lett., 91:010406, 2003.
- [77] T.-L. Ho. Bose-Einstein condensates with large number of vortices. Phys. Rev. Lett., 87:060403, 2001.

- [78] E. Hodby, G. Hechenblaikner, S. A. Hopkins, O. M. Maragò, and C. J. Foot. Vortex nucleation in Bose-Einstein condensates in an oblate, purely magnetic potential. Phys. Rev. Lett., 88:010405, 2002.
- [79] M. A. Hoefer, M. J. Ablowitz, I. Coddington, E. A. Cornell, P. Engels, and V. Schweikhard. On dispersive and classical shock waves in Bose-Einstein condensates and gas dynamics. Phys. Rev. A, 74:023623, 2006.
- [80] W. Hofstetter, J.I. Cirac, P. Zoller, E. Demler, and M. D. Lukin. High-temperature superfluidity of fermionic atoms in optical lattices. Phys. Rev. Lett., 89:220407, 2002.
- [81] M. Holzmann, M. Chevallier, and W. Krauth. Semiclassical theory of the quasi two-dimensional trapped Bose gas. arXiv:0801.2758, 2008.
- [82] B.A. Huberman and S. Doniach. Melting of two-dimensional vortex lattices. Phys. Rev. Lett., 43:950, 1979.
- [83] M. Hugbart, J.A. Retter, F. Gerbier and A.F. Varón, S. Richard, J.H. Thywissen, D. Clément, P. Bouyer, and A. Aspect. Coherence length of an elongated condensate. Eur. Phys. J. D, 35:155, 2005.
- [84] T. Isoshima. Vortex oscillations in confined Bose-Einstein condensate interacting with 1d optical lattice. J. Phys. Soc. Jpn., 74:2764, 2005.
- [85] D. Jaksch, C. Bruder, J. I. Cirac, C. W. Gardiner, , and P. Zoller. Cold bosonic atoms in optical lattices. Phys. Rev. Lett., 81:3108, 1998.
- [86] D. Jaksch and P. Zoller. Creation of effective magnetic fields in optical lattices: the Hofstadter butterfly for cold neutral atoms. New J. Phys., 5:56, 2003.
- [87] J. Javanainen. Phonon approach to an array of traps containing Bose-Einstein condensates. Phys. Rev. A, 60:4902, 1999.
- [88] K. Kasamatsu. Vortex lattices in rotating Bose-Einstein condensate in an optical lattice: Analogy to uniformly frustrated Josephson-junction arrays. J. Low Temp. Phys., 150:593, 2008.
- [89] K. Kasamatsu and M. Tsubota. Dynamical vortex phases in a Bose-Einstein condensate driven by a rotating optical lattice. Phys. Rev. Lett., 97:240404, 2006.
- [90] K. Kasamatsu, M. Tsubota, and M. Ueda. Vortex phase diagram in rotating two-component Bose-Einstein condensates. Phys. Rev. Lett., 91:150406, 2003.
- [91] M. Kasevich. Presentation at BEC 2007 conference, Sant Feliu de Guixols, Spain. 2007.
- [92] U. Al Khawaja and H.T.C. Stoof. Skyrmions in a ferromagnetic Bose-Einstein condensate. Nature, 411:918, 2001.
- [93] T. Kinoshita, T. Wenger, and D. S. Weiss. A quantum Newton's cradle. Science, 305:1125, 2004.

- [94] J. Kosterlitz and D. Thouless. Ordering, metastability and phase transitions in two-dimensional systems. J. Phys. C, 6:1181, 1973.
- [95] S. Kragset, E. Babaev, and A. Sudbø. Thermal fluctuations of vortex matter in trapped Bose-Einstein condensates. Phys. Rev. Lett., 97:170403, 2006.
- [96] P. Krüger, Z. Hadzibabic, and J. Dalibard. Critical point of an interacting two-dimensional atomic bose gas. Phys. Rev. Lett., 99:040402, 2007.
- [97] T. Lahaye, T. Koch, B. Fröhlich, M. Fattori, J. Metz, A. Griesmaier, S. Giovanazzi, and T. Pfau. Strong dipolar effects in a quantum ferrofluid. Nature, 448:672–675, 2007.
- [98] R. B. Laughlin. Nobel lecture: Fractional quantization. Rev. Mod. Phys., 71:863, 1999.
- [99] A. J. Leggett. Bose-Einstein condensation in the alkali gases: Some fundamental concepts. Rev. Mod. Phys., 73:307, 2001.
- [100] K. Lehnert. private communication.
- [101] M. Lewenstein, A. Sanpera, V. Ahufinger, B. Damski, A. Sen De, and U. Sen. Ultracold atomic gases in optical lattices: mimicking condensed matter physics and beyond. Advances in Physics, 56:243, 2007.
- [102] K. W. Madison, F. Chevy, W. Wohlleben, and J. Dalibard. Vortex formation in a stirred Bose-Einstein condensate. Phys. Rev. Lett., 84:806, 2000.
- [103] J.-P. Martikainen and H. T. C. Stoof. Quantum theory of a vortex line in an optical lattice. Phys. Rev. A, 69:053617, 2004.
- [104] M. R. Matthews, B. P. Anderson, P. C. Haljan, D. S. Hall, M. J. Holland, J. E. Williams, C. E. Wieman, and E. A. Cornell. Watching a superfluid untwist itself: Recurrence of Rabi oscillations in a Bose-Einstein condensate. Phys. Rev. Lett., 83:3358, 1999.
- [105] Michael R. Matthews. Two-Component Bose-Einstein Condensation. PhD thesis, University of Colorado (Boulder), 1999.
- [106] T. Mizushima, Y. Kawaguchi, K. Machida, T. Ohmi, T. Isoshima, and M. M. Salomaa. Collective oscillations of vortex lattices in rotating Bose-Einstein condensates. Phys. Rev. Lett., 92:060407, 2004.
- [107] A. G. Morris and D. L. Feder. Gaussian potentials facilitate access to quantum Hall states in rotating Bose gases. Phys. Rev. Lett., 99:240401, 2007.
- [108] O. Morsch, J.H. Müller, M. Cristiani, D. Ciampini, and E. Arimondo. Bloch oscillations and mean-field effects of Bose-Einstein condensates in 1d optical lattices. Phys. Rev. Lett., 87:140402, 2001.
- [109] E. Mueller. Artificial electromagnetism for neutral atoms: Escher staircase and Laughlin liquids. Phys. Rev. A, 70:041603R, 2004.

- [110] E. J. Mueller. Spin textures in slowly rotating Bose-Einstein condensates. Phys. Rev. A, 69:033606, 2004.
- [111] E. J. Mueller and T.-L. Ho. Two-component Bose-Einstein condensates with a large number of vortices. Phys. Rev. Lett., 88:180403, 2002.
- [112] M. Naraschewski and D. Stamper-Kurn. Analytical description of a trapped semi-ideal bose gas at finite temperature. Phys. Rev. A, 58:2423, 1998.
- [113] K.-K. Ni, S. Ospelkaus, M. H. G. de Miranda, A. Pe'er, B. Neyenhuis, J. J. Zirbel, S. Kotochigova, P. S. Julienne, D. S. Jin, and J. Ye. A High Phase-Space-Density Gas of Polar Molecules. Science, 322:231–235, 2008.
- [114] M.Ö. Oktel, M. Nita, and B. Tanatar. Mean-field theory for Bose-Hubbard model under a magnetic field. Phys. Rev. B, 75:045133, 2007.
- [115] C. Orzel, A.K. Tuchman, M.L. Fenselau, M. Yasuda, and M.A. Kasevich. Squeezed states in a Bose-Einstein condensate. Science, 291:2386, 2001.
- [116] Yu. B. Ovchinnikov, J. H. Müller, M. R. Doery, E. J. D. Vredenburg, K. Helmer-son, S. L. Rolston, and W. D. Phillips. Diffraction of a released Bose - Einstein condensate by a pulsed standing light wave. Phys. Rev. Lett., 83:284, 1999.
- [117] W. Pan, H.L. Störmer, D.C. Tsui, L.N. Pfeiffer, K.W. Baldwin, and K.W. West. Transition from an electron solid to the sequence of fractional quantum Hall states at very low Landau level filling factor. Phys. Rev. Lett., 88:176802, 2002.
- [118] B. Paredes, P. Fedichev, J. I. Cirac, and P. Zoller. 1/2-Anyons in small atomic Bose-Einstein condensates. Phys. Rev. Lett., 87:010402, 2001.
- [119] C.J. Pethick and H. Smith. Bose-Einstein Condensation in Dilute Gases. Cambridge University Press.
- [120] D. Petrov, G.V. Shlyapnikov, and J.T.M. Walraven. Phase-fluctuating 3D Bose-Einstein condensates in elongated traps. Phys. Rev. Lett., 87:050404, 2001.
- [121] K. I. Petsas, A. B. Coates, and G. Grynberg. Crystallography of optical lattices. Phys. Rev. A, 50:5173, 1994.
- [122] L. Pitaevskii and S. Stringari. Bose-Einstein Condensation. Oxford University Press.
- [123] L. Pitaevskii and S. Stringari. Thermal vs quantum decoherence in double well trapped Bose-Einstein condensates. Phys. Rev. Lett., 87:180402, 2001.
- [124] M. Polini, R. Fazio, and A.H. MacDonald. Realization of fully frustrated Josephson-junction arrays with cold atoms. Phys. Rev. A, 95:010401, 2005.
- [125] A. Polkovnikov, Ehud Altman, and Eugene Demler. Interference between independent fluctuating condensates. PNAS, 103:6125, 2006.

- [126] P. Pedri, L. Pitaevskii, S. Stringari, C. Fort, S. Burger, F. S. Cataliotti, P. Maddaloni, F. Minardi, and M. Inguscio. Expansion of a coherent array of Bose-Einstein condensates. *Phys. Rev. Lett.*, 87:220401, 2001.
- [127] N. Prokof'ev, O. Ruebenacker, and B. Svistunov. Critical point of a weakly interacting two-dimensional Bose gas. *Phys. Rev. Lett.*, 87:270402, 2001.
- [128] H. Pu, L. O. Baksmaty, S. Yi, and N. P. Bigelow. Structural phase transitions of vortex matter in an optical lattice. *Phys. Rev. Lett.*, 94:190401, 2005.
- [129] C. Reichhardt, G.T. Zimanyi, R.T. Scalettar, A. Hoffmann, and I.K. Schuller. Individual and multiple vortex pinning in systems with periodic pinning arrays. *Phys. Rev. B*, 64:144509, 2001.
- [130] J. W. Reijnders and R. A. Duine. Pinning of vortices in a Bose-Einstein condensate by an optical lattice. *Phys. Rev. Lett.*, 93:060401, 2004.
- [131] J. W. Reijnders and R. A. Duine. Pinning and collective modes of a vortex lattice in a Bose-Einstein condensate. *Phys. Rev. A*, 71:063607, 2005.
- [132] J. W. Reijnders, F. J. M. van Lankvelt, K. Schoutens, and N. Read. Rotating spin-1 bosons in the lowest Landau level. *Phys. Rev. A*, 69:023612, 2004.
- [133] D. Resnick, J.C. Garland, J.T. Boyd, S. Shoemaker, and R.S. Newrock. Kosterlitz-Thouless transition in proximity-coupled superconducting arrays. *Phys. Rev. Lett.*, 47:1542, 1981.
- [134] A. M. Rey, V. Gritsev, I. Bloch, E. Demler, and M. D. Lukin. Preparation and detection of magnetic quantum phases in optical superlattice. *Phys. Rev. Lett.*, 99:140601, 2007.
- [135] S. Richard, F. Gerbier, J. H. Thywissen, M. Hugbart, P. Bouyer, and A. Aspect. Momentum spectroscopy of 1d phase fluctuations in Bose-Einstein condensates. *Phys. Rev. Lett.*, 91:010405, 2003.
- [136] C. Ryu, M.F. Andersen, P. Cladé, V. Natarajan, K. Helmerson, and W.D. Phillips. Observation of persistent flow of a Bose-Einstein condensate in a toroidal trap. *Phys. Rev. Lett.*, 99:260401, 2007.
- [137] L. E. Sadler, J. M. Higbie, S. R. Leslie, M. Vengalattore, and D. M. Stamper-Kurn. Spontaneous symmetry breaking in a quenched ferromagnetic spinor Bose-Einstein condensate. *Nature*, 443:312, 2006.
- [138] A. Safonov, S.A. Vasilyev, I.S. Yasnikov, I.I. Lukashevich, and S. Jaakkola. Observation of quasicondensate in two-dimensional atomic hydrogen. *Phys. Rev. Lett.*, 81:4545, 1998.
- [139] M. M. Salomaa and G. E. Volovik. Quantized vortices in superfluid ^3He . *Rev. Mod. Phys.*, 59:533, 1987.
- [140] T. Sato, T. Ishiyama, and T. Nikuni. Vortex lattice structures of a Bose-Einstein condensate in a rotating triangular lattice potential. *Phys. Rev. A*, 76:053628, 2007.

- [141] D. R. Scherer, C. N. Weiler, T. W. Neely, and B. P. Anderson. Vortex formation by merging of multiple trapped Bose-Einstein condensates. Phys. Rev. Lett., 98:110402, 2007.
- [142] V. Schweikhard. Ultracold atoms in a far detuned optical lattice. Diploma Thesis, University of Stuttgart (2001).
- [143] V. Schweikhard, I. Coddington, P. Engels, V. P. Mogendorff, and E. A. Cornell. Rapidly rotating Bose-Einstein condensates in and near the lowest Landau level. Phys. Rev. Lett., 92:040404, 2004.
- [144] V. Schweikhard, I. Coddington, P. Engels, S. Tung, and E. A. Cornell. Vortex-lattice dynamics in rotating spinor Bose-Einstein condensates. Phys. Rev. Lett., 93:210403, 2004.
- [145] V. Schweikhard, S. Tung, and E. A. Cornell. unpublished. See chapter 4.
- [146] V. Schweikhard, S. Tung, and E. A. Cornell. Vortex Proliferation in the Berezinskii-Kosterlitz-Thouless Regime on a Two-Dimensional Lattice of Bose-Einstein Condensates. Phys. Rev. Lett., 99:030401, 2007.
- [147] D. E. Sheehy and L. Radzihovsky. Vortex lattice inhomogeneity in spatially inhomogeneous superfluids. Phys. Rev. A, 70:051602(R), 2004.
- [148] D. E. Sheehy and L. Radzihovsky. Vortices in spatially inhomogeneous superfluids. Phys. Rev. A, 70:063620, 2004.
- [149] T. Simula and P. Blakie. Thermal activation of vortex-antivortex pairs in quasi-two-dimensional Bose-Einstein condensates. Phys. Rev. Lett., 96:020404, 2006.
- [150] T. P. Simula, P. Engels, I. Coddington, V. Schweikhard, E. A. Cornell, , and R. J. Ballagh. Observations on sound propagation in rapidly rotating Bose-Einstein condensates. Phys. Rev. Lett., 94:080404, 2005.
- [151] J. Sinova, C. B. Hanna, and A. H. MacDonald. Quantum melting and absence of Bose-Einstein condensation in two-dimensional vortex matter. Phys. Rev. Lett., 89:030403, 2002.
- [152] J. Sinova, C. B. Hanna, and A. H. MacDonald. Measuring the condensate fraction of rapidly rotating trapped Boson systems: Off-diagonal order from the density profile. Phys. Rev. Lett., 90:120401, 2003.
- [153] Michiel Snoek and H. T. C. Stoof. Theory of vortex-lattice melting in a one-dimensional optical lattice. Phys. Rev. A, 74:033615, 2006.
- [154] Michiel Snoek and H. T. C. Stoof. Vortex-lattice melting in a one-dimensional optical lattice. Phys. Rev. Lett., 96:230402, 2006.
- [155] E.B. Sonin. Continuum theory of Tkachenko modes in rotating Bose-Einstein condensate. Phys. Rev. A, 71:011603(R), 2005.
- [156] A.S. Sørensen, E. Demler, and M.D. Lukin. Fractional quantum Hall states of atoms in optical lattices. Phys. Rev. Lett., 94:086803, 2005.

- [157] Dan M. Stamper-Kurn. Peeking and poking at a new quantum fluid: Studies of gaseous Bose-Einstein condensates in magnetic and optical traps. PhD thesis, MIT, 2000.
- [158] P.W. Stephens, P.A. Heiney, R.J. Birgeneau, P.M. Horn, D.E. Moncton, and G.S. Brown. High-resolution x-ray-scattering study of the commensurate-incommensurate transition of monolayer Kr on graphite. Phys. Rev. B, 29:3512, 1984.
- [159] T. Stöferle, H. Moritz, C. Schori, M. Köhl, and T. Esslinger. Transition from a strongly interacting 1D superfluid to a Mott insulator. Phys. Rev. Lett., 92:130403, 2004.
- [160] S. Teitel and C. Jayaprakash. Josephson-junction arrays in transverse magnetic fields. Phys. Rev. Lett., 51:1999, 1983.
- [161] M. Tinkham. Introduction to Superconductivity. McGraw-Hill, Inc.
- [162] V. K. Tkachenko. Stability of vortex lattices. Sov. Phys. JETP, 23:1049, 1966.
- [163] A. Trombettoni, A. Smerzi, and P. Sodano. Observable signature of the Berezinskii-Kosterlitz-Thouless transition in a planar lattice of Bose-Einstein condensates. New J. Phys., 7:57, 2005.
- [164] S. Tung, V. Schweikhard, and E. A. Cornell. Observation of vortex pinning in Bose-Einstein condensates. Phys. Rev. Lett., 97:240402, 2006.
- [165] S. Viefers. Quantum hall physics in rotating Bose-Einstein condensates. arxiv:0801.4856, 2008.
- [166] P. Vignolo, R. Fazio, and M.P. Tosi. Quantum vortices in optical lattices. Phys. Rev. A, 76:023616, 2007.
- [167] J.E. Villegas, S. Savelev, F. Nori, E.M. Gonzalez, J.V. Anguita, Garcia, and J.L. Vicent. A superconducting reversible rectifier that controls the motion of magnetic flux quanta. Science, 302:1188, 2003.
- [168] Congjun Wu, Han dong Chen, Jiang piang Hu, and Shou-Cheng Zhang. Vortex configurations of bosons in an optical lattice. Phys. Rev. A, 69:043609, 2004.
- [169] Hui Zhai, Qi Zhou, Rong Lv, and Lee Chang. Double-layer Bose-Einstein condensates with large number of vortices. Phys. Rev. A, 69:063609, 2004.
- [170] W. Zwerger. Mott-hubbard transition of cold atoms in optical lattices. J Opt. B: Quant. Semiclass. Opt., 5:S9–16, 2003.

Appendix A

Accurate optical dipole potential calculation

In this Appendix I describe the formulae used in this thesis to precisely calculate the dipole potential exerted on atoms by off-resonant light. As shown in Section 1.5.1, the potential energy of an atom in a light field of intensity $I(\vec{r})$ may be written as

$$U_{dip}(\vec{r}) = -\frac{1}{2\epsilon_0 c} \text{Re}(\alpha) I(\vec{r}) \quad (\text{A.1})$$

For multilevel atoms, the polarizability contains contributions from all excited states, which have to be summed up.

Depending on the laser detuning with respect to a given transition, fine structure and hyperfine structure components may have to be considered individually, with the transition strength of the respective line distributed over all sublevels. In this thesis the laser detuning is always much larger than any of the relevant hyperfine splittings, but not necessarily much larger than fine structure splittings.

Following Grimm and coworkers [70], the polarizability then contains a scalar term, independent of the ground state magnetic sublevel m_F , as well as a vector term which acts differently on the magnetic sublevels, and is therefore called a fictitious magnetic field [52]. For the example of the dominant $5S_{1/2} \rightarrow 5P_J$ transition of ^{87}Rb , which is split into two fine structure components, the D1 line ($J = 1/2$) at a wavelength

of $\lambda = 794.98 \text{ nm}$ and D2 line ($J = 3/2$, $\lambda = 780.24 \text{ nm}$), one obtains

$$U_{dip}(\vec{r}) = \sum_{J=1/2, J=3/2} \frac{\pi c^2}{2\omega_{at,J}^3} \left(\frac{\Gamma_J}{\delta_J} - \frac{\Gamma_J}{\delta_{+,J}} \right) \left[c_J^2 - i\sigma_J g_F m_F (\vec{\mathcal{E}}^* \times \vec{\mathcal{E}}) \cdot \hat{B} \right] I(\vec{r}) \quad (\text{A.2})$$

Here, $\delta = \omega - \omega_{at}$ is the detuning of the light field at frequency ω from the atomic resonance at ω_{at} , and $\delta_+ = \omega + \omega_{at}$ represents the so-called counter-rotating term. $\vec{\mathcal{E}}(\vec{r})$ is the polarization unit vector, and * denotes the complex conjugate. \hat{B} is a unit vector along the magnetic field direction. \hat{I} is the unity operator, c_J is a coefficient for the transition $5S_{1/2} \rightarrow 5P_J$ ($c_{3/2}^2 = 2$, $c_{1/2}^2 = 1$), and $\sigma_J = \begin{Bmatrix} +1 \\ -1 \end{Bmatrix}$ for the transition to $5P_J$, with $J = \begin{Bmatrix} 3/2 \\ 1/2 \end{Bmatrix}$.

Spontaneous scattering of laser photons occurs at a rate

$$\Gamma_{scat}(\vec{r}) = \sum_{J=1/2, J=3/2} \frac{\pi c^2}{2\hbar\omega_{at,J}^3} \left(\frac{\Gamma_J}{\delta_J} - \frac{\Gamma_J}{\delta_{+,J}} \right)^2 \left[c_J^2 - i\sigma_J g_F m_F (\vec{\mathcal{E}}^* \times \vec{\mathcal{E}}) \cdot \hat{B} \right] I(\vec{r}) \quad (\text{A.3})$$

Each scattering event imparts a recoil momentum to the atom, on average increasing its energy by $\hbar^2 k^2 / 2m \times 4 \langle \cos^2(\theta) \rangle = 2E_{rec}$. Here, θ is the half angle between incoming and scattered photon, and $E_{rec} = \hbar^2 k^2 / 2m$ is the laser recoil energy. The rate of temperature increase is therefore of the order of $\Gamma_{scat}(\vec{r}) \times 2E_{rec}$.

Appendix B

Numerical determination of finite-T BEC parameters in a double well potential

Here, the numerical procedure is outlined for determining the Josephson coupling J for the experiments on the BKT transition described in Chapter 3. To our knowledge, no accurate analytical formula exists that relates the Josephson coupling J to the number of particles per well N_{well} and the applied optical lattice depth V_{OL} . In the framework of the two-mode approximation, the Josephson coupling is found from energy differences between the two lowest states of the double well potential [9]:

$$J = N_{well}((E_{tot}^{AS} - E_{tot}^{SYM}) - \frac{1}{2}(E_{int}^{AS} - E_{int}^{SYM})) \quad (\text{B.1})$$

where E_{tot}^{SYM} (E_{tot}^{AS}) is the total energy per particle of the lowest spatially symmetric (antisymmetric) state in the double well potential, given N_{well} particles in each well, and E_{int}^{SYM} (E_{int}^{AS}) are the respective interaction energies per particle.

To evaluate (B.1) we numerically find the three-dimensional ground and first excited state of the Gross-Pitaevskii equation, Eq. (1.9), for an interacting BEC in a double well potential. This potential, a 2D cut of which is shown in in Fig. B.1, is constructed from a hexagonal optical lattice of $4.7 \mu m$ period formed from three beams intersecting in the xz plane ¹ at 120° , and a harmonic confining potential with a harmonic oscillator frequency of $15 Hz$ along the y-direction. The potential is padded

¹ The convention for the y and z axes in this Appendix is different than throughout the thesis! Everywhere else, the 2D lattice is in the xy plane and z is the transverse axis.

with a constant value outside dashed lines in Fig. B.1 to confine the wavefunction to two wells, with the section lines chosen such as to avoid discontinuities in the potential. Initial, spatially symmetric (antisymmetric) trial wavefunctions, are constructed from the sum (difference) of two Gaussians in the xz plane, centered at the two potential minima, while in the y -direction a wavefunction resulting in a parabolic Thomas-Fermi density profile is employed.

Calculations are performed on a 3D grid of $210 \times 180 \times 70$ points (directions x,y,z). Here x is the axis connecting the two wells, z is the second dimension in the optical lattice plane, and y is the third dimension, along which each lattice site is elongated and cylindrically symmetric. The real space size of the grid is $21 \mu m \times 180 \mu m \times 14 \mu m$, resulting in spatial grid steps of $dx = 0.1 \mu m$; $dy = 1 \mu m$; $dz = 0.2 \mu m$.

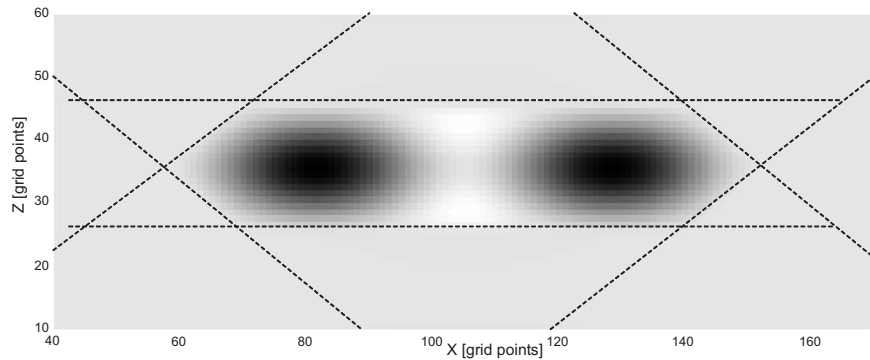


Figure B.1: 2D cut through the potential energy grid used for numerical solution of GPE. Dark regions show the double well potential minima. Outside the dashed lines the optical lattice potential was replaced by a constant potential to isolate one double-well. Note that the vertical dimension of the image is compressed by 2x compared to real space!

The iterative numerical procedure, based on a split-step-Fourier imaginary time propagation, is sketched in Fig. B.2. As is well known, imaginary-time propagation finds the ground state of a given system. What is less well known is that for an initial trial wavefunction of odd spatial symmetry, that symmetry is preserved throughout the propagation, and thus in our case the first excited state is found.

The zero-temperature part of the calculation is sketched in the upper loop of

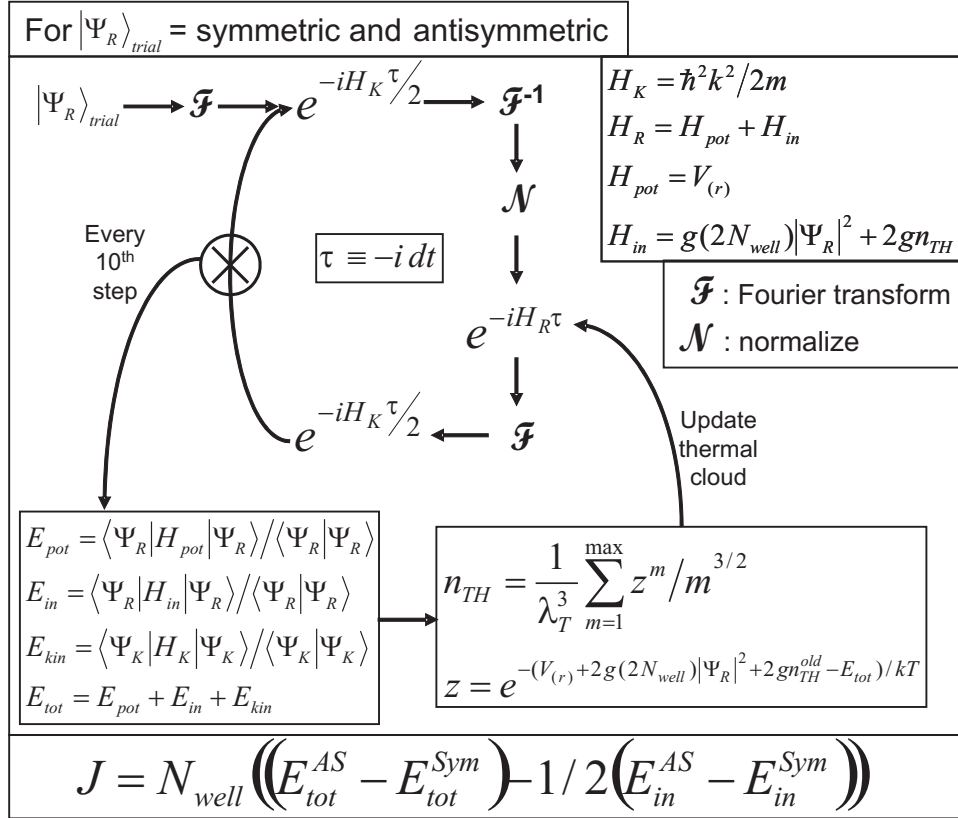


Figure B.2: Finite-temperature code for numerical solution of the Gross-Pitaevskii equation, to determine the Josephson coupling energy J . Ψ_R is a real-space wavefunction, that is propagated by a series of steps τ in imaginary time until convergence of the total energy E_{tot} is achieved. The procedure is repeated twice, for a symmetric (antisymmetric) Ψ_R , to find the ground (first excited) state, respectively. J is then computed according to Eq. (B.1). For finite-temperature calculations, a thermal cloud density profile n_{TH} is constructed and iteratively updated as well. Thermal cloud and condensate mutually influence each other through their mean-field repulsion.

Fig. B.2. To find the ground state, a spatially symmetric trial wavefunction is Fourier-transformed to k-space and propagated under the influence of the kinetic-energy term H_k for 1/2 imaginary-time-step. After inverse Fourier-transform and normalization, it is propagated for a full step under influence of potential (H_{pot}) and nonlinear interaction energy (H_{in}). It is then again transformed to k-space, and propagated following the kinetic-energy term H_k for the second 1/2 step. At this point, all contributions to the total energy are evaluated. The loop repeats until the total energy converges to a desired

accuracy. The calculation is then repeated to find the first excited state, starting from a spatially antisymmetric trial wavefunction. At this point J is calculated according to Eq. (B.1).

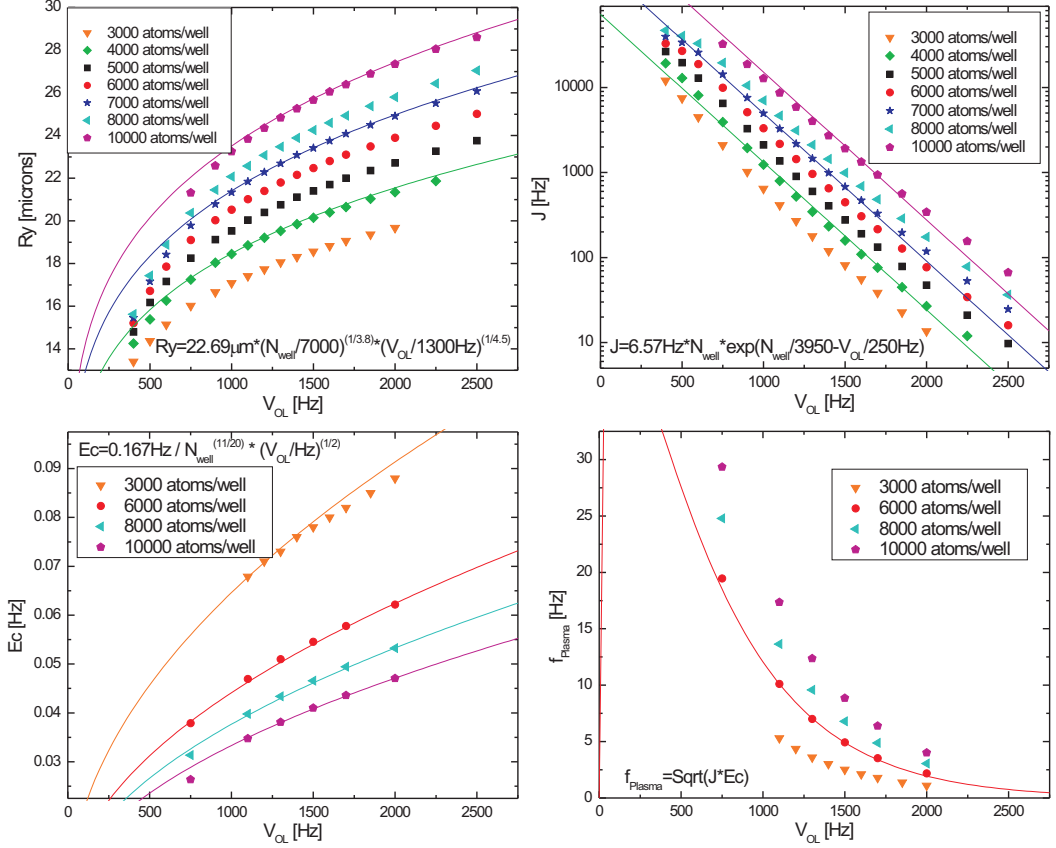


Figure B.3: Results of double-well GPE simulations at zero T. Plotted are numerical data points for axial condensate radius R_y , Josephson coupling J , charging energy E_c and plasma frequency f_p vs. optical lattice depth V_{OL} for various number of condensed particles per well N_{well} .

Results of zero-temperature calculations, repeated for various optical lattice depths V_{OL} and condensate numbers per site, N_{well} , are shown in Fig. B.3. In addition to $R_y(V_{OL}, N_{well}, T = 0)$ and $J(V_{OL}, N_{well}, T = 0)$, the charging energy E_c and plasma frequency f_p are shown.

We have extended our procedure to take into account finite- T corrections, by including the mutual mean-field repulsions between BEC and thermal cloud. This is

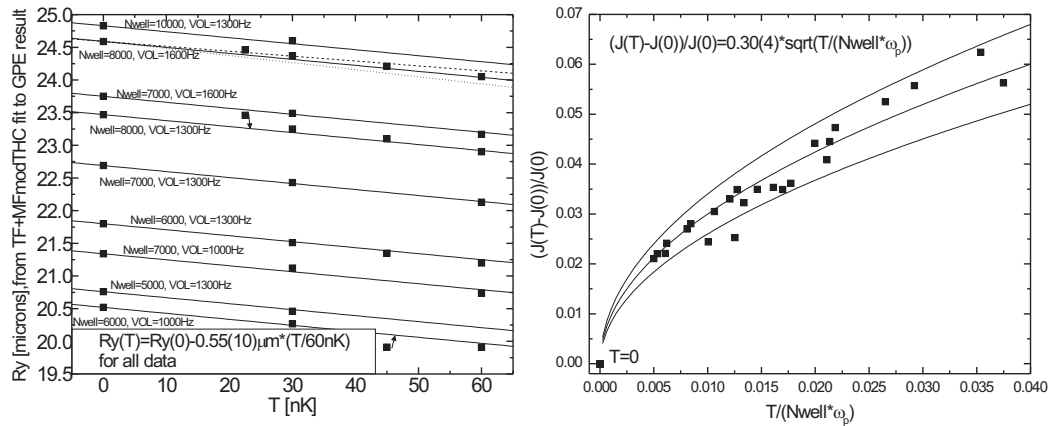


Figure B.4: Finite T corrections to GPE simulation results. Left: slight compression of the axial BEC radius with increasing T by the repulsive mean field of the thermal cloud. Right: increase in J due to lifting-up of the condensate chemical potential by the repulsive thermal cloud.

achieved by employing a Hartree-Fock-type density profile for the thermal cloud [112], as given in the lower right box in Fig. B.2. This thermal cloud density n_{th} enters the BEC wavefunction through its repulsive mean field exerted onto the BEC, i.e. the $2gn_{th}$ term in H_{in} . Conversely, the BEC's mean field repels the thermal cloud. Therefore the thermal cloud density is iteratively updated after every tenth step of the propagation, according to the evolution of the BEC density profile.

Finite- T corrections are shown in Fig. B.4. They consist of two separate effects: the left panel shows the slight compression of the axial BEC radius R_y with increasing T due to mean field repulsion by the inhomogeneous thermal cloud density. The right panel shows the second effect, the increase of J due to the lifting-up of the BEC chemical potential by the thermal cloud's mean field. The peculiar x-axis $T/(N_{well}\omega_p)$ was chosen because for this parameter combination, numerical data from different N_{well} , T , VOL showed best collapse onto one common curve.

Putting it all together, we obtain two results: First, accurate parameter determination for every experimental shot is achieved by interpolation between nearest numerical data points, as described in Section 3.3. Second, a useful approximation for

J results, valid in the range of N_{well} and V_{OL} employed in our experiments

$$J(V_{OL}, N_{well}, T) \approx 0.315 \text{ nK} \times N_{well} \exp\left(\frac{N_{well}}{3950} - \frac{V_{OL}}{244 \text{ Hz}}\right) \times \left(1 + \frac{0.59 T}{100 \text{ nK}}\right) \quad (\text{B.2})$$

We note however that at the edges of the range of V_{OL} in Fig. B.3, the limitations of this approximation become visible. For the axial condensate radius we find

$$R_y(T) = R_y(0) - 0.55(10) \mu\text{m} \times T/60 \text{ nK} \quad (\text{B.3})$$

with

$$R_y(0) \equiv R_y(V_{OL}, N_{well}, T = 0) = 22.69 \mu\text{m} \times (N_{well}/7000)^{(1/3.8)} \times (V_{OL}/1300 \text{ Hz})^{(1/4.5)} \quad (\text{B.4})$$

The charging energy is found to be

$$E_c = E_c = 0.167 \text{ Hz} / N_{well}^{(11/20)} \times (V_{OL}/\text{Hz})^{(1/2)} \quad (\text{B.5})$$

which allows e.g. calculation of the plasma frequency according to $f_p = \sqrt{J E_c}$.

Appendix C

Calculation of the vortex pinning potential

Here I calculate the pinning potential experienced by a vortex. Pinning is due to the density modulation in the BEC created by the optical lattice. A vortex position (x) in a region of low density $n_{SF}(x)$ ¹ is less costly, as can be seen by the total energy $E(x)$ of one vortex of length L given by Eq. (1.20) in the introduction

$$E(x) = \pi\hbar^2/m n_{SF}(x)L \ln(R/\xi) \quad (\text{C.1})$$

Here R the Thomas-Fermi radius and ξ the healing length. The logarithmic term is $\sim 4 - 5$ for our BEC.

For the density I use the Thomas-Fermi approximation and assume $V_{OL} < \mu$

$$n_{SF}(x) = 1/g (\mu - V_{OL}(x)) \quad (\text{C.2})$$

with $g = 4\pi\hbar^2 a_{sc}/m$, the chemical potential μ and the optical lattice potential $V_{OL}(x) = V_0(\sin^2(\pi x/d))$ with period d . Keeping only vortex-position dependent terms this gives a pinning energy

$$E_{pin}(x) \approx -\frac{L}{a_{sc}} V_{OL}(x) \quad (\text{C.3})$$

which is up to a numerical factor consistent with the result of Reijnders et al. [130, 131] (their results indicate a \sim half as strong pinning potential).

¹ $n_{SF}(x)$ is the superfluid density imposed by the external potential, *without* the presence of the vortex. For the derivation to be valid, $n_{SF}(x)$ must vary smoothly on the scale of the vortex core.

Appendix D

Rapidly rotating Bose gases: Vortex lattice physics and beyond

This extended appendix details several interesting scenarios for rotating Bose gases [4]. Many of the considerations described herein provided a major motivation for the general direction of experiments conducted during this thesis.

We are interested here in superfluids containing large numbers of vortices, such that the coarse-grained superfluid velocity profile (and with it, the vortex lattice) undergoes rigid-body rotation $\vec{v}_s = \vec{\Omega} \times \vec{r}$. One of the most fascinating aspects of such rotating superfluids is their fundamental analogy to superconductors, or two-dimensional electron gases, subjected to a strong magnetic field. This is perhaps easiest understood by noting that the Coriolis force $\vec{F}_C = 2m\vec{v} \times \vec{\Omega}$ experienced by a particle with mass m moving with a velocity \vec{v} *in the rotating frame* $\vec{\Omega}$ is fully analogous to the Lorentz force $\vec{F}_L = q\vec{v} \times \vec{B}$ on a charged particle ($q \equiv 2e$ for Cooper pairs in a superconductor, $q \equiv e$ for a 2D electron gas) in a magnetic field \vec{B} . The fields $\vec{\Omega}$ and \vec{B} can be written in terms of a vector potential \vec{A} , most conveniently expressed as $\vec{A}_C = \frac{1}{2}\vec{\Omega} \times \vec{r}$ and $\vec{A}_L = \frac{1}{2}\vec{B} \times \vec{r}$, respectively.

Upon transforming to the coordinate frame co-rotating with the vortex lattice, the GPE, Eq. (1.9), is modified by the usual $-\vec{\Omega} \cdot \vec{L}$ term. In order to clarify the physical effects occurring in the rotating frame, this equation may be rewritten to take the form

$$\left(\frac{1}{2m} (-i\hbar\vec{\nabla} - \vec{\Pi})^2 + g|\Psi|^2 + V_{(\vec{r})} - \frac{m}{2}\Omega^2(x^2 + y^2) \right) \Psi = \mu\Psi \quad (\text{D.1})$$

Here, $\vec{\Pi} \equiv 2m\vec{A}_C$ describes the effects of the Coriolis force, $V(\vec{r}) = \frac{1}{2}m(\omega_\rho^2 r^2 + \omega_z^2 z^2)$ is the magnetic trapping potential, which is radially weakened by the anti-confining effect $-\frac{m}{2}\Omega^2(x^2 + y^2)$ of the centrifugal force, resulting in a reduced radial trap frequency $\sqrt{\omega_\rho^2 - \Omega^2}$.

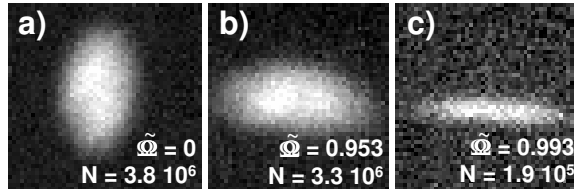


Figure D.1: Side view images of BECs in trap. The rotation axis is vertical. (a) Static BEC. The aspect ratio $R_z/R_\rho = 1.57$ follows the prolate trap shape. (b) Rotating BEC, $\tilde{\Omega} = 0.953$, (c) $\tilde{\Omega} = 0.993$. Centrifugal distortion causes the BEC to spin out into a low-density quasi-2D cloud. From Ref. [143].

In this section we examine the high rotation limit, i.e. $\tilde{\Omega} \equiv \Omega/\omega_\rho \rightarrow 1$ [143], where the centrifugal force quite nearly cancels the radial confining force, and the BEC spins out into a low-density cloud, as shown in Fig. D.1. For sufficiently high rotation rates, the BEC approaches the quasi-two-dimensional regime, where the strength of interactions gn is reduced below the axial oscillator energy, $\Gamma_{2D} \equiv \frac{gn}{\hbar\omega_z} < 1$, and axial motion is frozen out. We are then left with a quasi-2D system described by

$$\left(\frac{1}{2m}(-i\hbar\vec{\nabla}_\perp - m\vec{\Omega} \times \vec{r})^2 + g|\Psi|^2 \right) \Psi = \mu\Psi \quad (\text{D.2})$$

The first term describes the 2D kinetic energy of particles moving in the external vector potential introduced by the rotation. It is identical to the *integer* quantum-Hall Hamiltonian, whose eigenvalues are the Landau levels with an energy spacing $2\hbar\Omega$. The interaction energy term provides the necessary ingredient to observe *fractional* quantum Hall physics. The situation is illustrated in Fig. D.2.

The physics of such rapidly rotating 2D Bose gases is characterized by two parameters. The first one is the so-called Landau level parameter

$$\Gamma_{LLL} = \frac{gn}{2\hbar\Omega} \quad (\text{D.3})$$

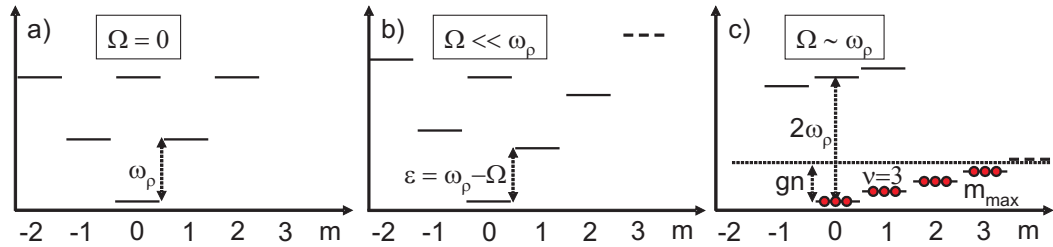


Figure D.2: a) single-particle energy levels of the static 2D harmonic oscillator, in a circular basis where m denotes angular momentum projection quantum number. b) rotation Ω induces an energy splitting between positive and negative m sublevels. c) in the limit of fast rotation the positive m states form a band of near-degenerate levels - the lowest Landau level (LLL). Higher Landau levels are separated by $2\omega_\rho \sim 2\Omega$. Dotted line: the interaction energy per particle, gn , indicates which states are occupied by the interacting rotating Bose gas. If the LLL parameter $\Gamma_{LLL} = \frac{gn}{2\hbar\Omega}$ is smaller than unity, only states in the LLL are occupied. The maximum index m_{max} is identical to the number of vortices (flux quanta) in the system. The filling factor ν gives the occupancy of m -sublevels by bosons, here $\nu = 3$. For $\nu \gg 1$ a mean field vortex lattice results, while for $\nu \sim 1$ correlated states similar to fractional quantum Hall states appear.

which describes the ratio of interaction energy per particle to Landau level spacing. Under the condition $\Gamma_{LLL} < 1$, the condensate primarily occupies single-particle states in the lowest Landau level (LLL). These form a ladder of near-degenerate states, with a frequency splitting of $\epsilon = \omega_\rho - \Omega$ as shown in Fig. D.2 (the degeneracy is lifted by the residual imbalance between centrifugal force and radial trapping force). The number of occupied states in the LLL is $m_{max} \approx \frac{gn}{\hbar\epsilon}$, and is identical to the number of vortices (flux quanta) in the system. In order to observe effects of the near-degeneracy in the LLL, $m_{max} \gg 1$ is required.

The second parameter is the filling factor ν , given by the ratio of the number of particles N_p to the number of vortices N_v (or occupied sublevels in the LLL)¹:

$$\nu \equiv N_p/N_v \equiv n_{SF,2D}/n_v \quad (\text{D.4})$$

which can interestingly be expressed in terms of the energy scale $\hbar\Omega$ and the BKT

¹ Note that for fermions $\nu \leq \Gamma_{LLL}$ (“=” applies at $T = 0$), enforced by the Pauli principle. For bosons no such restriction applies, and ν may be arbitrarily big for any given Γ_{LLL} .

temperature of the static superfluid $k_B T_{BKT}$

$$1/\nu \equiv \frac{n_v}{n_{SF,2D}} = \frac{\hbar\Omega}{2\frac{\pi\hbar^2}{2m}n_{SF,2D}} = \frac{1}{2} \frac{\hbar\Omega}{k_B T_{BKT}} \quad (\text{D.5})$$

For rotating bosons in the LLL, the filling factor distinguishes three regimes: For $\nu \gg 1$ the condensate forms a classical superfluid in the mean-field LLL regime [77, 22, 21] and continues to form an ordered vortex lattice. With decreasing filling factor, the elastic shear strength of the vortex lattice decreases. For filling factors below $\nu \approx 10$ the shear strength is predicted to drop sufficiently for quantum fluctuations to melt the vortex lattice [47, 151]. For $\nu \sim 1$ a variety of correlated states similar to those in the Fermionic fractional QHE are predicted to appear [47], as well as quasiparticle excitations obeying fractional statistics [118]. In the third regime, $\nu \ll 1$, a Wigner-crystal like phase is expected, where rotating bosons form an ordered lattice immersed in a huge number of flux quanta (analogous to vortices forming a lattice when $\nu \gg 1$). This regime is admittedly esoteric given present experimental capabilities.

We note here that in a 2D system, Landau level parameter and filling factor are proportional to each other

$$\Gamma_{LLL} = \nu \times \sqrt{\frac{2}{\pi}} a_{sc}/l_z \quad (\text{D.6})$$

where $l_z \equiv \sqrt{\frac{\hbar}{m\omega_z}}$ is the harmonic oscillator length of the axial trap potential.

D.1 Lowest Landau level: Vortex core overlap and transition to normal state?

This section is a short note on the mean-field LLL regime, Refs. [143, 45]. For low rotation rates, vortex cores are essentially line-like, well separated objects, whereas for large rotation rates, the vortex cores occupy a finite fraction of the condensate volume, see Fig. D.3. This is analogous to the behavior of magnetic-field induced vortices in Type-II superconductors, where the growth, and ultimately overlap, of vortex cores with increasing magnetic field triggers the breakdown of superfluidity at the so-called upper

critical field $H_{c,2}$. In this section we investigate whether this happens analogously in a weakly interacting Bose gas.

We define the fractional surface area \mathcal{A} occupied by the vortices to be $\mathcal{A} = n_v \pi r_v^2$, where n_v is given by (1.22) and r_v by (1.19). The resulting prediction for the fractional vortex core area \mathcal{A} may be cast in terms of the Landau level parameter Γ_{LLL}

$$\mathcal{A} = 1.34 \times (\Gamma_{LLL})^{-1} \quad (\text{D.7})$$

The prediction for \mathcal{A} exceeds unity when $\Gamma_{LLL} < 1.34$, which has led to the prediction that vortices should merge in the LLL limit, as is observed in type-II superconductors (and as should be expected in a Cooper-paired rotating Fermi gas): Due to strong interactions in these systems, the vortex cores are filled with material in the normal phase, and vortex core overlap leads to the breakdown of type-II superconductivity. This occurs at a critical field $\mu_0 H_{c,2} \approx \frac{\Phi_0}{\pi \xi^2}$, where there is one magnetic flux quantum Φ_0 per vortex core area $\pi \xi^2$ ².

But careful, not so in a BEC! Vortex cores cease to grow according to (D.7) when Γ_{LLL}^{-1} reaches unity – they even get compressed with increasing rotation! Ultimately, the reason for this difference in behavior is that the freedom of breaking a Cooper pair is not available, and the system HAS to remain condensed until a different kind of physics destroys BEC. A more elaborate treatment by Baym and coworkers [22] consequently predicts that \mathcal{A} saturates at 0.225 in the LLL.

Our measured data for \mathcal{A} are plotted in Fig. D.3 vs. $\Gamma_{LLL}^{-1} \equiv 2\hbar\Omega/(gn)$. For $\Gamma_{LLL}^{-1} < 0.1$ the data agree reasonably well with the numerical result (D.7). For larger Γ_{LLL}^{-1} the data clearly show saturation of \mathcal{A} at a value close to the LLL limit $\mathcal{A} = 0.225$ [22], rather than a divergence of \mathcal{A} as $\tilde{\Omega} \rightarrow 1$.

² For rotating He-II, this regime is unattainable: Due to the small healing length $\xi \approx$ a few \AA , the condition for vortex core overlap, $\xi \approx \ell$, yields the unattainably large value $\Omega \approx 10^{15} \text{ rad/s}$.

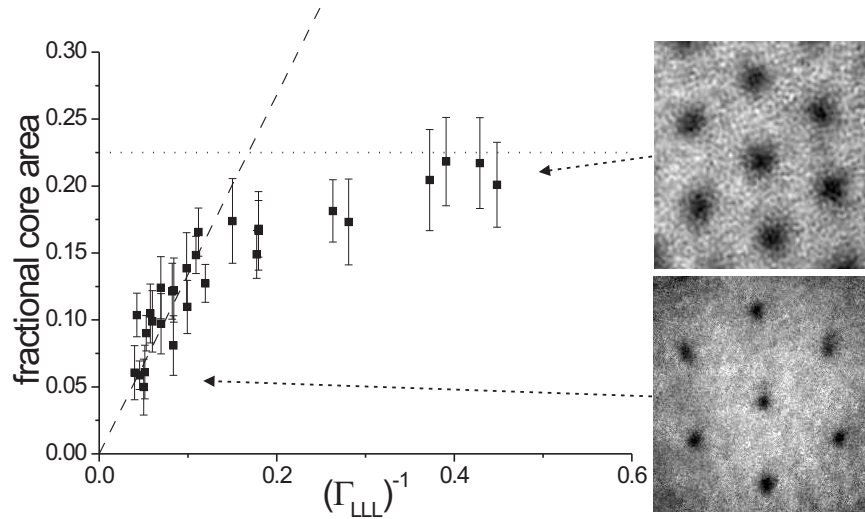


Figure D.3: Fraction of the condensate surface area occupied by vortex cores, \mathcal{A} , measured after condensate expansion, plotted vs. the inverse of the lowest Landau level parameter, $(\Gamma_{LLL})^{-1} = 2\hbar\Omega/\mu$. The data clearly show a saturation of \mathcal{A} , as $\tilde{\Omega} \rightarrow 1$. Dashed line: prediction for isolated vortices, valid at low rotation rate and for superconductors. Dotted line: result of Ref.[8] for the saturated value of \mathcal{A} in the LLL. Adapted from Ref. [45].

D.2 Vortex lattice melting in a quasi-2D BEC

A second possibility of how the vortex lattice may play havoc with superfluidity is the introduction of new low energy degrees of freedom to the superfluid, in the form of long-wavelength vortex lattice fluctuations.

Due to its ordered crystalline structure, the vortex lattice has an associated rigidity and supports transverse elastic modes. These modes were proposed for He-II by Tkachenko in 1966 [162], but never conclusively observed [19]. It was suggested by Anglin [12] that Tkachenko oscillations are also attainable in BEC. A description of Tkachenko modes over the full range of rotation rates was outlined by Baym [20, 21, 63]. Further theoretical studies can be found in [49, 50, 106, 16, 41, 155, 27]. Fig. D.4 shows our measurements of the frequency of the longest-wavelength Tkachenko oscillation in BECs at various rotation rates. In the high rotation limit, the vortex lattice's elastic shear strength is reduced, as evidenced by the observed very low frequency of long wave-

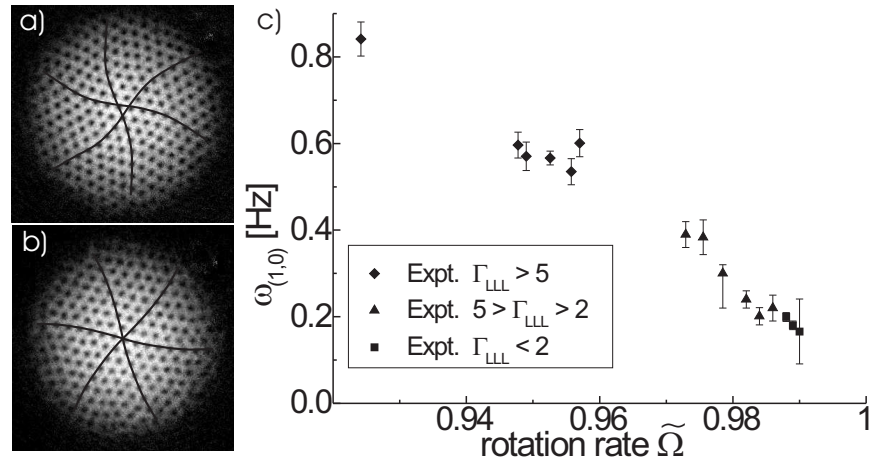


Figure D.4: Tkachenko oscillation in rotating BECs, (a) after the excitation drive is turned off. (b) after one half oscillation period. The low frequency is due to the very small elastic shear strength of the vortex lattice. (c) Measured Tkachenko mode frequency $\omega_{(1,0)}$ vs. BEC rotation rate $\tilde{\Omega}$. Adapted from Refs. [143, 44].

length Tkachenko oscillations. This effect is a precursor to the predicted melting of the lattice under more extreme conditions of rotation or temperature.

The vortex lattice may melt due to quantum or thermal fluctuations [151, 152, 21], which we describe separately below. The situation for a finite-size, trapped BEC has been analyzed by Monte Carlo methods [95].

D.2.1 Quantum melting

To a certain degree it is valid to think of a vortex as an elementary quantum mechanical object, and as such its coordinates (x, y) must undergo a zero point motion. Motion along the two coordinates (x, y) is coupled by the Magnus force. For a two-dimensional superfluid of density n_{2D} , this force is $\vec{F} = mn_{2D} \vec{v} \times \hat{k}$, as seen from eq. (1.28), with the replacement $n_{SFL} \rightarrow n_{2D}$. Here, \vec{v} is the vortex velocity with respect to the superfluid, and $\kappa = h/m$ is the circulation quantum, Eq. (1.18). The corresponding Hamilton's equations reveal that (x, y) are canonically conjugate variables:

$$\frac{\partial H}{\partial x} = -\kappa mn_{2D} \frac{\partial y}{\partial t} \quad \frac{\partial H}{\partial y} = \kappa mn_{2D} \frac{\partial x}{\partial t} \quad (\text{D.8})$$

Comparison to the conventional form of Hamilton's equations

$$\partial H/\partial q = -\partial p/\partial t \quad \partial H/\partial p = \partial q/\partial t \quad (\text{D.9})$$

shows that $q \equiv \sqrt{\kappa m n_{2D}} x$ and $p \equiv \sqrt{\kappa m n_{2D}} y$ are canonically conjugate, and hence must fulfill an uncertainty relation $\Delta q \Delta p > \hbar$, or $\Delta x \Delta y > \hbar/(\kappa m n_{2D})$. For isotropic displacements $\Delta x = \Delta y = \Delta r/\sqrt{2}$ we find the zero point motion of the vortex, expressed in terms of the ‘‘magnetic length’’, Eq. (1.23), which is related to the 2D vortex density by $n_v = 1/(\pi \ell^2)$:

$$\Delta r^2/\ell^2 = n_v/n_{2D} \equiv \frac{1}{\nu}. \quad (\text{D.10})$$

According to the Lindemann criterion (see e.g. [21]) a vortex lattice melts when the zero point motion exceeds 10 – 20% of the vortex spacing, i.e. $\Delta r \sim 0.15 b \sim 0.28 \ell$. Inserting this criterion into Eq. (D.10) we obtain a result consistent with the one of Baym's elaborate calculation [21]

$$n_v/n_{2D} \equiv \frac{1}{\nu} \sim 0.07 \quad (\text{D.11})$$

We thus predict a critical filling factor of $\nu_{crit} \approx 10$ for vortex lattice quantum melting. In Chapter 4 I describe experiments where the lowest filling factors to date, $\nu \approx 100$ were reached. Effects of quantum fluctuations were however not observed, as they were superseded by thermal and possibly technical fluctuations.

D.2.2 Thermal melting

At finite temperature, the vortex lattice may melt due to thermal fluctuations. We have to distinguish between two effects. Low energy, long-wavelength, phonon-like excitations can cause the loss of long-range positional order in the vortex lattice. On the other hand, a BKT-type melting proceeds locally and suddenly, by formation and dissociation of thermally activated vortex-antivortex pairs, which will perturb and ultimately destroy the ordering of the surrounding vortex lattice.

Long wavelength lattice fluctuations. At finite temperature, vortex position fluctuations become thermally activated. We describe the fluctuations by a 2D displacement field $\varepsilon(\vec{r}) \equiv (\varepsilon_x, \varepsilon_y)$. In an ordered vortex lattice such fluctuations cost an energy $E = \int d^2x C_2 \left[\left(\frac{\partial \varepsilon_x}{\partial x} - \frac{\partial \varepsilon_y}{\partial y} \right)^2 + \left(\frac{\partial \varepsilon_x}{\partial y} + \frac{\partial \varepsilon_y}{\partial x} \right)^2 \right]$ [21], where $C_2 = n_{2D} \hbar \Omega / 8$ [50] is the vortex lattice shear modulus. Expansion of $\varepsilon(\vec{r})$ in Fourier components $\varepsilon(\vec{r}) = \sum_{\vec{k}} \varepsilon_{\vec{k}} \exp(i\vec{k} \cdot \vec{r})$ yields $E \approx \sum_{\vec{k}} C_2 \pi R^2 k^2 |\varepsilon_{\vec{k}}|^2$ (R is the condensate radius, and $k \equiv |\vec{k}|$). The Fourier amplitudes $|\varepsilon_{\vec{k}}|$ are determined by equipartition, which states that every Fourier mode contains an energy $\frac{k_B T}{2} \approx C_2 \pi R^2 k^2 |\varepsilon_{\vec{k}}|^2$. The variance of thermally activated vortex displacements $(\Delta r)^2$ thus becomes

$$(\Delta r)^2 \equiv \sum_{\vec{k}} |\varepsilon_{\vec{k}}|^2 \approx \frac{1}{(\Delta k)^2} \int_{k_{min}}^{k_{max}} \frac{2\pi k dk}{k^2} \times \frac{k_B T}{2\pi C_2 R^2} \quad (\text{D.12})$$

The lower momentum cutoff $k_{min} \propto 1/R$ is given by system size R , while $k_{max} \propto 1/\ell$ is set by the minimum lengthscale for vortex fluctuations. $(\Delta k)^2 \approx \frac{\pi k_{max}^2}{N_v} = \frac{\pi}{R^2}$ is the 2D k -space volume per Fourier mode, where we have used $N_v = \frac{\pi R^2}{\pi \ell^2}$. With $\int_{k_{min}}^{k_{max}} dk/k = \ln(R/\ell) = \frac{1}{2} \ln(N_v)$, the final result is, up to numerical factors of order unity, in agreement with Baym's elaborate calculation [21]

$$(\Delta r)^2 / \ell^2 \approx \frac{8 \ln(N_v)}{n_{2D} \lambda_{th}^2}. \quad (\text{D.13})$$

$\lambda_{th} = h / \sqrt{2\pi m k_B T}$ is the thermal de Broglie length. Again, the Lindemann criterion for vortex lattice melting may be applied, $\Delta r \approx 0.15 b \approx 0.28 \ell$, resulting in

$$T_{M,long} \approx T_{BKT} \frac{1}{2 \ln(N_v)}. \quad (\text{D.14})$$

with the static BKT transition temperature T_{BKT} given by Eq. (1.36). For typical conditions $\ln(N_v) \approx 5$, i.e. $T_{M,long} \approx T_{BKT}/10$.

BKT type vortex lattice melting. The two-dimensional vortex lattice falls into the class of “materials” undergoing a BKT transition to a normal state. Huberman and Doniach [82], as well as Gifford and Baym [64] give a condition relating the

vortex lattice melting temperature $T_{M,BKT}$ to the BKT temperature T_{BKT} of the static underlying superfluid

$$T_{M,BKT} \approx T_{BKT} \times \frac{1}{4\pi\sqrt{3}} \quad (\text{D.15})$$

again with Eq. (1.36) for T_{BKT} . The relation (D.5) allows this to be rewritten as

$$k_B T_{M,BKT} \approx \hbar\Omega \times \frac{\nu}{8\pi\sqrt{3}} \approx \hbar\Omega \times \frac{\nu}{44} \quad (\text{D.16})$$

For the rapidly rotating BECs obtained in our magnetic trap [143] we reached $\Omega \gtrsim 0.99\omega_\rho$, i.e. $T_c(\tilde{\Omega}) = T_{c,0} \times (1 - \tilde{\Omega}^2)^{1/3}$ roughly $5.5 nK$. Filling factors were of order $\nu = 500$, and with $\hbar\Omega \sim k_B \times 0.4 nK$ this resulted in a melting temperature $T_{M,BKT} \approx 4.7 nK$, i.e. smaller than the condensation temperature $T_c(\tilde{\Omega})$. An estimate of the actual temperature of the samples is as follows: The coldest temperatures achievable by evaporative cooling are of order of or larger than gn . For $\Gamma_{LLL} \approx 1$ in these condensates, $T \approx gn = 2\hbar\Omega \times \Gamma_{LLL} \approx 1 nK$, i.e. lower than the melting temperature. This is consistent with our observations, which showed that the vortex lattice remained ordered, but became very fragile if temperatures were not kept to the very lowest values possible.

In the experiments on rotating BECs loaded into a 1D optical lattice, described in Chapter 4, thermal fluctuations are much stronger, and thermally induced vortex lattice melting is expected. Signatures consistent with vortex lattice melting are indeed observed, as discussed in detail in Chapter 4.

In conclusion, even though quantum fluctuations are not yet expected to be observable in current experiments, thermal melting of the vortex lattice might well be observable in current and possible near-future experiments rapidly rotating BECs.

D.3 Fractional quantum Hall physics in a rotating Bose gas?

From the considerations above we know that for a superfluid of very low two-dimensional density, the vortex zero point motion is strong enough to melt the ordered vortex lattice. Once the vortex lattice has melted, theory has shown that – at low

enough temperatures, to be specified below – strongly correlated states of the rotating boson system are expected, in analogy to the strongly correlated fractional quantum Hall (FQHE) states of a two-dimensional electron gas in a strong magnetic field [98]. It is not the aim of this section to describe the physics of that regime, but rather to clarify the required experimental conditions and summarize our current knowledge of experimental limitations.

For a harmonic trapping potential, the upper limit on the number N of atoms for obtaining the Laughlin state for a given rotation rate Ω and harmonic trap frequency ω_ρ is on the order of (following e.g. [18]) $N^2(\Omega - \omega_\rho) < \tilde{g}$, where $\tilde{g} = \sqrt{8\pi}\omega_\rho a_{sc}/l_z$. With $\tilde{g} = 0.5\omega_\rho$ (realized for rotating BECs in optical lattices in Chapter 4) and $\Omega = 0.995\omega_\rho$ (realized in our experiments of Ref [143])³, the upper limit is of order $N \sim 10$, a number that would be extremely challenging to be studied in detail with present experimental methods. Experimental efforts are thus blocked by the extreme requirements on achieving rotation frequencies extremely close to the external trapping frequency and working with very small atomic samples, making the system extremely vulnerable to experimental imperfections and instability, as well as placing high requirements on the detection apparatus.

A further consideration in experiments is the achievement of the required low temperatures. The Laughlin state, in essence, is a correlated state in which atoms avoid being in the same place, thus avoiding their effective contact interaction. Therefore the energy gap Δ that protects FQHE states is of the order of the interparticle interaction energy, and the sample temperature must be lower than this gap for correlated states to form:

$$\Delta \sim g_{2D}n_{2D} \equiv \frac{4\pi\hbar^2 a_{sc}}{m\sqrt{2\pi}l_z}n_{2D} \sim 5T_{BKT} \times \frac{a_{sc}}{l_z} \quad (\text{D.17})$$

where Eq. (1.31) was used. In absolute terms, it appears therefore to help if one works in samples with high 2D density to boost T_{BKT} , and in an axially tightly confined

³ Note that $\Omega = 0.995\omega_\rho$ and $\tilde{g} = 0.5\omega_\rho$ were never realized in the *same* experimental setup.

situation, where $\frac{a_{sc}}{l_z}$ is not a small number. Our magnetic trap is quite unsuitable in this respect, as $\frac{a_{sc}}{l_z} \approx 10^{-3}$. In our deep 1D optical lattices in Chapter 4 on the other hand, axial confinement is very tight, $\frac{a_{sc}}{l_z} \approx \frac{1}{10}$. Another approach to boost $\frac{a_{sc}}{l_z}$ would be the use of a Feshbach resonance to increase a_{sc} [28]. Note however that large values of $\frac{a_{sc}}{l_z}$ imply that for filling factors $\nu \approx 1$ the lowest Landau level approximation may break down, see Eq. (D.6), which might possibly alter the appearing correlated states.

On a more sobering note, evaporative cooling does not appear to be a safe strategy to reach the fractional quantum Hall regime, as it is generally speaking limited to temperatures of the order of $g_{2D}n_{2D} \sim \Delta$. Other possible cooling schemes, such as cooling by superfluid immersion, proposed by Zoller and colleagues [68], may be desirable.

Having stated the problems, there are several possible routes that have not been fully explored: The application of an axial optical lattice potential to reduce the filling factor, and to boost axial confinement to make the system two-dimensional, which we have begun to explore in Chapter 4, is certainly worth further study. Even if it turns out that fractional quantum Hall physics is not accessible in this system, thermal fluctuations of 2D vortex lattices will allow further interesting studies.

A recent theoretical proposal [107] indicates that a modification of the radial trapping potential can significantly relax the requirements on rotation rate and small atom number for achieving fractional quantum Hall states.

A particularly attractive scenario would be the creation of FQHE states in rotating Josephson junction arrays. This situation has been studied in a series of articles by R. Bhat, J. Cooper, M. Holland and coworkers [25, 26]. A closely related possibility is the creation of artificial gauge fields in *static* optical lattices, as proposed by Sørensen and coworkers [156, 72] and Mueller [86] and Jaksch and Zoller [109]. This proposal would avoid all technical difficulties associated with mechanical rotation of a quantum system.

Appendix E

Image magnification calibration

The precise calibration of the magnification factor of BEC images is essential for accurate parameter estimation, as all quantitative information is retrieved from measured radii of BECs and thermal clouds. Here we present two – probably highly unusual – ways of determining the magnification factor from in-situ BEC images.

E.1 Top view calibration from in-trap vortex lattice images

For the top view calibration we rely on the precise relation between vortex spacing and BEC rotation rate, given by Eqs. (1.24) and (1.22). During this thesis, we were able for the first time to take in-situ images of the vortex lattice, as shown in Fig. E.1 (a), allowing an accurate extraction of the vortex separation. Precisely, we perform a spatial Fourier Transform of the images, and extract the vortex separation from the position of the reciprocal lattice peaks in Fig. E.1 (a), right panel. The rotation rate *of the same rotating cloud* is accurately measured from the BEC aspect ratio in a non-destructive side-view image. Results are shown in Fig. E.1 (b) for several BECs rotating at various rotation rates.

There are two significant systematic effects. The first one is a known slight modification of the vortex spacing from the prediction of Eq. (1.24). This modification has been calculated [147, 148] and measured [45] to be less than one percent for our conditions. The second systematic effect is a lensing effect from the inhomogeneous

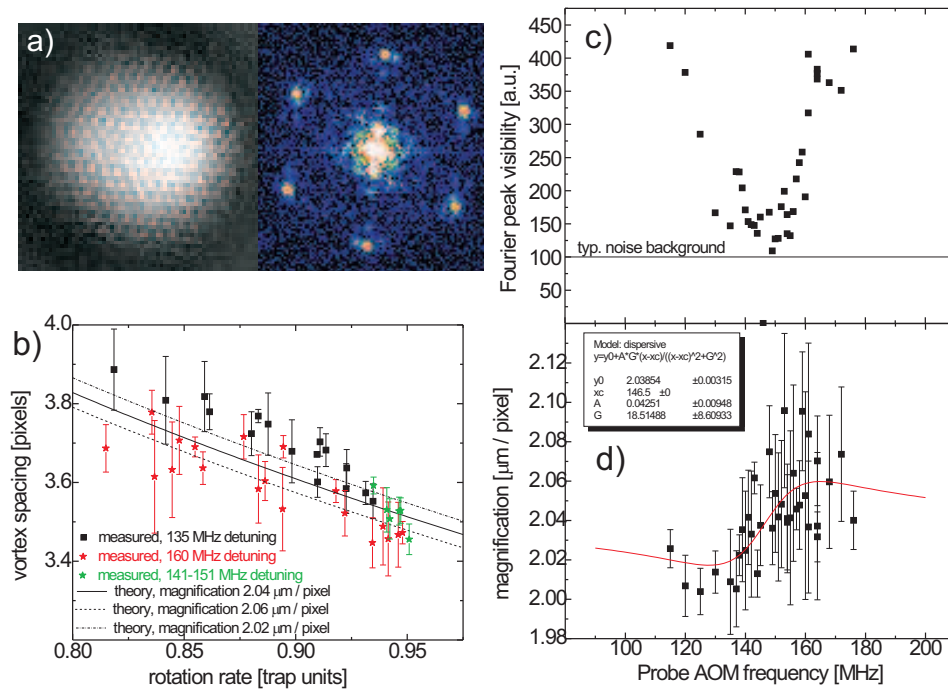


Figure E.1: Calibration of top view image magnification using in-trap vortex lattice images. (a) in-trap vortex lattice image and its spatial Fourier transform (FFT). The vortex separation is inferred from the position of the reciprocal lattice peaks occurring in the FFT. (b) dependence of the measured vortex separation on rotation rate (symbols), and theory (lines) assuming different image magnifications. (c), (d) dependence of Fourier peak amplitude and inferred vortex separation on probe laser detuning from the D2 ($F = 1 \rightarrow F' = 0$) optical transition (150 MHz is on resonance). (c) the Fourier peak amplitude tends to zero on-resonance due to the high optical density of the BEC which overwhelms the density dips of the vortex cores. (d) dependence of the inferred vortex spacing on detuning, showing a slight dispersive variation, originating from a lensing effect originating from the inhomogeneous BEC density.

BEC density, which modifies the apparent magnification of the imaging system. This lensing effect follows a dispersive shape around the D2 ($F = 1 \rightarrow F' = 0$) resonance used for imaging. Figure E.1 (d) shows the inferred vortex spacing as a function of probe laser detuning from atomic resonance, exhibiting the expected slight dispersive variation. The *unperturbed* vortex spacing is given by the constant value at large positive and negative detuning.

The resulting image magnification, in lab units, is $2.04(2) \mu\text{m}$ per CCD pixel. The CCD pixel separation is $13 \mu\text{m}$, giving a magnification of $13 \mu\text{m} / 2.04 \mu\text{m} = 6.37$.

E.2 Side view calibration by releasing a BEC from a 1D optical lattice

For determination of the side view imaging magnification, we release the BEC suddenly from an applied vertical optical lattice (Fig. E.2, left image) of known lattice period d ($d = \lambda/2$ where $\lambda = 852.2\text{ nm}$ is the wavelength of the lattice laser whose frequency is locked to the D2 transition in ^{133}Cs). We employ a release procedure, described below, which causes the BEC to split into two momentum components $\pm\hbar k$ ($k = \pi/d$). These components separate spatially after a certain free time-of-flight t , see Fig. E.2, right image. This separation is given by (m is the mass of ^{87}Rb)

$$\Delta x_{calc} = \frac{2\hbar k}{m}t \quad (\text{E.1})$$

From the accurately measured time-of-flight of $t = 13.5\text{ ms}$, the measured separation of the BEC momentum components Δx_{meas} and the accurately known lattice period d the image magnification is determined as $\frac{\Delta x_{calc}[\mu\text{m}]}{\Delta x_{meas}[\text{pixel}]}$. The result, an average over ≈ 20 individual shots, is $2.27(5)\ \mu\text{m}$ per camera pixel, i.e. a magnification of 5.73.

The precise experimental procedure is as follows: we adiabatically load a BEC into the optical lattice and allow it to equilibrate. We then turn off the magnetic trap but keep the optical lattice on. The hold time $T_B/2 = h/(2mgd)$, where h is Planck's constant and $g = 9.81\text{ m/s}^2$, allows gravity to induce half a Bloch oscillation, as described in Chapter 4. The effect is to transfer the BEC momentum state from the center to the edge of the Brillouin zone, creating a superposition of two momentum components $\pm\hbar k$. At this point we release the BEC abruptly from the optical lattice.

Again, there are possible systematic effects. We worked with the tiniest possible BEC to minimize a mean-field effect arising when the two BECs separate, as well as to minimize s-wave scattering during separation of the momentum components which can distort their density profiles after separation. A second systematic is a possible tilt

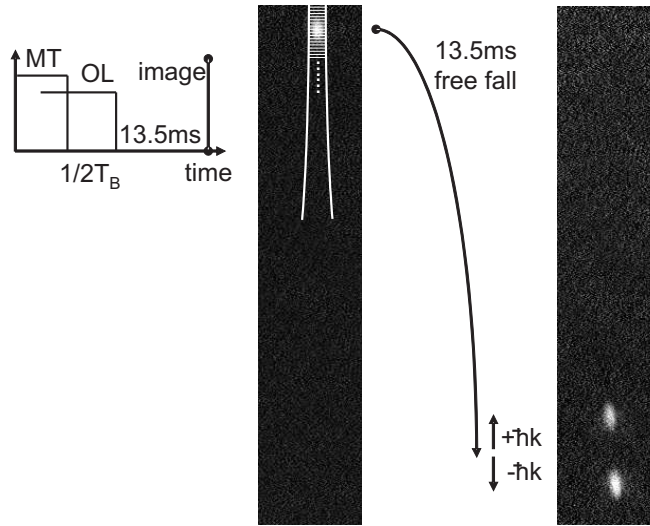


Figure E.2: Calibration of side view image magnification by releasing Bloch-oscillating BEC from vertical optical lattice. Left: time sequence of the experiment. MT: magnetic trap. OL: optical lattice. T_B : Bloch period, see text. Center image: BEC in the optical lattice. Right image: BEC after time-of-flight. From the separation of the two momentum components the image magnification is determined.

of the optical lattice perpendicular to the image plane¹. We estimate this tilt to be not larger than $\approx 5^\circ$, and hence the error due to projection in the image plane to be smaller than 1%. A last possible systematic effect has to do with the Guoy phase shift acquired by a Gaussian beam upon traversing its focus. This phase shift causes the effective optical lattice period at positions close to the focus to deviate slightly from $\lambda/2$. We find that the effective period is $\frac{\lambda}{2}(1 + \frac{\lambda^2}{2\pi^2 w^2})$ where $w \approx 100 \mu m$ is the optical lattice waist. In our case, the relative change of the lattice period is negligible, $\approx 10^{-5}$. This effect might however be important in precision measurements in optical lattices.

This method of determining the image magnification is preferable to switching off the magnetic trap, releasing the BEC and measuring its fall distance vs. time. In that procedure, initial BEC slosh and possible accelerations in the process of magnetic trap turn-off are could systematically influence the measurement. The measurement of *relative* motion performed here is largely immune to these effects.

¹ The visible tilt of the axis connecting the separating BECs is due to optical lattice tilt in the image plane, and is taken into account in the measurement of the separation of the momentum components.

Appendix F

The End



Figure F.1: Thanks, everyone!